SERIES IN OPTICS AND OPTOELECTRONICS

Principles of Adaptive Optics

Third Edition

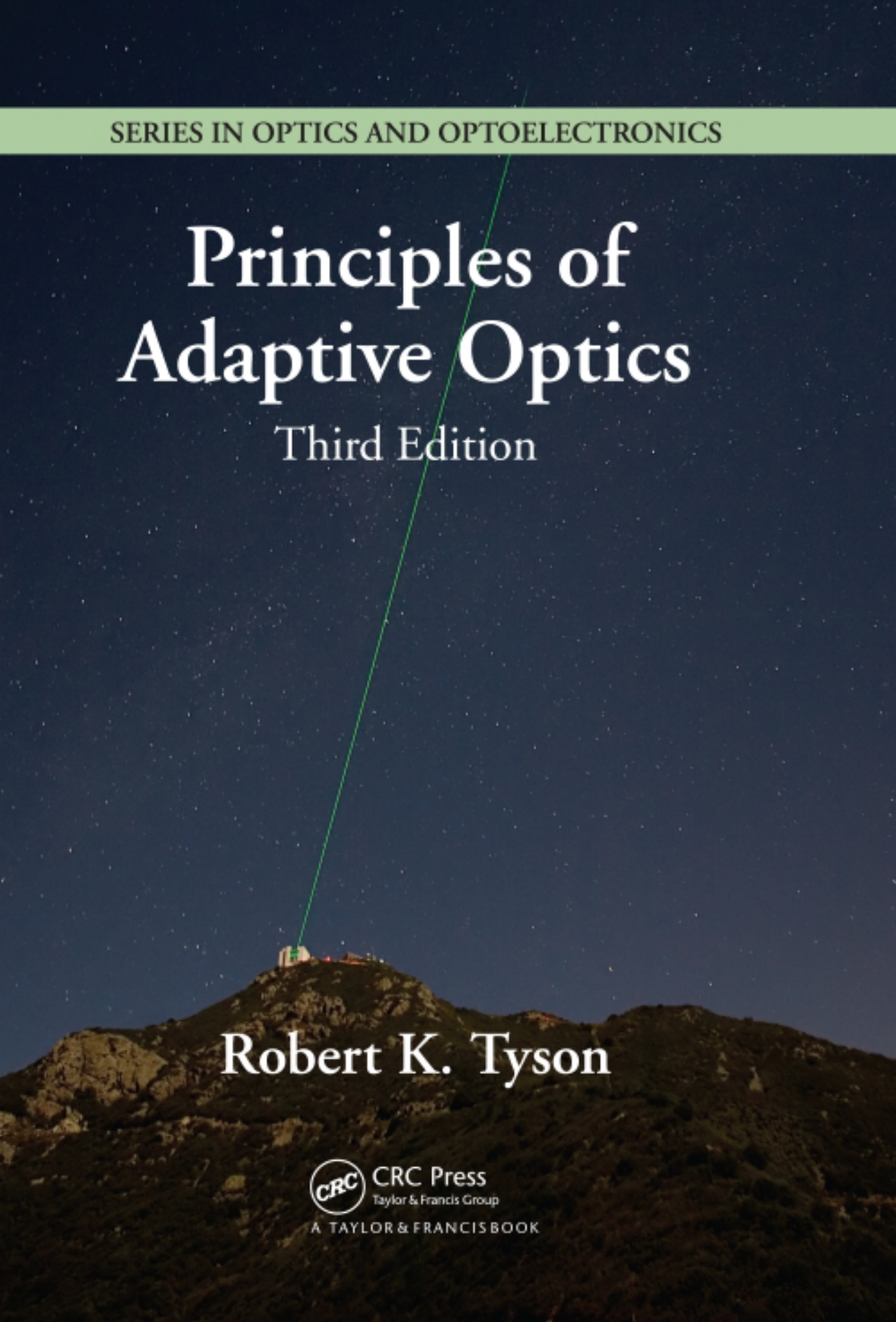

Robert K. Tyson

CRC Press
Taylor & Francis Group
A TAYLOR & FRANCIS BOOK

Principles of Adaptive Optics

Third Edition

SERIES IN OPTICS AND OPTOELECTRONICS

Series Editors: **E. RoyPike**, Kings College, London, UK
Robert G. W. Brown, University of California, Irvine

Recent titles in the series

Thin-Film Optical Filters, Fourth Edition
H Angus Macleod

Optical Tweezers: Methods and Applications
Miles J Padgett, Justin Molloy, David McGloin (Eds.)

Principles of Nanophotonics
Motoichi Ohtsu, Kiyoshi Kobayashi, Tadashi Kawazoe
Tadashi Yatsui, Makoto Naruse

The Quantum Phase Operator: A Review
Stephen M Barnett, John A Vaccaro (Eds.)

An Introduction to Biomedical Optics
R Splinter, B A Hooper

High-Speed Photonic Devices
Nadir Dagli

Lasers in the Preservation of Cultural Heritage: Principles and Applications
C Fotakis, D Anglos, V Zafiropulos, S Georgiou, V Tornari

Modeling Fluctuations in Scattered Waves
E Jakeman, K D Ridley

Fast Light, Slow Light and Left-Handed Light
P W Milonni

Diode Lasers
D Sands

Diffractional Optics of Millimetre Waves
I V Minin, O V Minin

Handbook of Electroluminescent Materials
D R Vij

Handbook of Moire Measurement
C A Walker

Next Generation Photovoltaics
A Martí, A Luque

Stimulated Brillouin Scattering
M J Damzen, V Vlad, A Mocofanescu, V Babin

Principles of Adaptive Optics

Third Edition

Robert Tyson
University of North Carolina
Charlotte, USA

CRC Press
Taylor & Francis Group
Boca Raton London New York

CRC Press is an imprint of the
Taylor & Francis Group, an **informa** business

A TAYLOR & FRANCIS BOOK

CRC Press
Taylor & Francis Group
6000 Broken Sound Parkway NW, Suite 300
Boca Raton, FL 33487-2742

Printed in the United States of America on acid-free paper
10 9 8 7 6 5 4 3 2 1

International Standard Book Number-13: 978-1-4398-0859-7 (Ebook-PDF)

To Peggy, Andy, Chip, Kia, and Chase

Contents

Foreword

Adaptive optics (AO) is one of the most exciting advances in optical imaging in the past twenty years. Conceived in 1953 by Horace Babcock, the subject remained a scientific curiosity until it was developed, at enormous expense, for military purposes. A rebirth of the subject occurred in the late 1980s, when astronomers built the first 19-actuator AO system, "COME-ON," for the European Southern Observatory's 3.6-meter telescope at La Silla, Chile. Now, all of the world's large telescopes have sophisticated AO systems, and there is an alphabet-soup of acronyms—laser guide star adaptive optics (LGSAO), multi-conjugate adaptive optics system (MCAO), laser tomography adaptive optics (LTAO), ground layer adaptive optics (GLAO), extreme adaptive optics (XAO), and multi-object adaptive optics (MOAO)—for the different varieties of AO being developed for astronomy. The next generation of ground-based telescopes, with diameters upward of 30 meters, will have AO systems whose deformable mirrors will have more than 5,000 actuators.

Concurrent with the development of top-end AO for astronomy, there has been a growing list of applications for "low-cost" AO. Until a decade ago, AO had a big-science mentality: teams of dedicated engineers were required to build successful AO systems. In fact, AO is not rocket science, and any competent graduate student can build his or her own AO system in a few months for a cost as low as $10,000 (and a copy of this book). The lowest-cost AO system, using a 14-actuator spatial light modulator and costing less than $1, is used in one manufacturer's DVD players.

When Bob Tyson's *Principles of Adaptive Optics* was first published in 1991, it immediately became the reference text for everyone working in the field. The comprehensive coverage of all aspects of the field, clear explanations, and extensive reference to the original literature ensured its success. This completely revised and updated third edition retains the strengths of the original text. Everyone involved in AO should have a copy on the shelf, and like the original, the extensive list of references (more than 900) provides an excellent pointer to the original literature.

Christopher Dainty
National University of Ireland, Galway

Preface

Since the publication of the second edition of *Principles of Adaptive Optics* in 1997, there has been a virtual explosion in the developments and applications of adaptive optics. Observatories are now producing outstanding science with adaptive optics technology rather than developing first-generation adaptive optics systems, as was the case in the 1990s. Many components, such as micromachined deformable mirrors and very low noise detectors, have revolutionized the field. While the principles remain essentially the same, the application and complexity of those principles has increased dramatically.

There also has been a rapid rise in industrial and medical applications of adaptive optics, including improvements in laser propagation for free-space laser communications, beam control in laser-induced fusion, and medical retinal imaging. This edition, similar to the last, is intended to compile recent developments and add a fresh supply of new references. Well over 10,000 publications in books, journals, and conference proceedings now document this multidisciplinary field. I have tried to cite recent papers, major contributions, or seminal papers along the way. I sincerely apologize to those who have not received recognition in the bibliography. If you care to help fund my research over the next few years, you will be prominently mentioned in the fourth edition.

Robert K. Tyson
Charlotte, North Carolina

Author

Robert K. Tyson is an associate professor of physics and optical science at the University of North Carolina (UNC) at Charlotte. He has a bachelor's degree in physics from Pennsylvania State University and MS and PhD degrees in physics from West Virginia University. He has been working in the field of adaptive optics for over thirty years and has taught many courses on the topic, in addition to writing numerous books, this being the seventh. Before joining UNC-Charlotte in 1999, he worked in the aerospace industry designing systems and supporting technology for strategic-defense high-energy laser weapons systems.

1

History and Background

1.1 Introduction

Adaptive optics is a scientific and engineering discipline whereby the performance of an optical signal is improved by using information about the environment through which it passes. The optical signal can be a laser beam or a light that eventually forms an image. The principles used to extract that information and apply the correction in a controlled manner make up the content of this book.

Various deviations from this simple definition make innovation a desired and necessary quality of the field. Extracting the optical information from beams of light coming from galaxies light-years away is a challenge [47,524]. Applying a correction to a beam that has the power to melt most man-made objects pushes the state of technology. Adaptive optics is changing; it is growing. It has become a necessary technology in optical systems that are constrained by dynamic aberrations.

Developments in adaptive optics have been evolutionary. There is no single *inventor* of adaptive optics. Hundreds of researchers and technologists have contributed to the development of adaptive optics, primarily over the past thirty-five years. There have been great strides and many, many small steps. The desire to both propagate an undistorted beam of light, or to receive an undistorted image [71], has made the field of adaptive optics a scientific and engineering discipline in its own right.

Adaptive optics has clearly evolved from the understanding of wave propagation. Basic knowledge of physical optics is aided by the development of new materials, electronics, and methods for controlling light. Adaptive optics encompasses many engineering disciplines. This book will focus on the *principles* that are employed by the technological community that requires the use of adaptive optics methods. That community is large, and the field could encompass many of the topics normally found in texts dealing with optics, electronic controls, and material sciences. This book is intended to condense the vast array of literature and provide a means to apply the principles that have been developed over the years.

If everything concerned with actively controlling a beam of light is considered adaptive optics, then the field is indeed very broad. However, the most commonly used restriction of this definition leads to the approach that adaptive optics deals with *the control of light in a real-time closed-loop fashion*. Therefore, *adaptive optics* is a subset of the much broader discipline, *active optics*. The literature often confuses and interchanges the usage of these terms,* and examples in this book show that discussion of *open-loop* approaches to some problems often should be considered [672].

Other restrictions on the definition of *adaptive optics* have been observed. For the purposes of this book, adaptive optics includes more than *coherent, phase-only* correction. There are a number of techniques that use intensity correction for the control of light, and other techniques that make multiple corrections over various pupil conjugates. Incoherent imaging is definitely within the realm of adaptive optics.

The existence of the animal visual system is an example of adaptive optics having been in use for much longer than recorded history. The eye is capable of adapting to various environmental conditions to improve its imaging quality. The active focus "system" of the eye–brain combination is a perfect example of adaptive optics. The brain interprets an image, determines the correction, either voluntary or involuntary, and applies that correction through biomechanical movement of parts of the eye, such as the lens or cornea. When the lens is compressed, the focus is corrected. The eye–brain system can also track an object's direction. This is a form of a tilt-mode adaptive optics system. The iris can open or close in response to light levels, which demonstrates adaptive optics in an intensity-control mode; and the muscles around the eye can force a "squint" that, as an aperture stop, is an effective spatial filter and phase-controlling mechanism. This is both *closed-loop* and *phase-only* correction.

The easiest answer to the layman's question, "What is adaptive optics?" is straightforward, albeit not completely accurate: "It's a method of automatically keeping the light focused when it gets out of focus." Every sighted person understands when something is not in focus. The image is not clear and sharp; it is fuzzy. If we observe light that is not in focus, we can either move to a position where the light is in focus or, alternately, apply a correction without any movement to bring the beam into focus. This is a principle that our eyes apply constantly. The adaptive process of focus sensing is a learned process, and the correction (called an *accommodation*) is a learned response. When the correction reaches its biophysical limit, we require outside help, that is, corrective lenses. The constant adjustment of our eyes is a closed-loop adaptive process performed using optics. It is therefore called adaptive optics.

* Wilson et al. [869] differentiate them by bandwidth. They refer to systems operating below 1/10 Hz as *active* and those operating above 1/10 Hz as *adaptive*. This definition is used widely in the astronomy community.

1.2 History

Many review authors [320,603] cite Archimedes's destruction of the Roman fleet in 215 BC as an early use of adaptive optics. As the attacking Roman fleet approached the army defending Syracuse, the soldiers lined up so that they could focus sunlight on the sides of the ships. By polishing their shields or some other "burning glass" and properly positioning each one, hundreds of beams were directed toward a small area on the side of a ship. The resultant intensity was apparently enough to ignite the ship and defeat the attackers. The "burning glass" approach by Archimedes was clearly innovative; however, details of the scientific method are scarce [144,743]. Whether a feedback loop or phase control was used was never reported, but the survival of Syracuse was.

The use of adaptive optics has been limited by the technology available. Even the greatest minds of physical science failed to see its utility. Isaac Newton, writing in *Opticks* in 1730, saw no solution to the problem of limitations imposed by atmospheric turbulence in astronomy [559].

> If the Theory of making Telescopes could at length be fully brought into Practice, yet there would be certain Bounds beyond which Telescopes could not perform. For the Air through which we look upon the Stars, is in perpetual Tremor; as may be seen by the tremulous Motion of Shadows cast from high Towers, and by the twinkling of the fix'd Stars. But these Stars do not twinkle when viewed through Telescopes which have large apertures. For the Rays of Light which pass through diverse parts of the aperture, tremble each of them apart, and by means of their various and sometimes contrary Tremors, fall at one and the same time upon different points in the bottom of the Eye, and their trembling Motions are too quick and confused to be perceived severally. And all these illuminated Points constitute one broad lucid Point, composed of those many trembling Points confusedly and insensibly mixed with one another by very short and swift Tremors, and thereby cause the Star to appear broader than it is, and without any trembling of the whole. Long Telescopes may cause Objects to appear brighter and larger than short ones can do, but they cannot be so formed as to take away that confusion of the Rays which arises from the Tremors of the Atmosphere. The only Remedy is a most serene and quiet Air, such as may perhaps be found on the tops of the highest Mountains above the grosser Clouds.

In 1953, Babcock [45] proposed the use of a deformable optical element, driven by a wavefront sensor, to compensate for atmospheric distortions that affected telescope images. This appears to be the earliest reference to use of adaptive optics as we define the field today. Linnik described how a beacon placed in the atmosphere could be used to probe the disturbances [466]. Although Linnik's paper is the first reference to what we now refer to as "guide stars," his concept precedes the invention of the laser and was, until the early 1990s, unknown to Western scientists developing laser guide stars.

Development of the engineering disciplines involved in adaptive optics has taken a course common to technology development. As problems arose, solutions were sought. Directed research within the field was often aided by innovations and inventions on the periphery. The need to measure the extent of the optical problem and to control the outcome was often dependent upon the electronics or computer capability of the day, the proverbial "state-of-the-art."

Other methods that do not employ real-time wavefront compensation, such as speckle interferometry [441,662] or hybrid techniques combining adaptive optics and image postprocessing, have been successful. These are described by Roggemann and Welsh [672].

A review article by Hardy [320] gives an excellent account of the history of active and adaptive optics, describing the state-of-the-art as it was in 1978. The developments of the first three decades are described in detail through this book and reviewed by Babcock [46], Hardy [322], Greenwood and Primmerman [309], Benedict et al. [77], and others [794]. In 1991, much of the military work in adaptive optics in the United States was declassified [257,632]. Research involving laser guide stars [210] was published and discussed to enhance the research work that was developing in the astronomical community [229].

Scientific journals and technical societies continually publish new techniques and results. In addition to technology development and field demonstrations, the first results for an infrared adaptive optics system on an astronomical telescope were presented in 1991 [526]. Results from other systems around the world continue to be presented One example of the exciting improvements in astronomical imaging is shown in Figure 1.1. The history of adaptive optics continues to be written.

1.3 Physical Optics

The principles of adaptive optics are based on the premise that one can change the effects of an optical system by adding, removing, or altering optical elements. For most optical systems of interest, diffraction effects are harmful. In other words, they make the propagation of a beam of light or the image of an object *different*. When a beam is propagated, either collimated or focused, we normally want *all* of the light to reach the receiver in the best condition. Similarly, for an imaging system, we want the image to be the best reproduction of the object that we can get. Diffractive effects degrade the image because they degrade the propagation process. We cannot get rid of diffractive effects; they are inherent in Maxwell's laws. The best that we can do is reach the limit of diffraction. When mechanical or thermal defects degrade the image or propagation process beyond the diffraction limit, we can try to alter the optical system to compensate for the defects even though we cannot get rid of them.

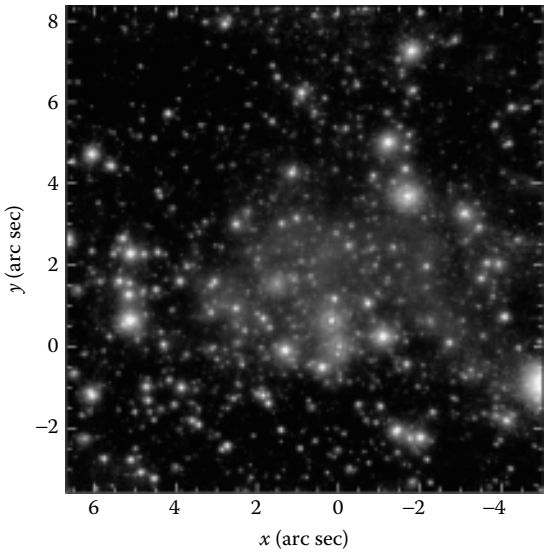

FIGURE 1.1
Image of the irregular dwarf galaxy IC-10 in the constellation Cassiopeia, taken using the W. M. Keck Observatory adaptive optics system. (Photo courtesy of SOFIA-USRA, NASA Ames Research Center, Moffett Field, CA. Vacca, W. D., C. D. Sheehy, and J. R. Graham. 2007. *Ap J* 662, 272–83. With permission.)

1.3.1 Propagation with Aberrations

One way to describe the propagation of light as it applies to adaptive optics is through mathematical formalism. Literally hundreds of volumes have been written describing optical propagation. The classic text by Born and Wolf [89] describes it in a manner that clearly shows the effects of the phase of an optical field in a pupil plane on the resultant field in an "image" plane.

For a beam of coherent light at wavelength λ, the intensity of light at a point P on the image, or focal, plane at a distance of z is given by

$$I(P) = \left(\frac{Aa^2}{\lambda R^2}\right)^2 \left| \int_0^1 \int_0^{2\pi} e^{i[k\Phi - \upsilon\rho\cos(\theta-\psi) - \frac{1}{2}u\rho^2]} \rho d\rho d\theta \right|^2 \tag{1.1}$$

where the circular pupil has radius a and coordinates (ρ, θ); the image plane has polar coordinates (r, ψ); the coordinate z is normal to the pupil plane; R is the slant range from the center of the pupil* to point P; $k = 2\pi/\lambda$; and $k\Phi$ is the deviation in phase from a perfect sphere about the origin of the focal

* R is also the radius of the wavefront sphere that would perfectly focus at P.

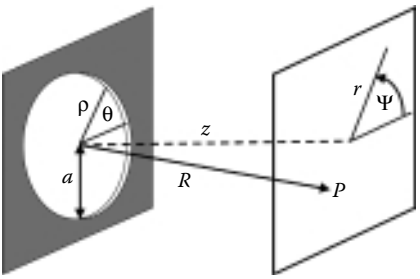

FIGURE 1.2
The coordinate system for the calculation of the diffraction with an aberration **Φ**.

plane (Figure 1.2). To simplify the presentation, normalized coordinates in the focal plane are used as follows:

$$u = \frac{2\pi}{\lambda}\left(\frac{a}{R}\right)^2 z \tag{1.2}$$

$$\upsilon = \frac{2\pi}{\lambda}\left(\frac{a}{R}\right) r \tag{1.3}$$

The amplitude of a uniform electric field in the pupil plane is A/R; and therefore, the intensity in the pupil plane, $I_{z=0}$, is A^2/R^2.

From the viewpoint of adaptive optics, the most important quantity in the above expressions is Φ, which is often mistakenly called simply *phase*. It is more commonly referred to as the *wavefront*. The symbol Φ represents all the aberrations that are present in the optical system before its propagation to point *P*. If no aberrations are present, the intensity is a maximum on-axis ($r = 0$) intensity, which is called the Gaussian image point.

$$I_{\Phi=0}(P_{r=0}) = \pi^2\left(\frac{Aa^2}{\lambda R^2}\right)^2 = \left(\frac{\pi^2 a^4}{\lambda^2 R^2}\right) I_{z=0} \tag{1.4}$$

The *Strehl ratio* (*S*), also called the normalized intensity, is the ratio between the on-axis intensity of an aberrated beam and that of an unaberrated beam. If the tilt (distortion) aberration is not removed, the *axis* of this definition would be normal to the plane of that tilt, rather than parallel to the *z*-axis. Static tilt should be removed when the Strehl ratio is used as a figure of merit for the quality of beam propagation.

Combining Equations 1.1 and 1.4, the Strehl ratio becomes

$$S = \frac{I(P)}{I_{\Phi=0}} = \frac{1}{\pi^2}\left|\int_0^1\int_0^{2\pi} e^{i[k\Phi - v\rho\cos(\theta-\psi)-\frac{1}{2}u\rho^2]}\rho d\rho d\theta\right|^2 \tag{1.5}$$

For small aberrations, when tilt* is removed and the focal plane is displaced to its Gaussian focus, the linear and quadratic terms in the exponential of Equation 1.5 disappear. If the remaining aberrations, which are now centered about a sphere with reference to point *P,* are represented by Φ_P, the Strehl ratio simplifies to

$$S = \frac{1}{\pi^2}\left|\int_0^1\int_0^{2\pi} e^{ik\Phi_P}\rho d\rho d\theta\right|^2 \tag{1.6}$$

which shows how the wavefront affects the degradation of the propagation. If the beam at the pupil is unaberrated, $\Phi_P = 0$, and the Strehl ratio reduces to unity, $S = 1$; that is, the intensity at the focus is diffraction-limited. Equation 1.4 shows that the absolute intensity is enhanced by a factor proportional to the square of the *Fresnel number*, $a^2/\lambda R$. A larger aperture, a smaller wavelength, or a shorter propagation distance will increase the maximum intensity in the focal plane. All systems with *any* aberration at all, that is, $\Phi_P > 0$, will have a Strehl ratio less than 1. If the wavefront aberration is small, its variance can be directly related to the Strehl ratio. The wavefront variance $(\Delta\Phi_P)^2$ can be found from the expression

$$(\Delta\Phi_P)^2 = \frac{\int_0^1\int_0^{2\pi}(\Phi_P - \overline{\Phi_P})^2\rho d\rho d\theta}{\int_0^1\int_0^{2\pi}\rho d\rho d\theta} \tag{1.7}$$

where $\overline{\Phi_P}$ is the average wavefront. It can be shown [89] that the Strehl ratio for $\Delta\Phi_P < \lambda/2\pi$ is as follows:

$$S = 1 - \left(\frac{2\pi}{\lambda}\right)^2(\Delta\Phi_P)^2 \cong \exp\left[-\left(\frac{2\pi}{\lambda}\right)^2(\Delta\Phi_P)^2\right] \tag{1.8}$$

which gives a simple method of evaluating the propagation quality of a system by considering only the small variance in the wavefront. The square root of the variance, formally, the standard deviation of the wavefront, $\Delta\Phi_P$, is often called the root-mean-square phase error, the rms phase error, phase error, or

* For the purposes of this text, tilt is a component of Φ linear in the coordinates $\rho\cos\theta$ or $\rho\sin\theta$ in the pupil plane.

wavefront error. These terms are used interchangeably in the literature The fact that the quality of beam propagation can be directly related to the rms phase error is a very powerful result.

1.3.2 Imaging with Aberrations

The physical processes behind imaging combine the process of propagation with the effects of lenses, mirrors, and other imaging optics. The process that combines these effects results from an examination of Kirchoff's formula for propagation, which is a more generalized form of Equation 1.1. The field at point P, in the x–y plane $U(P)$, is given by [89]

$$U(x,y) = \frac{-iA}{2\lambda}\int\int_{Ap} \frac{e^{ik(r+s)}}{rs}[\cos(n,r) - \cos(n,s)]dS \tag{1.9}$$

where the coordinates are defined in Figure 1.3 and the integral is over the aperture. Here, A is the amplitude of the field with a plane wave, represented by $U(z)_{\text{plane}} = Ae^{\pm ikz}$, and a spherical wave, represented by $U(z)_{\text{sph}} = A/re^{\pm ikr}$. The source is in the x_0–y_0 plane with a distance z_0 to the x'–y' pupil plane. The distance z represents the distance from the pupil to the image plane.

For large propagation distances, that is, $z >$ the largest of x, y, x', y', x_0, or y_0, Equation 1.9 reduces to the Fresnel integral as follows:

$$U(x,y) = C'\int\int_{Ap} e^{ikf(x',y')}dx'dy' \tag{1.10}$$

where the term C' is not a function of the pupil coordinates and can be represented as follows:

$$C' \equiv \frac{-A}{2\lambda}[\cos(n,r) - \cos(n,s)]\frac{e^{ik(z_0+z)}}{zz_0}\exp\left[\frac{ik}{2z_0}\left(x_0^2 + y_0^2\right)\right]\exp\left[\frac{ik}{2}(x^2 + y^2)\right] \tag{1.11}$$

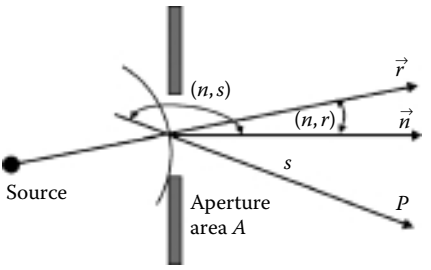

FIGURE 1.3
The geometry of the Kirchoff formula.

and the function in the exponent is

$$f(x',y') = \frac{1}{2}(x'^2 + y'^2)\ (z_0^{-1} + z^{-1}) - x'\left(\frac{x_0}{z_0} + \frac{x}{z}\right) - y'\left(\frac{y_0}{z_0} + \frac{y}{z}\right) \tag{1.12}$$

In many beam-propagation or astronomical-imaging applications, the propagation distances are quite large. Applying the following approximations,

$$z_0 \gg \frac{(x'^2 + y'^2)_{\max}}{\lambda}; \quad \text{and} \quad z > \frac{(x'^2 + y'^2)_{\max}}{\lambda} \tag{1.13}$$

the Kirchoff integral reduces to the Fraunhofer integral as follows:

$$U(x,y) = C' \int\int_{A\mathrm{p}} \exp\left\{-ik\left[\left(\frac{x_0}{z_0} + \frac{x}{z}\right)x' + \left(\frac{y_0}{z_0} + \frac{y}{z}\right)y'\right]\right\} \mathrm{d}x'\mathrm{d}y' \tag{1.14}$$

Combining the terms in C' and the terms in the kernel that relate to the source in the x_0–y_0 plane, the integral takes the form of a Fourier transform:

$$U(x,y) = C' \int\int_{-\infty} U(x',y')_{A\mathrm{p}} \exp\left\{\frac{ik}{z}(xx' + yy')\right\} \mathrm{d}x'\,\mathrm{d}y' \tag{1.15}$$

Equation 1.15 can be written in a shortened notation as follows:

$$U(x,y) \propto F[U(x',y')] \tag{1.16}$$

In the preceding equation, F represents the Fourier transform operation and $U(x', y')$ is the *pupil function* or *aperture function*. When the optical system contains aberrations Φ, the pupil function can be written as

$$U(x',y') = A(x',y')e^{ik\Phi(x',y',x_0,y_0)} \tag{1.17}$$

which uses the fact that aberrations are derived from all elements of the optical system, including the physical pupil in the (x', y') plane.

When no aberrations are present and the aperture is a simple geometrical shape, Equation 1.15 can be solved exactly. For a rectangular aperture of sides $2a$ and $2b$, after a propagation distance L, the normalized field that results from Fraunhofer diffraction is

$$U(x,y) = \frac{4L^2 \sin\left(\frac{kax}{L}\right)\sin\left(\frac{kby}{L}\right)}{k^2 xy} \tag{1.18}$$

An important result is the Fraunhofer diffraction from a circular aperture. In polar coordinates, the normalized field becomes

$$U(r,\theta) = \frac{\lambda L}{\pi a r} J_1\left(\frac{2\pi a r}{\lambda L}\right) \tag{1.19}$$

where J_1 is the first-order Bessel function of the first kind. The intensity of light from the diffracted field is the square of the magnitude of these fields, that is, $I = |U|^2$.

The pupil function of an imaging system is modified by the effect of lenses and other focusing optics. A lens transmission function is given in one form by Gaskill [265]:

$$T_{\text{lens}} = \exp\left[\frac{-i\pi}{\lambda f}(x^2 + y^2)\right] \tag{1.20}$$

where f is the focal length of the lens. The process of adding lens transmission functions and intermediate propagations to the integral equations reduces Equation 1.15 to

$$U(x,y) = C' \int\int U(x',y') \exp\left[-ik\left(\frac{1}{z} - \frac{1}{f}\right)(xx' + yy')\right] dx'dy' \tag{1.21}$$

which shows the retention of the Fourier transform properties of the imaging system with f as its effective focal length. By introducing a coordinate change in the image plane,

$$\xi = \frac{kx}{f} \tag{1.22}$$

and

$$\eta = \frac{ky}{f} \tag{1.23}$$

the Fraunhofer diffraction becomes

$$U(\xi,\eta) = C' \int\int U(x',y') e^{-i(\xi x' + \eta y')} dx'dy' \tag{1.24}$$

which shows that the Fraunhofer diffraction pattern, at focal distance f, is the Fourier transform of the pupil function.

For pupils with and without aberrations, this diffraction pattern is called the *point spread function*, or PSF. The new coordinates (ξ, η) have the units of inverse distance and are called *spatial frequencies*. This is analogous to the

spectra calculated in the time domain, where frequency is the inverse of time. In imaging applications, spatial frequencies are usually two dimensional.

Some important physical results can be derived from Equation 1.24. If the pupil function is spatially limited, such as that with a finite aperture, the Fourier transform operation cuts out the high spatial frequencies of the objects, which contain the fine detail of the object. Therefore, an imaging system that can pass these high frequencies, such as one with a large aperture, is "better" because it can produce images with high resolution. In addition, an aberration-free pupil will not produce an image where the high-frequency characteristics of the aberrations screen the high-frequency content of the object. This is the principal need for adaptive optics in imaging systems. The fact that image-forming quality can be specified by a function that describes how much spatial frequency content is passed to the image is an important result of Equation 1.24.

The field of the image for a coherent imaging system* can be expressed [265] as the convolution of the geometrical image with the PSF as follows:

$$U_{\text{im}} = W[(U_{\text{geom im}}) ** \text{PSF}] \tag{1.25}$$

The geometrical image is the distribution of the object that has been adjusted for imaging system magnification, shifting along the plane, and geometrical (ray trace) shadows and differences of intensity. In many discussions of imaging in literature [299], the terms *geometrical image* and *object* are used interchangeably. This is not a problem until exact calculations are performed, because the principles of imaging are the same. The constant W takes into account the radiance of the object and the constant transmission or absorption of elements within the system. The two-dimensional (2-D) convolution process, represented by $**$ in Equation 1.25, accounts for the diffraction effects of the optics. The convolution operation can be Fourier-transformed on both sides [299] as follows:

$$F(U_{\text{im}}) = W \bullet [F(U_{\text{geom im}})F(\text{PSF})] \tag{1.26}$$

The Fourier transform of the PSF is itself a measure of the imaging quality of a system. The *optical transfer function*, or OTF, represents how each spatial frequency in an object field is *transferred* to the image [351,352] as follows:

$$\text{OTF} = F(\text{PSF}) \tag{1.27}$$

One definition of the *resolution* of a system is the spatial frequency at which the OTF vanishes. In many circumstances, this is more descriptive of the optical system than the simple Rayleigh criterion of resolution [89].†

---

* Incoherent and white light imaging systems are treated in a similar manner, but the exact form of the expression is different.

† Lord Rayleigh proposed that two equal, but displaced, objects are "resolved" when the principal intensity maximum of one coincides with the first intensity minimum of the other [639].

Because one observes the intensity distribution of images rather than the electric fields, the magnitudes of the fields are important. The objects and images are formed from the Fourier components of the intensity. Considering one frequency component, ξ for instance, the intensity of the object, I_{obj}, can be represented by a constant and a frequency component as follows:

$$I_{obj} = b_0 + b_1 \cos 2\pi\xi x \tag{1.28}$$

Similarly, the intensity of the image can be written as

$$I_{im} = c_0 + c_1 \cos 2\pi\xi x \tag{1.29}$$

The modulation, or contrast, M, is the relationship between the peaks and valleys of the intensity at the designated frequency.

$$M = \frac{I_{max} - I_{min}}{I_{max} + I_{min}} \tag{1.30}$$

When substituting the expressions for the individual intensities, the modulation M becomes normalized to the constant level of intensity. The results are

$$M_{obj}(\xi) = \frac{b_1(\xi)}{b_0(\xi)} \quad \text{and} \quad M_{im}(\xi) = \frac{c_1(\xi)}{c_0(\xi)} \tag{1.31}$$

It can be shown as follows [265] that the ratio of these modulations is the magnitude of the OTF:

$$|\,\mathrm{OTF}(\xi)\,| = \frac{M_{im}}{M_{obj}} \tag{1.32}$$

The magnitude of the OTF is the ratio of how much modulation in the object was transferred to modulation in the image. This function, called the *modulation transfer function* (MTF), is a very useful measure of the ability of an imaging system to transfer spatial detail. The MTF contains no phase information because it is only the magnitude of the OTF. A perfect system has an MTF equal to 1 at all frequencies, which requires an infinitely large aperture. The MTF of realistic systems is less than 1 for all spatial frequencies greater than zero.

1.3.3 Representing the Wavefront

A number of mathematical constructs are used to describe the phase of a beam. The deviation of phase from a reference sphere [89] is the wavefront. In adaptive optics, the wavefront is usually the quantity that is changed to alter the propagation characteristics of the beam.

The *wavefront* is a 2-D map of the phase at an aperture or any other plane of concern that is normal to the line of sight between the origin of the beam and the target. In an imaging system, the plane of concern would be normal to

the line of sight between the object and the image. By this definition, the tilt of the beam would be considered part of the wavefront. In many instances, the tilt and the piston* are of interest for adaptive optics and are included. The wavefront is positive in the direction of propagation.

1.3.3.1 Power-Series Representation

One way to represent the 2-D wavefront map is using a power series in polar (ρ, θ) coordinates:

$$\Phi(\rho,\theta) = \sum_{n,m=0}^{\infty} S_{n,m1}\,\rho^n \cos^m\theta + S_{n,m2}\,\rho^n \sin^m\theta \tag{1.33}$$

In this series, the primary, or Seidel, aberrations [89] are explicit. A coordinate transformation to Cartesian coordinates is easily made ($x = \rho\cos\theta$, $y = \rho\sin\theta$). Table 1.1 shows the first few Seidel terms.

1.3.3.2 Zernike Series

The commonality of circular apertures, telescopes, and lenses make treatment in polar coordinates very attractive. The power-series representation is, unfortunately, not an orthonormal set over a circle. One set of polynomials that are orthonormal over a circle, introduced by Zernike [903], has some very useful properties. The series, called a *Zernike series*, is composed of sums of power series terms with the appropriate normalizing factors. A detailed description of the Zernike series is given by Born and Wolf [89], and an analysis of Zernike polynomials and atmospheric turbulence, including their Fourier transforms, was done by Noll [570].† Roddier [665] shows how

TABLE 1.1

Representation of the First Few Seidel Terms

n	*m*	Representation	Description
0	0	1	Piston
1	1	$\rho\cos\theta$	Tilt, distortion
2	0	ρ^2	Focus, field curvature, "sphere"
2	2	$\rho^2\cos^2\theta$	Astigmatism, cylinder
3	1	$\rho^3\cos\theta$	Coma
4	0	ρ^4	Spherical aberration

* Piston is the constant retardation or advancement of the phase over the entire beam.

† There is a difference in the normalization between the series described by Born and Wolf and that of Noll. Each of Noll's polynomials should be multiplied by the factor $(2(n+1))^{-1/2}$ to obtain the Born and Wolf normalization.

Zernike polynomials can be used in modeling to describe the phase aberrations of the atmosphere. Winker expands the analysis technique to include the effects of a finite outer scale of turbulence [871], whereas Boreman and Dainty [88] present a generalization that includes non-Kolmogorov turbulence [291]. Other non-Kolmogorov models are used that better support local propagation measurements [73,451,904].

The general Zernike series contains all aberration terms, including piston and tilt, as follows:

$$\Phi(\rho,\theta) = A_{00} + \frac{1}{\sqrt{2}}\sum_{n=2}^{\infty} A_{n0}R_n^0\left(\frac{\rho}{R'}\right) + \sum_{n=1}^{\infty}\sum_{m=1}^{n}[A_{nm}\cos m\theta + B_{nm}\sin m\theta]R_n^m\left(\frac{\rho}{R'}\right) \tag{1.34}$$

for $n - m$ = even. R' is the radius of the circle over which the polynomials are defined. The radial polynomial R_n^m is defined as

$$R_n^{\pm m}\left(\frac{\rho}{R'}\right) = \sum_{s=0}^{\frac{n-m}{2}}(-1)^s \frac{(n-s)!}{s!\left(\frac{n+m}{2}-s\right)!\left(\frac{n-m}{2}-s\right)!}\left(\frac{\rho}{R'}\right)^{n-2s} \tag{1.35}$$

where the radial terms contain mixtures of the Seidel terms.

Although the Zernike series appears rather complicated and unwieldy, it does have a number of features useful to adaptive optics. It transforms easily under rotations about the Cartesian axes; it includes a polynomial for each pair of radial (n) and azimuthal (m) orders [89], and the coefficients of the series can be used for aberration balancing. This is helpful for simple systems when defocus, for instance, can be used to correct for some amounts of spherical aberration [89]. The amounts of the various modes needed are related to the normalization constant of the radial polynomial [104,566,882]. If all the modes are counted up through radial order n, the relationship between the total number of Zernike modes Z_m and the number of the radial order is found from

$$Z_m = \frac{1}{2}(n+1)(n+2) \tag{1.36}$$

Table 1.2 shows the first few radial Zernike terms. Another useful property of the Zernike series is the simple manner in which the rms wavefront error can be calculated. If all the coefficients of the series that represent a wavefront are known, the geometric sum of the nonpiston terms yields the wavefront variance,

$$(\Delta\Phi)^2 = \sum_{n=1}^{\infty}\sum_{m=0}^{n}\frac{A_{nm}^2 + B_{nm}^2}{2(n+1)} \tag{1.37}$$

TABLE 1.2

First Few Radial Zernike Terms

Radial Term	Description
$R_0^0 = 1$	Piston
$R_2^0 = 2\left(\frac{\rho}{R'}\right)^2 - 1$	Zernike focus contains piston
$R_4^0 = 6\left(\frac{\rho}{R'}\right)^4 - 6\left(\frac{\rho}{R'}\right)^2 + 1$	Zernike spherical aberration contains focus and piston
$R_3^1 = 3\left(\frac{\rho}{R'}\right)^3 - 2\left(\frac{\rho}{R'}\right)$	Zernike coma contains tilt

This variance can be used to calculate the Strehl ratio directly. In the special case where the wavefront is symmetric about the meridional plane ($B_{nm} = 0$), the power-series expansion coefficients can be calculated from the Zernike coefficients [787]. Similarly, the Zernike coefficients can be calculated from the power-series coefficients [151]. Because we can calculate the Zernike coefficients A_{nm} and B_{nm} using simple integrals, the Zernike series provides a manageable representation of the wavefront for computational purposes or for determining the effects of primary aberrations on circular beams.

1.3.3.3 Zernike Annular Polynomials

Some optical systems (Cassegrain and Newtonian telescopes for instance) have a centrally obscured beam. A wavefront for these systems is not easily represented using a power series or Zernike polynomials, because the obscuration is represented by very high spatial frequencies in the radial direction. A large number of terms of the series are required to represent even primary aberrations. Mahajan [496] discusses a series that is orthonormal over an annulus. By using the Gram–Schmidt orthogonalization process, a series of polynomials based on the Zernike polynomials is obtained. This series includes the quantity representing the inner radius of the optical wavefront and uses terms similar to the radial Zernike polynomials.

1.3.3.4 Lowest Aberration Modes

In addition to the piston, which is only a uniform shift in the entire wavefront, tilt and focus are the primary aberrations that mostly affect propagation or an image. According to the rigorous theory, these are not even "aberrations" [89]. They have a fundamental geometrical significance. Repeating Equation 1.1 for the intensity of light at a point P in a focal plane

$$I(P)=\left(\frac{Aa^2}{\lambda R^2}\right)^2\left|\int_0^1\int_0^{2\pi} e^{i[k\Phi-\upsilon\rho\cos(\theta-\psi)-\frac{1}{2}u\rho^2]}\rho d\rho d\theta\right|^2 \tag{1.38}$$

one can see that the exponent contains three basic terms, the wavefront contribution $k\Phi$, the tilt contribution $\upsilon\rho\cos(\theta-\psi)$, and the focus contribution $u\rho^2$. If we determine that the wavefront Φ contains tilt of a magnitude K_x in the x direction, we can perform a coordinate transformation $\Phi = \Phi' + K_x\rho\sin\theta$. With the tilt term separated into its x–y components, the focal length represented by f, and the aperture radius, a, the exponent becomes

$$k\Phi' + kK_x\rho\sin\theta - \frac{ka}{f}r\rho\sin\psi\sin\theta - \frac{ka}{f}r\rho\cos\psi\cos\theta - \frac{1}{2}kz\left(\frac{a}{f}\right)^2\rho^2 \tag{1.39}$$

Removing the tilt from the higher-order wavefront term Φ' and transforming according to $x' = x - (R/a)K_x$, $y' = y$, $z' = z$, the exponent becomes

$$k\Phi - \frac{ka}{f}\rho'\cos(\theta-\psi') - \frac{1}{2}kz\left(\frac{a}{f}\right)^2\rho^2 \tag{1.40}$$

which is the same form as Equation 1.1. The distribution of light in the image plane will be the same as the original untilted wavefront. The centroid of the image will shift, however, by an amount equal to $f K_x/a$.

A similar transformation can be made for a focal shift. If the wavefront contains the term $K_z\rho^2$, then the distribution of light will not change in the focal plane, but the focal distance f will shift an amount proportional to K_z. This very important result is fundamental to the measurement of the focus or the tilt in a beam and will be discussed in detail in Chapter 5.

1.3.4 Interference

Interference occurs when two or more coherent light beams are superimposed. White light interference can occur because (incoherent) white light can be thought of as the sum of coherent components that interfere. Basic principles of optical interference can be used for practical applications such as measuring wavefronts in adaptive optics [424].

The *intensity* is the time-averaged squared magnitude of the electric field. We can begin by expressing the electric field vector of a plane wave as

$$\mathbf{E} = \frac{1}{2}[\mathbf{A}(\mathbf{r})e^{-i\omega t} + \mathbf{A}^*(\mathbf{r})e^{i\omega t}] \tag{1.41}$$

where the vector components of the amplitude are

$$A_x = a_x e^{ikr-\delta_x} \tag{1.42}$$

$$A_y = a_y e^{ikr-\delta_y} \tag{1.43}$$

$$A_z = a_z e^{ikr-\delta_z} \tag{1.44}$$

and the phases of the components are the δ's. The magnitude of the field $|E|^2$ takes the form

$$|E|^2 = \frac{1}{4}(\mathbf{A}^2 e^{-2i\omega t} + \mathbf{A}^{*2} e^{2i\omega t} + 2\mathbf{A}\cdot\mathbf{A}^*) \tag{1.45}$$

Averaging the magnitude of the field over a large time interval becomes the intensity, as follows:

$$I = \langle \mathbf{E}^2 \rangle = \frac{1}{2}\mathbf{A}\cdot\mathbf{A}^* = \frac{1}{2}\left(a_x^2 + a_y^2 + a_z^2\right) \tag{1.46}$$

If two such fields are superimposed, the vectors add as follows:

$$\mathbf{E} = \mathbf{E}_1 + \mathbf{E}_2 \tag{1.47}$$

The magnitude of the sum of the two fields becomes

$$\langle \mathbf{E}^2 \rangle = \langle \mathbf{E}_1^2 \rangle + \langle \mathbf{E}_2^2 \rangle + 2\langle \mathbf{E}_1 \cdot \mathbf{E}_2 \rangle \tag{1.48}$$

and the intensity of the two superimposed fields is

$$I = I_1 + I_2 + 2\langle \mathbf{E}_1 \cdot \mathbf{E}_2 \rangle = I_1 + I_2 + (a_{x1}a_{x2} + a_{y1}a_{y2} + a_{z1}a_{z2})\cos\delta \tag{1.49}$$

where δ is the phase difference between the two fields. Without loss of generality, but for simplifying the presentation, the light can be treated as transverse and linearly polarized, that is, $a_{yi} = a_{zi} = 0$. The intensities of the individual beams are, from Equation 1.41,

$$I_1 + \frac{1}{2}a_{x1}^2 \tag{1.50}$$

$$I_2 = \frac{1}{2}a_{x2}^2 \tag{1.51}$$

and the intensity of the superimposed beams is

$$I = I_1 + I_2 + 2\sqrt{I_1 I_2}\cos\delta \tag{1.52}$$

The maximum intensity occurs when cos δ = 1, that is, δ = 0, 2π, 4π, …, and the minimum occurs when the cosine term is zero, that is, δ = π, 3π, 5π, ….

For the special, but not so uncommon, case $I_1 = I_2$, the intensity of the superimposed beams is

$$I = 4I_1 \cos^2(\delta/2) \tag{1.53}$$

with the maximum intensity $I_{max} = 4I_1$ and the minimum intensity $I_{min} = 0$.

Measuring the interference pattern is equivalent to measuring the spatial coherence function of an optical field. The Van Cittert–Zernike theorem [672] states that the spatial coherence properties of an optical field are a Fourier transform of the irradiance distribution of the source. The fields of optical and radio interferometry are based on this theorem. The application of these principles of interference is also fundamental to the development of wavefront control. Adaptive optics is, if nothing more, an engineering field, where controlling the phase δ at one place leads to managing the optical intensity I at another place.

1.4 Terms in Adaptive Optics

A number of terms are commonly used throughout the adaptive optics community. Some of the terms have evolved from electrical or mechanical engineering. Some are derived from the terminology of special military applications [806], and others uniquely apply to adaptive optics.

Many authors use various definitions for the same or similar terms. This is not unusual in a growing international field. To maintain consistency in this book, some terms are defined as they are generally applied in the adaptive optics–engineering community involved with both astronomy and propagation. Other definitions will be found in the context in which they are used.

The difference between *active* and *adaptive* optics was discussed in Section 1.1. It requires a rather broad definition of *open* and *closed* loops. If an optical system or an electro-optical system employs feedback in any fashion, it can be deemed a *closed loop*. This applies to both positive and negative feedback, and to optical, electrical, mechanical, or any other method of closing the loop between *information* and *compensation*.

If the optical information is gathered at the receiver or the target end (in beam propagation) or the image plane (in an imaging application), the system is considered a *target loop*. If the information is intercepted before the target or the image plane or before the application of some correction, the short-circuited loop is called a *local loop*.

If optical information is received by the adaptive optics system before a propagating beam reaches the target, it is considered an *outgoing wave*. If information about the propagation is conveyed from the target back to the correction system, it is called a *return wave*. Rough, extended objects that

are targets of a propagating beam present special problems with speckled return. These speckles can be mitigated with a process called "speckle-average phase conjugation" [834]

If the *compensation* requires the movement of a macroscopic mass, it is deemed *inertial*. If the *compensation* alters the state of matter, rather than grossly moving it, it is called *noninertial*. If the compensation is carried out by spatially dividing the region of correction and treating each region independently (possibly with crosscoupling), it is called *zonal correction*. Conversely, if the compensation is carried out by dividing the region of correction in another manner, such as mathematically decomposing the correction into normal modes, it is called *modal correction*.

Understandably, some of these definitions have gray areas. For instance, acousto-optic variance of the index of refraction moves mass on a molecular level, but because it is not a gross macroscopic application, it is noninertial. Similarly, there might be no "target" defined in the case of adaptive optics inside a laser resonator. This target loop might then be called simply the *output loop*.

When a beam strikes an opaque surface, the spot of light can take on almost any shape depending on the apertures and the wavefront of the beam. If the beam is circular and has a sharp edge, it is easy to specify the spot radius or diameter. Gaussian intensity profiles do not have sharp cutoffs at the edge. The *edge* is usually specified as the point where the intensity reaches 13.5% of the maximum. This is the $1/e^2$ point of the beam intensity, also called the beam *waist*. A beam shape that has an easily defined edge is the Fraunhofer diffraction pattern of a circular aperture (Equation 1.19). Because the Bessel function reaches its first zero at a well-known value, $\boldsymbol{J}_1(3.8) = 0.0$, the "edge of the circular spot" is defined as the first dark ring, a region of destructive interference. The "spot" in this case contains 84% of the energy (Figure 1.4).

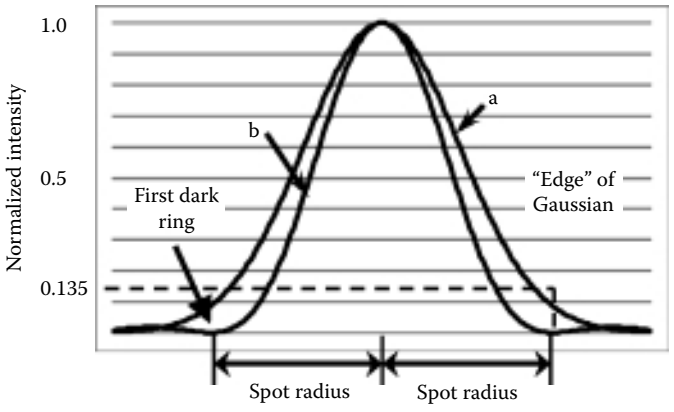

FIGURE 1.4
The *spot size* is defined differently for various intensity profiles: (a) Gaussian profile and (b) the far-field spot of a uniform beam diffracted by a circular aperture.

Other beam spots may be asymmetric, greatly distorted, or have numerous pockets of high and low intensity (similar to the speckle pattern on a rough diffuse surface.) By taking the area of the smallest spot that has 84% of the energy and computing the diameter of its equivalent circle, an approximation for the *spot size* is achieved.

Using Huygens' wavelet concept [80,89], we can see that a plane wave passing through an aperture will begin to diverge from its collimated form as soon as it leaves the aperture. The amount of divergence is dependent on the amplitude and the phase of the initial beam, the distribution over the aperture, the propagation medium that scatters and diffracts the beam, and one's definition of the "edge" of the beam. The *beam divergence* is usually expressed in terms of an angle between the axis of propagation and the line joining the edge of the beam at different points of the beam path. The solid angle defined by the beam edge over the path of the beam is occasionally used to express beam divergence.

The use of the Strehl ratio is a fundamental description of the amount of intensity reduction due to aberrations. Another quantity, the *beam quality*, is used in a similar manner. A number of definitions for beam quality are used in the optics community. The most common definition states that the beam quality is the square root of the inverse of the Strehl ratio.

$$BQ = \sqrt{1/S} \tag{1.54}$$

For a Gaussian beam, the beam quality is equivalent to the linear increase in beam waist due to beam divergence. In general, the linear size growth of the diffraction spot is the beam quality. Some investigators have redefined the diffraction limit of a beam to better describe a particular system. For instance, the Strehl ratio relates the intensity of the aberrated beam to that of the unaberrated beam. If a beam is not uniform when it is unaberrated, such as an annular beam or any other obscured beam, the intensity of the unaberrated beam will not be as high as a similar, equal-area unobscured beam. The addition of phase aberrations would normally reduce the on-axis intensity of the beam. However, in some cases, the addition of phase aberrations could increase the on-axis intensity of a strangely obscured beam. This results in a Strehl ratio greater than one, and a subsequent beam quality less than one. By replacing the on-axis intensity of the obscured but unaberrated beam in the definition of Strehl ratio, the beam quality can be viewed as a single number relating only the phase aberrations to the propagated intensity. Beam quality should always be related to the unaberrated beam of the same size and shape.

Jitter is the dynamic tilt of a beam. It is usually expressed in terms of angular variance or its square root, the rms deviation of an angle. The dynamics are often expressed in terms of a power spectral density, similar to any mechanical vibration. If the jitter is very slow, usually slower than the response of the system under consideration, it is called *drift*. Because tilt alters the direction and not the shape of a propagated beam, it does not have any effect on the Strehl ratio according to its formal definition. However, if a system is

constructed to maintain a beam on a receiver, a physical spot in space, jitter will cause the beam to sweep across the spot. The time-averaged intensity on the target is reduced by an amount related to the jitter.

The on-axis far-field intensity I_{ff} for a circular aperture with reductions due to diffraction, expressed as variance of the wavefront $\sigma^2 = (k\Delta\Phi)^2$, jitter, and transmission losses for m optical elements is given by [715]

$$I_{ff} \cong \frac{I_0 TK \exp[-\sigma^2]}{1+\left(\frac{2.22\alpha_{jit}D}{\lambda}\right)^2} \tag{1.55}$$

where

$$T = \prod_{i=1}^{m} T_i \tag{1.56}$$

is the transmission of m optics, K is an aperture-shape correction described in reference [349], D is the aperture diameter, λ is the wavelength, and α_{jit} is the one-axis rms jitter. The intensity without aberrations or jitter is found by substitution in Equation 1.4,

$$I_0 = \frac{\pi D^2 P}{(2\lambda L)^2} \tag{1.57}$$

where L is the propagation distance and P is the uniformly distributed input power into a circular aperture.

According to Babinet's principle, the intensity of a circular aperture with an obscuration ratio ε becomes [89]

$$I_0\big|_{obsc} = \frac{\pi D^2 P}{(2\lambda L)^2}(1-\varepsilon^2) \tag{1.58}$$

Knowing the on-axis intensity is sufficient to describe the far-field effects when the beam has a relatively simple analytical form for the intensity distribution. For greatly aberrated beams or those with complicated apertures, the on-axis intensity is insufficient to describe the far-field effects. A measurement of the total power in the focal or the target plane or over a portion of the focal plane is needed. Integrating the power deposited in a circle on the focal plane results in a quantity called the *total integrated power*. If one places a "bucket" of a specified radius in the focal plane, the "bucket" would catch that amount of power; thus the term *power-in-the-bucket*. For the perfect circular aperture, the power-in-the-bucket is expressed as [89]

$$\text{PB} = 1 - J_0^2\left(\frac{2\pi ab}{\lambda L}\right) - J_1^2\left(\frac{2\pi ab}{\lambda L}\right) \tag{1.59}$$

where a is the aperture radius and b is the bucket radius.

It is often necessary to express the propagation capability of a system in terms that are independent of the propagation distance. The expression for far-field intensity I_{ff}, Equation 1.55, when multiplied by the square of the propagation distance, L^2, results in a quantity expressed in units of power per solid angle. This term, called *brightness*, is a description of the propagating system, rather than the effect of the propagation itself.

$$\text{Brightness} \approx \frac{\pi D^2 PTK \exp[-\sigma^2]}{4\lambda^2 \left[1+\left(\frac{2.22\alpha_{jit} D}{\lambda}\right)^2\right]} \tag{1.60}$$

Astronomical brightness, the number of photons reaching the Earth's surface, in a given area in unit time, depends on the magnitude of the star. It is defined for a visible passband by the expression

$$B_{astro} = (4\times 10^6)10^{-m_v/2.5} \text{ photons/cm}^2 \bullet \text{s} \tag{1.61}$$

where m_v is the visual magnitude of the observed star. The limit of vision of an unaided human eye in a dark location is roughly equal to a visual magnitude of 6. A visual magnitude of 14 is roughly the brightness of a sunlit geosynchronous satellite.

Astronomers use the term "seeing" to describe the condition of turbulence in the atmosphere. It is based on the ability to resolve two point objects when observed through the atmosphere. It is essentially the same as the Rayleigh criterion [89,639] for resolving two point objects. That is, the full-width-half-maximum of the PSF stated as an angle is the "seeing." It is normally expressed in arc seconds (or arc minutes), recognizing that 1 arc sec = 4.8 μ radians. Uncompensated atmospheric seeing can be as low as 0.45 arc sec [27] or, sometimes, as high as 2.0 arc sec [664]. For surveillance of low Earth orbit space objects, the seeing should be less than 0.02 arc sec [509]. For astronomy, good seeing is 0.1–0.5 arc sec. Adaptive optics is used to improve the seeing.

2

Sources of Aberrations

Unwanted variations in the intensity during an image capture or beam propagation create the need for adaptive optics. Chapter 1 showed that it is the deviation of the phase from the reference sphere (the wavefront), that is, the principal cause of the intensity variations, that can be treated by adaptive optics. There are many sources of wavefront errors.

Astronomers are mostly concerned with the turbulence in the atmosphere that degrades an image. Engineers working to propagate a beam and to maximize its useful energy into a receiver must be concerned with errors introduced by lasers themselves, the optics that direct them, and the propagation medium that they encounter. This chapter will discuss the many sources of phase aberrations addressed by adaptive optics systems. These include linear effects due to turbulence, optical manufacturing, and misalignments, as well as errors that result from nonlinear thermal effects and fluid properties. The minimization of these effects is always a consideration while developing any optical system from the ground up. Real-time compensation for these disturbances is the realm of adaptive optics.

2.1 Atmospheric Turbulence

Naturally occurring small variations in temperature (<1°C) cause random changes in wind velocity (eddies), which we view as turbulent motion in the atmosphere. The changes in temperature give rise to small changes in the atmospheric density and, hence, in the index of refraction. These index changes, on the order of 10^{-6}, can accumulate, and the cumulative effect can cause significant inhomogeneities in the index profile of the atmosphere. The wavefront of a beam will change in the course of propagation. This can lead to beam wander, intensity fluctuations (scintillations), and beam spreading.

These small changes in the index of refraction act as small lenses in the atmosphere. They focus and redirect waves and eventually, through interference, cause intensity variations. Each of these "lenses" is roughly the size of the turbulence eddy that caused it. The thin lens model is a useful approximation, but it is not completely accurate because there are few discontinuities in the atmosphere.

The most common effects of turbulence can be seen manifested in the twinkling and quivering of stars. *Twinkling* is the random intensity variation of light from a star because of the random interference between waves from the same star passing through slightly different atmospheric paths. The average position of the star also shows a random *quiver* because the average angle-of-arrival of light from the star is affected by the changing index of refraction along its path through the atmosphere. A third effect, known a long time ago to astronomers, is the apparent *spreading* of a star's image due to turbulence. The aberrations introduced by optics do not account for the large spot image of the star, a point object. Turbulence produces random higher-order aberrations that cause the spreading.

These three primary effects of turbulence will be examined here because they are subject to compensation by adaptive optics. Other atmospheric effects, such as aerosol scattering and molecular absorption, will only be introduced when they affect the performance of the adaptive optics. The control of large spatial and temporal changes of a wavefront can reduce the phase changes caused by the random temperature fluctuations. This is the principal reason for using adaptive optics.

Several volumes [130,374,746,755] and hundreds of papers have been written on this topic, examining the theoretical basis for describing the effects of turbulence and the experimental verification of those theories [209]. A 1986 book by Lukin, recently updated and translated from Russian [488], is a comprehensive theoretical examination of adaptive optics–related turbulence phenomena.

Turbulence, as it applies to adaptive optics, can be summarized using basic principles that relate the physical turbulence phenomena with optical propagation and phase effects. Propagation through atmospheric turbulence is not completely understood, especially in terms of small-scale phenomena. The theories of turbulence are based on statistical analyses, because the complexity of the real atmosphere is beyond the capabilities of deterministic prediction or numerical analysis. The emphasis on a statistical description of atmospheric turbulence has resulted in a number of very useful theories and scaling laws that describe the average effects on gross properties, such as total beam wander, beam spread, and scintillation [208].

2.1.1 Descriptions of Atmospheric Turbulence

Areas of high- and low-density air are moved around by random winds. This process can be described by statistical quantities. Kolmogorov [425] studied the mean-square velocity difference between two points in space separated by a displacement vector **r**. The structure tensor D_{ij} is defined as

$$D_{ij} = \left\langle [\upsilon_i(\mathbf{r}_1 + \mathbf{r}) - \upsilon_i(\mathbf{r}_1)][\upsilon_j(\mathbf{r}_1 + \mathbf{r}) - \upsilon_j(\mathbf{r}_1)] \right\rangle \tag{2.1}$$

where υ_i and υ_j are the different components of the velocity and the brackets represent an ensemble average. It is not a simple equation to evaluate with real velocity descriptors; however, if three assumptions about the atmosphere are made, the structure tensor can be simplified. First, the atmosphere is locally homogeneous (velocity depends on vector **r**); second, the atmosphere is locally isotropic (velocity depends only on the magnitude of **r**); and third, the turbulence is incompressible ($\nabla \bullet \mathbf{v} = 0$). The tensor now becomes a single structure function [65] as follows:

$$D_\upsilon = \left\langle [\upsilon_r(\boldsymbol{r}_1 + \boldsymbol{r}) - \upsilon_r(\boldsymbol{r}_1)]^2 \right\rangle \tag{2.2}$$

If the separation r is small (within the inertial subrange of turbulence), the structure function takes on a 2/3 law dependence on r:

$$D_\upsilon = C_\upsilon^2 r^{2/3} \tag{2.3}$$

The constant C_υ^2 is the velocity structure constant, which is a measure of the energy in the turbulence. This form of the structure function is valid when the value of r is above the smallest eddy size l_0 and below the largest eddy size L_0. The small eddy, called the *inner scale* or the *microscale*, is the size below which viscous effects are important and energy is dissipated as heat. The inner scale is related to the rate of dissipation of the turbulent kinetic energy ε and the kinematic viscosity ν by the following equation [577]:

$$l_0 = 7.4\left(\frac{\nu^3}{\varepsilon}\right)^{1/4} \tag{2.4}$$

The large eddy, called the *outer scale*, is the size above which isotropic behavior is violated. One can approximate l_0 as being a few millimeters near the Earth's surface to a few centimeters or more in the troposphere. The outer scale L_0 ranges from a few meters to hundreds of meters. Near the ground, below 1 km, $L_0 \approx 0.4h$, where h is the height above the ground [755]. In the free atmosphere, the outer scale is normally on the order of tens of meters, but it can reach hundreds of meters [52].

Through the concept of passive additives, Tatarskii [755] and Corrsin [152] related the velocity structure to the index-of-refraction structure. This quantity D_n is much more important when we deal with propagation issues.

$$D_n(r) = C_n^2 r^{2/3}; \quad l_0 < r < L_0 \tag{2.5}$$

where C_n^2 is the refractive-index structure constant, a measure of the strength of the turbulence. The effects of a finite inner scale and the behavior of the structure function when r is close to l_0 are discussed by Whitman and Beran [858].

The atmosphere can be assumed to be made up of a mean index of refraction, $\langle n(r) \rangle$, and a fluctuating index part, $n_1(\mathbf{r})$. The covariance of the refractive-index field B_n becomes

$$B_n = \langle n_1(\mathbf{r} + \mathbf{r}_1) n_1(\mathbf{r}_1) \rangle \tag{2.6}$$

The power spectral density (PSD) is the Fourier transform of the covariance,

$$\Phi_n(\mathbf{K}) = \frac{1}{(2\pi)^3} \int \mathrm{d}^3 r B_n(r) \mathrm{e}^{-i\mathbf{K}r} \tag{2.7}$$

where **K** is the three-dimensional spatial wave number. Using Kolmogorov's inertial subrange expression (Equation 2.5), changing the coordinates to spherical terms, **K** = (K, θ, ϕ), and carrying out the ensemble averaging [746], the PSD becomes

$$\Phi_n(K) = \frac{5}{18\pi} C_n^2 K^{-3} \int_{l_0}^{L_0} \mathrm{d}r \sin(Kr) r^{-1/3} \tag{2.8}$$

If we let the integral limits diverge, $l_0 \to 0$ and $L_0 \to \infty$, the integral results in the *Kolmogorov spectrum*:

$$\Phi_n(K) = 0.033 C_n^2 K^{-11/3} \tag{2.9}$$

A zero inner scale and an infinite outer scale were convenient for performing the integration. Tatarskii [756] described a spectrum that could be used for finite inner scales [488], given by

$$\Phi_n(K) = 0.033 C_n^2 K^{-11/3} \exp\left(\frac{-K^2}{(5.92/l_0)^2} \right) \tag{2.10}$$

The *Von Karman spectrum* [755] is useful for cases with finite outer scales and is expressed as follows:

$$\Phi_n(K) = \frac{\Gamma(11/6)\pi^{-9/2}}{\Gamma(1/3)8} \delta^2 L_0^3 (1 + K^2/K_0^2)^{-11//(} \tag{2.11}$$

In this expression, the constant term is evaluated to yield the following value:

$$\frac{\Gamma(11/6)\pi^{-9/2}}{\Gamma(1/3)8} \cong 2.54 \times 10^{-4} \tag{2.12}$$

$K_0 = 2\pi/L_0$, and the variance of the refractivity fluctuations is given by

$$\delta^2 = \frac{C_n^2}{1.9K_0^{2/3}} \tag{2.13}$$

Each of these spectra is valid only for regions in the following inertial subrange:

$$\frac{2\pi}{L_0} \leq K \leq \frac{2\pi}{l_0} \tag{2.14}$$

2.1.2 Refractive-Index Structure Constant

The *refractive-index structure constant*, C_n^2, is a measure of the strength of turbulence. It is by no means constant. It varies with seasons as well as daily and hourly. It varies with both geographic location and altitude. Figure 2.1 shows a few measured variations and two well-known numerical models to approximate the average. It can be perturbed very easily by artificial means, such as the motion of an aircraft. There have been many measurements [163,362,817] of C_n^2. No theoretical model is accurate for the many cases of turbulence. Based on experimental observations, Hufnagel suggested [362]

$$C_n^2 = \{[(2.2\times10^{-53})h^{10}(W/27)^2]e^{-h/1000} + 10^{-16}e^{-h/1500}\}\exp[r(h,t)] \tag{2.15}$$

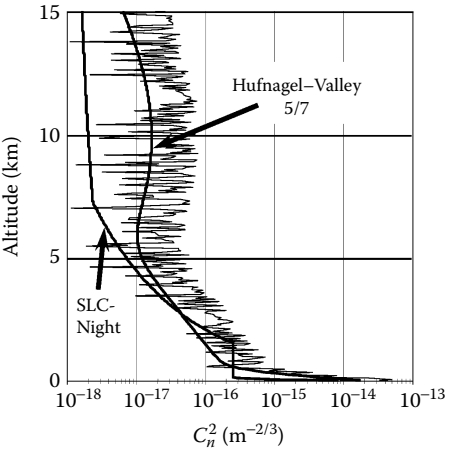

FIGURE 2.1
Measurement of the refractive-index structure constant C_n^2 as a function of altitude. The Hufnagel–Valley 5/7 model and the submarine laser communications–Night model are shown for comparison.

where h is the height above sea level in meters, W is the wind correlating factor that is defined as

$$W = \left[\left(\frac{1}{15\,\text{km}} \right) \int_{5\,\text{km}}^{20\,\text{km}} \upsilon^2(h)\,\text{d}h \right]^{1/2} \tag{2.16}$$

and $r(h, t)$ is a zero-mean homogeneous Gaussian random variable. The term $\upsilon(h)$ is the wind speed at height h. The unit of C_n^2 is $\text{m}^{-2/3}$.

The dependence of wind speed on altitude is required for a rigorous application of Equation 2.15. A wind model that is commonly used and is applicable to calculations throughout this book was developed by Bufton [106], as follows:

$$\upsilon(z) = 5 + 30 \exp\left\{ -\left[\frac{z - 9.4}{4.8} \right]^2 \right\} \tag{2.17}$$

where z is in kilometers and the wind velocity υ is in meters per second.

Valley [808] altered the wind model slightly in his study of anisoplanatism, which is discussed in Chapter 3. Ulrich added a term to account for the boundary layer, resulting in the Hufnagel–Valley boundary (HVB) model [800], which is expressed as follows:

$$C_n^2 = 5.94 \times 10^{-23} z^{10} e^{-z} \left(\frac{W}{27} \right)^2 + 2.7 \times 10^{-16} \text{e}^{-2z/3} + A\text{e}^{-10\,h} \tag{2.18}$$

where z is the height above mean sea level in kilometers, h is the height above the surface of the site in kilometers, and C_n^2 is in $\text{m}^{-2/3}$. W is an adjustable parameter related to the upper-atmosphere wind velocity, and A is a scaling constant [800,808]. If the site is at sea level, both W and A can be adjusted so that they correspond to specific integrated values of the coherence length r_0 and the isoplanatic angle θ_0.* For the case of r_0 = 5 cm, θ_0 = 7 μrad, and λ = 0.5 μm (the so-called Hufnagel–Valley 5/7 model), the parameters are $A = 1.7 \times 10^{-14}$ and W = 21. With the wavelength λ in micrometers, the coherence length r_0 in centimeters, and the isoplanatic angle θ_0 in microradians, the HVB parameters can be found for any site conditions [791] using

$$W = 27(75\theta_0^{-5/3}\lambda^2 - 0.14)^{1/2} \tag{2.19}$$

and

$$A = 1.29 \times 10^{-12} r_0^{-5/3}\lambda^2 - 1.61 \times 10^{13} \theta_0^{-5/3}\lambda^2 - 3.89 \times 10^{-15} \tag{2.20}$$

* The coherence length and isoplanatic angle are formally described in Section 2.1.3.

Another model commonly used to calculate the parameters associated with atmospheric turbulence is the submarine laser communications (SLC)–Night model, named after the SLC program for which it was developed, where h is the altitude above ground (in meters). The model is described as follows:

Altitude	C_n^2
$h \le 18.5$	8.40×10^{-15}
$18.5 < h \le 110$	$2.87 \times 10^{-12} h^{-2}$
$110 < h \le 1500$	2.5×10^{-16}
$1500 < h \le 7200$	$8.87 \times 10^{-7} h^{-3}$
$7200 < h < 20{,}000$	$2.00 \times 10^{-16} h^{-0.5}$

2.1.3 Turbulence Effects

Turbulence will cause high spatial frequency beam spreading, low spatial frequency beam wander, and intensity variations. Beam spread is produced by eddies that are smaller than the beam size. Wander is produced by eddies that are larger than the beam size [746]. The Kolmogorov spectrum suggests that intensity variations are produced by eddies with sizes on the order of $\sqrt{\lambda L}$, where L is the propagation distance.

2.1.3.1 Fried's Coherence Length

In a study of an optical heterodyne communications receiver, Fried [237] found that the maximum allowable diameter of a collector before atmospheric distortion seriously limits performance is r_0, where the "coherence *length*"* is

$$r_0 = \left[0.423k^2 \sec(\beta) \int_0^L C_n^2(z) \mathrm{d}z \right]^{-3/5} \tag{2.21}$$

In this expression, L is the path length, β is the zenith angle, and C_n^2 can vary with altitude z. The phase structure function for the Kolmogorov turbulence can be found for a number of cases in terms of this parameter [238]. For plane waves

$$D_\phi = 6.88 \left(\frac{r}{r_0} \right)^{5/3} \tag{2.22}$$

* This is often called the "seeing-cell size" [239].

The radial variable r is normal to the propagation direction. For spherical waves, the coherence length is slightly modified as follows:

$$r_{0\text{sph}} = \left[0.423k^2 \sec(\beta) \int_0^L C_n^2(z) \left(\frac{z}{L} \right)^{5/3} \mathrm{d}z \right]^{-3/5} \tag{2.23}$$

Equation 2.22 can be generalized for non-Kolmogorov turbulence. Nicholls et al. [563] discuss a generalized model for the structure function that takes the form

$$D_n(r) = \gamma_\eta \left(\frac{r}{R_0} \right)^{\eta - 2} \tag{2.24}$$

When $\eta = 11/3$, $R_0 = r_0$, and $\gamma_\eta = 6.88$, Kolmogorov turbulence is assumed. If η is less than 11/3, some of the energy for phase aberrations shifts from lower- to higher-order modes, requiring modifications to adaptive optics.

For a constant C_n^2 (i.e., for a horizontal path length), the coherence length for plane waves reduces to

$$r_0 \big|_{\text{pl}} = 1.68(C_n^2 L k^2)^{-3/5} \tag{2.25}$$

For spherical waves, the coherence length is

$$r_0 \big|_{\text{sph}} = 3.0(C_n^2 L k^2)^{-3/5} \tag{2.26}$$

In astronomy, starlight is a plane wave when it enters the atmosphere; hence, the plane-wave description is assumed. Typical nighttime median r_0 at wavelength λ can be approximated by [246]

$$[r_0]_{\text{median}} = 0.114 \left(\frac{\lambda}{5.5 \times 10^{-7}} \right)^{6/5} (\sec\beta)^{-3/5}$$ (2.27)

where λ is in meters.

Fried's coherence length has been used to describe various atmospheric turbulence phenomena. The coherence length can be measured [40,700] indirectly. By using a two-channel Shack–Hartmann sensor (Section 5.3.2) as a differential image motion monitor [227,690], atmospheric seeing can be measured. Because r_0 incorporates the turbulence strength C_n^2, the wavelength, and the propagation path into one parameter, it is widely used for scaling laws and descriptions of atmospheric phenomena. For instance, the spectrum of turbulence in the spatial domain (with spatial frequency ξ expressed in inverse meters) is expressed in terms of coherence length [570]. With r_0 in meters, the spectrum is

$$\Phi(\xi) = \left(\frac{0.023}{r_0^{5/3}} \right) \xi^{-11/3} \tag{2.28}$$

This spatial frequency spectrum can be used to describe all the aberration modes of atmospheric turbulence in terms of Zernike coefficients and other polynomials [665]. In addition, the spectrum can be integrated to give an overall wavefront variance as follows:

$$\sigma^2 = \int \Phi(\xi) d^2\xi \tag{2.29}$$

2.1.3.2 Scintillation

Intensity variations are usually expressed as fluctuations of the log of the amplitude (*log-amplitude fluctuations*). The Kolmogorov spectrum suggests that log-amplitude fluctuations are produced by eddies with sizes on the order of $\sqrt{\lambda L}$, where L is the propagation distance. Assuming the Von Karman spectrum and $l_0 << \sqrt{\lambda L}$, the log-amplitude variance σ_χ^2 is given by [755]

$$\sigma_\chi^2 = 0.307 k^{7/6} L^{11/6} C_n^2 \tag{2.30}$$

for a plane wave and

$$\sigma_\chi^2 = 0.124 k^{7/6} L^{11/6} C_n^2 \tag{2.31}$$

for a spherical wave. These formulae break down for long paths and strong turbulence [633], because perturbation theory was used to derive them. Tatarskii [755] used a technique derived by Rytov [681] to develop this theory. Because of the limitations of the *Rytov approximation*, these equations hold only for $\sigma_\chi^2 < 0.3$.

Using the simple multiple-lens model for the atmosphere, one can calculate the amplitude variance. Because each eddy of diameter l acts as a lens, it will have a focal length of $f \approx l/\Delta n$. In the geometric optics regime, $l > \sqrt{\lambda L}$ and $l_0 < \sqrt{\lambda L}$; then, the log-amplitude variance is [145]

$$\sigma_\chi^2 \approx k^{7/6} L^{11/6} C_n^2 \tag{2.32}$$

which is within a multiplicative constant of the more rigorous Tatarskii method.

The scintillation effects are most prominent when a small or point receiving aperture, like an optical communications receiver, a small optical tracker, or the human eye, is used. In some cases, scintillation can be interpreted in a centroid tracker as a tilt or jitter error when no phase tilt actually exists [350]. For larger apertures, the scintillation effects are averaged over the extent of

the aperture, and the focused irradiance varies less. Scintillation is observed as a variation in the irradiance, σ_I^2, and is expressed as

$$\sigma_I^2 = A[\exp(4\sigma_X^2) - 1] \tag{2.33}$$

where A is an *aperture-averaging factor* [20,139].

Churnside [139] presents a number of expressions for the aperture-averaging factor under various conditions For weak turbulence conditions and a small l_0, the aperture-averaging factor is

$$A = \left[1 + 1.07\left(\frac{kD^2}{4L}\right)^{7/6}\right]^{-1} \tag{2.34}$$

For other conditions, see [19,790].

Because atmospheric turbulence is dynamic, scintillation is dynamic. Tatarskii [755] gives the temporal power spectrum of scintillation in terms of the frequency f, and the zenith angle β:

$$P(f) = 8.27 \sec^{7/3}\beta k^{2/3} \int_0^L \frac{C_n^2(z) z^{4/3}}{\upsilon_w(z)} dz \times \int_0^\infty \left[x^2 + + \frac{f^2}{f_0^2(z)}\right]^{-11/6} \sin\left(x^2 + \frac{f^2}{f_0^2(z)}\right) dx \tag{2.35}$$

The frequency $f_0(z)$ is a function of the wind velocity $\upsilon_w(z)$:

$$f_0(z) = \left[\frac{2k}{z \sec\beta}\right]^{1/2} \upsilon_w(z) \tag{2.36}$$

The integral over the dummy variable x in Equation 2.35 can be approximated by [791]

$$\int [\cdots] dx = \exp\left[-1.8\left(\frac{f}{f_0} - 0.5\right)^{1.9}\right] \quad \text{for} \quad \frac{f}{f_0} \geq 0.5 \tag{2.37}$$

$$\int [\cdots] dx = 1 \quad \text{for} \quad \frac{f}{f_0} < 0.5 \tag{2.38}$$

2.1.3.3 Beam Wander or Tilt

The turbulent atmosphere will cause a beam to wander as it propagates. When the wander is fast, it is often called beam *jitter*. When the wander is slow, it is called *drift*. It is caused by the dynamic tilt of the wavefront. Sasiela [693] gives a general description of the wavefront variance as follows:

$$\sigma_{\mathrm{WF}}^2 = 0.2073k^2 \int_0^L \mathrm{d}z C_n^2(z) \int_{-\infty}^{\infty} \mathrm{d}\vec{\kappa}\vec{\kappa}^{-11/3} \cos^2\left[\frac{\vec{\kappa}\vec{\kappa}^2(z-L)}{2k}\right] \prod_{i=0}^{N} F_i(\vec{\kappa}, z) \tag{2.39}$$

where the z integral is over the atmospheric path, $\vec{\kappa}$ is a two-dimensional spatial frequency, N is the number of Zernike modes included, and $k = 2\pi/\lambda$. The filters F_i for the Zernike modes [695] are given by the following equations:

$$F_{\mathrm{even}\,m,n}(\kappa) = 2(n+1)\left[\frac{2J_{n+1}(\kappa D/2)}{\kappa D/2}\right]^2 \cos^2(m\phi) \tag{2.40}$$

$$F_{\mathrm{odd}\,m,n}(\kappa) = 2(n+1)\left[\frac{2J_{n+1}(\kappa D/2)}{\kappa D/2}\right]^2 \sin^2(m\phi) \tag{2.41}$$

$$F_{m=0,n}(\kappa) = (n+1)\left[\frac{2J_{n+1}(\kappa D/2)}{\kappa D/2}\right]^2 \tag{2.42}$$

Using the relations $n = 1$ and $m = 1$ from Equation 2.41 in the filters, Sasiela derives the following expression for wavefront tilt variance σ_{tilt}^2:

$$\sigma_{\mathrm{tilt}}^2 = 0.2073k^2 \int_0^L \mathrm{d}z C_n^2(z) \int_{-\infty}^{\infty}\int_{-\infty}^{\infty} \mathrm{d}\vec{\kappa}[\vec{\kappa}^2 + k^2]^{-11/6} \left(\frac{16}{kD}\right)^2 \left[\frac{J_2(\kappa D/2)}{\kappa D/2}\right]^2 \tag{2.43}$$

where J_2 is the second-order Bessel function of the first kind, $\vec{\kappa}$ is the spatial frequency, and D is the aperture diameter. A similar expression was derived for the tilt variance for an annular aperture with a centered obscuration of diameter εD, as shown in Equation 2.44:

$$\sigma_{\mathrm{tilt}}^2(\varepsilon D) = 0.2073k^2 \int_0^L \mathrm{d}z C_n^2(z) \times \int_{-\infty}^{\infty}\int_{-\infty}^{\infty} \mathrm{d}\vec{\kappa}[\vec{\kappa}^2 + k^2]^{-11/6} \left(\frac{16}{kD(1-\varepsilon^4)}\right)\left[\frac{J_2(kD/2)}{kD/2} - \varepsilon^3 \frac{J_2(k\varepsilon D/2)}{k\varepsilon D/2}\right]^2 \tag{2.44}$$

Using Equation 2.43 and evaluating the coherence length, the variance of the tilt angle α^2 can be found for two uncorrelated axes or a single axis using the expression

$$\alpha^2_{\text{two-axis}} = 0.364\left(\frac{D}{r_0}\right)^{5/3}\left(\frac{\lambda}{D}\right)^2 \quad \text{or} \quad \alpha^2_{\text{one--axis}} = 0.182\left(\frac{D}{r_0}\right)^{5/3}\left(\frac{\lambda}{D}\right)^2 \tag{2.45}$$

The dynamics of the tilt are manifested in their power spectra. For a gradient tilt (G-tilt), such as that measured by quadrant detectors, the one-axis tilt power spectrum assumes the following form [781]:

$$P(f) = 0.155D^{-1/3}\sec\beta f^{-8/3}\int_0^L F_G\left(\frac{f}{\upsilon_w}\right)C_n^2(z)\,\upsilon_{ww}^{5/3}\mathrm{d}z \tag{2.46}$$

where the function F_G is given by

$$F_G(y) = \int_0^1 \mathrm{d}x \frac{x^{5/3}}{\sqrt{1-x^2}} J_1^2(\pi y/x) \tag{2.47}$$

For low frequencies, this reduces to a –2/3 power law expression

$$P(f)_{\text{low}} \to 0.804D^{-1/3}\sec\beta f^{-2/3}\int_0^L C_n^2(z)\upsilon_w^{-1/3}\mathrm{d}z \tag{2.48}$$

and for high frequencies, it follows a –11/3 power law expression

$$P(f)_{\text{high}} \to 0.110D^{-1/3}\sec\beta f^{-11/3}\int_0^{LL} C_n^2(z)\upsilon_w^{8/3}\mathrm{d}z \tag{2.49}$$

Similar expressions follow for the Zernike tilt (Z-tilt)*

$$P(f) = 0.251D^{-1/3}\sec\beta f^{-14/3}\int_0^L F_Z\left(\frac{f}{\upsilon_w}\right)C_n^2(z)\upsilon_{ww}^{11/3}\mathrm{d}z \tag{2.50}$$

where the function F_Z is

$$F_Z(y) = \int_0^1 \mathrm{d}x \frac{x^{11/3}}{\sqrt{1-x^2}} J_2^2(\pi y/x) \tag{2.51}$$

* Z-tilt is the direction that is normal to a best-fit plane with reference to the wavefront.

For low frequencies, this reduces to the same –2/3 power law expression that was found for the G-tilt

$$P(f)_{\text{low}} \rightarrow 0.804D^{-1/3} \sec\beta f^{-2/3} \int_0^{LL} C_n^2(z)\, \upsilon_w^{-1/3} dz \tag{2.52}$$

For high frequencies, the Z-tilt power spectrum follows a –17/3 power law

$$P(f)_{\text{high}} \rightarrow 0.014D^{-1/3} \sec\beta f^{-17/3} \int_0^{L} C_n^2(z)\, \upsilon_w^{14/3} dzz \tag{2.53}$$

A single parameter can represent the entire spectrum for adaptive optics compensation analysis. The characteristic frequency of the tilt of atmospheric turbulence, often called the tilt Greenwood frequency, is expressed by Tyler [781]. For G-tilt, the expression is

$$f_{\text{TG}} = 0.331D^{-1/6}\lambda^{-1} \sec^{1/2}\beta \left[\int_0^{L} C_n^2(z)\upsilon_w^2 dz \right]^{1/2} \tag{2.54}$$

For Z-tilt, the constant in Equation 2.54 becomes 0.368.

2.1.3.4 Higher-Order Phase Variation

Turbulent eddies that are smaller than the beam size break up the beam and spread out the energy. The wavefront variations arise because the refractive index is a random function of space and time. The phase difference $\delta\phi$ between two parallel paths through the atmosphere separated by distance ρ is $\delta\phi \simeq k\rho[\Delta n(\rho)]$, where the difference in index is Δn. By averaging over many statistical realizations and assuming a path length L, the *phase structure function* can be determined as follows:

$$D_\phi = 1.46k^2 C_n^2 L\, \rho^{5/3}, \quad l_0 < \rho < L_0 \tag{2.55}$$

When propagation occurs over long paths and many eddies, the wave can lose *coherence*. If the wavefront is strongly aberrated before it encounters an eddy, the plane-wave approximations used thus far are no longer valid. If the phase difference $\langle(\delta\phi)^2\rangle < \pi^2$, the beam becomes coherent. If ρ_0 is the largest eddy for which a plane wave is considered coherent, from Equation 2.55, the *coherence distance* is calculated as follows:

$$\rho_0 \approx \left[\frac{\pi^2}{\pi^2 C_n^2 L} \right]^{3/5} \tag{2.56}$$

This coherence limitation can be used to derive the total beam spread. Lutomirski and Yura [493] used the extended Huygens–Fresnel principle to show that the angular spread θ of a collimated uniform beam of radius α in uniform turbulence* is

$$\theta^2 \approx \frac{1}{k^2 a^2} + \frac{1}{k^2 \rho_0^2} \tag{2.57}$$

For the specific case of a Gaussian beam [384],

$$I = \frac{w_0^2}{w_b^2} \exp\left(-\frac{2\rho^2}{w_b^2}\right) \tag{2.58}$$

For short propagation distances ($z << \pi w_0^2/\lambda$), the beam waist w_b increases from its initial size w_0 according to the following expression:

$$w_b^2 = w_0^2 + 2.86 C_n^2 k^{1/3} L^{8/3} w_0^{1/3} \tag{2.59}$$

For long distances ($z >> \pi w_0^2/\lambda$), it increases according to the relation

$$w_b^2 = \frac{4z^2}{k^2 w_0^2} + 3.58 C_n^2 L^3 w_0^{-1/3} \tag{2.60}$$

The Strehl ratio and the imaging system's spatial resolution can be computed from the phase variance. Noll [570] shows that the uncompensated turbulence wavefront variance is

$$\sigma_{\text{uncomp}}^2 = 1.02\left(\frac{D}{r_0}\right)^{5/3} \tag{2.61}$$

Because we are concerned with beam spread and not the wander of the beam centroid, the wavefront variance after removal of the two-axis tilt becomes

$$\sigma_{\text{tiltcomp}}^2 = 0.134\left(\frac{D}{r_0}\right)^{5/3} \tag{2.62}$$

The Strehl ratio S can be calculated using Equation 1.60, disregarding the terms that do not contribute to beam spreading. In addition to the beam spread from small turbulent eddies, large eddies also jitter the beam. Over

* When C_n^2 is assumed to be independent of altitude, the turbulence is said to be uniform.

a long exposure, a beam that is spread due to high-order turbulence effects will be spread to a greater extent by high-frequency jitter. The long-exposure Strehl ratio is [268]

$$S = \frac{e^{-\sigma_{comp}^2}}{1 + \left(\frac{2.22\alpha_{jit}D}{\lambda}\right)^2} \tag{2.63}$$

where σ_{comp}^2 is the wavefront variance with tilt removed and α_{jit} is the one-axis tilt jitter. The image of a star captured with an astronomical telescope, that is, using the optical system's point spread function (PSF), will have a bright central core and a wider background halo similar to that shown in Figure 2.2. Parenti [598] shows a modified Strehl ratio expression that accounts for the background halo:

$$S = \frac{e^{-\sigma_{comp}^2}}{1 + \left(\frac{2.22\alpha_{jit}D}{\lambda}\right)^2} + \frac{1 - e^{-\sigma_{comp}^2}}{1 + \left(\frac{D}{r_0}\right)^2} \tag{2.64}$$

The full-width-half-maximum (FWHM) of the central PSF core can be approximated by

$$\text{FWHM}_{core} = \sqrt{\left(\frac{1.22\lambda}{D}\right)^2 + (2.7\alpha_{jit})^2} \tag{2.65}$$

The halo has an FWHM equal to $1.22\lambda/r_0$ (see Figure 2.2).

The resolution R of an optical system imaging through the atmosphere (using Rayleigh's criterion [639]) becomes slightly complicated by the halo being superimposed upon the image core [598]. The resolution is given by

$$R = 1.22\left(\frac{\lambda}{D}\right)\frac{Q}{S} \tag{2.66}$$

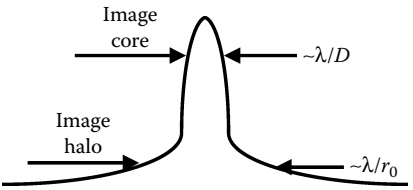

FIGURE 2.2
Point spread function through the atmosphere, which exhibits a diffraction-limited central core and a halo.

where S is the Strehl ratio from Equation 2.64 and

$$Q = \sqrt{\frac{e^{-2\sigma_{comp}^2}}{1+\left(\frac{2.22\alpha_{jit}D}{\lambda}\right)^2} + \frac{1-e^{-\sigma_{comp}^2}}{1+\left(\frac{D}{r_0}\right)^2}} \tag{2.67}$$

Turbulence is a random process that has temporal statistics as well as spatial statistics. From an adaptive optics viewpoint, these statistics are important. If turbulence moves very slowly, then an adaptive optics system can view the disturbance as static. Correction would only be required in the spatial domain. However, if the turbulence is very fast, an adaptive optics system would only see the time-averaged disturbance. Fortunately, the actual turbulence is driven by winds and local eddies, which can be tracked by electronic means. A beam will pass through a different part of the air every time the wind moves it one beam diameter, $t \approx D/\upsilon_w$ (D is the beam diameter, and υ_w is the wind velocity). When a beam is much larger than the coherence length, the time of interest is the time τ the wind takes to transport the beam one coherence length [907], and is calculated as follows:

$$\tau \approx 0.53\left(\frac{r_0}{\upsilon_w}\right)\left(\frac{D}{r_0}\right)^{1/6} \tag{2.68}$$

When the wind velocity is high, the movement of eddies across the beam edges becomes very fast. The result is high-frequency fluctuations of amplitude and phase. The power frequency spectrum for higher-order wavefront variations $P_\phi(f)$ shows the $f^{-8/3}$ power law dependence as follows:

$$P_\phi(f)_{f\to\infty} = 0.0326k^2 f^{-8/3}\int_0^L C_n^2(z)\upsilon_w^{5/3}(z)dz \tag{2.69}$$

An adaptive optics system with a closed-loop servo response should reject most of the phase fluctuations. Greenwood [307] calculated the characteristic frequency f_G (often called the *Greenwood frequency*) as follows:

$$f_G = 2.31\lambda^{-6/5}\left[\sec\beta\int_0^L C_n^2(z)\upsilon_w^{5/3}(z)dz\right]^{3/5} \tag{2.70}$$

In the case of a constant wind, the Greenwood frequency can be approximated by

$$f_G = 0.43\frac{\upsilon_w}{r_0} \tag{2.71}$$

For most cases of interest, the Greenwood frequency of the atmosphere is in the range of tens to hundreds of Hertz. Beland and Krause-Polstorff [72] present measurements that show how the Greenwood frequency can vary between sites. Mt. Haleakala in Maui, Hawaii, has an average Greenwood frequency of 20 Hz. For strong winds (jet stream, etc.) and ultraviolet wavelengths, the Greenwood frequency can reach 600 Hz.

2.1.4 Turbulence Modulation Transfer Function

The distortion due to optics, turbulence, atmospheric absorption, and scattering were combined into a simple formulation by Lutomirski [492]. The modulation transfer function (MTF) of the system is the product of the MTF of turbulence and the MTF of optics, with an attenuation by the atmospheric extinction ε, and is found using the following expression:

$$M_{\text{sys}} = \mathrm{e}^{-\varepsilon z} M_{\text{opt}} M_{\text{turb}} \tag{2.72}$$

where z is the propagation path length. The MTF for a diffraction-limited circular aperture of diameter D is

$$M_{\text{opt}} = \frac{2}{\pi}\left\{\cos^{-1}\left(\frac{\xi F\lambda}{D}\right) - \left(\frac{\xi F\lambda}{D}\right)\left[1 - \left(\frac{\xi F\lambda}{D}\right)^2 J\right]^{1/2}\right\} \tag{2.73}$$

where F is the focal length of the optical system, ξ is the spatial frequency, and the turbulence MTF [300] is given by the following equations:

$$M_{\text{turb}} = 1, \quad z << (0.4k^2 C_n^2 L_0^{5/3})^{-1} \tag{2.74}$$

$$M_{\text{turb}} = \exp\left[-\left(\frac{2.01\xi F\lambda}{r_0}\right)^{5/3}\right], \quad z >> (0.4k^2 C_n^2 L_0^{5/3})^{-1} \tag{2.75}$$

Belen'kii [74] derived the MTF for turbulence when a finite inner scale l_0 is assumed:

$$M_{\text{turb}}(l_0) = \exp\left\{-\frac{[(\xi F\lambda)^2 + l_0^2]^{5/6} - l_0^{5/3}}{(r_0/2)^{5/33}}\right\} \tag{2.76}$$

2.1.5 Multiple Layers of Turbulence

Although turbulence is continuous throughout the atmosphere, some regions have stronger turbulence and will greatly affect astronomical images. When phase conjugation is described in Section 3.1, it will be assumed that all the wavefront errors are concentrated in a single horizontal layer. The optical conjugate of the adaptive optics sensors and correctors is placed at the position of this layer. The strongest turbulence is typically found at low altitudes, often only a few meters above the ground and the telescope. The optical system is then designed to conjugate this layer of turbulence, assuming that all the integrated turbulence above it is included in the ground layer, or, more simply, completely ignoring the turbulence at other altitudes.

Because atmospheric conditions change, the distance to the strongest turbulent layer may change; therefore, the optical system conjugate pupils must be adaptable in themselves.

The next-strongest turbulent layer is typically at the altitude of the jet stream, near 10 km. The jet stream turbulence is very high, in spite of the low density of air, because large wind differences occur over only a few hundred meters and strong eddies form. The jet stream appears in the C_n^2 models at an altitude specified by an average position. As any weather report tells us, the jet stream is highly variable in its strength, location, and duration. An adaptive optics system that has conjugate pupils at the jet stream must also be adaptable to the varying conditions. The statistics of the Strehl ratio can be determined by measuring a few relevant turbulence parameters, such as r_0, f_G, or σ_I^2, at various sites of interest [785].

Because the strength of turbulence is variable and continuous along a vertical path, it is not important for objects exactly on the optical axis. The combined integrated index of refraction is indifferent to the vertical position of the turbulence which caused it. On the other hand, for objects or optical paths that are off-axis, the total integrated index is strongly geometrically dependent on the altitude of the disturbance. To compensate for multiple layers of different degrees of turbulence, multiple pupil phase conjugates must be present in the system, greatly complicating the design and the construction of such systems. The system design consequences of multiconjugate systems are discussed in detail in Chapter 4.

2.2 Thermal Blooming

Atmospheric turbulence occurs whenever any amount of thermal agitation is present, whereas thermal blooming occurs whenever the atmosphere absorbs enough energy from a beam to alter the local index of

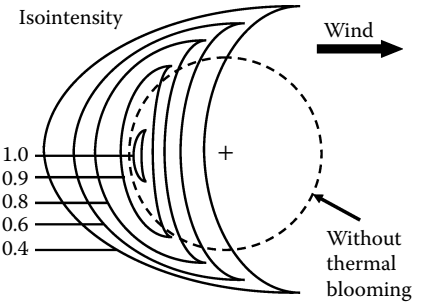

FIGURE 2.3
Computer-generated isointensity plot of a high-power beam in the atmosphere shows the effects of thermal blooming. The beam takes on a characteristic crescent shape bending into the wind.

refraction. The resultant self-induced distortion is called thermal blooming. In one study, when continuous-wave laser beams were sufficiently developed in the kilowatt range, expansion of the beam size ("blooming") was observed [732]. Both steady-state and transient thermal blooming have been investigated.

When the absorbed laser power is balanced by thermal conduction, natural convection, or forced convection due to wind or beam motion, the thermally bloomed beam *turns into the wind*. For a zero-wind case, thermal blooming, often called *thermal defocusing* [674], occurs, because the lowest index of refraction occurs near the center of the beam, where the beam intensity is the highest. This atmospheric negative lens causes the beam to defocus.

An important case occurs when the wind, or an artificial wind caused by beam slewing, causes the beam to take on a characteristic crescent-shaped pattern (Figure 2.3). Light is refracted more toward the dense portion of the air, the least intense region. The kinetics of the atmospheric effects are discussed in detail by a number of authors [276,732]. The effects of convection and conduction are straightforward. Interaction with a compensated high-power beam has been a subject of many studies. The combined effects of blooming and turbulence are even more complex and are being investigated with detailed wave optics and fluid models.

2.2.1 Blooming Strength and Critical Power

As a beam propagates through the atmosphere, its power is absorbed. For a uniformly absorbing atmosphere, the intensity changes according to the following expression [731]:

$$I(r, L) = I(r, 0)\exp(-\alpha L - N_B e^{-r^2/a^2}) \tag{2.77}$$

where the linear absorption coefficient is α, the beam radius is a, the propagation path is L, and the dimensionless parameter N_B is the magnitude of the blooming distortion [92].

For a case when a wind (or the beam is being slewed through the air), the distortion is not symmetric. The blooming strength then becomes a function of the wind velocity υ_w, the beam radius a, the specific heat at constant pressure C_p, and the density of the air ρ. The Bradley–Herrmann blooming distortion number N_B is [87,92]

$$N_B = \frac{-4\sqrt{2}P(\mathrm{d}n/\mathrm{d}T)k\alpha L}{\rho C_p \upsilon_w 2a} \tag{2.78}$$

where P is the beam power, ρ is the mass density, and $\mathrm{d}n/\mathrm{d}T$ is the change of index of refraction with temperature. The index of refraction of air at temperature T is given by [608]

$$(n_0)_{\mathrm{air}}(T) = 1 + (n_{15} - 1)\left(\frac{1.0549}{1 + 0.00366T}\right) \tag{2.79}$$

where T is in degrees Celsius. The index for air at 15°C is given by Edlen [186] as

$$(n_{15} - 1) \times 10^8 = 8342.1 + \frac{2406030}{130 - \lambda^{-2}} + \frac{15996}{38.9 - \lambda^{-2}} \tag{2.80}$$

where λ is in microns. For example, $(n_0)_{\mathrm{air}} = 1.000276$ at 15°C and $\lambda = 0.6328\ \mu$m. For a focused beam, the radius a is replaced by an effective radius a_{eff} over the propagation length L as follows:

$$a_{\mathrm{eff}} = \left(\frac{La\lambda}{\pi}\right)^{1/3} \tag{2.81}$$

where the absorption coefficient is not constant along the propagation path and physical slewing of the beam occurs, Karr [403] presents a more general expression for the distortion number as follows:

$$N_D = 8\sqrt{2}\pi\left[\frac{\partial n/\partial T}{\rho C_p}\right]\frac{P}{2\lambda a}\int_0^\infty \frac{\alpha(z)}{\upsilon_w(z) + \dot{\theta}z}\exp\left\{-\int_0^z [\alpha(z') + \alpha_s(z')]\mathrm{d}z'\right\}\mathrm{d}z \tag{2.82}$$

where $\alpha(z)$ is the path-dependent absorption coefficient, $\alpha_s(z)$ is the path-dependent scattering coefficient, and $\dot{\theta}$ is the angular slew rate.

The effect of thermal blooming on the propagation of the beam is the physical spreading of the energy and the reduction of the on-axis energy. The blooming strength (or distortion number) is roughly the number of *radians* of wavefront error induced by the blooming. Experiments and wave optics calculations [732] verify that this reduction, which is represented by the Strehl ratio S, empirically takes the form

$$S = \frac{1}{1 + K' N_B^m} \tag{2.83}$$

where $K' = 0.0625$ and $m = 2$ for an infinite Gaussian beam, and $K' = 0.01$ and $m = 1.2$ for a uniform beam. If the on-axis intensity is modified by the Strehl ratio for thermal blooming distortion (Equation 2.83) the intensity becomes

$$I_{\text{Bloom}} \propto \frac{Pa^2 S}{\lambda^2 L^2} \propto \frac{P}{1 + \kappa P^m} \tag{2.84}$$

The constant $\kappa = K'(N_B/P)^m$ absorbs the parameters affecting blooming strength. Note that the intensity of the bloomed beam is nonlinear in power P. For any finite value of κ (that is, any level of thermal blooming), an increase of power will only result in an increase in intensity until the power reaches a certain value (Figure 2.4). This *critical power* P_{crit} is related to the blooming strength by

$$P_{\text{crit}} = \left(\frac{-1}{\kappa(1-m)} \right)^{1/m} \tag{2.85}$$

The distortions due to thermal blooming can be reduced in a number of ways without applying adaptive optics. An increase in wind, or slew rate, reduces

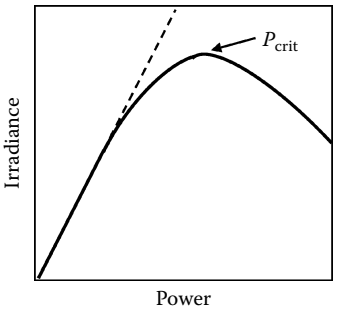

FIGURE 2.4
Increases in power result in increased intensity until the critical power is reached.

the blooming strength and increases the Strehl ratio directly [426]. Although this is simple, it is often impractical because the wind on a specific day in a specific place is unpredictable and the beam-propagation scenario might not allow slewing the beam in an arbitrary manner.

If the power in the beam is applied for a duration that is too short for the atmosphere to develop a thermal lens, blooming could be avoided. This principle can be applied by using pulse lasers. Blooming will occur whenever density changes are propagated transverse to the beam by acoustic waves. By properly controlling the pulse length and the pulse repetition frequency, thermal blooming often can be reduced.

Pulsing a laser to avoid thermal blooming is not possible in all cases. Reducing the pulse length without simultaneously reducing power can cause other phenomena worse than blooming. *Gas breakdown* is the ionization of the air path that results from intense radiation in the gas. The result is often total laser beam absorption [733].

When the pulse is long compared to the time a/υ_s, where a is the beam radius and υ_s is the velocity of sound, the *long-time thermal blooming* strength is given by

$$N_{lt} = \frac{2(-dn/dT)\alpha I_0 t L^2}{\rho C_p a^2} \tag{2.86}$$

where $\alpha L \ll 1$. Although the expression for long-time blooming strength shows a linear increase in time, there is a limiting factor. Ulrich [799] showed that there exists a time when the on-axis intensity drops because of thermal blooming, such that the blooming can no longer continue. This point is achieved when the intensity is about one-tenth of its initial value. The time taken for this saturation to occur is given by

$$t_s = 0.04\left[\frac{8n_0\rho C_p}{(dn/dT)\upsilon_s^2\alpha}\right]^{1/2}\frac{\lambda^2 L}{a\sqrt{E}} \tag{2.87}$$

where E is the pulse energy.

When the pulse length t_p is short compared to the hydrodynamic lens-forming time t_h, the pulse thermal blooming strength N_p becomes [732]

$$N_p = \frac{8(-dn/dT)\upsilon_s^2 E\alpha L^2 t^3}{3\pi\rho C_p t_p a^6} \tag{2.88}$$

where E is the pulse energy and the quantity αL is assumed to be small, that is, $\alpha L \ll 1$. Equation 2.88 shows a cubic dependence on the time t after the onset of the pulse. Short-term transient thermal blooming is often called *t-cubed blooming*.

When a number of pulses are strung together, a condition called *multiple-pulse thermal blooming* occurs [183,588] The parameters that describe the effects of blooming for this case are the blooming strength N_{mp} and the number of pulses per flow time (NP), so that

$$N_{mp} = \frac{2(-dn/dT)\alpha EL^2}{\rho C_p \pi a^4} \tag{2.89}$$

and

$$NP = [PRF]\frac{2a}{\upsilon} \tag{2.90}$$

These basic expressions can be used in Equation 2.83 to evaluate the effects of thermal blooming in the atmosphere. The application of adaptive optics to correct for thermal blooming phenomena will require knowledge of the temporal and spatial effects of blooming distortion [602]. Other than the pulse and multiple-pulse effects described earlier, the overall frequency for atmospheric response f_b under blooming conditions [562] is $f_b = \upsilon/(2a)$, where the wind velocity υ can be caused by slewing or actual wind or a combination of both, and the beam radius a must be evaluated for each case. For a collimated beam, the aperture radius is a suitable approximation, and for a focused beam, the beam radius at $0.75L$ can be used for an approximation [7].

The historical summary and the simple expressions given here can be used for order-of-magnitude analyses. The nonlinear behavior of the high-power beam in the atmosphere requires both extensive analysis and supporting experimentation [489].

2.2.2 Turbulence, Jitter, and Thermal Blooming

The combined and often closely coupled effects of atmospheric turbulence, beam jitter, and thermal blooming are the topics of much investigation. Although we can show simple rules for estimating the three effects independently, the response of the atmosphere for the three competing phenomena is extremely complicated. For example, thermal blooming strength is a function of the beam radius a and the wind velocity υ. Beam jitter has the effect of a false wind, which would alter the degree of blooming. If the jitter is of high frequency, the beam intensity is smeared before the atmosphere has time to respond, giving the appearance of a larger effective radius. For intermediate frequencies, the beam's own jitter might follow the *bending into the wind* phenomenon or even counteract it. All of these phenomena might occur simultaneously [276].

Atmospheric turbulence has the effect of inducing dynamic tilt, which has the same characteristics as complicated beam jitter. Turbulence can also

induce beam spreading because of its high spatial frequency content. This can increase the apparent beam radius, thus reducing the local intensity and the magnitude of the turbulence.

Another phenomenon occurs when adaptive optics is used to try to correct for the combined effects of thermal blooming and turbulence. The errors in the wavefront that occur in the propagation path tend to defocus or spread the beam. Compensation for the negative atmospheric lens involves the application of the conjugate positive lens in beam-transmitting optics. This effectively increases the intensity, which, on one hand, is the desired effect, but on the other hand, increases the strength of the thermal blooming and forces the atmosphere into a more *negative* lens. This instability [404] along the beam path has been observed in a number of experiments [391] and is observed as small spatial scale (high spatial frequency) phase-conjugate instabilities [57,392,705,706].

Many investigators have studied the complexities of turbulence and thermal blooming [200,277,572,844]. They have investigated simple scaling relationships [94], the detailed physics of the distortion process [97,337], and the applications of adaptive optics [540,706,842]. They have used four-dimensional wave-optics models [154,540,551] supported by experimental verification [89,390,631]. The limitations of adaptive optics compensation for thermal blooming, especially the requirement for full-field* compensation, generate the most interest [402]. The complex interaction of diffraction, turbulence, and the high-power thermal blooming phenomenon at small scales limits the applicability of phase-only corrections [550].

2.3 Nonatmospheric Sources

Although turbulence is the major source of concern for astronomers using adaptive optics, and thermal blooming is a limiting factor for high-power beam propagation, adaptive optics are often used to correct for aberrations that enter a system in other ways.

2.3.1 Optical Misalignments and Jitter

The inadvertent introduction of tilt or dynamic tilt (jitter) into a system can reduce its performance. In some cases, this performance is only slightly reduced, as in the case of an imaging system where tilt simply moves the

* Full-field compensation applies a correction to both the amplitude and the phase. This differs from the conventional phase-conjugate approach, discussed in Section 3.1, where correction is applied to the phase only.

position of the image without affecting its quality. These problems often can be accepted. On the other hand, slight misalignments in optics inside a laser resonator can greatly reduce its performance and, in many cases, can eliminate the possibility of lasing altogether. Errors in setting up or mounting, external error sources (such as mechanical (acoustic) vibration [599]), and thermal problems can all contribute negatively to a poorly performing system. Defects such as tilt [898] and decenter [515] can be studied using ABCD matrices (see Section 3.1).

Adaptive optics in a tilt-correction mode can be used to correct for these errors [100]. The problem of maintaining alignment or beam pointing has evolved from early electromechanical telescope- and radar-control systems to the present-day scanning and control systems that operate in the megahertz range. This book treats tilt as a fundamental low-order wavefront aberration. A tilted component in a system can induce other higher-order aberrations. A tilted mirror or beam splitter intercepting a converging beam will introduce the next higher-order aberration, astigmatism. A tilted spherical optical element in a telescope will introduce coma. Severe tilts in complicated optical configurations can introduce many high-order aberrations.

The elimination of tilt, or pointing error, is the first business of adaptive optics. Control of fast tilt (jitter) or slow tilt (drift) is often all that is needed in an adaptive optics system.

2.3.2 Large Optics: Segmenting and Phasing

Striving for ever-better means of collecting faint starlight or focusing laser beams to extremely small spots requires larger and larger optical elements, the manufacture of which presents new problems for investigators and new challenges for adaptive optics. Extending technology from the Keck telescopes' alignment and phasing of the thirty-six 1.8-m segments into a 10-m diameter aperture has evolved into the phasing of 8-m segments into behemoths as large as the 42-m diameter European Extremely Large Telescope.

In large optics, small local deviations from perfect curvature are manifested as high spatial frequency aberrations that require correction. Casting large mirrors requires extreme care [182]. Even after a perfect casting, figuring, and coating, large optics (mostly mirrors) are placed in relatively hostile environments. One operation that often produces aberrations is simply placing the mirror. The effects of gravity on massive objects (weighing thousands of pounds and stretching many feet across) cause the mirror to sag and deform [23]. If this mirror is placed on a movable mount, the direction of the deformation will change with the motion. The sag can neither be calibrated out nor be polished away, because it will change during operation.

The gravitational sag of a large mirror can be calculated. The deflection ω_z, normal to the surface, of a circular plate of radius a, which is placed horizontally is [58]

$$\omega_z = \frac{3\rho g(1-\nu^2)}{16Eh^2}\left[\frac{5+\nu}{1+\nu}a^4 - \frac{2(3+\nu)}{1+\nu}a^2r^2 + r^4\right] \tag{2.91}$$

where ρ is material density, E is Young's modulus, ν is Poisson's ratio, h is disk thickness, and g is gravitational acceleration. The aberrations for a mirror or large lens under the influence of gravity are a constant piston, a sphere term proportional to r^2, and a spherical aberration proportional to r^4. For a 2.4-m fused-silica mirror (the Hubble Space Telescope), for instance, there can be a total deflection of 3 μm and a spherical aberration component of 0.7 μm on the ground during polishing that would not be present in orbit.

Adaptive optics can be used to correct for gravity effects and other effects of large size. Large mirrors present interesting problems and interesting solutions. Large mirrors can be self-correcting; that is, they can contain the necessary physical elements that adjust their figure and correct aberrations in other parts of the system as well [446].

Large optics can be subdivided into smaller segments. These segments can then be coaligned or *phased* to act as a larger mirror. The aberrations induced in large mirrors and the systems that are used to phase segments have been studied for a number of years [212,728]. For the purpose of the study of adaptive optics, aberrations due to gravity (low spatial frequency), local defects, or deformation (high spatial frequency) can be treated in the same manner as similar aberrations in smaller optics, with only the magnification of spatial frequency taken into account.

Large mirror jitter is the same as small mirror jitter in terms of temporal frequency.* The spatial frequency of the aberration is usually expressed in *cycles/diameter* (cyc/diam). Thus, a defect in a large 1-m mirror that is 1 cm across has much higher spatial frequency content (100 cyc/diam) than the same defect in a 20-cm mirror (20 cyc/diam).

The aberrations that occur at mismatched edges have very high spatial frequency content. These almost-infinite spatial frequencies must be treated separately. The correction over the edges (which is usually a very small portion of the area of the aperture) can be simply disregarded, or the light that impinges on these edges can be masked out. The appearance of a sharp edge in a wavefront can disrupt an adaptive optics system. If the wavefront is measured at two points on either side of the edge and it senses a difference in phase, the control system may perceive this to be a local tilt, whereas it is actually a piston error on one or both sides of the edge. If the error is greater than one wavelength, the adaptive optics system may become unstable. These difficulties are addressed in Chapter 5.

* Even though it is difficult to get a large mirror jittering quickly, it is generally treated the same by an adaptive optics system.

2.3.3 Thermally Induced Distortions of Optics

When a beam of light strikes an optical surface, some of the energy is absorbed. For low-power beams, imaging systems, and transparent glasses, the absorption is rarely noticed. High-power beams (>1.0 kW/cm^2) can induce a temperature rise in the optics that is proportional to the absorbed incident intensity. Passive or uncooled mirrors and actively cooled mirrors exhibit distortions under high-power illumination.

For a mirror modeled as a flat plate, the strain ε induced is proportional to the temperature rise T,

$$\varepsilon = \alpha T \tag{2.92}$$

where α is the coefficient of linear thermal expansion of the material. For a plate in the x–y plane, the in-plane stresses σ_{xx} and σ_{yy} are given by

$$\sigma_{xx} = \frac{E}{1-\nu^2}[(\varepsilon_{xx} + \nu\varepsilon_{yy}) - \alpha(1+\nu)T] \tag{2.93}$$

$$\sigma_{yy} = \frac{E}{1-\nu^2}[(\varepsilon_{yy} + \nu\varepsilon_{xx}) - \alpha(1+\nu)T] \tag{2.94}$$

where the strain tensors are ε, Young's modulus is E, and ν is Poisson's ratio. Myers and Allen [550] show as follows how the in-plane stresses result in the strain:

$$\varepsilon_{xx} = \frac{\nu}{E}(\sigma_{xx} + \sigma_{yy}) + \alpha T \tag{2.95}$$

With uniform incident intensity, a flat circular plate of thickness h shows an out-of-plane displacement $\omega(r, \theta)$

$$\omega(r,\theta) = [C_0 + C_2 r^2] + [C_1 r + C_3 r^3]\exp(i\theta) \tag{2.96}$$

This is a solution of Poisson's equation $\nabla^2\omega = -m_t$, where m_t is the thermal moment density, calculated as follows:

$$m_t = \frac{-\alpha E}{1-\nu}\int_{-h/2}^{h/2} T(x,y,z)z\,dz \tag{2.97}$$

The constants C_i are computed from the specific boundary conditions. For a plate uniformly constrained at the edges (i.e., $C_1 = C_3 = 0$), the distortion is a constant plus a function of the radial distance from the center. Thus,

if uniform power P is absorbed, the temperature profile results in stresses that cause a characteristic paraboloidal bowing of the plate, as shown in the following equation:

$$\omega_z(r) = P(C_0' + C_2' r^2) \tag{2.98}$$

Because *bowing distortion* is proportional to the total absorbed power, it is also called *power-induced distortion*.

If the intensity profile $I(x, y)$ on the plate is not uniform, regions of local temperature increases will result in another form of distortion. The displacement in the out-of-plane direction ω_z can be found by solving the expression

$$\nabla^4 \omega_z = \frac{P_0}{D} \tag{2.99}$$

with the appropriate boundary conditions. Here, P_0 is the load density, and the plate modulus D is given by

$$D = \frac{Eh^3}{12(1 - \nu^2)} \tag{2.100}$$

The result for a circular plate is the integral of the strain tensor ε_{zz} [655], given by

$$\omega_z(x, y) = \int_{-h/2}^{h/2} \varepsilon_{zz} \mathrm{d}z = \int_{-h/2}^{h/2} \alpha T(x, y, z) \mathrm{d}z \tag{2.101}$$

Because the temperature *profile* is nearly proportional to the intensity *profile*, the resultant out-of-plane thermal growth is proportional to the absorbed intensity distribution where α_{abs} is the absorption coefficient.

$$\omega_z(x, y) = \xi \alpha_{abs} I(x, y) \tag{2.102}$$

The proportionality symbol ξ, used in much of the literature, resembles a worm and has been called the *worm factor*. This constant describes the amount of thermal growth due to local intensity variations. It is a function of the material parameters, cooling system design, and coolant flow rates. Measured worm factors range from 5 to 100 Å/W/cm^2.

Because this form of thermal distortion produces a map of the flux or intensity pattern, it is called *thermal-mapping distortion*, *flux-induced distortion*, or *intensity-mapping distortion*. It is proportional to the intensity *distribution* rather than the total power. Thermal mapping has an interesting property. Because the optical surface responds to the intensity of the impinging beam by distorting along the axis of the beam, reflections from that surface are

advanced or retarded by the surface map. Thermal mapping translates intensity information from a beam into the phase (wavefront). Nonuniformity in the intensity results in reduction of the Strehl ratio and more severe beam-propagation limitations.

The thermomechanical response of a plate cannot always follow the intensity pattern exactly. Thermal diffusion tends to smooth the temperature distribution, and the mechanical response of the plate tends to smooth it more. A more exact treatment of thermal mapping would show these effects as convolutions (represented by $*$) among the responses of the material to thermal load R_{T}, mechanical stress R_{M}, and absorbed intensity forcing function $\alpha I(x, y, t)$, as follows:

$$\omega_z(t) = R_{\mathrm{T}}(t) * R_{\mathrm{M}}(t) * \alpha \xi I(x, y, t) \tag{2.103}$$

These responses can often be calculated numerically for different conditions. Both steady-state and transient solutions are often needed. For instance, a continuous beam impinging on a mirror with active cooling reaches steady-state distortion in a few seconds or less. The temperature profile, used in Equation 2.97, for the surface of a mirror when it is illuminated by a pulsed beam is a function of the thermal diffusivity ζ and thermal conductivity k_{t}:

$$T(x, y, \tau) = T_0(x, y, 0) + \frac{I(x, y)}{k_{\mathrm{t}}} \sqrt{\frac{4\zeta\tau}{\pi}} \tag{2.104}$$

where τ is the pulse length and T_0 is the surface temperature before the pulse [114].

2.3.4 Manufacturing and Microerrors

Manufacturing of optics has always been limited by the available technology. The choice of glass or metal substrates is dependent on their ultimate performance. In 1730, Isaac Newton wrote [559]:

> But because Metal is more difficult to polish than Glass, and is afterwards very apt to be spoiled by tarnishing, and reflects not so much Light as Glass quick-silver'd over does: I would propound to use instead of the Metal, a Glass ground concave on the foreside, and as much convex on the back-side, and quick-silver'd over on the convex side. The Glass must be every where of the same thickness exactly.

The manufacturing technology of the optical surfaces limits the overall performance of the optical system. With adaptive optics technology, many of the defects that arise from manufacturing can be corrected. The materials chosen for refractive or reflective optics may have surface errors that figuring and polishing cannot remove. Generally, they are of such low magnitude or high

spatial frequency that adaptive optics is useless against them. Occasionally, a large systematic error may occur that produces a low-order aberration. A variation in polishing pressure, for instance, may produce such a defect that can be removed with adaptive optics when the optical element is used. Usually, these static, low-order defects can be calibrated out or compensated for during system setup, without relying on closed-loop control.

Even after polishing and coating, there may be roughness on the surface (called microstructure) that would affect an adaptive optics system. The adverse effects of the aberrations are usually less than the increased scattering from the optical surface. Scattered light affects sensors and can result in reduced-control system performance. The microstructure of polished optical materials is expressed in root mean square (rms) roughness [199]. The roughness can range from about 10 Å for fused quartz to over 100 Å for materials such as molybdenum and beryllium. The fraction of incident light scattered, the total integrated scatter (TIS), from a surface with rms roughness δ is

$$\mathrm{TIS} \cong \left(\frac{4\pi\delta}{\lambda}\right)^2 \tag{2.105}$$

where λ is the incident light wavelength. For roughnesses approaching even small fractions of a wavelength, the negative effects of scattering can be severe. Large roughnesses are also known to be extremely sensitive to incident high powers. If light is multiply reflected in the hills and valleys of the surface, absorption and *microthermal mapping* can lead to stresses that result in permanent damage to a mirror surface.

Another characteristic of the microstructure or any other random surface property is its autocovariance length. Polishing or figuring processes may have some spatial correlation [638]. By calculating the autocovariance $G(r)$ of the surface $z(\rho)$ over the surface, we can obtain a statistical description of the surface roughness or figure error as follows:

$$G(r) = \lim_{L\to\infty} \int_{-L/2}^{L/2} z(\rho) z(\rho + r)\,\mathrm{d}\rho \tag{2.106}$$

where L is the one-dimensional extent of the surface under investigation. Examination of the autocovariance in either one or two dimensions can lead to knowledge about the spatial characteristics of the random surface. A narrow $G(r)$ suggests a very fine grain roughness with no interaction across large regions. This is characteristic of surface microroughness. A wide $G(r)$ suggests some spatial correlation. This occurs mostly as a result of systematic and repeatable figuring or coating processes. A spike in the autocovariance function suggests a strong correlation at one particular separation. A radial-pattern diamond-turning machine may produce small defects that exhibit this periodic behavior. A cooled mirror with improperly pressurized

coolant channels may also exhibit periodic "print-through" of the coolant channels that show up as a spike or bump in the autocovariance function. Even though adaptive optics cannot correct for many of the very small or high spatial frequency errors, these errors can mask the disturbances that adaptive optics is supposed to correct.

2.3.5 Other Sources of Aberrations

Adaptive optics is also used for purposes other than air or vacuum propagation and simple reflections or refractions. Advanced applications include imaging the human retina [463], supporting light transmission through sea water [622], ground-to-ground free-space laser communications, ground-to-space laser communications, transmission through fiber optics, in laser fusion systems [543,825], and in solid or gas lasing media. Each of these applications presents different possibilities for introducing aberrations that require correction by adaptive optics. Turbulence in the vitreous humor of the eyeball distorts imagery, but this defect can be compensated with conventional adaptive optics. Details of this application are given in Chapter 4. The refractive index of sea water is above 1.3. It is transmissive in the blue-green spectral region and is the obvious medium of propagation for surface-to-submarine communications. The sea has large thermal gradients that produce turbulence [622]. The turbulence results in aberrations that degrade the signal. Light in a free-space communications system acts as the carrier, but severe aberrations can distort the modulation such that the bit-error-rate is increased dramatically [673]. Details of adaptive optics laser communication systems will also be discussed in Chapter 4.

2.3.6 Aberrations due to Aircraft Boundary Layer Turbulence

Imaging from a moving aircraft presents some problems. An aircraft moving through ambient air produces turbulence in the boundary layer directly in front of the objective of an aerial camera. The expression for the boundary-layer MTF [453], which follows an exponential similar to that for Kolmogorov atmospheric turbulence (Equation 2.75), is given by

$$M_{\mathrm{BL}} = \exp\left[-3.44\left(\frac{\lambda \xi F}{r_{\mathrm{BL}}}\right)^{5/3}\right] \tag{2.107}$$

where F is the focal length of the objective and r_{BL} is the correlation length for the boundary layer. The correlation length, analogous to Fried's parameter, depends upon the flight speed, aircraft surface form, and air density. At visible wavelengths, r_{BL} varies from 5 to 20 mm [406]. Many mechanical methods are used to reduce the boundary-layer aberration and to characterize the remaining aberration [303].

2.3.7 Aberrations in Laser Resonators and Lasing Media

Laser resonators present many opportunities for aberrations to arise. The multiple-pass nature of most resonators lets an aberrated propagating wave diffract into intensity fluctuations. The intensity fluctuations can cause further degradation [6]. Optics inside a resonant cavity can become misaligned, similar to optics in any beam train. Tilts, defocus [14,234], and astigmatism can appear in resonators and greatly affect their performance [594,595,741]. Coupling between various aberrations has been investigated [594]. Static wavefront tilt and dynamic tilt (jitter) can reach critical levels at which the resonator can no longer support lasing [433].

The laser gain medium can be responsible for a number of aberrations. Because lasing can take place in solids, liquids, gases, or plasmas, any imperfections in these media that result in inhomogeneous distributions of gain can reduce laser performance. Structural imperfections in solid-state lasers [894] and turbulence in liquid or gas lasers [328,601,674] are the most common problems. Dynamic gas lasers and free-electron lasers have rapidly moving laser media that provide another source of disturbance to the wavefront [168]

Some common pass resonators [722,723], such as an unstable annular resonator, can be insensitive to some effects. For instance, the misalignment of a conical mirror or an axicon [518] will cause a shortening of the path on one side of a device but an equal lengthening on the other side [548]. The round-trip photon experiences no phase variation. In such resonators, the radiation is not confined to a small central core, as it usually is in stable resonators. When the radiation spreads and encounters conical mirrors and output scraper mirrors, the edge effects become very important [15,716]. Edges impart very high spatial frequency aberrations to the wavefront, which often results in more divergence than that seen in an apodized or slowly decaying intensity edge.

Adaptive optics systems have been used for correction of aberrations inherent in resonators and lasing media. In some cases, the adaptive optics systems were placed inside the resonant cavity [234,625,222]. Other systems have been designed to correct the aberrated output of a laser resonator regardless of the source of the disturbances. Details of the sensing and correction methods are discussed in Chapters 5 and 6.

3

Adaptive Optics Compensation

When the various disturbances discussed in Chapter 2 are unavoidable, adaptive optics comes to the rescue. Each adaptive optics system should enhance the performance of its "parent" optical system. Adaptive optics should be added to an imaging system only if it improves the images and should be added to a laser fusion system only if it enhances the fusion process [825].

There are many ways to approach the problem of compensating for the aberrations. Conventional approaches that use wavefront sensors, electronic controls, and correction optics can be used to overcome the effects of the aberrations. Some passive methods have also been suggested. Beckers [68,69] describes a method of after-the-fact optical correction that is possible on astronomical optical interferometers. Since the point spread function of an imaging system consists of a central spike of "good" information surrounded by a broad background of noise (Figure 2.2), he suggests a placement of an aperture or single-mode fiber that restricts the amount of light to the central spike. Other *unconventional methods* use the nonlinear properties of certain optical materials to correct the effects of aberrations. In any case, the application of corrections is generally a closed-loop real-time process. Non–real-time techniques of image processing using wavefront information are usually inadequate. The modulation transfer function (MTF) of the aberrated image is so low that the signal is corrupted by noise. Adaptive optics are necessary up front to improve the MTF and the signal-to-noise ratio (SNR).

The most common approach to correcting the various aberrations is the principle of *phase conjugation*, which is sometimes referred to as *phase-only conjugation* to distinguish it from systems that also correct amplitude effects. The term "phase conjugation" is widely used synonymously with *nonlinear phase conjugation*. However, the principle of applying a conjugate phase to a beam is the basis for most forms of adaptive optics, either linear (conventional) or nonlinear.

3.1 Phase Conjugation

The principle of phase conjugation is the core of adaptive optics [340]. It can be analyzed in a number of ways. The method for applying phase conjugation is shown in Figures 3.1 and 3.2. The wavefront of a beam entering from the left (Figure 3.1a) is distorted by a piece of glass because the index of refraction is higher than one. The wavefront is retarded as it goes

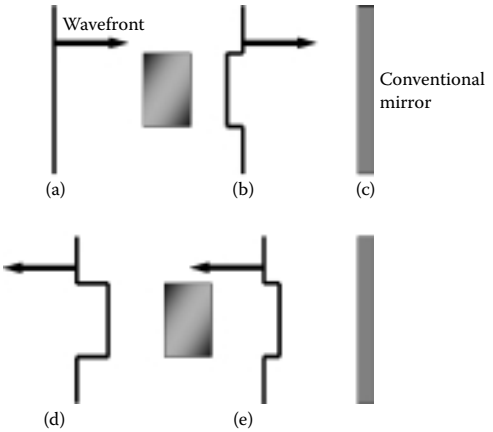

FIGURE 3.1
Wavefront distortion traversing an aberrator: (a) The plane wavefront passes through an aberrator and the wavefront is delayed. (b) The wavefront with the delay reflects from (c) a conventional mirror and (d) travels toward the left with the delay. (e) As it passes a second time through the aberrator, the wavefront is delayed further.

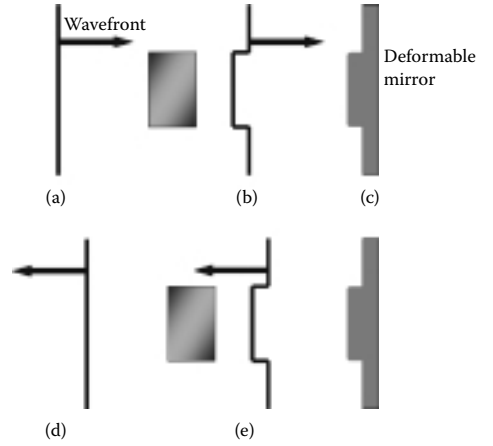

FIGURE 3.2
Wavefront distortion traversing an aberrator with a correcting mirror: (a) The plane wavefront passes through an aberrator and the wavefront is delayed. (b) The wavefront with the delay reflects from (c) the deformable mirror with the conjugate shape and (d) travels toward the left with the delay reversed. (e) As it passes a second time through the aberrator, the wavefront is returned to a plane.

through the glass (Figure 3.1b). After reflection from the mirror (Figure 3.1c), the wavefront has the same shape but propagates in the opposite direction. As it traverses the glass again (Figure 3.1d), it receives the same retardation as before. The exiting wavefront (Figure 3.1e) is greatly distorted, since it has passed through the aberrator twice.

If we want to achieve a plane wavefront after a beam passes through the glass twice, there may be a way to alter the surface of the mirror in such a way as to invert the wavefront so that the second passage leaves no residual distortion. Looking at Figure 3.2, we can see that a bump in the mirror *at just the right place* and *at just the right amount* can cause the leading edge of the wavefront to be reversed. When this wavefront (Figure 3.2d) passes through the aberrator again, the final wavefront (Figure 3.2e) is once again a plane. The amount of "bump" needed in the mirror is proportional to the wavefront itself and has the reverse sign. This in essence multiplies the field $|E|e^{-i\phi}$ by its complex conjugate $|E|e^{+i\phi}$; thus the name *phase conjugation*.

There are some very big "ifs" in the preceding argument. If we can put the *right amount* of phase conjugate at the *right place*, then we can accomplish the correction. As discussed in Chapter 2, many aberrations are dynamic; we must also place the phase conjugate on the beam at the *right time*. These three constraints to the relatively simple problem of applying a phase conjugate are the reasons for difficulties that have had to be addressed before there were significant advances in adaptive optics. Another way to understand the phase conjugate concept and its limitations is by examining a simple imaging system Using the paraxial approximation, that is, geometric optics, and the method of ABCD matrices, we can see how phase conjugation can be used to correct aberrations outside an imaging system. If a ray entering from the left is represented by its displacement from the axis x and its slope s, we can trace it to the focal point of a simple imaging system (Figure 3.3). The lens of the imaging system (focal length f) forms an image at the distance $F = f$ behind the lens. The characteristic of the ray after traversing the imaging system x' and s' is given by the matrix equation

$$\begin{pmatrix} 1 & F \\ 0 & 1 \end{pmatrix} \begin{pmatrix} 1 & 0 \\ -1/f & 1 \end{pmatrix} \begin{pmatrix} x \\ s \end{pmatrix} = \begin{pmatrix} x' \\ s' \end{pmatrix} \tag{3.1}$$

A ray normal to the lens ($s = 0$) will cross the axis at a distance f from the lens. Now, if there is an aberration represented by another lens f_a a distance d from the imaging system, the ray will not cross the axis at the focal point of the

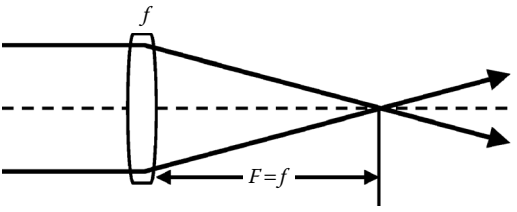

FIGURE 3.3
Simple imaging system.

imaging system. See the top of Figure 3.4. The position of axis crossing (the new focus for the rays) is given by

$$F = f\left[\frac{d - f_a}{d - f - f_a}\right] \tag{3.2}$$

That means that we can compensate for the aberration by refocusing the beam. If we simply apply a correcting lens with focal length f_c directly after the imaging system lens (bottom of Figure 3.4), we find that the "adaptive optics" imaging system has an apparent focal length of $(f_c f)/(f_c + f)$ and the correcting lens focal length is given by

$$f_c = \left[\frac{1}{F} - \frac{1}{f} - \frac{1}{(f_a + d)}\right]^{-1} \tag{3.3}$$

This shows that measurement of the wavefront (the displacement and the slope of the ray) can lead to a correction for the misfocus introduced by some outside source. In a special case where the focal plane is left at distance F from the lens and the aberration is near the imaging system $d \to 0$, the focal length of the correcting system is the opposite of the aberration: $f_c = -f_a$.

If a wavefront is made up of the leading edges of spherical waves (Huygens' principle), we can see how the ABCD matrix method can be used to understand adaptive optics. If each part of a wavefront is measured in terms of its slope s, we can produce the characteristics of the entire wavefront. Knowing where each slope measurement comes from is equivalent to knowing the displacement from the axis, x. Repeated and simultaneous adjustment of the correction device f_c can result in a conjugated wavefront.

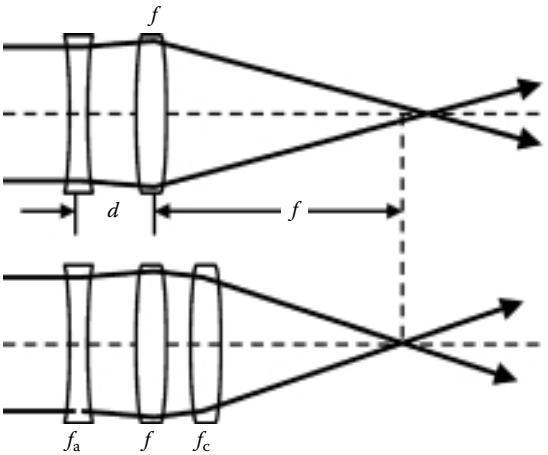

FIGURE 3.4
Simple imaging system with aberrating lens.

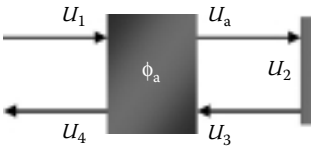

FIGURE 3.5
Simple propagation with aberrating object.

A more rigorous treatment can show the phase-conjugation principle without the restrictive geometric approximations. From Figure 3.5 we can calculate the field $U_4(x_2, y_2)$ after transmission through an aberrating plate, propagation to a correcting mirror, reflection, and propagation back through the aberrating plate. The input field propagating left to right is a constant plane wave $|U_1|$. After transmission through the aberrating plate, the field has a phase component $U_a = |U_1| e^{ik\phi_a}$. Propagation to the mirror results in a field U_2

$$U_2 = \frac{ike^{ikd}}{2\pi d} \int dx_a dx_b U_a \exp\left[\frac{ikr_{a2}^2}{2d}\right] \tag{3.4}$$

where $r_{a2}^2 = (x_a - x_2)^2 + (y_a - y_2)^2$ and the integral is over the limiting aperture. The mirror has the correction applied to its surface, ϕ_c, so that the field leaving the mirror is $U_2 e^{ik\phi_c}$. After propagation back to the aberrating plate, the field has the form

$$U_3(x_a, y_a) = \frac{ike^{+ikd}}{2\pi d} \int_{\text{mirror}} dx_m dy_m U_2 e^{ik\phi_c} \exp\left[\frac{ikr_{2a}^2}{2dd}\right] \tag{3.5}$$

After a final pass through the aberrating plate, the field has the form

$$U_4 = e^{ik\phi_a} \frac{-k^2}{(2\pi d)^2} |U_1| \int dx_m dy_m e^{-ikf_{2a}^2/2d} e^{ik\phi_c} \int dx_a \; y_a e^{ik\phi_a} e^{-ikf_{a2}^2/2d} \tag{3.6}$$

This equation has no analytical solution for a general case, since the form of the aberration and the boundaries of the integration (the apertures) are unspecified. However, for a case analogous to the single slab of glass discussed earlier, the exponential aberration terms can be brought outside the integral as follows:

$$U_4 = e^{2ik\phi_a} e^{ik\phi_c} \frac{-k^2}{(2\pi d)^2} |U_1| \int dx_m dy_m e^{-ikf_{2a}^2/2d} \int dx_a dy_a e^{-\; kf_{a2}^2/2d} \tag{3.7}$$

For the field U_4 to exactly equal the field U_1, the aperture effects must be neglected and the correction applied $\phi_c = -2\phi_a$. Accounting for the double-pass nature of this problem, the correction must be the conjugate of the aberration.

This brings up a fundamental limitation of adaptive optics. If the wavefront cannot be precisely determined or precisely replicated or if diffraction effects dominate, the phase conjugation cannot be exactly employed. This limits the

effectiveness of adaptive optics in many places. For instance, high-altitude aerosols can enhance thermal blooming. The wavefront changes at high altitudes are seldom seen by wavefront sensors at the ground level, since diffractive effects mask the phase measurement. Many systems designed for adaptive optics correction must specifically take into account the relationship of the aberrations to the position of the corrections. One method applies correction in the image plane of the phase disturbance. Some nonlinear optical methods (e.g., stimulated Brillouin scattering) use the aberrated beams themselves to instigate the correction. Other methods apply correction of the wavefront near the aberration source to limit diffractive effects (the *keeping it in the near-field* approach). Some adaptive optics systems recognize the limitations and just correct as much as they can [569,574,627,734].

3.2 Limitations of Phase Conjugation

Up to now, we have implied that adaptive optics systems can have perfect phase conjugation and the systems are only "performing well" when such perfect phase conjugation is achieved. Perfect phase conjugation is not a necessary condition for adaptive optics to show usefulness. For speckle interferometry [569] or astronomy, partial compensation is not only useful, but because of the high cost of adaptive optics, it is the only option. An 8-m terrestrial telescope requires more than 1500 correction zones to compensate for turbulence in the visible waveband and achieve near diffraction-limited performance [59,524]. Even though the mathematics of nonlinear optics show that fields are conjugated, the fidelity of that conjugation is highly dependent upon the quality of the pump beams, the homogeneity of the medium, and the extent to which the expansion of the nonlinear susceptibility terms holds.

For conventional adaptive optics, the limitations on phase conjugation are due to many sources. The quality of wavefront measurement, speed and fidelity of interpretation, and quality of wavefront surface contour reproduction all have an effect on the phase-conjugation process. A number of researchers have developed expressions relating the parameters of adaptive optics systems to their system-level performance. The limitations can be based on spatial constraints, such as the spatial resolution of the sensors or correctors. They can also be based on temporal constraints such as the detector integration time or the computer system speed.

3.2.1 Turbulence Tilt or Jitter Error

The tilt or jitter error due to turbulence was discussed in Section 2.1.3 and expressed in Equation 2.45.

3.2.2 Turbulence Higher-Order Spatial Error

3.2.2.1 Modal Analysis

Chapter 2 gave an expression for the wavefront variance in terms of the number of Zernike modes included. Specifically, Equation 2.39 and the accompanying filters from Equation 2.41 can be used to rigorously derive a variance with Zernike modes compensated. Because Zernike modes are orthogonal, we can modify Equation 2.39 to describe the compensated wavefront variance with Zernike terms removed as follows:

$$\sigma_{\mathrm{WF}}^2 = 0.2073k^2 \int_0^L dz C_n^2(z) \int_{-\infty}^{\infty} d\vec{\kappa}\vec{\kappa}\left(-\frac{11}{3}\right)\cos^2\left[\frac{\kappa^2(z-L)}{2k}\right]\left[1-\sum_{n,m}^{N'} F_{n,m}(\kappa)\right] \tag{3.8}$$

where N' is the number of Zernike terms removed.

Another approach to describe the effect of modal correction is given by Noll [570] with a rigorous analysis by Conan [148]. By Fourier-transforming the atmospheric turbulence wavefront represented by Zernike polynomials, an expression was derived for determining the residual wavefront variance after correction. For Kolmogorov turbulence, the residual variance σ^2 is a function of the number of modes corrected. With respect to the mean phase (piston removed), uncorrected turbulence over an aperture of diameter D results in a residual $\sigma^2 \approx 1.0299(D/r_0)^{5/3}$ radians squared. Correction of the next few modes is as follows:

$$\text{One-dimensional tilt } \sigma^2 = 0.582\left(\frac{D}{r_0}\right)^{5/3}$$

$$\text{Two-dimensional tilt } \sigma^2 = 0.134\left(\frac{D}{r_0}\right)^{5/3}$$

$$\text{Focus } \sigma^2 = 0.111\left(\frac{D}{r_0}\right)^{5/3}$$

For higher-mode correction, Noll developed the approximation

$$\sigma^2 = 0.2944N_m^{-\sqrt{3}/2}\left(\frac{D}{r_0}\right)^{5/3} \text{ (radians}^2\text{)} \tag{3.9}$$

where N_{m} is the number of modes corrected.

3.2.2.2 Zonal Analysis: Corrector Fitting Error

Knowing that a mechanical deformable mirror surface cannot exactly match the aberration patterns of the eddies of atmospheric turbulence, nor can it exactly duplicate Zernike modes, Hudgin developed an expression to show the wavefront error that resulted after a least-squares fit between the surface and the atmospheric turbulence [360]. The wavefront variance after correction σ_{fit}^2 is a function of the coherence length r_0 and the spacing r_s between correction zones, such as deformable mirror actuators, and is given by

$$\sigma_{\text{fit}}^2 = \kappa\left(\frac{r_s}{r_0}\right)^{5/3} \tag{3.10}$$

This error is valid when the atmosphere is assumed to have a Kolmogorov spectrum [325]. The value of the fitting parameter κ is determined by estimating the response of the atmospheric turbulence spectrum to the spectrum generated by various basic functions made from mirror influence functions.* The parameter ranges from 0.23 for Gaussian influence, 0.28 for pyramidal influence, and 1.26 for piston-only influence to 0.39 for an experimental case [360]. Some researchers have used fitting parameters 0.15 [605], 0.31 [873], and 0.987 [76]. An extensive analysis of the fitting error for Gaussian influence in the presence of atmospheric turbulence showed that $\kappa = 0.349$ was applicable for many influence functions that are not constrained at the edge [796]. These simulations were compared to a spatial-filtering approach applied to the adaptive optics atmospheric turbulence correction problem (Section 3.5). For these cases, a fitting parameter can be approximated by 0.319 [796]. Obviously, the exact parameter used for analyses must be determined empirically from each mirror design and aberration-forcing function, and the effective actuator spacing for various geometries must be calculated.

The number of correction channels (or correction modes) can be determined for a given Strehl ratio spatial requirement. By substituting the approximation for the Strehl ratio $S = e^{-\sigma^2}$ into Equation 3.10, where N_a is the number of zones derived from the actuator spacing r_s and the aperture diameter is

$$D = \sqrt{\frac{4N_a}{\pi}}r_s \tag{3.11}$$

the equation for the number of zones becomes

$$N_a = \frac{\pi}{4}\left(\frac{D}{r_0}\right)^2\left[\frac{\kappa}{\ln(1/s)}\right]^{6/5} \tag{3.12}$$

* Influence functions are discussed in detail in Section 6.2.

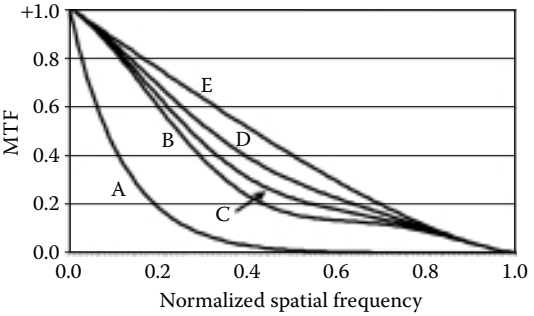

FIGURE 3.6
MTF with adaptive optics compensation, $D/r_0 = 2.0$: curve A, no correction; curve B, tilt correction; curve C, tilt plus focus corrections; curve D, tilt, focus, plus astigmatism corrections; and curve E, ideal wavefront compensation and diffraction-limited performance.

Rapid calculation of system complexity can be made if the assumed conditions are met: Kolmogorov turbulence with a constant C_n^2; the diameter of the aperture is sufficiently large, $D_A > 4r_s$; and the turbulence-induced wavefront error is not too severe, $\sigma^2 < \sim 1.6$.

Rather than relying on the wavefront error approach, Wang [849] determined the effect of mirror influence functions on the MTF of an imaging system in atmospheric turbulence. Figure 3.6 shows how the MTF improves when even low-order spatial modes are corrected. Modal analysis is useful in determining the overall performance of the adaptive optics system [398].

3.2.3 Turbulence Temporal Error

The atmospheric turbulence conjugation process can be limited by temporal deficiencies as well as spatial ones [405]. Assuming perfect spatial correction, Greenwood [307] showed that the variance of the corrected wavefront due to temporal limits is given by

$$\sigma_{\text{temp}}^2 = \int_0^\infty |1 - H(f, f_c)|^2 P(f)\, df \tag{3.13}$$

where the disturbance power spectrum $P(f)$ for wavefront tilt is given by Equation 2.46 and that for higher-order aberrations is given by Equation 2.69. The adaptive optics system provides correction represented by the filter $H(f, f_c)$. Two types of filters can be easily analyzed. A sharp cutoff filter with bandwidth f_c is represented by

$$H = 1, \quad f < f_c \tag{3.14}$$

$$H = 0, \quad f \geq f_c \tag{3.15}$$

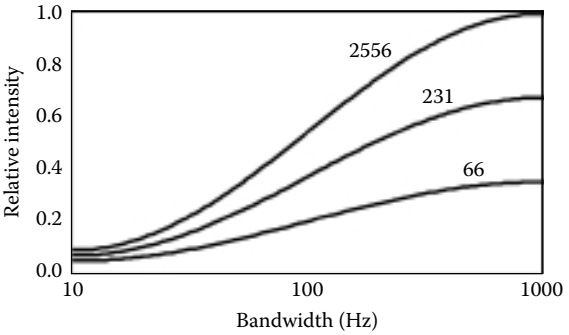

FIGURE 3.7
Spatial and temporal requirement for correcting ground-to-space transmission. The number on each curve is the number of modes corrected.

An RC filter is represented by

$$H = \left(1 + \frac{if}{f_c}\right)^{-1} \tag{3.16}$$

For a tilt-control system with a bandwidth (3-dB cutoff frequency) of f_{3dB}, the angular tilt variance after compensation is

$$\alpha^2_{comp} = \left(\frac{f_{TG}}{f_{3dB}}\right)^2 \left(\frac{\lambda}{D}\right)^2 \tag{3.17}$$

The tilt Greenwood frequency is Equation 2.54. The higher-order wavefront variance due to temporal constraints, σ^2_{temp}, is

$$\sigma^2_{temp} = \left(\frac{f_G}{f_{3dB}}\right)^{5/3} \tag{3.18}$$

where the Greenwood frequency is Equation 2.70.

Winocur combined the expression for modal spatial correction with Greenwood's temporal considerations [873]. The result was not in analytic form, but an extensive numerical analysis showed how the relative intensity, or Strehl ratio, was improved by increasing spatial and temporal bandwidths. Considering the control system requirements for transmission from ground to space (300 km altitude) with a 2-meter aperture at a 0.5 μm wavelength shows how 70 radial modes (2556 Zernike aberration terms) are required, at a servo bandwidth of greater than 300 Hz, to achieve a Strehl ratio of 0.9 (Figure 3.7).

One way to avoid the temporal limitations is to "get lucky." So-called lucky imaging systems take many short exposures with adaptive optics doing the best that it can, and then, choose the images that are sharpest because they were captured in the short period that the atmosphere was benign [852]. To reduce the data storage and processing burden, wavefront sensor measurements can be used to select the images that were taken under the best atmospheric conditions [112]. Clear imaging in visible wavelengths is now possible where only infrared adaptive optics were once considered [450].

3.2.4 Sensor Noise Limitations

A restriction to the adaptive optics process, expressed in terms of wavefront variance, is due to the limitations of the wavefront sensor. It is related to the signal strength and processing properties of the sensor. Kern et al. [410] use the expression

$$\sigma^2_{\text{WFS}} = \frac{2\pi^2}{n}\left(\frac{\lambda_A}{\lambda}\right)^2 \tag{3.19}$$

where n is the number of photons detected per subaperture, usually less than 1000 [326]. The mean wavelength of the wavefront sensor detection band is λ_A. Hardy [321,326] shows an explicit expression for the variance for the special case of a shearing interferometer in visible light (Section 5.3.1),

$$\sigma^2_{\text{WFS(SI)}} = \frac{2}{\pi\gamma^2 n}\frac{d_s^2}{s^2} \tag{3.20}$$

where γ is the fringe contrast, d_s is the subaperture diameter, and s is the shear distance.

For the case of the Hartmann sensor, the subaperture tilt measurement limitations apply. The wavefront variance is

$$\sigma^2_{\text{WFS(H)}} = \frac{2\pi^2\left[\left(\frac{3}{16}\right)^2 + \left(\frac{s}{8}\right)^2\right]^{1/2}}{\text{SNR}} \tag{3.21}$$

The term s in Equation 3.21 is the size of the source. For a natural star or an object at infinity, $s = 0$. Where a CCD array is used to determine the centroids in a Hartmann sensor, with n_{pix} pixels used in each subaperture, the SNR is

$$\text{SNR} = \frac{N}{\left[N + n_{\text{pix}}\left(\sigma_r^2 + \sigma_{bg}^2\right)\right]^{1/2}} \tag{3.22}$$

where N is the number of signal electrons, σ_r are the noise electrons, and σ_{bg} are the background electrons.

The wavefront sensor must have a sufficiently bright source to keep the SNR high. For astronomical imaging, bright natural guide stars are required. Roddier [661] suggests that there is about a 30% chance of finding a suitable guide star for an 8- to 10-m telescope. Tip/tilt control of an 8-m telescope with low noise detectors is possible with about 10,000 stars per square degree. Low-order compensation is possible with about 4,000 stars per square degree [20]. If the angular density of stars with magnitude m or brighter is given by $\rho(m)$, using for instance $\rho(m) = 1.45 \exp(0.96m)$ stars/rad^2 [598], the probability of detecting N stars in solid angle Ω in the magnitude range from m_1 to m_2 is [198]

$$P(N, m_1, m_2) = \frac{\left[\int_{m_1}^{m_2} \Omega_\rho(m)\mathrm{d}m\right]^N}{N!} \exp\left[-\int_{m_1}^{m_2} \Omega_\rho(m)\mathrm{d}m\right] \tag{3.23}$$

3.2.5 Thermal Blooming Compensation

Thermal blooming can be partially corrected with adaptive optics [87]. When thermal blooming is expressed in terms of the distortion number N_B (Section 2.2), an adaptive optics system correcting N_m modes will reduce the wavefront variance to [575]

$$\sigma^2_{\text{bloom}} = \frac{\sqrt{2}}{5\pi^4}\left(\frac{N_B^2}{N_m^{2.5}}\right) \tag{3.24}$$

3.2.6 Anisoplanatism

The atmosphere can be considered a plane normal to the direction of the propagation of a beam. This plane has various phase changes over the surface. If a beam is sent through any portion of the plane and sees the same wavefront error, it would be considered *isoplanatic*. From the discussion in Section 2.1, we know that this is not the case. One part of the atmosphere distorts the beam in a different manner than another part. Even though the statistics are the same, the atmospheric turbulence realizations are different. Propagation through turbulence is *anisoplanatic* [123]. There will be different wavefront errors for two small beams and different wavefront errors for different parts of a large beam. Anisoplanatism has serious consequences for adaptive optics for large apertures, compensating a large field of view, or for

concepts such as spatial-sharing return-wave systems [308]. Although anisoplanatism is a spatial phenomenon, it can arise under other stimuli. Two beams displaced and parallel to each other produce *displacement* anisoplanatism. Two beams propagating at slightly different angles with respect to each other produce *angular* anisoplanatism [745]. Two beams whose sources are at a different distance from the receiver, where the region sampled by the receiver is in the shape of a cone, exhibit the *cone effect* or focal anisoplanatism. A time delay between the propagation of two beams coupled with a wind that is moving the atmosphere results in *temporal* anisoplanatism. Lastly, two beams of slightly different wavelengths that experience different amounts of turbulence-induced aberration represent an example of *chromatic* anisoplanatism (Section 5.6).

The amount of the angular anisoplanatic aberration can be calculated from the Kolmogorov spectrum [243]. Experimental measurements have been made to verify these expressions [870]. Referring to Figure 3.8, the wavefront variance (in square radians) for two beams separated by an angle θ pointing at a target or a turbulence layer a distance L away is

$$\sigma_{\text{iso}}^2 = 2.91k^2 \int_{\text{path}}^{L} C_n^2(\theta z)^{5/3}\,dz \tag{3.25}$$

When $(D/r_0)/(\theta/\theta_0) \to \infty$, the variance becomes

$$\sigma_{\text{iso}}^2 = \left(\frac{\theta}{\theta_0}\right)^{5/3} \tag{3.26}$$

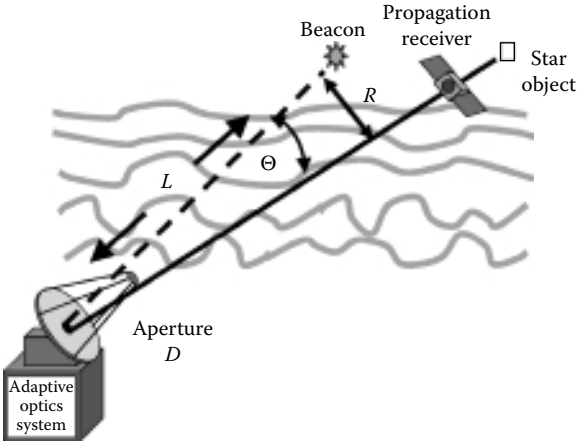

FIGURE 3.8
Geometry related to anisoplanatism.

where θ_0 is defined as the *isoplanatic angle* as follows:

$$\theta_0 = \left[2.91k^2 \int_{\text{path}}^{L} C_n^2(z) z^{5/3} \mathrm{d}z \right]^{-3/5} \tag{3.27}$$

For constant C_n^2, remembering that $r_0 = \left[0.423k^2 C_n^2 L \right]^{-3/5}$, the expression for the isoplanatic angle reduces to [659]

$$\theta_0 \approx \frac{0.6 r_0}{L} \tag{3.28}$$

If the angular separation θ is much smaller than the isoplanatic angle, the variance between the different paths is small and adaptive optics correction can be very good. When the opposite is true, the adaptive optics system will apply an incorrect conjugate and the correction will not be very good. In some cases, no correction is better than the wrong correction. Because the isoplanatic angle for tilt is approximately four times θ_0, and the full aperture can be used to measure tilt from a natural guide star, the source can be faint and not as close to the science object as would be required for higher-order correction.

Temporal anisoplanatism occurs in a beam-propagation scenario. The light from the beacon is delayed by its time of flight $\Delta t = L/c$. The corrected beam will reach the target another Δt later. The atmosphere has had time to move and change [105]. An analysis by Tyler [779] indicates that an old correction is worse than no correction at all in the case of small diameters. For larger apertures, a correction, even if it is using time-delayed information, may be helpful.

Some stellar imaging systems are so photon-starved that light from the object itself cannot be used for adaptive optics. In other cases, the imaging system may be at a different wavelength than the adaptive optics sensing system. A beacon or *guide star* in the approximate direction of the object star can be used. Both chromatic and angular anisoplanatism are present. In these instances, the angle between the beacon and the target (measured from the transmitter or observer's position) becomes the important parameter [662]. A temporal filter associated with the use of the beacon is [779]

$$H(f) = \exp(-i2\pi f \Delta t) \tag{3.29}$$

where f is temporal frequency; Δt is the time delay associated with the difference of the two paths, $\Delta t = \theta/\dot{\theta}$. The effective movement of the atmosphere with respect to the optics is the time-derivative of the angle, denoted by $\dot{\theta}$. The resultant wavefront error after anisoplanatic effects is the inverse Fourier transform of the filtered spectrum of the wavefront,

$$\phi_{\text{cor}} = \int F\phi_{\text{unc}} [1 - H(f)] \exp(i2\pi\, ft) \mathrm{d}f \tag{3.30}$$

The transform leads again to the expression

$$\sigma_{\text{iso}}^2 = \left(\frac{\theta}{\theta_0} \right)^{5/3} \tag{3.31}$$

which is similar to the expression for the wavefront variance due to finite servo bandwidth [307,779],

$$\sigma^2 = \left(\frac{f_{\text{G}}}{f_{\text{3dB}}} \right)^{5/3} \tag{3.32}$$

where f_{3dB} is the adaptive optics system temporal bandwidth.

The Greenwood frequency can be redefined here in terms of the angles,

$$f_{\text{G}} = \left[\frac{1}{2} \Gamma(8/3) \right]^{3/5} \frac{\dot{\theta}}{2\pi\theta} \tag{3.33}$$

Anisoplanatism can be thought of as a coupling of spatial and temporal effects. Since the atmosphere is moving, a beam traversing a different portion of the air will be similar to a beam traversing the same portion of the air at a different time. An *old* correction is almost the same as a correction over a slightly offset path. Tyler [779] combined the two effects. The wavefront variance due to a combination of finite bandwidth and the isoplanatic angle is

$$\sigma_{\text{iso}}^2 = \left(\frac{\theta'}{\theta_0} \right)^{5/3} \tag{3.34}$$

The angle is limited by the atmosphere's anisoplanatism as well as the bandwidth. The angle is

$$\theta' = \left\{ \int_0^\infty \mathrm{d}\tau \mathrm{e}^{-\tau} \left[\left(\theta + \frac{1.186\theta_0 f_{\text{G}} \tau}{f_{\text{3dB}}} \right)^{5/3} - \frac{1}{2} \left(\frac{1.186\theta_0 f f_{\text{G}} \tau}{f_{\text{3dB}}} \right)^{5/3} \right] \right\}^{3/5} \tag{3.35}$$

where $\tau = 2\pi t f_{\text{3dB}}$.

3.2.7 Postprocessing

In telescopes that have fields-of-view far exceeding the isoplanatic angle, the space-variant aberrations can be removed after the images are captured by any one of many postprocessing techniques [42,761].

3.3 Artificial Guide Stars

The anisoplanatic effects translate into fundamental restrictions on field of view, which is roughly $2L\theta_0$. A beacon's angular subtense should be as small as possible, ~$1.22\lambda/r_0$. Few natural visible guide stars fall within the isoplanatic angle of the object. For infrared objects, the isoplanatic angle is larger and the system is less restricted. Some researchers have investigated the effect of partially correcting for the atmosphere in astronomy [569,734]. Since the early 1980s, researchers within the U.S. Air Force [181,255,257,258] and the astronomy community [229,232,765] have been investigating the use of artificial guide star techniques to sample the atmosphere [813]. The technique employs lasers to stimulate a portion of the upper atmosphere to create an artificial guide star for sampling the atmospheric turbulence [210,541,751].

Rayleigh scattering [766] can create guide stars in the stratosphere at around 20 km altitude. Since the atmosphere sampled and detected by the wavefront sensor is only the portion below the guide star in the cone between the guide star and the wavefront sensor aperture, there is the *cone effect* or focal anisoplanatism [751]. The wavefront variance due to focal anisoplanatism was derived by Fried [244,248],

$$\sigma^2_{\text{cone}} = \left(\frac{D}{d_0}\right)^{5/3} \tag{3.36}$$

where D is the full telescope aperture diameter. Where β is the zenith angle, z_{LGS} is the altitude of the laser guide star, and the C_n^2 profile is given, Tyler [783] gives the following expression for d_0:

$$d_0 = \lambda^{6/5} \cos^{3/5}\beta \left[19.77 \int \left(\frac{z}{z_{\text{LGS}}}\right)^{5/3} C_n^2(z)\mathrm{d}z \right]^{-3/5} \tag{3.37}$$

where z_{LGS} is the altitude of the artificial star (in kilometers), the focal anisoplanatism parameter d_0 (in meters) can be approximated from an empirical curve fit to the model results of Fried. For the Hufnagel–Valley turbulence model,

$$d_0[\text{HV5/7}] = 0.018 z_{\text{LGS}} + 0.39 \tag{3.38}$$

For the SLC – Day turbulence model,

$$d_0[\text{SLC} - \text{Day}] = 0.041 z_{\text{LGS}} + 0.29 \tag{3.39}$$

For the SLC – Night turbulence model [60],

$$d_0[\text{SLC} - \text{Night}] = 0.046 z_{\text{LGS}} + 0.42 \tag{3.40}$$

For a wavefront error of λ/10 with an aperture of 4 m, the SLC – Night model results in a d_0 of 7 m and a required laser guide star altitude of 143 km, a physically unrealizable result. To overcome this difficulty and reduce the cone effect, multiple laser guide stars can be employed [245,247]. The focal anisoplanatism parameter can then be approximated by

$$d_0[\text{Multiple Stars}] = 0.23 N_{\text{LGS}} + 0.95 \tag{3.41}$$

where N_{LGS} is the number of artificial guide stars. There is a lot of work being done to merge the information from multiple guide stars to tomographically reconstruct a three-dimensional map of the atmosphere above the telescope [475,556,782].

Above 20 km, the atmosphere is too thin to provide enough backscatter to produce a sufficiently bright guide star. Happer et al. [319] suggested the use of resonant backscatter in the mesospheric sodium layer, which will produce a guide star near 92-km altitude [597], well above most of the turbulent atmosphere [264, 854]. Although chemical species other than sodium may be used for an artificial guide star [759], the bulk of guide star development is at the 589-nm sodium D_2 line.

Since the beacon cannot be placed directly in front of the object, angular anisoplanatism effects still must be considered. The guide star must be sufficiently bright to be detected and be within the anisoplanatic angle of the object. These restrictions can be examined with an example calculation. Equation 3.21 can be used to determine that a SNR of about 6 is required for a λ/10 residual wavefront error. For a CCD array detector, the SNR is given by Equation 3.22. Assuming 10 noise electrons per pixel $\sigma_r = 10$, zero background photons $\sigma_{bg} = 0$, and 4 pixels in each wavefront sensor subaperture $n_{\text{pix}} = 4$, we require 137 photons per subaperture. To be slightly conservative, we will look for conditions where we can detect 150 photons per subaperture.

Assuming a site where the visible r_0 is 15 cm (an average of the Keck and Lick observatories), a wavefront sensor subaperture is one r_0, and a wavefront sensor sample rate of 100 Hz, from Equation 1.61, we find that we need a 12th magnitude star ($m_v = 12$) or brighter to achieve the wavefront sensor requirement.

There are, on average, $1.45e^{0.96 m_v}$ stars per square radian. For magnitude 12 stars or brighter, there are roughly 150,000 stars per square radian. Thus, for any specific region of the sky where a science object might be, there is probably not a natural $m_v = 12$ star within a nominal 10 μradian isoplanatic patch. Thus, artificial stars are needed.

3.3.1 Rayleigh Guide Star

For a given laser energy, the brightness of the guide star is proportional to the density of the air within the laser volume. The detected Rayleigh photon flux is derived from the lidar equation,

$$F_{\text{Rayleigh}} = \eta T_{\text{A}}^2 \frac{\sigma_R n_R}{4\pi z_0^2} \frac{\Delta z \lambda_{\text{LGS}} E}{hc} \tag{3.42}$$

where η is the telescope and detector efficiency, T_{A} is the one-way transmission of the atmosphere from the telescope to the guide star, σ_{R} is the Rayleigh backscatter cross section, n_{R} is the atmospheric density, Δz is the thickness of the atmospheric layer that is observed, λ_{LGS} is the wavelength of the laser guide star, E is the laser energy per pulse, z_0 is the height of the focused star above the telescope entrance, h is Planck's constant (6.63×10^{-34} J • s), and c is the velocity of light (3.0×10^8 m/s).

The cross-sectional density product $\sigma_{\text{R}} n_{\text{R}}$ is a function of the altitude in the atmosphere where the guide star is formed and approximated by

$$\sigma_{\text{R}} n_{\text{R}} \approx 2.0 \times 10^{-4} \exp\left[\frac{-(z_0 + z_{\text{t}})}{6\ \text{km}}\right] \tag{3.43}$$

where z_{t} is the height of the laser transmitter above sea level. For Equation 3.43, a laser wavelength of 351 nm was assumed. The thickness of the layer Δz is derived from geometric considerations and the spreading of the laser energy up to the guide star altitude from a laser projector with aperture D_{proj}.

$$\Delta z = \frac{4.88 \lambda z_0^2}{D_{\text{proj}} r_0} \tag{3.44}$$

For projector optics of 1 m, a site altitude of 3 km, and a guide star altitude of 20 km (above mean sea level), $\Delta z = 33$ m. Using the basic geometry shown in Figure 3.9, the flux can be determined. From Equation 3.42, with $\eta = 0.075$ and $T_{\text{A}} = 0.85$, the photon flux (in photons per square meter) is $6.2 \times 10^5 E$; remember that E is the laser energy in joules/pulse. For a subaperture diameter r_0, the number of photons per subaperture is

$$N_{\text{s}} = \left(\frac{\pi}{4}\right) r_0^2 F = 1.1 \times 10^4 E \tag{3.45}$$

For $N_{\text{s}} = 150$ photons, we require a 14 mJ/pulse.

There are numerous engineering concerns dealing with Rayleigh laser guide stars. There is Rayleigh backscatter from the surface up to the focus

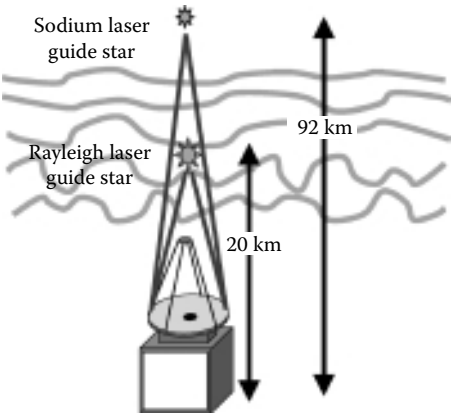

FIGURE 3.9
Laser guide star geometry.

of the laser guide star. To eliminate the wavefront sensor from detecting the backscatter in the region below the guide star, range gating is employed [257]. The pulse should be short in order to stay within the Δz layer. About 66 μs after transmission, the pulse reaches the guide star altitude of 20 km. The return energy (the guide star pulse) reaches the wavefront sensor at 132 μs after transmission. Thus, to eliminate receiving energy continuously backscattered all along the path, an electronic range gate equal to the length of Δz, centered at 132 μs after each pulse, triggers the opening of the wavefront sensor detector. At 5 kHz, the next pulse is transmitted 200 μs after transmission and will not interfere or cause confusion from multiple pulses. If the guide star is pulsed at a slower rate, 300 Hz for example, the pulse transmission and return in 132 μs is much quicker than the 3333 μs between pulses. It has been shown that varying the range gate depth during closed-loop operation can help to optimize performance [542]. Other engineering concerns include effects due to the direction of the laser guide star. An operational laser guide star at Steward Observatory is shown in Figure 3.10.

Atmospheric tilt cannot be sampled from a single laser guide star [647]. Because the propagation path up from the laser to the artificial star position follows the same reciprocal path back down to the wavefront sensor, the absolute position of the guide star, and therefore its relative position with respect to an object or fixed reference frame, is unknown. Use of multiple wavelengths [230,231,252] or extended artificial stars [65] has been proposed to overcome this difficulty [165]. Other promising concepts are those that use multiple guide stars [856] and sensors and then computationally "stitch together" the information to achieve a measure of tilt and increase the size of the isoplanatic patch [560,598,686,692,712,752,780,784].

With multiple guide stars, the effect of focal anisoplanatism can be reduced. However, because only one beacon can be on the optic axis, a *conic tilt error*

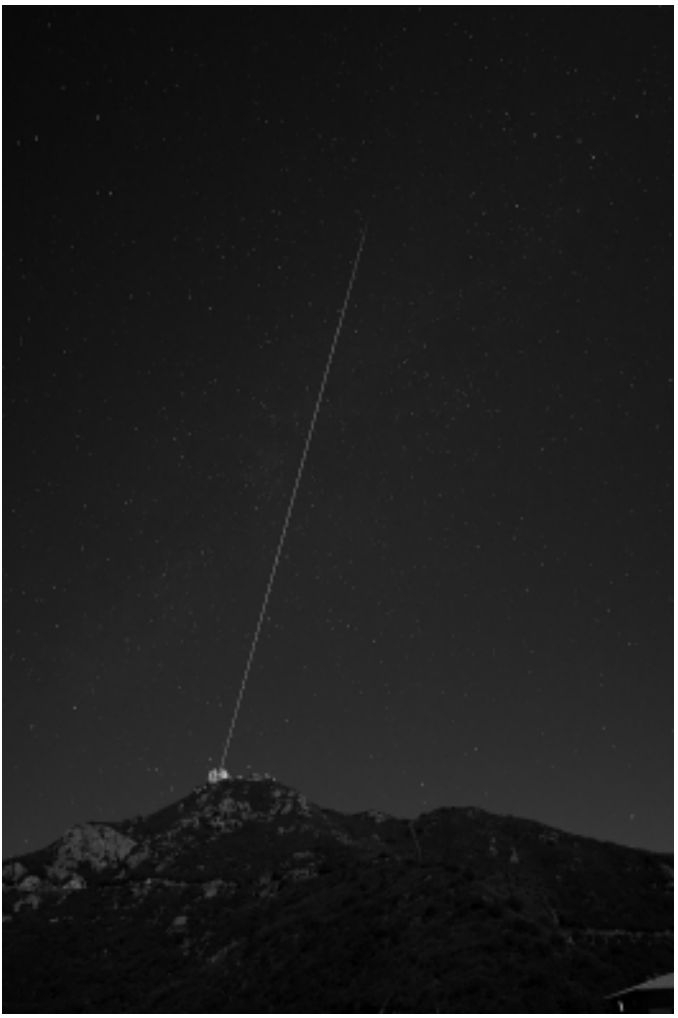

FIGURE 3.10
The laser guide star at the 6.5-meter monolithic mirror telescope at the Steward Observatory in Arizona. (Photo courtesy of Thomas Stalcup, Steward Observatory, Tucson, AZ.)

is introduced along with a beacon position error due to turbulence on the upward propagation [323]. Conic tilt phase-error variance σ_{ct}^2 is

$$\sigma_{ct}^2 = \left(\frac{D_B}{d_1}\right)^{5/3} \tag{3.46}$$

where D_B is the diameter of the aperture for a single beacon. D_B can be the full aperture. The term d_1 is the aperture diameter over which the tilt error of a single

beacon is 1 rad². For example, at $\lambda = 0.5$ μm, at 0° zenith angle, $d_1 = 0.23$ m for a 10-km beacon altitude (assuming a Hufnagel–Valley 20/20 model for turbulence). The calculation for beacon position error variance contains a term below the beacon separation height, σ^2_{PL}, and a term above, σ^2_{PH}.

Two beams are focused by a telescope of diameter D to an altitude H_B and are separated by distance b. The beams begin to overlap at a height h_c, which is below the altitude of the beacons themselves. The oblique path length is $L = H_B \sec\beta$ where β is the zenith angle. The variance in radians squared of phase below the separation height is

$$\sigma^2_{PL} = k^2 b^2 D^{-1/3} \int_0^{h_c} dz C_n^2(z) F_{PL}(b, z, D, L) \tag{3.47}$$

where

$$F_{PL}(b, z, D, L) = 0.6675\left[\left(\frac{bz}{DL}\right)^2 \left(1 - \frac{z}{L}\right)^{-1/33} - 2.067\left(\frac{bz}{DL}\right)^4 \left(1 - \frac{z}{L}\right)^{-7/3} - 1.472\left(\frac{bbz}{DL}\right)^{14/3} \left(1 - \frac{z}{L}\right)^{-3} + \mathrm{L}\right] \tag{3.48}$$

The variance in radians squared of phase above the separation height is

$$\sigma^2_{PH} = k^2 b^2 D^{-1/3} \int_{h_c}^{H_{Bc}} dz C_n^2(z) F_{PH}(b, z, D, L) \tag{3.49}$$

where

$$F_{PL}(b, z, D, L) = 0.7600\left[\left(1 - \frac{z}{L}\right)^{-5/3} - 0.6637\left(\frac{bz}{DLl}\right)^{-1/3} \left(1 - \frac{z}{L}\right)^2 - 0.0031\left(\frac{bz}{DL}\right)^{-7/3} \left(1 - \frac{z}{L}\right)^4 - \mathrm{L}\right] \tag{3.50}$$

The total beacon position error variance is

$$\sigma^2_P = \sigma^2_{PL} + \sigma^2_{PH} \tag{3.51}$$

The oblique path to the guide star and the size of the finite laser guide star must be considered [412]. In many cases, the laser output aperture is not shared with the telescope-receiving aperture, avoiding unwanted backscatter from the optics, possible fluorescence in the optics, and the complexity of high power optical coatings on the receiving optics. When multiple laser

guide stars are used, all but one will have an oblique path and be elongated [763]. When an off-axis guide star is used, both angular anisoplanatism and focal anisoplanatism must be considered. Tyler [784] concludes that low- to mid-altitudes should be used when there is significant axial separation between the Rayleigh guide star path and the receiving telescope path. For oblique paths (not to zenith), the amount of atmosphere traveled is longer until the laser pulse reaches 20 km and must be considered. A larger and temporally longer guide star returns more photons, but since the approximation to a point source is corrupted [415], the pulse should be kept short [70]. The flux is proportional to sec β where β is the zenith angle.

3.3.2 Sodium Guide Stars

The flux of a resonant sodium guide star can be calculated in a manner similar to the Rayleigh guide star, recognizing that the density of sodium in the upper atmospheric layer and the resonant scattering limitations are considered [881]. The atomic sodium, a result of meteoric disintegration, remains at an altitude between 89 and 92 km because the conditions at this altitude prevent molecular reactions. The detected sodium photon flux, at a wavelength of 589.1583 nm, follows Equation 3.42

$$F_{\text{Sodium}} = \eta T_{\text{A}}^2 \frac{\sigma_{\text{Na}} \rho_{\text{col}}}{4\pi z_0^2} \frac{\lambda_{\text{LGS}} E}{hc} \tag{3.52}$$

where the altitude z_0 is about 92 km, σ_{Na} is the resonant backscatter cross section, and ρ_{col} is the column abundance, usually between 3×10^9 atoms/cm^2 and 1×10^{10} atoms/cm^2. The product of the cross section and the column abundance is roughly 0.02 [267]. Because of the finite amount of sodium (less than 600 kg for the entire Earth), and the decay rate for the backscatter, a sodium guide star is limited to about 1.9×10^8 photons per second [251]. Using Equation 3.46, for a subaperture diameter r_0, the number of photons per subaperture N_{s} is

$$N_{\text{s}} = \left(\frac{\pi}{4}\right) r_0^2 F = 550E \tag{3.53}$$

For $N_{\text{s}} = 150$ photons, we require 272 mJ/pulse.

It is not enough just to shine a sodium wavelength beam into the mesosphere. The sodium abundance (roughly 10^3–10^4 atoms/cm^3) represented by the column density can vary as much as 2.5 magnitudes on a seasonal or diurnal scale or as short as 10 minutes [162,179]. The effective height can vary between 89 and 92 km. The wavefront sensor must be focused correctly or a false defocus term results [150,809]. Techniques such as matched filtering [285] can improve performance over centroiding [284].

The intention is to excite the D_2 transition from the $3^2S_{1/2}$ state to the $3^2P_{3/2}$ state at 589.2 nm in a very small volume (to create a point source). These two states are broadened by various mechanisms. There is a magnetic interaction of the electron with nuclear spin. The ground state splits to two levels (1.77 GHz). The excited state splits to four levels (100 MHz). They further split to magnetic sublevels. There are 54 allowed transitions between the 8 sublevels.

Actually, very few of the sodium atoms even in the beam will be excited. The return flux should be proportional to beam intensity; however, at the saturation intensity, all the atoms are excited and an increase in beam power will not increase flux. Continuous wave lasers often produce more return energy than pulsed lasers because they have a lower peak power.

As a practical matter, suppression of Rayleigh backscatter in the sodium beacon must be considered [164,879]. For an atom, the radiative lifetime is 16 ns (10 MHz). The scattering rate is inversely proportional to the radiative lifetime. In addition, the atoms are moving because of thermal motion. This inhomogeneous Doppler-broadening of 1.2 GHz makes the 589.2 nm beam able to interact with only those in one "velocity group," or only about 1% of the sodium atoms. There have been suggestions to use multifrequency lasers to excite more velocity groups. It is amazing that the sodium beacon will work at all.

For large telescopes, off-axis sources can produce beacons that are not at all point sources. They can have very large elongations that fluctuate with time. The elongation angle can be approximated by $\alpha_{\text{Elong}} = 0.24\ d_{\text{sep}}$, where d_{sep} is the separation between the telescope and the laser projector in meters and α_{Elong} is in arc seconds. The beam projector should be about $3r_0$. If the beacon is projected from behind the secondary mirror, some light pollution or field blockage can occur. If the beacon is projected in the telescope optical train, scattered light and phosphorescence can occur. Elongated beacons appear on Shack-Hartmann sensors as elongated spots and affect the accuracy of the wavefront measurement.

The concept of *multiconjugate adaptive optics* [20,67,712,713] corrects for each "layer" of atmosphere independently. By placing correction devices (deformable mirrors) in series, and assigning each one a layer of atmosphere to correct, the isoplanatic patch is effectively increased. The terms multiconjugate adaptive optics, ground-layer adaptive optics [775], laser tomography adaptive optics, multiobject adaptive optics, and extreme adaptive optics [534] are used to describe the various multiple guide star configurations. Thus, we can replace what was once just an *adaptive optics system* with single conjugate adaptive optics [195,266,440,564,698,818,822,826].

In addition to conventional adaptive optics, many telescopes, such as those used to search for extrasolar planets, must use other novel optical techniques. For example, the light coming from an extrasolar planet is typically 7 or 8 orders of magnitude fainter than the parent star. The point spread function of the star often masks the planet. Long-exposure phase diversity [546], the use of coherent waveguides to remap pupil geometry [431], or novel coronagraphs are often used to enhance the imaging. In one case, an optical

vortex is imparted onto the phase of the incoming beam, effectively creating a zero-intensity hole in the center that can block the starlight [225]. Based upon the principles of Michelson stellar interferometry [753], large-aperture ground-based long-baseline interferometers, such as CHARA [760], are also candidates for adaptive optics [773].

3.4 Lasers for Guide Stars

Various lasers can be used for Rayleigh beacons. Frequency-doubled lithium niobate solid state lasers, doubled Nd:YAG lasers ($\lambda = 532$ nm) [331], tripled Nd:YAG lasers ($\lambda = 355$ nm) [29], excimer lasers, and copper vapor lasers have all been successfully used.

In addition, a number of laser sources can achieve the minimum power needed for sodium laser guide stars. A few types are flashlamp pumped Nd:YAG lasers, excimer lasers with organic dyes in the laser cavity [13], both continuous and pulsed dye lasers, and fiber lasers [609]. One fortuitous phenomena is the two laser wavelengths of Nd:YAG lasers, 1.06 and 1.32 μm. When these lines are mixed in a nonlinear crystal, the resultant wavelength for the sum-frequency is $(1.06\ \mu m)^{-1} + (1.32\ \mu m)^{-1} = (0.589\ \mu m)^{-1}$, precisely the wavelength needed to excite sodium [80,382,680,682].

In general, the laser-output beam quality should be a single transverse mode of TEM_{00}, $M^2 < 1.2$, and the bandwidth should be narrow compared with the Doppler-broadened sodium absorption spectrum (about 2.77 GHz). A continuous or quasi-continuous beam [169] of 4-W power should yield a stable photon return [682].

However, laser guide stars in adaptive optics systems have been demonstrated and used for astronomy and satellite imaging [44,249,250,366,376,383,473,510, 581,767,764,769]. Wavefront measurement from multiple guide stars has been demonstrated [445,549]. A summary of the laser sources up to the mid-1990s is given in the literature on the subject [256] and elsewhere [181].

3.5 Combining the Limitations

The expressions used in this section can be combined to achieve an approximation for the system performance. The compensated wavefront variance (expressed in square radians) is the sum of the contributors [268], as follows:

$$\sigma^2 = \sigma^2_{\text{fit}} + \sigma^2_{\text{temp}} + \sigma^2_{\text{WFS}} + \sigma^2_{\text{bloom}} + \sigma^2_{\text{iso}} + \sigma^2_{\text{cone}} \tag{3.54}$$

Equations 3.10, 3.18, 3.20 or 3.21, 3.24, 3.26, and 3.36 can be used for the contributors to approximate performance. This combination assumes that the limitations are uncorrelated. Though not strictly the case, the assumption is useful for system level analyses [855]. The compensated wavefront Strehl ratio is just Equation 2.64 with the compensated wavefront error and the compensated jitter variance used in the expression.

3.6 Linear Analysis

3.6.1 Random Wavefronts

The preceding expressions assumed that wavefront aberrations were primarily caused by a Kolmogorov atmosphere. As shown in Chapter 2, many forms of wavefront disturbance can be found. The capability of an adaptive optics system to compensate for other random aberrations often can be determined by the spatial filter method.

When the aberrations can be expressed as random disturbances with a specified correlation distance, the adaptive optics system can be studied with the assumption that the system performs as a spatial filter [334]. Since the spacing of correction zones r_s limits the spatial resolution of the adaptive optics system, it can be viewed as a high-pass filter, which removes all the low-frequency (low-order) modes but passes the high-frequency modes. The exact form of the filter is determined by its correcting ability on a particular wavefront [538,793]. The corrected wavefront ϕ_c is the difference between the uncorrected wavefront and the surface of the phase-conjugating mirror $M(x, y)$, and is given by

$$\phi_c(x,y) = \phi_u(x,y) - \gamma_m M(x,y) \tag{3.55}$$

where the constant γ_m is a function of the particular geometry of the adaptive optics beam train. For a system where reflection from the correcting mirror is at an angle θ, the constant becomes $\gamma_m = 2 \cos \theta$. For a nonlinear optics phase conjugating mirror (PCM), $\gamma_m = 1$. Taking the Fourier transform of Equation 3.49 and rearranging, we get

$$F(\phi_c) = F(\phi_u)\left[1 - \frac{\gamma_m F(M)}{F(\phi_u)}\right] \tag{3.56}$$

The term in the brackets is the filter of the uncorrected wavefront spectrum and is a *function of the spectrum*. This functionality makes the problem nonlinear in wavefront. When only low-order modes are considered, this nonlinearity can be disregarded [429]. Analytical aspects of the nonlinearity are often

avoided by assuming a sharp cutoff for the spatial filter rather than pursuit of its exact form in each case. The cutoff frequency ν_c is related to the Nyquist criterion $\nu_c = 1/2r_c$. In general, this filter [789] can be used to alter the spectrum of a wavefront to see the resultant wavefront after correction by an adaptive optics system. The filter takes into account sensing, controlling, and correcting spatial resolution, and cannot differentiate these functions. The nonlinearity in uncorrected phase can be visualized in the following manner. If the mirror correction ($\gamma_m M(x, y)$) is exactly equal to the uncorrected wavefront ϕ_u, the filter vanishes and the correction is perfect, that is, the corrected wavefront is zero. This can occur as long as the influence functions of the various correcting surface drivers add up to the point where the surface matches the wavefront exactly. For example, a mirror with *only one actuator* perfectly corrects a wavefront if the surface influence of that actuator exactly matches the conjugate of the uncorrected wavefront. Since this is very unlikely in any real case (except for simple tilt or focus correction), the spatial filter principle will hold for analyzing many multizone adaptive optics systems.

When the wavefront error is the result of a random process, such as microstructure deviations in optics or nonhomogeneity in propagation paths, the exact wavefront or its spectrum is often not known. In these cases, the autocovariance function of the wavefront is used to analyze the adaptive optics system. The autocovariance function contains the statistics of the random process, and the power spectral density (PSD) is the Fourier transform of the autocovariance. By filtering the PSD with the high-pass spatial filter of the adaptive optics system, the residual PSD is obtained. The integral of this function is the variance of the corrected wavefront. An inverse Fourier transform at this point results in the residual autocovariance function. The peak of this function, which occurs at the origin, is the wavefront variance after correction.

To illustrate this analytical process in one dimension, assume that the wavefront is random with Gaussian statistics. The correlation length l shows up in the form of the autocovariance, given by

$$A(x) = \sigma_{\text{unc}}^2 \exp\left(-\pi \frac{x^2}{l^2}\right) \tag{3.57}$$

The Fourier transform of the autocovariance is the PSD, given by

$$P(\nu) = l\sigma_{\text{unc}}^2 \exp(-\pi l^2 \nu^2) \tag{3.58}$$

When this PSD is spatially filtered, the residual PSD follows the condition

$$P(\nu)_{\text{res}} = F[A(x)] = l\sigma_{\text{unc}}^2 \exp(-\pi l^2 \nu^2), \quad \text{for } \nu \geq (1/2r_c) \tag{3.59}$$

$$P(\nu) = 0, \quad \text{for } \nu < (1/2r_c) \tag{3.60}$$

The inverse transform of this PSD gives the residual wavefront autocovariance function as follows:

$$A(x)_{\text{res}} = \sigma_{\text{unc}}^2 \exp\left(-\pi \frac{x^2}{l^2}\right)\left[1 - \text{erf}\left(-i\sqrt{\pi}\,\frac{x}{l} + \frac{\sqrt{\pi}l}{2r_{\text{cc}}}\right)\right] \tag{3.61}$$

where erf is the error function [1]. The residual wavefront variance is the value of the autocovariance at the origin, given by

$$\sigma_{\text{corr}}^2 = \lim_{x\to 0} A(x) = \sigma_{\text{unc}}^2\left[1 - \text{erf}\left(\frac{\sqrt{\pi}l}{2r_{\text{c}}}\right)\right] \tag{3.62}$$

Defining *correctability* as $C = (\sigma_{\text{unc}}^2 - \sigma_{\text{corr}}^2)/\sigma_{\text{unc}}^2$, the correctability of an adaptive optics system with correction zone spacing r_{c} for a random disturbance with correlation length l becomes

$$C = \text{erf}\left(\frac{\sqrt{\pi}l}{2r_{\text{c}}}\right) \tag{3.63}$$

From this expression, one can see that almost half the variance can be removed when correction zones are twice the correlation distance, $C = 0.47$, for $r_{\text{c}} = 2l$. For $r_{\text{c}} = l$, $C = 0.78$, and if the correction zone spacing is as low as $r_{\text{c}} = l/2$, the adaptive optics system is almost a perfect phase conjugator, $C = 0.99$.

3.6.2 Deterministic Wavefronts

When the uncorrected wavefront is deterministic, the spatial-filtering process can be followed to determine the corrected wavefront. In this case, however, the wavefront itself is Fourier-transformed rather than the autocovariance. The wavefront spectrum can be filtered in the same manner as before. The sharp-cutoff high-pass filter is used to determine the residual spectrum and its transform gives the corrected wavefront directly. Variances can be calculated from the wavefronts or the wavefronts can be used to calculate propagation of the beam. If we assume that the wavefront is a sum of Fourier components, then

$$\phi_{\text{unc}} = \sum_{m=0}^{\infty} a_{\text{m}} \cos(2\pi m\,\Delta\nu x) \tag{3.64}$$

The spatial filter removes the low-order components so that the corrected wavefront takes the form

$$\phi_{\text{cor}} = \sum_{m=1/(2\Delta\nu r_c)}^{\infty} a_m \cos(2\pi m \Delta\nu x) \tag{3.65}$$

Since the variance is a weighted sum of the squares of the coefficients, the corrected wavefront must have a lower variance than the uncorrected wavefront. In many cases, for example, atmospheric turbulence, the low-order coefficients are the largest contributors to Strehl ratio loss [570].

When the wavefront can be represented by Zernike polynomials, we can find the variance of the corrected wavefront. From Equation 1.37, the variance is determined from the Zernike coefficients A_{nm} and B_{nm} by the sum

$$\sigma^2 = \sum_{m=1}^{\infty} \sum_{m=0}^{n} \frac{A_{nm}^2 + B_{nm}^2}{2(n+1)} \tag{3.66}$$

The spatially filtered corrected wavefront variance is

$$\sigma_{\text{cor}}^2 = \sum_{n=1}^{\infty} \sum_{m=0}^{n} \frac{A_{nm}^2 + B_{nm}^2}{2(n+1)} - \sum_{n=1}^{\infty} \sum_{m=0}^{n} \sum_{n'=1}^{\infty} \sum_{m'=0}^{n'} (-1)^{(n-n')/2} (A_{nm} A_{n'm} + B_{nm} B_{n'm}) Z\left(\frac{R}{r_c}, n, n'\right) \tag{3.67}$$

with $B_{n0} = 0$ and R the radius of the aperture. The *correction function* $Z[(R/r_c), n, n']$ is found by spatially filtering the Fourier transforms of the Zernike polynomials [788]:

$$\begin{aligned} Z[(R/r_c), n, n'] &= \int_0^{1/2r_c} \frac{J_{n+1}(2\pi\rho R) J_{n'+1}(2\pi\rho R)}{\rho} d\rho \\ &= \sum_{k=0}^{\infty} \frac{(-1)^k (n+n'+2k+1)! \left(\frac{\pi R}{2r_c}\right)^{n+n'+2k+2}}{(n+1+k)!(n'+1+k)!(n+n'+k+2)!\,k!} \end{aligned} \tag{3.68}$$

Therefore, by knowing the Zernike coefficients of the uncorrected wavefront A_{nm}, B_{nm} and the correction zone, or actuator spacing, r_c, the resultant wavefront variance can be found algebraically using the spatial frequency filter method.

3.7 Partial Phase Conjugation

No adaptive optics system can achieve perfect phase conjugation, although many systems can come close. Winocur [873] and Noll [570] showed the effect of correction of individual modes and the residual effect of not correcting some of the atmospheric turbulence. Systems with limited degrees of freedom can provide quite suitable image compensation for many practical purposes [668,669]. Bruns [101] shows how a simple five-mode correction system would provide compensation for meter-class telescopes. In addition to image compensation, it has been shown that the log-intensity variance of scintillation with an adaptive optics system is inversely proportional to the number of Zernike modes that are being corrected [457]. Although correcting many modes is desirable, the compensation of a few low-order modes presents the most significant improvement.

4

Adaptive Optics Systems

In this chapter, we will review a number of adaptive optics concepts that have been used for applying correction to propagation and imaging systems. Functional block diagrams are used to illustrate the concepts. The blocks represent functions that can be optical, electronic, mechanical, or many combinations of these. The second half of this book deals with the details in the subsystems represented by the boxes in these diagrams. At this conceptual level, we can regard these boxes as having the following functions:

Optics: A train of transmissive or reflective optics

Corrector: An optical element that can change the wavefront of a beam

Sampler: An optical element that can separate one beam from another (presumably without distorting the phase)

WFS: Wavefront sensor

Imager: A collection of optics that forms an image and delivers it to detectors

Target: The plane in space where a well-corrected beam is required

Receiver: A device that converts optical information to electronic signals

Control: Electronic processing

Tagger: An optical device that can tag part of a beam

Laser: The laser

The system concept should be chosen carefully. A system used for correcting atmospheric turbulence in an astronomical telescope probably will not be useful correcting low-order modes in a high-power laser. The brute-force techniques for moving large optics will be much too slow for correcting high-frequency vibrations. We will examine these approaches and explore their pros and cons.

4.1 Adaptive Optics Imaging Systems

4.1.1 Astronomical Imaging Systems

By far, the most common application of adaptive optics is for imaging [688]. Since 1982, adaptive optics have been used for imaging through the atmosphere [322] using the basic components that consist of a wavefront

sampler, a wavefront sensor (WFS), a corrector such as a deformable mirror, and a control computer to perform real-time numerical calculations [325]. Referring to Figure 4.1, the basic function of the system is quite simple. Light from the object of interest, such as an astronomical science object or a satellite, is captured by the optical system consisting of a telescope and a beam train. Part of the light is sampled by the WFS. The control computer calculates the necessary changes to the optical path and sends signals to the corrector where the changes are made. The imager, a camera, collects the light through the compensated optical system. If the light from the object is insufficient for determining the wavefront, supplemental sources, such as nearby natural guide stars [829] or artificial guide stars, are used. Table 4.1 summarizes telescopes and adaptive optics systems that are either in place or being planned for most of the world's major observatories.

In addition to the imaging system configuration shown in Figure 4.1, systems can use the image signal itself for sharpening the images. When there is no explicit wavefront measurement and the sharpness of the image is measured in the image plane, varying the correction process can converge toward the "best image." This is analogous to trying on a number of pairs of glasses to find out which one is best. Trial and error with a "sharp" image as the figure of merit is the basis of this approach, which is discussed further in Section 5.4.2. A new technique in which many short exposures are surveyed to find sharp images when the observer is lucky enough for a calm atmosphere for a short time is referred to as *lucky imaging* [353].

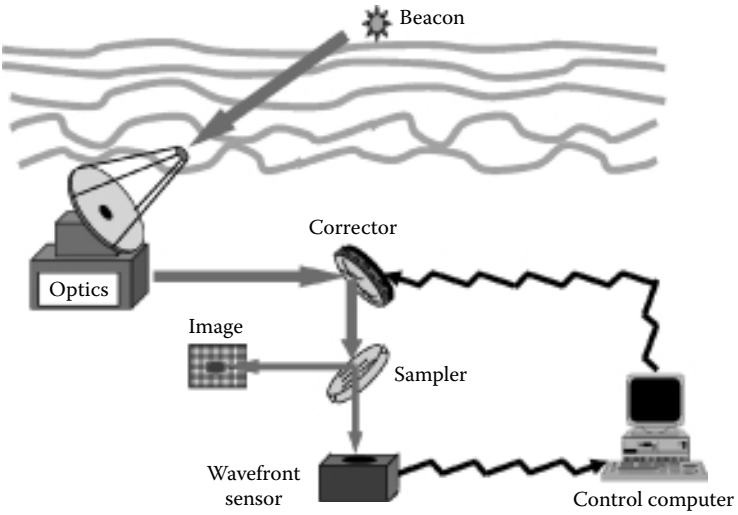

FIGURE 4.1
Conventional configuration of a closed-loop adaptive optics imaging system. Principal elements, the corrector, the sampler, and the wavefront sensor are shown. Other elements such as conjugate pupil optics, image focusing, and wavefront focusing optics are not shown.

TABLE 4.1

Observatories with Existing or Planned Adaptive Optics Systems

Observatory	Conventional Acronym	Telescope Size	References
Vacuum Tower Telescope	VTT	0.7 m	[736,830]
Sacramento Peak		0.76 m	[3,4,651]
Yunnan, China		1.2 m	[385,386,772]
Obs. De Haute Provence		1.52 m	[454,525]
Mt. Wilson		2.5 m	[717,718,768]
Nordic Optical Telescope	NOT	2.56 m	[28]
Shane Telescope (Lick Obs.)		3.0 m	[447]
Apache Point		3.5 m	[175,413]
Starfire Optical Range	SOR	3.5 m	[397]
Wisconsin Indiana Yale NOAO	WIYN	3.5 m	[699]
Astrophysical Research Consortium	ARC	3.5 m	[22]
Calar Alto Observatory		3.5 m	[78,153]
Telescopio Nazionale Galileo	TNG	3.58 m	[54,637]
California–France–Hawaii Telescope	CFHT	3.6 m	[33,648,649]
New Technology Telescope	NTT	3.6 m	[590,634,677]
Visible and Infrared Survey Telescope for Astronomy	VISTA	3.6 m	[161]
Advanced Electro-optical System	AEOS	3.67 m	[497,838]
U.K. Infrared Telescope	UKIRT	3.8 m	[132]
Anglo-Australian Telescope	AAT	3.9 m	[103,576]
Southern Astrophysics Research Telescope	SOAR	4.1 m	[762]
William Herschel Telescope	WHT	4.2 m	[110,171,552,770]
Hale Telescope, Mt. Palomar		5.0 m	[83,166]
Monolithic Mirror Telescope	MMT	6.5 m	[344,472,474]
Gemini North and South		8.0 m	[134,135,636,776]
Subaru		8.2 m	[750]
Large Binocular Telescope	LBT	2×8.4 m	[635]
Very Large Telescope	VLT	4×8.2 m	[282]
Keck Twin Telescopes		2×10 m	[387,878]
Giant Magellan Telescope	GMT	25 m	[389]
Thirty Meter Telescope	TMT	30 m	[359]
Ring Interferometric Telescope	RIT	30 m	[158]
European Extremely Large Telescope	E-ELT	42 m	[62,293,359,742]

4.1.2 Retinal Imaging

Since the late 1990s, researchers have been making great strides in adopting the principles and technology of adaptive optics and applying them toward medical imaging, especially imaging human retina photoreceptors (rods and cones) [462] or ganglion cells and retinal pigment epithelial cells [306] (Figure 4.2).

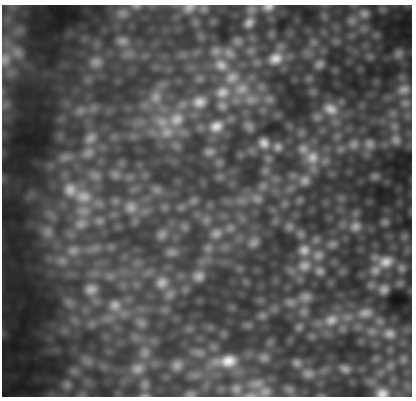

FIGURE 4.2
Image of the human retina taken with an adaptive optics system at the University of Rochester clearly shows photoreceptors (rods and cones). (Photo courtesy of the Center for Visual Science, University of Rochester, Rochester, NY.)

While specific configurations vary, the system elements remain a WFS, a deformable mirror, and a control computer. The fluid inside the eye, called the vitreous humor, is turbulent much like the atmosphere; however, it does not follow a Kolmogorov spectrum. In addition, keeping the eye steady and compensating for a varying tear film also presents practical challenges. Many researchers have built research and clinical systems using conventional Hartmann–Shack WFSs with low-power lasers acting as wavefront beacons reflecting off the retina [108,136,215,399,630]. Others have used different implementations such as a pyramid sensor [122] or no sensor at all, but rather a simulated annealing algorithm applied to the images [905]. With multiple images, researchers have developed techniques to automatically identify cone photoreceptors [460] or to evaluate changes in the lamina cribrosa, which is an early site of damage in glaucoma [824].

In support of the imaging efforts, much work is being done to understand the scatter of light in the eye [679,847] and higher-order aberrations [159,479, 683]. The effect of compensating higher-order aberrations is being investigated [128,544] in terms of visual acuity [490]. With the use of ultrabroadband sources and femtosecond lasers, adaptive optics optical coherence tomography can achieve ultrahigh-resolution retinal imaging [120,899].

4.2 Beam Propagation Systems

The same turbulent atmosphere that distorts an image by disturbing the light passing down through the atmosphere will distort a beam passing up through the atmosphere. Although propagation through the atmosphere

[889] of weapons-class lasers for ballistic missile defense was the impetus for much of the early adaptive optics development, the technology and systems can also be used for various peacetime applications. A system like that shown in Figure 4.3 can be used for laser power beaming to recharge batteries in orbiting satellites [254,531,555], laser power beaming to supply energy for a lunar base [444], or ground-to-space laser communications [791,868].

Often, a dynamic disturbance or aberration occurs after propagation away from the optical system. In this instance, it is difficult to predict the disturbance and apply its phase conjugate without first sampling the aberration source. The system shown in Figure 4.3 uses energy from the target, or near the target, to supply information about the aberrations. If a signal from the target, possibly a cooperative beacon, a laser guide star, or a reflection of sunlight, propagates back through the atmosphere, the adaptive optics system can sense the wavefront distortion of the beam returning from the target. By conjugating this field, remembering to scale for slightly different paths or wavelengths, the outgoing beam can be given a wavefront that allows radiation to reach the target near the diffraction limit. If the return wave shares the same optical path or aperture as the outgoing wave, the approach is called the *return-wave shared aperture* approach. Apertures can be shared spatially by physically dividing the return and outgoing beams into parts or can be shared temporally by dividing the two beams as a function of time. They can also be divided spectrally if the return wave and the outgoing wave are of a different wavelength or polarization. Methods of sharing will be covered in Section 5.5 during the discussion of wavefront sampling.

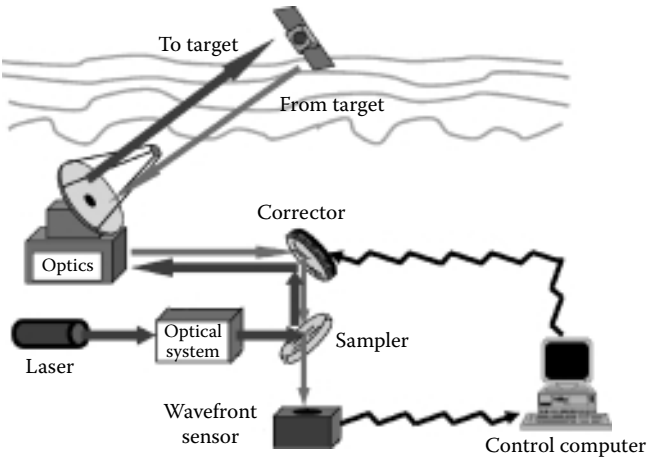

FIGURE 4.3
Laser propagation system.

4.2.1 Local-Loop Beam Cleanup Systems

If a beam is going toward a target, we can sometimes correct for aberrations in the beam in a local closed loop before it reaches the target. An example of this is shown schematically in Figure 4.4. The beam is presumably aberrated in its formation or by an optical train. A portion of this beam is sampled and sent to a WFS. The sensor measures the wavefront, the controller generates signals to a corrector, and the corrector applies the phase conjugate. In this concept, the sampler is *after* the corrector. This allows the adaptive optics system to be differential, that is, the wavefront sensor sees the combined output of the beam, optics, and corrector. The corrector will be driven flat if the wavefront is flat. As the wavefront deviates from flat, the wavefront sensor will see the difference between the beam and the corrector. This difference will be applied to the corrector until the wavefront sensor no longer sees any difference, indicating that the phase conjugate has been applied to the beam. Because of the need to avoid diffraction effects in the process, this must be done as close to the source of aberrations (the laser and optics) as possible. It is used in high-power applications such as laser fusion. Local loop beam cleanup is proposed as the principal adaptive optics configuration in each of the 192 optical trains in the 750-TW National Ignition Facility high-powered lasers [346].

If the sampler is before the corrector, the WFS sees only the beam and optics output. The system applies an open-loop phase conjugate to the corrector. If the beam changes, the WFS will detect a change, and, if the system is properly calibrated, the corrector will be moved to the conjugate position. This variation *should* be able to provide the same amount of correction. The conjugation process is the same; however, trusting the stability of the calibration and assuming the output of the corrector is really a conjugate, without measuring it, are not good engineering practices.

If the propagation of the beam, after it leaves the adaptive optics system, does not encounter any additional aberrations, the system is optimal. However, if the transmitting optics downstream of the adaptive optics system

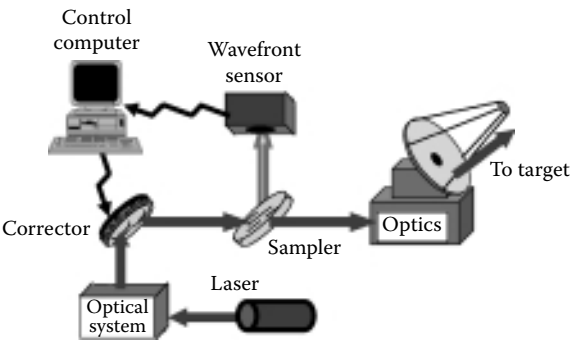

FIGURE 4.4
Local-loop beam cleanup adaptive optics system.

impart aberrations (not a vacuum propagation), many of the advantages of the cleanup can be lost by the time the beam reaches the target.

4.2.2 Alternative Concepts

In a propagation system like that shown in Figure 4.3, if the wave returning from the target enters the system through a different aperture, it is called the *return-wave separate aperture* approach (Figure 4.5).

If the target return wave is not used directly to conjugate the wavefront but is used to provide information about the beam path so that an outgoing wave approach can predictively impart a phase conjugate, the adaptive optics system can still perform. This approach is shown diagrammatically in Figure 4.6. It is called the *coherent optical adaptive techniques* (COAT) method,

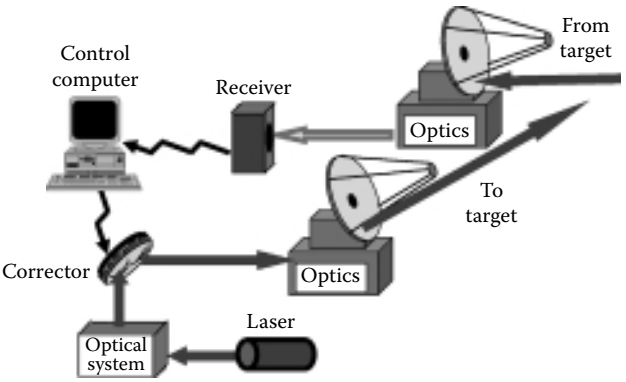

FIGURE 4.5
Return-wave separate aperture adaptive optics.

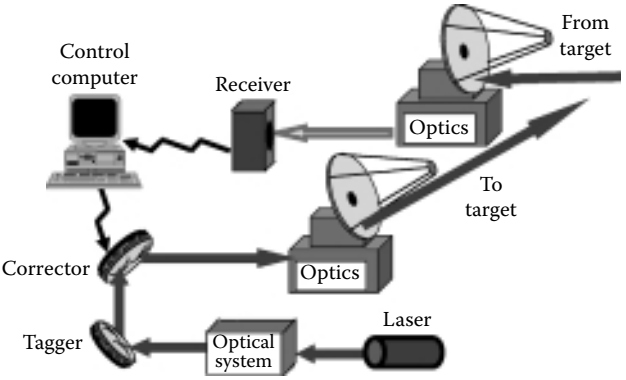

FIGURE 4.6
Coherent optical adaptive technique.

or the *multidither* approach. The outgoing wave is tagged both spatially and temporally, usually by modulating the phase of different parts of the beam with different modulation frequencies. Specular reflection from the target is decoded by a receiver and is used in a predictive sense to conjugate the outgoing beam. The details of the optics and electronic components necessary to do this are discussed in Chapter 5.

If the aberrations that alter the beam after the last optical element can be predicted with some certainty, the adaptive optics system can apply a phase conjugate without actually sensing the wavefront at all. This approach can use external information, such as the temperatures of optics, which can be used to predict thermal distortion, or the pointing direction of a large telescope, which can be used to predict gravitational sag. If the atmospheric turbulence is low enough to be disregarded or is corrected elsewhere, prediction of the target position is analogous to prediction of the lowest-order aberration, wavefront tilt. For example, Figure 4.7 shows a system in which a figure sensor [21] is used to observe the shape of the corrector. No information from the target is needed except its predicted position, which can be obtained from other sources such as radar or acoustics. If the figure sensor is combined with other information, such as a measure of beam power to predict thermal effects or a measure of target range to predict time-of-flight (of the photons) and other necessary information, the corrector can apply an appropriate phase conjugate to the beam. In some cases, predictive optimal estimators in the reconstruction process can be used to reduce the servo time delay and increase the system bandwidth [863].

There are special requirements for an adaptive optics system. For example, imaging objects that have a large spatial extent, such as nearby galaxies, planetary surfaces, the moon, some satellites, or extended fields of stars, require special consideration. Because the field of view is larger than the isoplanatic

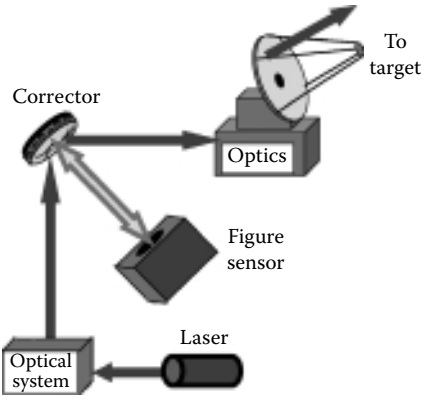

FIGURE 4.7
Predictive adaptive optics with figure sensor.

patch, methods such as deconvolution of the WFS signals themselves can be used to derive image information [670].

One variation on this method uses multiple views to gather sufficient data for tomographic reconstruction of the disturbances [378] and compensation of the images. Multiconjugate adaptive optics systems use multiple WFSs and deformable mirrors to compensate for individual layers of the atmosphere instead of a single integrated path [393]. Ellerbroek [195] presents an analysis of possible wide-field-of-view concepts.

A passive phase-conjugation method uses an array of corner cubes to form a conventional phase-conjugate mirror (PCM) [61,591]. Each small corner cube will reverse the direction of a beam entering it. The beam will be slightly offset (no more than the size of the cube aperture). If the cubes are small enough, each cube retroreflects a small portion of the beam (see Figure 4.8). The absolute phase is not maintained over the whole aperture, and the resolution is limited to the diffraction limit of one corner cube. The recombined beam will have an approximate phase conjugate of the incoming beam.

In addition to the variations of real-time systems, postprocessing of images taken with or without adaptive optics can be used to enhance the imaging capability of an optical system [294]. The postprocessing methods can be as basic as frame selection (throwing away the bad images) [228] or as sophisticated as direct deconvolution [469] or blind deconvolution [133]. Roggemann and Welsh [672] present an excellent description of the many postprocessing methods and a comprehensive discussion of hybrid systems (those that use postprocessing and real-time adaptive optics).

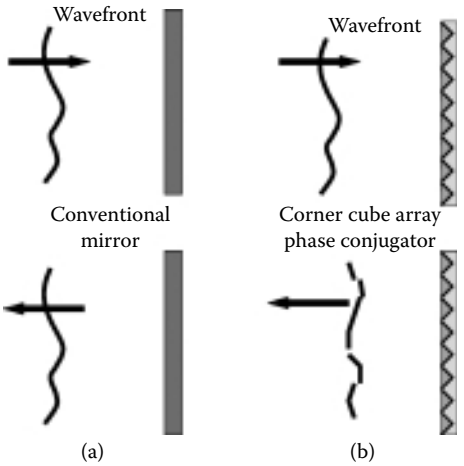

FIGURE 4.8
An incident wavefront can be approximated by a corner cube array: (a) conventional mirror and (b) corner cube array.

4.2.3 Pros and Cons of Various Approaches

Each of the conventional approaches has both advantages and disadvantages. Correcting for atmospheric turbulence in an astronomical imaging system is limited by the capabilities of the hardware to sense and correct the beam at a sufficient rate. The very low signal-to-noise ratios generated by faint starlight require long integration times to achieve a sufficient signal. The operating bandwidth of the system is seriously constrained.

The return-wave phase conjugate approach is useful in vacuum propagations or short-distance atmospheric propagations [436]. For instance, optics errors in a beam train can be corrected using an unresolved object in distance as a source of wavefront information. The wavefront reaching the optics is essentially a plane wave. Any wavefront error sampled by the adaptive optics system came from the optics themselves and can be conjugated by the corrector. The combination methods and the return-wave methods have limitations due to the time-of-flight characteristics. The round-trip time for a photon to travel to and from a target at distance d away is $t = 2d/c$. For disturbances that have significant spectra above 100 Hz (e.g., atmospheric turbulence and mechanical vibrations), the range is limited to about 500 km. This makes ground-to-space and satellite-to-satellite transmission with multidither impractical.

4.2.4 Free-Space Laser Communications Systems

There has been a recent growth in the need for and use of adaptive optics for free-space optical communications. Combining the concepts of local-loop beam cleanup and return-wave adaptive optics, compensation of the atmosphere by conjugating the phase of the outgoing transmitted beam can significantly improve performance. As the communication signal beam travels through the atmospheric turbulence, the phase changes result in scintillation, which cause fades and surges at the receiver [19,21]. The result of this is an increase in the bit-error rate that necessitates reduction of the bandwidth. By compensating for the turbulence prior to transmission, much of the scintillation can be reduced [792]. Various modulation schemes that have been studied include on-off keying [797], pulse position modulation [883], and optical vortex encoding [270]. Ground-to-space links [868], space-to-ground links [791], air-to-space links [567], air-to-ground links [710], and ground-to-ground links [545] have been under investigation.

There are a number of analyses to quantify the effect of turbulence, including understanding the fade statistics [64] and optimizing the aperture sizes in terms of level of disturbance and level of compensation [75]. Earlier studies have shown that using partially coherent beams can improve transmission through the atmosphere [430,888]. Determination of the correct level of coherence to optimize the transmission depends on the site, turbulence level, and range [125], but the level of coherence can be adjusted using devices such as adaptive arrays of fiber collimators [836,837].

Some systems use basic tip-tilt control [567,795], whereas some use higher-order controls [797]. AOptix Technologies, Inc. offers a commercially available two-way system that uses high-order adaptive optics [25]. Each transceiver in the AOptix system precorrects the transmitted beams using part of the received signal as a wavefront beacon. They report a communications capacity of 10 Gbps over distances up to 5 km.

Because free-space laser communication links will have to be plentiful, they must be low cost. One proposal is to use low-quality optics in the systems, either the primary mirrors or the secondary mirrors, or both, and then use the correction capability of the turbulence-correcting adaptive optics to compensate for the static aberrations in the telescope [339].

4.3 Unconventional Adaptive Optics

Each of the concepts described as *conventional* assumes optics that could correct the wavefront of a beam through inertial methods, that is, moving something to alter the wavefront. Some optical materials have the ability to alter the wavefront of a beam without inertial means on a macroscopic scale. These materials make use of the fact that susceptibility χ of a material is electric-field-dependent, and it often depends on a power of the field higher than 1. These nonlinear effects lead to the definition that is most common when referring to adaptive optics: *nonlinear optics* (NLO) are unconventional adaptive optics and *inertial adaptive optics* are conventional. Unfortunately, this is not always true. There are methods of correction that use neither inertial motion nor the nonlinear optical properties of any material [61]. These should probably be called *unconventional* because they are unique and interesting. Other methods use nonlinear properties of materials such as the Pockels effect in an otherwise conventional method. The confusion cannot easily be eliminated. These special systems will be addressed separately.

4.3.1 Nonlinear Optics

If the electric-field-dependent susceptibility is represented by an expansion given by

$$\chi(E) = \chi^{(1)} + \chi^{(2)}E + \chi^{(3)}E^2 + \ldots \tag{4.1}$$

Then the polarization is represented by

$$P(E) = E\chi(E) = \chi^{(1)}E + \chi^{(2)}E^2 + \chi^{(3)}E^3 + \ldots \tag{4.2}$$

The $\chi^{(1)}$ terms represent linear effects such as refraction, absorption, gain, and birefringence; the $\chi^{(2)}$ terms lead to second-harmonic generation, parametric mixing, and the Pockels effect; and the $\chi^{(3)}$ terms lead to effects such as third-harmonic generation, Raman scattering, the dc Kerr effect [831], nondegenerate four-wave mixing, and Brillouin scattering.

Although many of these processes have some application to different aspects of adaptive optics, four effects are more commonly used in phase conjugation. Stimulated Raman scattering (SRS), stimulated Brillouin scattering (SBS), Brillouin-enhanced four-wave mixing [642], and degenerate four-wave mixing (DFWM) have been used extensively for adaptive optics [372,891].

As shown in Sections 4.1 and 4.2, conjugate beams are the basis for many applications of adaptive optics. A beam propagating in the z direction is represented by the electric field $U(\mathbf{r}, t)$, as follows:

$$U(\mathbf{r}, t) = \frac{1}{2} U \exp[-i(\omega t - kz)] + \text{c.c} \tag{4.3}$$

where c.c indicates the complex conjugate. With a phase aberration $\phi(\mathbf{r})$, this field obeys the scalar wave equation given by

$$\nabla^2 U + [\omega^2 \mu \phi(\mathbf{r}) - k^2] U + 2ik\left(\frac{\partial U}{\partial z}\right) = 0 \tag{4.4}$$

A conjugate of this equation

$$\nabla^2 U^* + [\omega^2 \mu \phi(\mathbf{r}) - k^2] U^* - 2ik\left(\frac{\partial U^*}{\partial z}\right) = 0 \tag{4.5}$$

has a solution of the form

$$U(\mathbf{r}, t) = \frac{1}{2} U \exp[-i(\omega t + kz)] + \text{c.c} \tag{4.6}$$

which is a field propagating in the opposite direction. Because the backward conjugate wave obeys the same wave equation as the forward wave, the effect of the aberration $\phi(\mathbf{r})$ is reversed. This process holds for either inertial phase conjugators (Figure 3.2) or nonlinear (noninertial) conjugators [32].

4.3.2 Elastic Photon Scattering: Degenerate Four-Wave Mixing

If three waves U_1, U_2, and U_p are incident upon a nonlinear medium ($\chi^{(3)}$), a fourth wave will be generated due to elastic photon scattering in the medium. The two incoming waves are called *pump beams*.

$$U_1(\mathbf{r}, t) = \frac{1}{2} U_1(\mathbf{r}) e^{i(\omega_1 t - k_1 z)} + \text{c.c} \tag{4.7}$$

$$U_2(\mathbf{r}, t) = \frac{1}{2} U_2(\mathrm{r}) \mathrm{e}^{i(\omega_2 t - k_2 z)} + \mathrm{c.c} \tag{4.8}$$

The third wave of smaller amplitude is called the probe beam, given by

$$U_\mathrm{p}(\mathbf{r}, t) = \frac{1}{2} U_\mathrm{p}(\mathrm{r}) \mathrm{e}^{i(\omega_\mathrm{p} t - k_\mathrm{p} z)} + \mathrm{c.c} \tag{4.9}$$

A polarization will occur in the medium that is proportional to the product of these three waves and the third-order nonlinear optical susceptibility $\chi^{(3)}$, and is given by

$$P_\mathrm{NL} = \frac{1}{2} \chi^{(3)} U_1(\mathrm{r}) U_2(\mathrm{r}) U_\mathrm{p}^*(\mathrm{r}) \mathrm{e}^{i[(\omega_1 + \omega_2 - \omega_\mathrm{p}) - (k_1 + k_2 - k_\mathrm{p}) \cdot \mathrm{r}]} + \mathrm{c.c} \tag{4.10}$$

Polarization radiates a fourth wave with a frequency ω_c that is related to the frequencies of the other waves by

$$\omega_\mathrm{c} = \omega_1 + \omega_2 - \omega_\mathrm{p} \tag{4.11}$$

The fourth wave is called the *conjugate wave* because it propagates in the direction opposite the probe wave when the pump frequencies are equal to the probe frequency ($\omega_1 = \omega_2 = \omega_\mathrm{p} = \omega$). In this degenerate case, the conjugate wave has the same frequency ω as the probe beam. Because the pump beams are counterpropagating ($k_1 = -k_2$), the conjugate wave is counterpropagating to the probe beam ($k_\mathrm{c} = -k_\mathrm{p}$), which is equivalent to a phase conjugate of the probe wave:

$$U_\mathrm{c}(\mathbf{r}, t) = \frac{1}{2} U_\mathrm{c}(\mathrm{r}) \mathrm{e}^{i(\omega t + k_\mathrm{p} z)} + \mathrm{c.c} = U_\mathrm{p}^*(\mathbf{r}, t) \tag{4.12}$$

This method of phase conjugation is called DFWM.

Another application of this process occurs when the beams are not degenerate, but nearly so [221]. If the pump beams have equal frequencies ω and are opposite ($k_1 = -k_2$), but the probe is slightly frequency shifted, $\omega_\mathrm{p} = \omega + \delta$, the conjugate will be shifted in the opposite direction, $\omega_\mathrm{c} = \omega - \delta$.

The coupled beams can be expressed as follows:

$$\frac{\mathrm{d}U_\mathrm{p}^*}{\mathrm{d}z} = i\kappa_\mathrm{p} U_\mathrm{c} \mathrm{e}^{-\Delta k z} \tag{4.13}$$

and

$$\frac{\mathrm{d}U_\mathrm{c}}{\mathrm{d}z} = i\kappa_\mathrm{c}^* U_\mathrm{p}^* \mathrm{e}^{+\Delta k z} \tag{4.14}$$

where

$$\kappa_p = \frac{-2\pi\omega_p}{nc}\chi^{(3)}U_1U_2 \tag{4.15}$$

$$\kappa_c^* = \frac{2\pi\omega_c}{nc}\chi^{(3)}U_1U_2 \tag{4.16}$$

The phase mismatch that results (in Gaussian units) is given by

$$\Delta k = \frac{2n\pi\Delta\lambda}{\lambda^2} = 2n\frac{\delta}{c} \tag{4.17}$$

and shows up as decreased conjugate reflectivity because of the finite frequency detuning. In this manner, nearly DFWM can be used as an optical frequency filter.

4.3.3 Inelastic Photon Scattering

4.3.3.1 Raman and Brillouin Scattering

Phase conjugation by DFWM requires that pump beams of an intensity much higher than that of the probe beam to be conjugated. If the photons in a probe beam can extract energy from the medium by an inelastic collision, another beam need not be present. *Raman scattering* occurs when a beam transfers its energy (via polarizability changes) into molecular vibrations (optical phonons). When this occurs, another beam is backscattered. *Brillouin scattering* occurs when a beam transfers its energy via electrostriction into pressure-density fluctuations (acoustic phonons) and another beam is backscattered. Rayleigh scattering is also a useful phenomenon, but it is not widely used for phase conjugation. The frequency-downshifted, backscattered beam is called the *Stokes wave*. The normalized frequency shift is proportional to the acoustic velocity c_a of the medium

$$\frac{(\omega_1 - \omega_2)}{\omega_1} = \frac{2c_a}{c} \tag{4.18}$$

This downshift is on the order of 1000 cm^{-1} for SRS and 1 cm^{-1} for SBS. Details of these processes and the physics behind them are found extensively in literature Excellent reviews are given by Fisher [221], Shen [720], Pepper [612,611], and Zel'dovich et al. [902]. Although both processes are used extensively for phase conjugation, only the most commonly used adaptive optics process, SBS, will be discussed further.

SBS occurs when two time-periodic electric fields, U_1 and U_2, induce density variations in a medium by electrostriction [191,614]. Actually, the density variations alter the polarizability, which in turn drives the oscillatory motion

of the electric fields. The process is attractive for adaptive optics because there does not need to be a pump beam or beams as in DFWM, the gain can be very high (transferring much of the probe beam's energy to the conjugate Stokes wave), and the SBS-reflected Stokes polarization state is like a conventional mirror [901]. This last characteristic allows a practical way of substituting a nonlinear optical PCM into a beam train using conventional optics.

If the electric fields are represented by

$$U_1 = U_1 e^{i(k_1 z - \omega_1 t)} \tag{4.19}$$

and

$$U_2 = U_2 e^{i(k_2 z - \omega_2 t)} \tag{4.20}$$

and the acoustic wave field is

$$\rho = A e^{i(k_a z - \omega_a t)} \tag{4.21}$$

then the coupled wave equations representing the SBS process (for the resonant case $\omega_a = \omega_1 - \omega_2$; $k_a = k_1 - k_2$) become

$$\left(\frac{\partial}{\partial z} + \frac{\alpha}{2}\right) U_1 = \frac{i\omega_1^2}{2k_1 c^2} \frac{\partial \varepsilon}{\partial \rho} U_2 A \tag{4.22}$$

$$\left(\frac{\partial}{\partial z} + \frac{\alpha}{2}\right) U_2^* = \frac{i\omega_2^2}{2k_1 c^2} \frac{\partial \varepsilon}{\partial \rho} U_1^* A \tag{4.23}$$

$$\left(\frac{\partial}{\partial z} + \frac{\Gamma}{c_a}\right) A = \frac{ik_a \rho_0}{4\pi c_a^2} \frac{\partial \varepsilon}{\partial \rho} U_1 U_2^* \tag{4.24}$$

The frequency shift ω_a is typically on the order of 30 GHz; the acoustic damping coefficient Γ (the half-width of the line for spontaneous Brillouin scattering) is approximately 0.6 GHz. The acoustic wave density variation ρ is assumed to be a *variation* about the mean density ρ_0 of the medium, and $\rho_0 (\partial\varepsilon/\partial\rho)$ is the electrostrictive coefficient.

These equations cannot be solved analytically for all configurations of acoustic and electric fields. The gain can be determined for a particular case when the material properties are known. The Brillouin gain is found to be

$$g_B = \frac{\omega_1^2 \rho_0}{nc^3 c_a \Gamma'} \left(\frac{\partial \varepsilon}{\partial \rho}\right)^2 \tag{4.25}$$

where ω_1 is the pump frequency. The acoustic velocity is c_a, whereas the velocity of light is c. The acoustic properties of the medium are absorbed into Γ', whereas for liquid SBS media

$$\Gamma' = \frac{4\eta k_a^2}{3\rho_0} \tag{4.26}$$

and η is the shear viscosity. This gain factor has been measured for a number of liquids [207] and ranges from 0.005 cm/MW (water) to 0.13 cm/MW (carbon sulfide).

Studies involving xenon gas SBS cells show that there exists a threshold intensity for SBS to occur [859]. For a cell of length L, the threshold I_t is found from the transcendental equation

$$g_B L I_t = \ln\left(\frac{I_t}{I_n}\right) \tag{4.27}$$

where the initiation intensity I_n, arises from the random acoustic noise, is a function of the gas pressure and is on the order of 1.0 μW/cm^2. For a 1-cm-long cell, the threshold intensity is on the order of 109 W/cm^2. This was achievable for 1 μs pulses at 39 atm pressure with a 500-kW threshold power [860].

Adaptive optics systems that use NLO can appear in a number of configurations. The required high intensities and breakdown mechanisms of many of the materials limit their applicability. They usually cannot be used as the correcting optics in conventional outgoing or single-path concepts like those shown in Figures 4.1 and 4.6. Because the reflected wave is the (almost) exact conjugate of the incoming wave, the outgoing wave must repeat the path of the wave to be corrected in order for the "closed-loop" behavior to occur, and alternate system concepts are used.

A high-power laser can be given a conjugate phase by using SRS. In Figure 4.9, a beacon is sent backward through an aberrator like the atmosphere. The laser pump stimulates the Raman effect, which produces a backscattered beacon beam (a phase conjugate of the incoming beacon) with most of the power transferred from the laser pump to the conjugate. This is a very efficient way to impart a conjugate phase to a higher-power beam. If a high-power beam is aberrated, we can use part of it as a seed for the

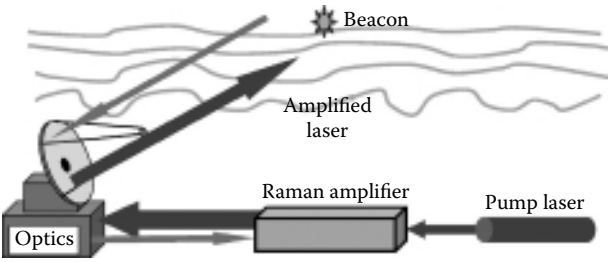

FIGURE 4.9
Wavefront conjugation with stimulated Raman scattering.

Raman process [872]. Figure 4.10 shows a system in which an aberrated high-power beam is wavefront corrected. A fraction of the high-power beam is split away. The small sample is spatial-filtered to remove high-order aberrations. This acts as the Stokes wave and is injected into the Raman amplifier cell. The gain of this beam depends on the intensity and aberrations present in the initial beam, because that beam acts as a pump wave. In many cases, the amplified Stokes output beam is near diffraction limited.

Another common usage of NLO is straightforward usage of an SBS cell as a PCM. As described in Section 2.3.4, a gain medium in a laser amplifier can impart aberrations to a beam. In general, the bigger the amplifier, the noisier the source, and the more aberrated the wavefront. A number of small beams can be combined to simulate a large beam from a common amplifier. In Figure 4.11, an SBS cell is used to combine and amplify a number of beams. A seed laser beam of good quality and moderate power is split into a number of beams. Each passes through a separate amplifier. While passing through the amplifiers, the beams pick up aberrations from the gain medium. When they are reflected off the PCM, the conjugate waves retrace their paths through the amplifiers. The resultant output is a high-power beam with a wavefront nearly as good as the wavefront of the low-power seed.

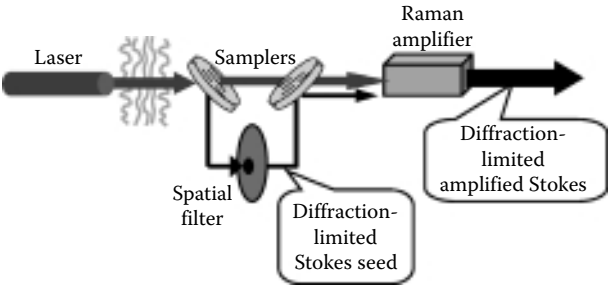

FIGURE 4.10
Beam cleanup with stimulated Raman scattering.

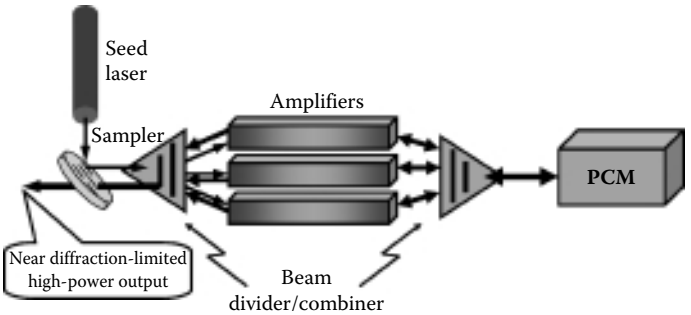

FIGURE 4.11
Beam combining with stimulated Brillouin scattering.

A similar situation arises for a single-beam case when the propagation path is highly aberrated. The polarization conservation of SBS can be used to send a beam through an aberrating medium and back. Figure 4.12 shows a system where the source beam is aberrated by the beam path. Reflection from the PCM instills the phase conjugate so that the beam returning through the medium has a wavefront as good as the initial seed. By placing a quarter-wave plate in the beam before the PCM, the polarization is changed with the double pass. The outcoupler can be polarization-selective to deliver the beam.

If the source of Figure 4.12 is replaced by a concave mirror and the aberrating medium is a laser gain medium, the system has the form of a nonlinear optical resonator (see Figure 4.13). As the beam reflects back and forth between the concave mirror and the PCM, it alternately picks up the aberrations present in the medium and, through conjugation, rejects them. The output can have a wavefront limited only by the quality of the optics rather than by the disturbances of the gain medium [62,443,565,896].

When a wavefront is measured after the focus of a high-numerical-aperture optical system, a high-intensity laser beam will exhibit aberrations due to optical quality and alignment. Adaptive correction can be achieved using a third-harmonic signal generated at an air-dielectric interface in conjunction with a genetic algorithm [621].

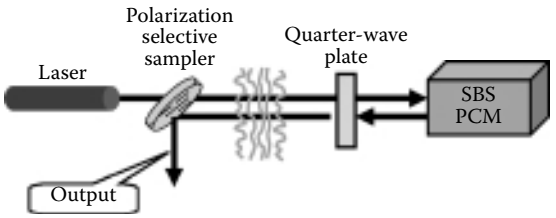

FIGURE 4.12
Aberration removal with stimulated Brillouin scattering (SBS).

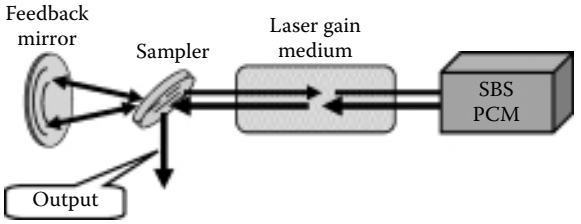

FIGURE 4.13
Nonlinear optical resonator with a stimulated Brillouin scattering phase-conjugate mirror (SBS PCM).

4.4 System Engineering

Adaptive optics systems can be designed and analyzed using a number of very effective system engineering tools. The use of linear systems theory (Section 3.5) to describe the adaptive optics system as a spatial filter is one example, and the use of other tools, such as functional trees, performance trees, and interface matrices, also is effective. Other system trees, such as hardware component trees, are used to identify and track the various pieces of hardware in a system [124,138,805,806].

The *functional tree* method describes the adaptive optics system, or any system, in terms of functions and subfunctions until the simplest functions are identified. This can often be done to any degree of complexity and completeness, because the definition of *simple function* is subjective. An example of a functional tree for a conventional adaptive optics system is shown in Figure 4.14. A typical breakdown of the functions of the system has each function further reduced to subfunctions, and so on. The highest level of this figure could also be considered a function of a much larger system, such as an imaging system. The function blocks may or may not correspond directly to unique hardware components. For example, the WAVEFRONT sensor function has a subfunction DETECTION, which will probably be performed by hardware consisting of optics, electro-optic detectors, preprocessing and postprocessing, and the supporting power supplies and other

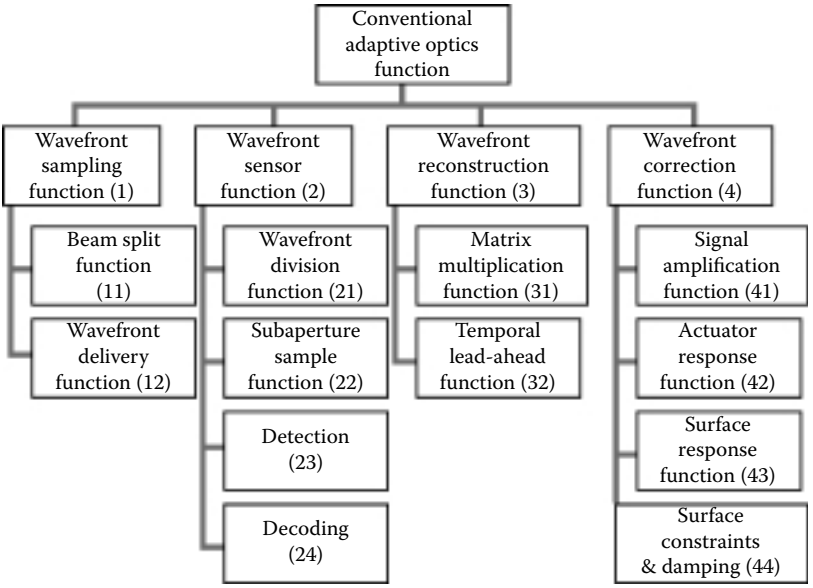

FIGURE 4.14
Functional tree for a conventional adaptive optics system.

electronics. Similarly, the subfunction MATRIX MULTIPLICATION in the function RECONSTRUCTION might consist of computer hardware, software, bulk storage, and supporting power and signal conditioning. The functions can be subdivided to include these details or they can be left at this level. Only whatever is necessary for understanding the hierarchy of system functions is needed [167].

Another type of system tree that is more quantitative in nature is the *system performance tree* [823]. By defining the various quantities that affect the overall adaptive optics performance, an error budget or performance hierarchy, is generated. These quantities are often called *system performance parameters*, or SPPs. Figure 4.15 shows an example of a simple adaptive optics system performance tree. In this case, the tree represents an adaptive optics system used for controlling the wavefront of a beam delivery system. Each of the blocks represents a quantity that could be either measurable or just expressed as a variable in an equation. The nodes of the tree represent the equations or relationships between the quantities. The highest measure of performance is the PEAK IRRADIANCE on TARGET. It is the result of BRIGHTNESS divided by RANGE to TARGET squared. The units of these quantities are usually expressed in the most commonly used units, often with little regard for mixing units. Therefore, a performance tree might have blocks on equal levels with different units and different sensitivity to the next higher quantity. The example

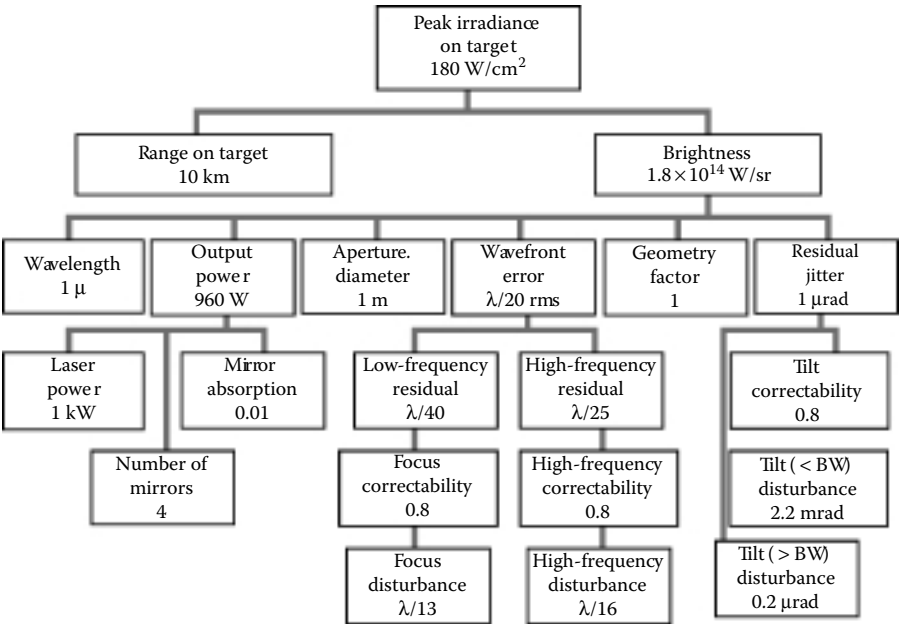

FIGURE 4.15
Performance tree for a conventional adaptive optics system.

shows how a brightness of 1.8×10^{14} W/sr and a range of 10 km combine for a peak intensity on target of 180 W/cm^2. The brightness is computed from an equation that includes laser power, system optical transmission T, residual jitter, the aperture diameter D, the wavelength, and the resultant rms wavefront error $\Delta\phi$. The equation for Node 1, relating these quantities (Equation 1.60), is repeated here; care should be taken, because the units are often mixed in a performance tree:

$$\text{Brightness} = \frac{\pi D^2 PTK \exp\left[-\left(\frac{2\pi\Delta\phi}{\lambda}\right)^2\right]}{4\lambda^2\left[1+\left(\frac{2.22\alpha_{\text{jit}}D}{\lambda}\right)^2\right]} \tag{4.28}$$

The output power is different from the laser power due to the absorption and scattering of the optics. It is explicit in this example so that the effect of mirror absorption is emphasized. For m identical partially absorbing optics (absorption α), the equation for Node 2 is simply

$$P_{\text{out}} = P_{\text{las}}(1-\alpha)^m \tag{4.29}$$

The adaptive optics system is shown as simple *correctability* in a performance tree. The detailed calculations including integrals, bandwidth considerations, and correcting system limitations are absorbed into the nodes. As the example tree indicates, the adaptive optics system is divided into low and high spatial frequency components to better identify the contributions to system performance. They are root-sum-squared to compute the total residual rms wavefront error. The system trees are often used as a quick look to identify sensitivities in overall performance. They can also be used to track hardware performance and to provide a requirements flowdown to individual components. The utility of the system trees is limited only by their complexity and the willingness to develop individual trees for the engineering discipline.

One spin-off from the system functional tree is a *system interface matrix*. This is a cross reference between functions to visualize the need for communications during the design process and hardware that might be needed. This is particularly important when certain functions are performed only when other functions are performed. The output of one function is often the input of another function. An example of an interface matrix is shown in Figure 4.16. The various interface modalities are E, *electronic*; F, *fluid*; I, *information*; M, *mechanical*; and O, *optical*. The user can add arrows to indicate the direction of the interface if it is important. Any sort of modality can be chosen as well. For instance, *electronic* can be subdivided into *digital, analog*, *power*, and so on. The level of functions can be chosen to be any level of the functional tree.

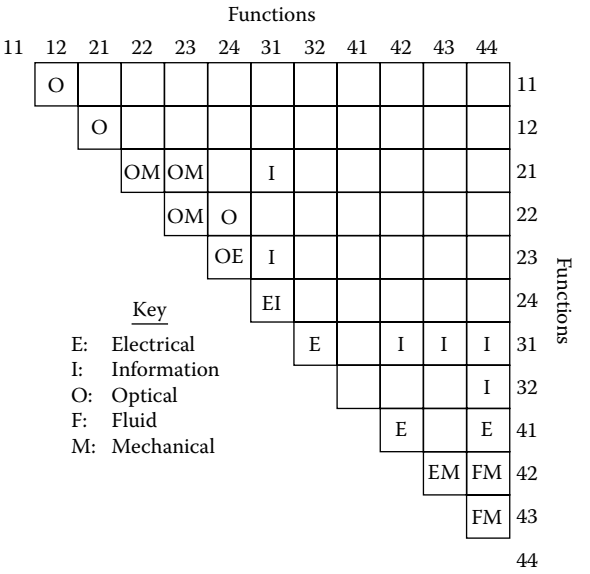

FIGURE 4.16
Adaptive optics system interface matrix.

These are by no means all the system analysis tools available for adaptive optics system design. Many other forms are in use. One method uses blocks to represent functions but does not display them in a hierarchy. Rather, it represents input and output data as lines entering and exiting horizontally; lines entering from the top represent controls or constraints, whereas lines entering each block from below represent supporting hardware segments [167]. Many of these can be computerized to aid the analysis and design of more complex systems. The main consideration is the information contained in the system analysis tool, not the strict adherence to any particular format [553,853].

An adaptive optics system normally is part of a larger optical system, and its purpose is to enhance the output of that optical system without degrading the performance. The system designer must (1) determine the overall adaptive optics system performance requirements, (2) consider the properties of the optical beam that the system is designed to enhance, and (3) integrate the system in such a way that it performs properly in the optical system environment where it is placed.

Adaptive optics systems are diverse, and their complexity varies greatly. There is no simple "cookbook" formula for designing, assembling, or integrating an adaptive optics system. Good engineering principles, balancing cost and performance, are needed at all levels of the design and installation phases. The development of adaptive optics systems over the past four decades has resulted in the identification of a number of issues that should be addressed during the system design effort.

4.4.1 System Performance Requirements

The first consideration is the quantification of the adaptive optics system performance requirements. Most systems will not perfectly conjugate a beam or compensate for all aberrations. One must determine the level of the correctability that can be tolerated. Computer modeling and laboratory experimentation are imperative to reduce the overall design time and cost prior to building and integrating a system. Theoretical modeling of atmospheric turbulence phase screens with realistic time delay characteristics [671] and laboratory wavefront generators with variable coherence lengths [345], temporal frequencies, and isoplanatic effects [503] are useful tools to avoid many engineering pitfalls.

With knowledge of the aberration sources and the choice of a tolerable residual wavefront error, we can determine the spatial and temporal bandwidths of the adaptive optics system. The spatial bandwidth will be used to determine the number of correction zones or modes (number of actuators). The temporal bandwidth requirement determines the type of electronic servo control. The amplitude of the disturbances also is a factor. For instance, if the amplitude of the tilt-mode disturbance is low, correction can be accomplished with only a deformable mirror. However, if the tilt disturbance is high, a separate tilt, or beam steering, mirror is used. Fugate [255] suggests that, no matter what high-order adaptive optics system is used, the source or target must be tracked to within about 1/10 of a diffraction spot, or a fundamental tracking requirement of $0.3\lambda/D$.

4.4.2 Compensated Beam Properties

The properties of the beam to be compensated often drive adaptive optics system component considerations. The size and shape of the beam are important considerations. If the beam is large, it may be advantageous to demagnify it for adaptive optics compensation. On the other hand, if it is small and has many higher-order aberration modes, it may be necessary to magnify it for correction. If the beam has an unusual shape or obscurations, it may have to be reshaped for compensation, which can add optics to the system that are costly in performance and price.

The beam power level is a major concern. For very low light levels, such as those found in astronomy, the addition of beam splitters or special optics for sampling or correction can seriously degrade the overall performance. For high-power beam propagation, the optics added for adaptive optics must be capable of withstanding the power levels while remaining operational. Stray light must be controlled to prevent damage or degradation of the front measurement. The adaptive optics system must operate when the beam power distribution is not spatially or temporally uniform. Large intensity irregularities must be considered in overall adaptive optics system design. For example, if most of the light is concentrated in one region of the beam, wavefront

compensation is usually unnecessary elsewhere. If this region moves around during operation, the system may need to monitor its location.

4.4.3 Wavefront Reference Beam Properties

The physical location, power, temporal modulation, and spectral characteristics of the wavefront reference are very important. Some WFSs work only with narrow-band, coherent sources. Others need compensating optics to function in a broadband environment. The selection of detectors is governed by their sensitivity and spectral band. Optical throughput to the detectors must be managed so that the power reaching the detector is in its operating range. Samples of a high-power laser must be attenuated greatly to avoid saturation or damage, but light from an astronomical object must be allowed to reach the detector with minimum attenuation. The polarization state of the beam is important because sampling optics, such as beam splitters and gratings, and WFSs with diffraction gratings are sensitive to polarization.

The temporal distribution of power is significant. Many WFSs have different operating characteristics for pulsed or continuous beams. The sensing technique must be considered if the beam is modulated, or chopped, or if it has an unusual pulse shape.

4.4.4 Optical System Integration

In most cases, the science objectives, the image collecting equipment, or the optical coatings drive the wavelength of operation for the adaptive optics system. When one or more of these constraints is removed, we can optimize the wavelength in terms of limiting the distorting effects of the atmosphere [778]. The choice of visible wavelength wavefront sensing and infrared imaging is driven by the low cost and low noise characteristics of visible wavelength CCD cameras and the better compensation at longer imaging wavelengths.

The placement of the adaptive optics components in relationship to other optics is critical to system performance. The wavefront that is measured should be the same as the one to be compensated. The beam sampling components described in Chapter 5 and the optics that transfer the sample to the WFS must not distort the wavefront. It is important that the components and the environment that contribute to the wavefront disturbance be in the path that is common to the correcting optics. Optics that are not in the correction path (i.e., that are in the uncommon path) should add minimal distortion to the wavefront.

In an adaptive optics system that uses a WFS and deformable or segmented correcting mirror, the WFS detector array must be at a conjugate pupil of the correcting mirror. It is often desirable to have them both at conjugate pupils of the telescope primary mirror. Because the wavefront changes as it propagates from mirror to mirror, reimaging ensures that the correction

is applied to the same wavefront that it senses. Correct pupil reimaging is required when line-of-sight variations are not removed by the beam-steering mirrors.

To avoid cross talk between control channels and to enhance control system stability, the WFS subapertures should be aligned with the actuators on the corrector. Most control systems and wavefront reconstructors use the absolute position of the actuators and subapertures and their relationship. A one-for-one registration is neither possible nor necessary, because most systems have a different number of subapertures and actuators in different geometric patterns. However, the positions should be well-characterized and maintained for optimum system operation.

5

Wavefront Sensing

An inertial adaptive optics system must have a way to sense the wavefront with enough spatial resolution and speed to apply a real-time correction [275]. The *direct* approach employs a step where there is an explicit determination of the phase or optical path difference (OPD) of the wave. After the wavefront is reconstructed, the information is used as feedback to correct the unwanted components of the phase. The *indirect* approach never reduces the information to an explicit indication of the wavefront; rather, it translates information related to the phase into signals that are used to compensate for the wavefront. For example, the multidither system mentioned in Section 4.2 is an inertial indirect system.

The requirements of wavefront sensing for adaptive optics differ from the requirements of phase or figure determination in optical testing in a number of ways [320]. In optical testing, the phase can be measured and reconstructed very slowly (minutes, hours, even days). Wavefront sensors in an adaptive optics system are used for real-time operation. Because many disturbances can be on the order of hundreds of hertz, the sensors must operate much faster. In some cases, the wavefront of individual pulses, which are as short as 2 μsec, must be measured in real time [641,867]. The spatial resolution requirement of adaptive optics wavefront sensors is usually very high. It is not uncommon to require a resolution to 1/100 of an aperture diameter, which requires many channels of parallel sensing.

In many cases, optical testing can be done in a narrow range of parameters, since the optics under test is well-characterized through previous examinations. For instance, mass production optics have only a few aberrations to be checked each time, since some high-order components may not be important for the application. On the other hand, adaptive optics are often required to deal with largely random wavefronts like atmospheric turbulence. This randomness requires a greater number of degrees of freedom. Adaptive optics wavefront sensing requires a large dynamic range (many wavelengths) to account for the vast OPD over the pupil of interest.

The final, yet fundamental, requirement of adaptive optics wavefront sensing is its ability to determine OPD independent of intensity. For many applications, imaging resolves objects through the atmosphere; for instance, the adaptive optics system will sense vast differences of intensity. Since the adaptive optics system is only normally capable of varying OPD over the aperture, the OPD must be determined without the confusing variation in the amplitude, manifested by the intensity nonuniformity. The use of

broadband (white) light is required when the absolute OPD cannot be determined at a single wavelength.

5.1 Directly Measuring Phase

The effect of the phase on the propagation of light is calculated from the Huygens–Fresnel integrals discussed in Section 1.3:

$$U(x,y) = \frac{-iA}{\lambda R} e^{-ikR} \int\int_{\text{Surf}} \frac{e^{ik(\Phi+s)}}{s} dS \tag{5.1}$$

where $U(x, y)$ is the complex amplitude of the input spherical wave represented by $\frac{A}{R} e^{ik(\Phi-R)}$ at distance s from a point on the aperture surface S.

The projected intensity pattern is $I(x, y) = |U(x, y)|^2$. Intensity is of great importance in most adaptive optics applications, and is determined by the amplitude and phase of the wave at the pupil, or input, plane. The intensity pattern is the image of a resolved object, or it represents the point-spread function (PSF) of the optical system for an unresolved object.

Unfortunately, there is no direct way to measure the phase of a single photon. There has been some progress in directly measuring the electric field, but not sufficient to be used in adaptive optics [851]. A beam will interact with itself or another beam of light. The principles of interference were discussed briefly in Section 1.3.4. These principles, along with those of diffraction, are the bridges between the optical phase and its intensity distribution. Conventional adaptive optics is forced into using these interactions to infer the phase of a beam and apply a correction.

A number of investigators have approached the problem. Some methods employ direct evaluation of the Fraunhofer diffraction pattern [297]. Some authors evaluate the moments of the diffraction pattern [758]. Others use multiple intensity measurements to extract the wavefront information [224,296,656,738]. The multiple measurement approach is the basis for most adaptive optics wavefront sensors.

5.1.1 Nonuniqueness of the Diffraction Pattern

If the diffraction pattern of a beam of light produced from a wave of the form

$$U(x,y) = |U(x,y)| \exp[-i\Phi(x,y)] \tag{5.2}$$

was unique, there would be solutions of the inverse equation that are functions of the field $U(x, y)$ and its amplitude

$$\Phi(x,y) = f\left[U(x,y), |U(x,y)|\right] \tag{5.3}$$

Similarly, since the function $u(\xi, \nu)$ is the Fourier transform of the input field $U(x, y)$ (the Fraunhofer diffraction pattern of the pupil), there would be solutions of the form

$$\Phi(x,y) = f\left[|u(\xi,\nu)|^2\right] \tag{5.4}$$

Solutions to this equation would make the wavefront sensing problem trivial. One could just measure the diffraction-pattern intensity distribution and operate on it to determine the phase $\Phi(x, y)$ either by a closed-form solution or by iteration. For practical purposes, it would be only restricted by the speed of the optoelectronics and the number of degrees of freedom desired.

It has been shown [224,296,656,657,758] that there is no unique solution in the general case for phase retrieval from a single measurement of the PSF. Consider the following simple example based on the derivation of the Strehl ratio [86], where the intensity at the center of the PSF compared to the diffraction-limited intensity is given by a sum of aberration coefficients, namely the Zernike coefficients:

$$\mathrm{SR} = 1 - \left(\frac{2\pi}{\lambda}\right)^2 \sum_{n=1}^{\infty} \sum_{m=0}^{n} \frac{A_{nm}^2 + B_{nm}^2}{2(n+1)} \tag{5.5}$$

Clearly, there are an infinite number of coefficients A_{nm} and B_{nm} that can satisfy this equation for SR < 1. This means that the intensity at the peak is not unique to any particular wavefront, and the rest of the intensity pattern is probably not unique. This relationship (Equation 5.5) only holds for small aberrations, those that are on the order of 1/10 wave or less. It is this level of aberration, however, that is most important in the realm of adaptive optics. There are, however, approaches to the problem that have some degree of utility in a practical manner, such as only small phase disturbances [461].

5.1.2 Determining Phase Information from Intensity

Solutions to the phase retrieval problem can be found from multiple measurements of the pupil plane intensity and the image plane (Fraunhofer diffraction) intensity. Fienup [216] reviews and compares a number of phase-retrieval techniques. Gonsalves [296] shows how two measurements can lead to the solution of the phase if the field derived from the magnitude of the image plane intensity is "analytic," that is, all derivatives must be finite [587]. Foley and Abdul Jalil [224] show that a fourfold degeneracy (which they term "nonuniqueness") can be reduced to a twofold degeneracy by judicious

application of aperture stops. Jeong et al. [381] reconstructs the phase in the focal plane by comparing the inverse Fourier transform of the intensity distribution with a reference electric field.

Robinson [656] explains a twofold degeneracy that results from symmetric intensity distributions. He derives, as many authors have done in various ways, the two solutions for the symmetric magnitude problem. He shows that the two solutions for the phase differ by the sign. The general result of his analysis is that there is always a solution to the problem under physical conditions. However, it is not unique for large duration-spatial bandwidth product situations. This result is not so surprising, since the large duration (big aperture), large spatial bandwidth (many aberration modes or cycles across the aperture) product would have so many cross terms in the diffraction integral that the uniqueness is almost certainly destroyed. Robinson derives a method of determining the phase from a single image plane- intensity measurement under extremely restrictive conditions. He shows that the phase $\Phi(x)$ is related to the magnitude of the image plane field $U(x)$ through the Hilbert transform (HT) by

$$\Phi(x) = -\mathrm{HT}\left[\ln|U(x)|\right] \tag{5.6}$$

Unfortunately, this simple solution is only valid for the specific cases of *minimum phase fields*. These fields, such as when the power is concentrated at the edge of an aperture, rarely occur in actual optical fields.

A general technique called phase diversity can be used on image plane measurements requiring no pupil plane detectors [85,93,174,895]. Another method, using multiple intensity measurements in the image plane, employs an iterative computation of the *maximum likelihood* of the wavefront [738]. This computation is equivalent to minimizing the merit function

$$\frac{1}{2}\sum_i \frac{[I_{\mathrm{meas}} - I_i]^2}{\sigma^2} \tag{5.7}$$

where I_i are the intensities due to various wavefront error terms. This minimization assumes a known amplitude and requires solution by nonlinear methods. The determination of the wavefront is found by using the two- dimensional basis functions based upon the intensity patterns from individual aberrations The iteration process begins by choosing a likely set of aberrations and then evaluating Equation 5.7. Convergence is achieved by forming derivatives of the merit function with respect to the phase parameters. A detailed analysis of this technique, using a maximum-likelihood algorithm, in the presence of noise, is given by Barrett et al. [60].

Ivanov et al. [375] describe the iterative algorithm that uses the Gerchberg–Saxton algorithm [279]. They show how the use of pupil plane and image plane-intensity distributions can be used to recover the phase with improved

convergence over just image plane distributions. Roddier and Roddier [656] employ dual out-of-focus images to recover the phase. Their method is the basis for *curvature sensing*, described in Section 5.3.3.

Harvey et al. [336] proposed an interesting phase retrieval method using the spot of Arago that occurs on-axis behind a circular obscuration. The edge-diffracted PSF characterizes the aberrations. It is particularly useful for annular beams where no auxiliary beam sampling optics would be required. It has not been applied to an adaptive optics wavefront sensing system.

Teague [758] proposed a method of phase retrieval by measuring the irradiance moments of the image plane-intensity distribution as follows:

$$M_{pq}(z) = \iint I(x,y)x^p y^q \,\mathrm{d}x\,\mathrm{d}y \tag{5.8}$$

Making as many measurements (N) as unknown aberrations (N), allows a matrix multiplication scheme to be adopted. The coefficients a, defined by

$$\Phi(x,y) = \sum_{n=1}^{\infty}\sum_{m=0}^{n} a_{n-m,m}x^{n-m}y^m \tag{5.9}$$

can be found from the multiplication of $[\Phi] = [U][M]$, where $[\Phi]$ and $[M]$ are N-element row vectors, and $[U]$ is an $N \times N$ matrix that is determined from basis functions dependent upon the pupil shape. Although the calculation appears to be simple, it is only because of the simplified notation. The calculation of moments in the image plane, the determination of the elements of $[U]$, the effect of noise, and the limitations of a finite image plane complicate the problem and make its realization in a high-speed optical system difficult.

The recovery of phase from intensity distributions was required to diagnose the aberrations of the Hubble Space Telescope (HST) [432]. Since the telescope was in orbit, only the intensity distributions from various images were known. Because the HST is a multiple-element optical system, and the source of the aberrations is unknown, an iterative method using "Fresnel-like" transforms is employed. Fienup [217] describes the method of phase retrieval that included consideration for absorption in the optics and bad detector pixels. Similar to the work of Teague, these iterative methods are not yet applicable to real-time adaptive optics, but they can be used as a basis for limited iterative procedures as computational ability increases.

Iterative techniques for real-time wavefront sensing have limitations because of the often large number of iterations required to generate a wavefront solution. The solution must be found before the disturbance changes and these changes can be between tens of milliseconds (astronomy) and hundreds of microseconds (imaging low Earth orbiting satellites).

Algorithms [502] that have been demonstrated include genetic algorithms [292,621,757,894], simulated annealing [539,905], simplex [416], iterative Fourier

transforms [295], and the iterative shadowgraphic method [623]. One promising method is Vorontsov's modification to the gradient-descent algorithm that introduces a stochastic (random) component [832,833,839,893].

5.1.3 Modal and Zonal Sensing

The wavefront information that is derived from measured data will be used to close the loop to apply a phase correction. The actual reconstruction of the phase from this data is discussed in Chapter 7. The format of the information often drives the ability to use it in an optimal manner. Two basic types of wavefront information are used. When the wavefront is expressed in terms of the OPD over a small spatial area, or zone, the wavefront is said to be *zonal*. When the wavefront is expressed in terms of coefficients of the modes of a polynomial expansion over the entire pupil, it is said to be *modal*. There are advantages and disadvantages of each method of presentation. Some reconstruction schemes limit the flexibility in choosing the wavefront representation. Some wavefront sensing schemes lend themselves to one or the other presentation. Both modal and zonal representations can be interchanged, since they represent the same wavefront; however, the complexity of the conversion will often limit their usefulness in a practical sense.

The zonal method is easily understood by considering the wavefront over an aperture. The wavefront is normally continuous unless it is in the plane of a physical stop. If the wavefront is broken into N subapertures, and the phase at each subaperture is expressed as a number, then the entire wavefront is the characteristic set of N numbers. If N approaches infinity, the wavefront is exactly represented. If N is finite, each subaperture may be represented by more than one number; for instance, piston and local tilt. In this case, each zone is represented by its fundamental modes.

Sometimes a $2N$ representation is sufficient. This is the case where only the tilt modes in each subaperture are represented. It can be shown how these tilts, $d\Phi/dx$ and $d\Phi/dy$, in each zone can be combined to determine the full aperture modes [499], which may be necessary if the wavefront sensor produces zonal information and the correcting optics require a full aperture phase or OPD. For the specific case of correcting atmospheric turbulence, a combination of zonal and modal measurements is useful [172].

There are some wavefront sensing schemes in which measurements are made that generate modal information directly with the zonal information deduced [111]. Measurements of the wavefront distortion due to atmospheric turbulence $\Phi(r, \theta')$, taken on the edge of an aperture of radius R, provide the basis to interpolate the wavefront $\Phi(r, \theta)$ in the remainder of the aperture,

$$\Phi(r,\theta) = \frac{R^2 - r^2}{2\pi} \int_0^{2\pi} \frac{\phi(R,\theta')\,d\theta'}{R^2 + r^2 - 2Rr\cos(\theta - \theta')} \tag{5.10}$$

The decision to use modal, zonal, or a combination of sensing schemes to measure the wavefront is usually left to the application. If low-order modes (tilt, defocus) are dominant, then modal analysis and corrections should be used. If high-order aberrations are present, the zonal approach should be used. For atmospheric turbulence compensation, both zonal and modal sensing have been used. Using Equation 3.10 for fitting error, the Strehl ratio is

$$S = \exp\left[-\kappa\left(\frac{r_s}{r_0}\right)^{5/3}\right] \tag{5.11}$$

An expression for the Strehl ratio in terms of the number of modes corrected, N, has a similar form [570], given by

$$S = \exp(-\sigma_N^2) \tag{5.12}$$

For $N \leq 21$,

$$\begin{array}{l|l}
\sigma_1^2 = 1.0299(D/r_0)^{5/3} & \sigma_{12}^2 = 0.0352(D/r_0)^{5/3} \\
\sigma_2^2 = 0.582(D/r_0)^{5/3} & \sigma_{13}^2 = 0.0328(D/r_0)^{5/3} \\
\sigma_3^2 = 0.1134(D/r_0)^{5/3} & \sigma_{14}^2 = 0.0304(D/r_0)^{5/3} \\
\sigma_4^2 = 0.111(D/r_0)^{5/3} & \sigma_{15}^2 = 0.0279(D/r_0)^{5/3} \\
\sigma_5^2 = 0.0880(D/r_0)^{5/3} & \sigma_{16}^2 = 0.00267(D/r_0)^{5/3} \\
\sigma_6^2 = 0.0648(D/r_0)^{5/3} & \sigma_{17}^2 = 0.0255(D/r_0)^{5/3} \\
\sigma_7^2 = 0.0587(D/r_0)^{5/3} & \sigma_{18}^2 = 0.0244(D/r_0)^{5/3} \\
\sigma_8^2 = 0.0525(D/r_0)^{5/3} & \sigma_{19}^2 = 0.0232(D/r_0)^{5/3} \\
\sigma_9^2 = 0.0463(D/r_0)^{5/3} & \sigma_{20}^2 = 0.0220(D/r_0)^{5/3} \\
\sigma_{10}^2 = 0.0401(D/r_0)^{5/3} & \sigma_{21}^2 = 0.0208(D/r_0)^{5/3} \\
\sigma_{11}^2 = 0.0377(D/r_0)^{5/3} &
\end{array}$$

For $N > 21$,

$$S_{N>21} = \exp\left[-0.2944\, N^{-(\sqrt{3}/2)}\left(\frac{D}{r_0}\right)^{5/3}\right] \tag{5.13}$$

These values are shown graphically in Figure 5.1.

For identical adaptive optics correction, using $\kappa = 0.32$ that is, equating Equations 5.11 and 5.13, we find that N, the number of modes, is given by

$$N = 0.92\left(\frac{D}{r_s}\right)^{1.93} \tag{5.14}$$

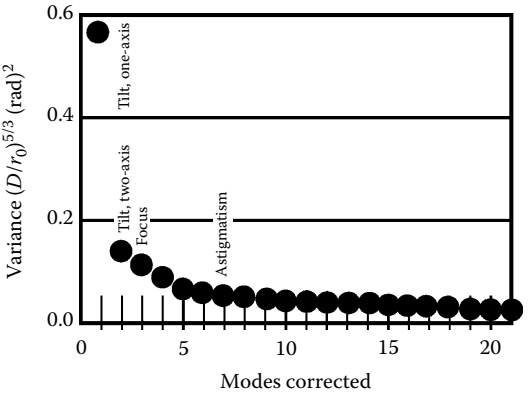

FIGURE 5.1
Wavefront variance for varying levels of modal correction.

and is roughly equivalent to the number of zones, given by

$$Z = 0.78\left(\frac{D}{r_s}\right)^{2.00} \tag{5.15}$$

Both expressions represent the number of degrees of freedom for the system. In conclusion, for the regions of practical interest in adaptive optics, the choice of zonal or modal correction transcends the theoretical analysis and reverts to the capabilities of the hardware and the level of correction desired.

5.1.3.1 Dynamic Range of Tilt and Wavefront Measurement

The maximum amount of full aperture tilt through the atmosphere (from space) that will appear on a tilt sensor is

$$\alpha_{\text{tilt}} = 2.2\left(\frac{D}{r_0}\right)^{5/6}\frac{\lambda}{D}M_{\text{tele}} \tag{5.16}$$

where D is the full telescope aperture diameter and M_{tele} is the magnification of the telescope. The tracking system should measure the tilt to half the tracking accuracy requirement; thus, the accuracy should be at least

$$\text{Accuracy} = 0.05\frac{\lambda}{D}M_{\text{tele}} \tag{5.17}$$

The wavefront should be measured to an accuracy of $\lambda/10$ to $\lambda/20$ with a maximum wavefront error dynamic range (DR) in a subaperture of

$$\mathrm{DR} = 5\left(\frac{r_s}{r_0}\right)^{5/6} \tag{5.18}$$

where the subaperture size is r_s.

5.2 Direct Wavefront Sensing—Modal

5.2.1 Importance of Wavefront Tilt

Wavefront tilt, classically called *distortion* [89], is a mode that is fundamental in zonal sensing schemes. As mentioned in Section 5.1.3, if the wavefront can be spatially divided and individual subaperture tilts (wavefront slopes) can be determined, then the entire wavefront across an aperture can be determined. Fitting a plane to the full aperture phase results in a value for the first Zernike term, the tilt term; thus, it is called Zernike tilt or *Z-tilt*. Averaging the tilts across multiple subapertures results in an average gradient of the wavefront; tilt of this type is called gradient tilt or *G-tilt*. Although some sensors more closely measure G-tilt and others measure Z-tilt, the difference in Strehl ratio calculation is less than 10%.

The control of beam tilt is important in itself in any adaptive optics system. In 1956, Babcock et al. showed [48] that tilt compensation alone can significantly improve an image. Modern adaptive optics systems have tilt control to stabilize the image or the propagated beam and improve the signal for low-order mode compensation. Olivier and Gavel [580] calculate that tilt correction is possible with natural stars on the 10-m Keck telescope.

Two methods are used to determine wavefront tilt. The interference of two beams creates an intensity that is proportional to the difference in phase between the beams. If those beams are small adjacent portions of the same beam, then the differential phase and the tilt in that region can be determined. Interference methods are discussed in Section 5.3.1.1.

Another method exploits the characteristic that wavefront tilt displaces a focused image in the direction of the tilt and at a distance proportional to amount of tilt [194]. For example, recall the expression for the intensity of light near the axis at diffraction focus, given in Equation 1.1 and repeated here:

$$I = \left(\frac{Aa}{\lambda R^2}\right)^2 \left| \int_0^1 \int_0^{2\pi} \exp\left[i\left(k\Phi - \frac{ka}{R} r\rho\cos(\theta - \psi) - \frac{1}{2} kz\left(\frac{a}{R}\right)^2 \rho^2 \right)\right] \rho\, d\rho\, d\theta \right|^2 \tag{5.19}$$

If the aberration consists of tilt in the x direction ($K\rho\sin\theta$) plus higher-order terms Φ', the exponent in the integral [89] can be written*

$$i\left[k\Phi' - \frac{ka}{R}r'\rho\cos(\theta - \psi') - \frac{1}{2}kz\left(\frac{a}{R}\right)^2\rho^2\right] \tag{5.20}$$

which is the same form as Equation 5.19. The image intensity distribution will be the same as the unshifted image with the same contributions from higher-order aberrations. The focus has not changed ($z = z'$), but the origin of the image plane has been shifted in a plane perpendicular to the direction of propagation by an amount $(R/a)K$. The shift, proportional to the magnitude of the tilt term, K, is the basis for measurement of the wavefront tilt. This principle is the basis for noninterferometric wavefront dividing methods and many full-aperture beam-tracking problems. The practical techniques rely on measuring the image position shift and extrapolating that to the wavefront G-tilt.

A simple geometric illustration shows this relationship. As shown in Figure 5.2, a beam enters an aperture of radius a, with a tilt K, the small angle formed between the beam direction (normal to the wavefront) and the plane of the aperture is K/a. The displacement after propagating a distance R to the image plane is simply $(R/a)K$.

The determination of the image shift is done in many ways. For an unaberrated (except tilt) beam passing through a circular aperture, the center of the image is the position of the maximum intensity as follows:

$$I \propto \frac{J_1^2(\upsilon)}{\upsilon^2} \tag{5.21}$$

where $\upsilon = kar/R$.

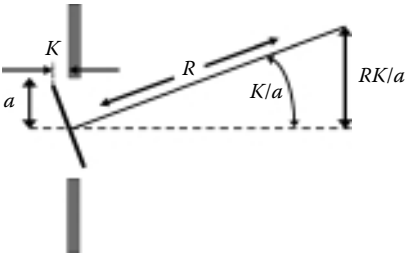

FIGURE 5.2
Displacement of the center of a beam due to wavefront tilt of magnitude K.

* The exponent $k\Phi' + kK\rho\sin\theta - (ka/R)r\rho\sin\psi\sin\theta - (ka/R)r\rho\cos\theta\cos\psi - (1/2)kz(a/R)^2\rho^2$ is transformed by making a linear displacement coordinate transformation in the image plane, $x' = x - (R/a)K$, $y' = y$, and $z' = z$, which is equivalent to $r'\sin\psi' = r\sin\psi - (R/a)K$ and $r'\cos\psi' = r\cos\psi$.

The position of the peak intensity is sensitive to tilt, and its absolute position is a function of all the aberrations. The centroid of the intensity distribution, however, is equal to the shifted origin of the image plane, which is proportional to the tilt.

The centroid is defined as the first moment of the pattern, and is given by

$$\bar{x} = \int\int I(x,y)x\,\mathrm{d}x\,\mathrm{d}y \Big/ \int\int I(x,y)\,\mathrm{d}x\,\mathrm{d}y \tag{5.22}$$

$$\bar{y} = \int\int I(x,y)y\,\mathrm{d}x\,\mathrm{d}y \Big/ \int\int I(x,y)\,\mathrm{d}x\,\mathrm{d}y \tag{5.23}$$

The limits of the integrals are $-\infty$ to $+\infty$. To illustrate the process, a Gaussian image distribution is assumed. It is offset by the values x_0, y_0. The centroid is calculated from Equations 5.22 and 5.23 as follows:

$$\bar{x} = \int\int x\mathrm{e}^{-[(x-x_0)^2+(y-y_0)^2]}\,\mathrm{d}x\,\mathrm{d}y \tag{5.24}$$

$$\bar{y} = \int\int y\mathrm{e}^{-[(x-x_0)^2+(y-y_0)^2]}\,\mathrm{d}x\,\mathrm{d}y \tag{5.25}$$

$$\bar{x} = x_0 \quad \bar{y} = y_0, \quad \text{Q.E.D.}$$

The centroid is equal to the offset, which is exactly what is required when determining wavefront tilt from the intensity distribution.

Summarizing, tilt will shift the position of the intensity centroid in the focal plane. Other aberrations change the shape of the pattern and position of the maximum, but do not shift the centroid. Axially symmetric aberrations change the shape, but do not alter the position of the maximum or the centroid.

As an example of the centroid's insensitivity to aberrations, consider the centroid of an intensity pattern that is subject only to coma. The intensity pattern is skewed in the direction of the comatic aberration. The field in the image plane was shown to be [89]

$$U(u,\upsilon,\psi) = C\left[U_0 + i\alpha_{\ln m}U_1 + (i\alpha_{\ln m})^2U_2 + (i\alpha_{\ln m})^3U_3 + \cdots\right]\cdot \tag{5.26}$$

$$= C\sum_{s=0}^{\infty}(i\alpha_{\ln m})^s U_s \tag{5.27}$$

The contributing fields U_n are

$$U_0 = 2\frac{J_1(\upsilon)}{\upsilon} \tag{5.28}$$

$$U_1 = i\cos\psi 2\frac{J_4(\upsilon)}{\upsilon} \tag{5.29}$$

$$U_2 = \frac{1}{2\upsilon}\left\{\frac{1}{4}J_1(\upsilon) - \frac{1}{20}J_3(\upsilon) + \frac{1}{4}J_5(\upsilon) - \frac{9}{20}J_7(\upsilon) - \cos 2\psi\left[\frac{2}{5}J_3(\upsilon) + \frac{3}{5}J_7(\upsilon)\right]\right\}$$

where $\upsilon = kar/R$ and $\alpha_{\ln m}$ are proportional to Zernike coefficients.

The resultant intensity pattern consists of products of Bessel functions

$$\begin{aligned} I(\upsilon,\psi) = \frac{c^2}{\upsilon^2}\Bigg\{&\left(4 - \frac{\alpha^2}{2}\right)J_1^2 + \left(\frac{\alpha^2 b_1^2}{4}\right)J_3^2 - (4\alpha^2\cos^2\psi)J_4^2 \\ &+ \left(\frac{\alpha^2}{64}\right)J_5^2 + \left(\frac{\alpha^2 b_2^2}{4}\right)J_7^2 + \left(\frac{15}{8}\alpha^2 b_1\right)J_1J_3 - \left(\frac{3}{8}\alpha^2\right)J_1J_5 \\ &+ \left(\frac{15}{8}\alpha^2 b_2\right)J_1J_7 - \left(\frac{\alpha^2 b_1}{8}\right)J_3J_5 - \left(\frac{\alpha^2 b_2}{8}\right)J_5J_7 + \left(\frac{\alpha^2 b_1 b_2}{2}\right)J_3J_7\Bigg\} \end{aligned} \tag{5.30}$$

where the subscript of α is 031 (coma), the argument of all Bessel functions is υ, and

$$b_1 = \frac{1}{20} + \frac{2}{5}\cos 2\psi \tag{5.31}$$

and

$$b_2 = \frac{9}{20} + 35\cos 2\psi \tag{5.32}$$

Without explicitly performing the centroid calculation, Equation 5.22, the integral takes the form

$$\bar{x} = \int xI(\upsilon,\psi)\upsilon\, d\upsilon\, d\psi \tag{5.33}$$

$$\bar{x} = \int_0^{\infty}\int_0^{2\pi} \upsilon\cos\psi\sum_{s=0}^{\infty} C_s\left[\frac{\cos^2\psi}{\upsilon^2}\right]J_n(\upsilon)J_m(\upsilon)\upsilon\, d\upsilon\, d\psi = 0 \tag{5.34}$$

which, when evaluated term by term, will be zero from the azimuthal integration, verifying the centroid's insensitivity to aberrations.

5.2.2 Measurement of Tilt

The actual physical measurement of the centroid can be done in many ways. Placing a detector behind a narrow slit and scanning the slit across the intensity pattern will produce a signal that is proportional to the intensity in a small region in the direction of the scan while integrating the intensity in the

orthogonal direction (Figure 5.3). Another method commonly used in image trackers as well as wavefront sensors is the quadcell. This device has four detectors that are closely spaced as illustrated in Figure 5.4. The intensity pattern is made to focus on these detectors. Using the notation from Figure 5.4, the difference signals

$$\bar{x} = \frac{\int_1 I\,dS + \int_4 I\,dS - \int_2 I\,dS - \int_3 I\,dS}{\sum_i \int_i I\,dS} \tag{5.35}$$

$$\bar{y} = \frac{\int_1 I\,dS + \int_2 I\,dS - \int_3 I\,dS - \int_3 I\,dS}{\sum_i \int_i I\,dS} \tag{5.36}$$

are proportional to the position of the centroid. This can be proven by solving the bicell integration problem using Gaussian quadrature.

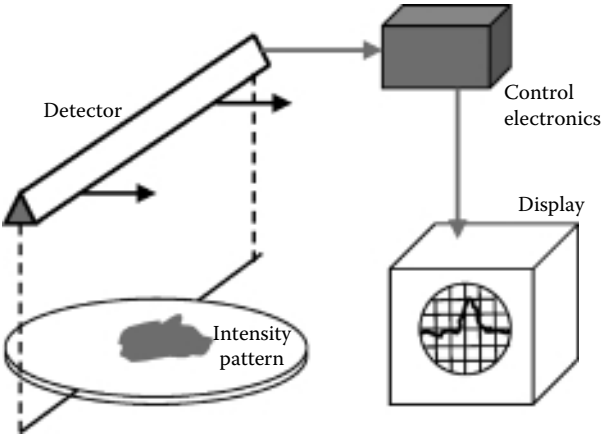

FIGURE 5.3
Illustration of temporal scanning of an intensity pattern with the resultant signal trace.

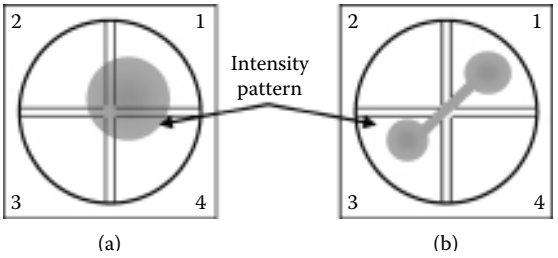

FIGURE 5.4
Quadcell geometries: (a) designation of the quadrants and (b) dumbbell-shaped image limitation.

Certain integrals can be approximated by their evaluation at the following two points [629]:

$$\int_{-a}^{a} x\, f(x) = a\left[\frac{-a}{\sqrt{3}} f\left(\frac{-a}{\sqrt{3}}\right) + \frac{a}{\sqrt{3}} f\left(\frac{a}{\sqrt{3}}\right)\right] \tag{5.37}$$

$$\int_{-a}^{a} f(x) = a\left[f\left(\frac{-a}{\sqrt{3}}\right) + f\left(\frac{a}{\sqrt{3}}\right)\right] \tag{5.38}$$

By this method, the quadcell can perform the integrations to determine the beam centroid

$$\bar{x} = \frac{\int_{-\infty}^{\infty} xI(x)\,\mathrm{d}x}{\int_{-\infty}^{\infty} I(x)\,\mathrm{d}x} \tag{5.39}$$

$$= \frac{a}{\sqrt{3}} \left\{ \frac{\left[I\left(\frac{a}{\sqrt{3}}\right) - I\left(\frac{-a}{\sqrt{3}}\right)\right]}{\left[I\left(\frac{a}{\sqrt{3}}\right) + I\left(\frac{-a}{\sqrt{3}}\right)\right]} \right\} \tag{5.40}$$

where $I\left(a/\sqrt{3}\right)$ is the evaluation of the intensity at the point $\left(a/\sqrt{3}\right)$. Although the quadcell actually integrates the energy on each quadrant, it is represented by a single point value.

The quadcell angular tracking error σ_{TE} is related to the voltage signal-to-noise ratio $(SNR)_v$,

$$\sigma = 0.6\frac{\lambda/D}{\mathrm{SNR}_v} \tag{5.41}$$

where the SNR is a function of signal electrons N_S, background electrons per pixel n_B, dark current electrons per pixel n_D, and read-noise electrons per pixel n_e:

$$\mathrm{SNR}_v = \frac{N_S}{\sqrt{N_S + 4\left(n_B + n_D + n_e^2\right)}} \tag{5.42}$$

State-of-the-art detectors have almost no background or dark current and can reach as low as 3 electrons per pixel read noise. Using these parameters [255], a minimum SNR of 2 is achieved with 14 electrons per pixel. To track 400 Hz, a 4-kHz signal is needed. Assuming 80% quantum efficiency and 20% optical transmission, about 3.5×10^5 photons are needed at the telescope. The astronomical brightness formula from Chapter 1 and the size of the telescope aperture can be used to calculate the minimum brightness object for sufficient tracking.

The quadcell integration method is restricted to images that deposit at least some energy in all four quadrants and have nearly uniform intensity distributions in the image plane. Quadrant detectors have limitations because of their geometry. For instance, a "dumbbell"-shaped distribution on a quadcell (Figure 5.4b) will cause a false centroid indication.

Resolved images on the quadcell can be used to determine wavefront tilt if errors due to the object shape and the SNR are not neglected. The error in the angular measurement of tilt for a circular object on a quadcell is given as [786]

$$\sigma_{qc} = \frac{\pi\left[\left(\frac{3}{16}\right)^2 + \left(\frac{n}{8}\right)^2\right]^{1/2} \frac{\lambda}{2a}}{\mathrm{SNR}_v} \tag{5.43}$$

where $n = (2ba)/(R\lambda)$, with b the object diameter, R the range, a the radius of the aperture, and SNR_v the voltage SNR. When the object is unresolvable, that is, b is small, R is large, and $n = 0$, the centroid measurement error is

$$\sigma_{qc} = \frac{\pi b}{8R(\mathrm{SNR}_v)} \tag{5.44}$$

and when the object is large, the other limit $(b\lambda/Ra) >> 3/16$, then the error is proportional to object size b,

$$\sigma_{qc} = \frac{\pi b(\lambda/a)^2}{32R(\mathrm{SNR}_v)} \tag{5.45}$$

Another method of determining the centroid of an intensity pattern uses only three detectors [13]. A mask that essentially performs the first-moment integration in real time covers each detector. Masks can have continuously variable transmission, like commercially available filters, or they can be photoetched-transmissive patterns like those in Figure 5.5. These masks may take any shape as long as the transmission function is proportional to the measurement along one axis. When two masks at orthogonal orientations are placed over separate detectors, and nothing (a "null mask") is placed over a third detector, the centroids in two orthogonal directions can be determined from the formulae

$$\bar{x} = \frac{I_{x\,\mathrm{det}}}{I_{\mathrm{tot}}} \tag{5.46}$$

$$\bar{y} = \frac{I_{y\,\mathrm{det}}}{I_{\mathrm{tot}}} \tag{5.47}$$

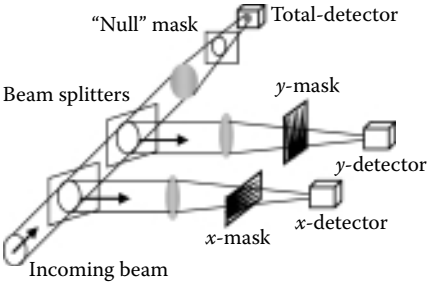

FIGURE 5.5
Application of opaque masks to perform centroid calculation.

With the advent of arrays of many small detectors, direct calculation of the centroid, Equation 5.22, is possible. Some investigators use either three- or five-point curve fitting to determine intensity maxima. The error associated with these measurements and algorithms was studied by Grossman and Emmons [311], who derived an expression for the error that is a function of detector geometry, the algorithm, the SNR, and array nonuniformity. Down [176] showed that the error is dependent upon noise and the pixel-to-spot size ratio.

Elbaum and Diament [193] derived similar expressions for the error of the centroid for rough and smooth extended targets. They found these variances to be functions of coherence, object size, optical resolution, and sensor integration time. Their equation for the standard deviation takes the form

$$\sigma_{\text{error}} = P\left[B^2 + \frac{A^2}{(\text{SNR})^2} + D^2\delta^2\right] \tag{5.48}$$

where P is the distance between detectors, B is algorithm error, A is sensor configuration error, D is algorithm nonuniformity error, and δ is the rms nonuniformity.

The quadcell lends itself quite readily to analog processing where electronic nulls are used. Some methods employing arrays use four or more adjacent cells to create a quadcell. Allen et al. [12] took advantage of the advances in digital information processing. Specific applications of these techniques will be explored in detail in Section 5.3.2, which describes individual wavefront sensors.

5.2.3 Focus Sensing

Sensing the focus of a beam directly is fundamental to any modal adaptive optics operation. As will be shown rigorously in Chapter 7, the focus (or defocus) can be constructed from zonal measurements across the aperture. The focus "aberration" is the most heavily weighted aberration when it comes to smearing an image. Defocus can be measured directly. A defocused image

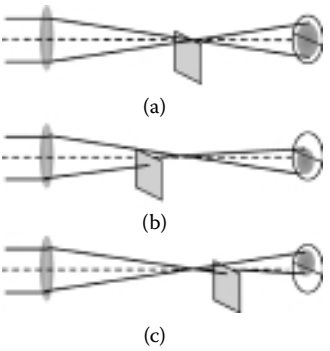

FIGURE 5.6
The Foucault knife-edge test for focus: (a) knife edge at focus: equal signals on bicell, (b) knife edge before focus: unequal signals, and (c) knife edge after focus: unequal signals, reversed polarity.

of a point object (the PSF) will have light spread out spatially more than the diffraction-limited PSF. The total intensity over a finite region will act as some measure of the defocusing.* The principle of image sharpening, widely applied in astronomy, uses this measurement.

Two interesting methods of measuring focus have been exploited in experimental systems. The Foucault *knife edge* test has been automated [419,420], and the measurement of focus using the characteristic speckle of coherent beams has been demonstrated [516]. Kocher [419] has shown how the blocking of half the beam near focus (Figure 5.6a) will affect the integrated intensities on the bicell, a pair of adjacent detectors. By calculating the intensity on each half of the bicell

$$X^+ = \frac{1}{2}\int\int_{x>0} I(x,y)\,dx\,dy - \int\int_{x>0} I(x,y)\frac{\partial\phi}{\partial x}dx\,dy \tag{5.49}$$

$$X^- = \frac{1}{2}\int\int_{x<0} I(x,y)\,dx\,dy - \int\int_{x<0} I(x,y)\frac{\partial\phi}{\partial x}dx\,dy$$

the difference

$$X^+ - X^- = -\int\int_{x>0} I(x,y)\frac{\partial\phi}{\partial x}dx\,dy + \int\iint_{x>0} I(x,y)\frac{\partial\phi}{\partial x}dx\,dy \tag{5.50}$$

is directly related to the distance between the knife edge and the focal plane. Kocher described the apparatus where the static knife edge is replaced by a rotating chopping wheel. A corresponding chopping wheel in the orthogonal direction, producing Y^+ and Y^- signals, is added. The intensities on each half

* The total intensity over an infinite region will be constant because of the conservation of energy.

of the bicell are translated into sinusoidal ac signals. The phase difference between the X^+ and X^- signals is proportional to the amount of focus (Figures 5.6b and 5.6c).

McLaughlin's [516] method uses the principle that laser speckle (the localized interference between portions of a coherent wave) will move in relation to the direction of the motion of the image plane or the source. If an observer, detector, or recording medium, such as film, moves and is inside of the focus, the speckle will move in the opposite direction from the observer. If the observer is outside of the focus, the speckle will move in the same direction as the observer (Figure 5.7). A linear expression relating the focal length change, Δr, the observation plane–speckle separation, s, the velocity of the speckle, υ_s, and the velocity of the observer near the focal plane, υ_f, is given as

$$\Delta r = \frac{s\upsilon_f K}{\upsilon_s} \tag{5.51}$$

where K is a proportionality constant evaluated at $K = 1.28$. The direction of motion is indicated by the difference in signs of υ_f and υ_s when the expression is evaluated. McLaughlin indicates that this method allows measurement of the position of the focal plane to within 0.02 of the Rayleigh limit.

5.2.4 Modal Sensing of Higher-Order Aberrations

It is generally impractical to measure higher-order aberration modes in a modal sense. The complexity of the higher-order diffraction phenomenon makes it difficult to separate the contributions from astigmatism or coma, for instance. However, recent progress with interferometric methods has been shown to work up to Zernike mode 21 [448]. The remainder of this chapter

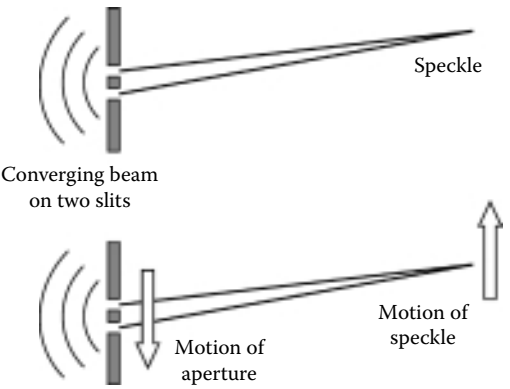

FIGURE 5.7
Observation of speckle.

will deal with the principles of wavefront sensing with spatially reduced fields, called *subaperture division*. These methods can be applied to all orders of aberrations.

5.3 Zonal Direct Wavefront Sensing

It is possible to reconstruct the wavefront of the entire field from the measurements of tilt in smaller regions. Wavefront division has various names; subaperture division and the Hartmann test are most common. By fitting a continuous curve to local tilted planes, a two-dimensional surface is generated. The tip and tilt of the local planes are measured using the methods of Section 5.2.2. The most common surface fitting methods are described in Section 7.4.

5.3.1 Interferometric Wavefront Sensing

Historically, the principle of optical interference has been used to prove that light has wavelike properties. Adaptive optics systems use this principle for more practical applications [424]. The methods of interferometry can be used to generate contours of the wavefront and also can be exploited to measure local wavefront tilts. A mathematical description of the interference process will be followed by a description of basic interferometric methods, electronic signal processing methods such as heterodyning, and then detailed descriptions of the most widely used interferometers for wavefront sensing.

Interference occurs when two or more coherent light beams are superimposed. The principle of interference was introduced in Section 1.3.4. If two linearly polarized transverse fields are superimposed, the magnitude of the sum of the two fields becomes

$$I = I_1 + I_2 + 2\sqrt{I_1 I_2}\cos\delta \tag{5.52}$$

For the case, $I_1 = I_2$, the intensity of the superimposed beams is

$$I = 4I_1 \cos^2\left(\frac{\delta}{2}\right) \tag{5.53}$$

with the maximum intensity $I_{max} = 4I_1$ and the minimum $I_{min} = 0$. While this method is straightforward for a single-phase measurement, the addition of integer multiples of 2π radians to δ results in a "2π ambiguity" of the measurement, essentially wrapping the phase back onto itself. In strong atmospheric turbulence, this ambiguity presents itself and must be unwrapped to avoid phase discontinuity [819].

5.3.1.1 Methods of Interference

There are two methods of interfering coherent beams. The method of *division of wavefront* makes use of the spatial coherence of the beam and interferes two, or more, spatially separated parts of the same beam. The method of *division of amplitude* interferes one part of the beam with itself after the beam is amplitude-divided.

Division of *wavefront* is interference by division of wavefront. This is the method that Young used to demonstrate the wave nature of light in 1803. Taking a plane wave that is generated by a point source at infinity, the wave passes through two slits separated by a distance d on an opaque screen (Figure 5.8). We wish to observe the intensity of light at points on a screen a distance a from the plane of the slits. The distance from slit 1 to the observation point is $\sqrt{a^2 + y^2 + (x - d/2)^2}$ and the distance from slit 2 is $\sqrt{a^2 + y^2 + (x + d/2)^2}$. The difference in the path is

$$\Delta s = s_2 - s_1 \approx \frac{2xd}{s_2 + s_1} \tag{5.54}$$

For small wavelengths like those for visible light, $d << a$ and

$$\Delta s = \frac{xd}{a} \tag{5.55}$$

The difference in OPD for this system in a medium of refractive index n is

$$\text{OPD} = n\Delta s = \frac{nxd}{a} \tag{5.56}$$

and the phase difference is

$$\delta = \frac{2\pi}{\lambda}\frac{nxd}{a} \tag{5.57}$$

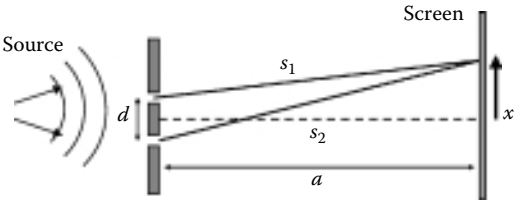

FIGURE 5.8
Young's double-slit experiment.

Maxima occur when the phase difference is an integral multiple of wavelengths, that is,

$$\cos^2\left(\frac{\delta}{2}\right)=1 \tag{5.58}$$

or

$$x=\frac{ma\lambda}{nd} \quad m=0,1,2,\ldots$$

Therefore, the positions on the screen (the interference plane) where maxima occur are

$$\frac{a\lambda}{nd},\frac{2a\lambda}{nd},\frac{3a\lambda}{nd},\ldots \tag{5.59}$$

and those where minima occur are

$$\frac{a\lambda}{2nd},\frac{3a\lambda}{2nd},\frac{5a\lambda}{2nd},\ldots \tag{5.60}$$

For the adaptive optics application, we need to measure the phase difference between one part of the beam (slit 1) and another part (slit 2). By observing the maxima, we can find that the phase difference is

$$\delta=\frac{2\pi}{\lambda}m\frac{nxd}{a} \tag{5.61}$$

and by counting the orders m from the central fringe and measuring the distance x, we can determine the OPD difference.

If the fringes are produced by light that is not purely monochromatic, the intensity of the pattern is the sum of the intensities of the composite monochromatic patterns. The maxima are spread out by

$$\Delta x=\frac{ma}{nd}\Delta\lambda \tag{5.62}$$

where the variation of the wavelength is $\Delta\lambda$.

One spinoff from this method of interference is the determination of the amount of coherence by observing the fringe visibility. The visibility V, or fringe contrast, is given by

$$V=\frac{I_{\max}-I_{\min}}{I_{\max}+I_{\min}} \tag{5.63}$$

For a purely monochromatic coherent beam, the result of Equation 5.53 is inserted into Equation 5.63 with the resulting visibility equal to unity. When

the fringes are spread out due to polychromaticity, the minima do not reach zero, and the visibility will always be less than one. For completely incoherent light, the fringes do not exist at all, and the visibility is zero. The fringe visibility can be used to determine the separation of sources at a long distance. A Michelson stellar interferometer is used to find the angular separation of two sources, θ, by simultaneously varying the aperture separation d while measuring the fringe visibility. The smallest value of the separation for which the fringe visibility is at a minimum is given by

$$d = \frac{A\lambda}{\theta} \tag{5.64}$$

where $A = .5$ for point sources and $A = 1.22$ for a single uniformly illuminated disk.

The division of wavefront method is used in a modified Young's double-slit experiment for an adaptive optics system. Van Workum et al. [809] scan an opaque screen with two small apertures (the double slit) across a beam (Figure 5.9). The interference term is a convolution of the intensity from infinitesimal slits, Equation 5.53, and the diffraction pattern of the apertures. For apertures of diameter D, Van Workum et al. show this function to be

$$I(x) = I_0 \left[\frac{2J_1(\alpha)^2}{\alpha} \right] \cos^2 \left(\frac{\pi dx}{\lambda f} \right) \tag{5.65}$$

where the Bessel function term is the aperture function (Airy pattern), $\alpha = \pi D/\lambda f$, and the cosine-squared term (the interference contribution) contains the aperture separation and focal length. As the apertures scan the wavefront, the slits will produce the fringe pattern on the detectors. The lateral position of the central fringe is directly proportional to the tilt (Figure 5.10). To determine the position of that central maximum, a chopper is placed at a focal plane. The relative position of the fringes on the square pattern of the chopper is decoded to determine the actual location of the fringe pattern, and thus the relative tilt of the beam. By rapidly scanning the apertures (10 μsec per element), and

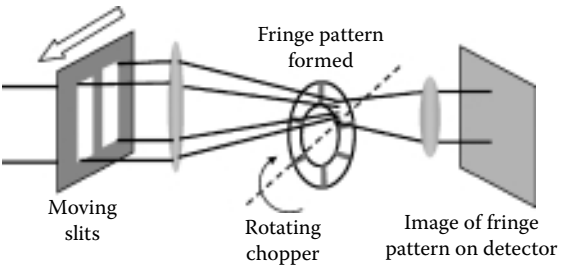

FIGURE 5.9
Wavefront sensor based on Young's experiment.

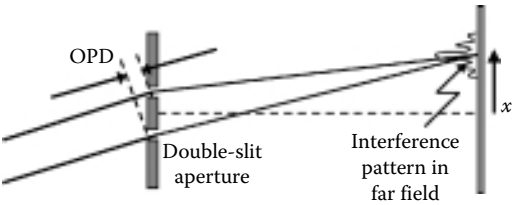

FIGURE 5.10
Position of the fringes is proportional to the wavefront tilt.

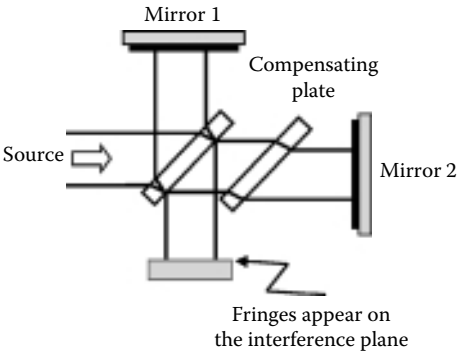

FIGURE 5.11
Michelson interferometer.

rapidly chopping the fringe pattern (1 MHz), a high-bandwidth, high- accuracy (focus changes measured to ±0.5%) wavefront sensor was demonstrated.

In division of amplitude, a beam is split so that part of its amplitude traverses one path and part of its amplitude traverses another path; when the two beams are superimposed, the difference in the paths will produce interference fringes. A simple form of amplitude division, used in a Michelson interferometer, is performed with a transmissive beam splitter.

In the Michelson interferometer, illustrated in Figure 5.11, a source from the left is partially reflected from the back surface of the beam splitter. That portion (beam 1) travels and reflects off mirror 1, and part of it is transmitted through the beam splitter onto the interference plane. The part of the beam that is transmitted through the beam splitter (beam 2) is reflected off mirror 2 and returns to the beam splitter to be reflected off the surface toward the interference plane. The compensating plate is placed in beam 2 to equalize the number of times (3) each beam passes through a transmissive element. The intensity at any point in the interference pattern is expressed by the interference equation, given in Equation 5.52,

$$I = I_1 + I_2 + 2\sqrt{I_1 I_2}\cos\delta \tag{5.66}$$

The reason for using the interferometer is manifested in the equation. If the phase δ is retarded by any manner, tilts of the elements, for instance, or the insertion of an aberrating medium, the intensity of the fringes is a direct response to that change. The use of a collimated source in a Michelson interferometer is the basis of the Twyman–Green interferometer [774]. Figure 5.12 shows the Twyman–Green interferometer in two configurations. Figure 5.12a shows a method of measuring the aberrations due to a nonflat reflective surface. Figure 5.12b shows the Twyman–Green interferometer used for measuring the aberrations of a transmissive medium.

From Figure 5.12b, one can see a disadvantage of using a Twyman–Green interferometer for transmissive test objects. The test beam must pass through the test object twice, thereby complicating alignment and data reduction. One solution to this problem is the use of a Mach–Zehnder interferometer [492,896], which allows the paths to be separated by relatively large distances (see Figure 5.13). Figure 5.14 shows a Mach–Zehnder interferometer with a

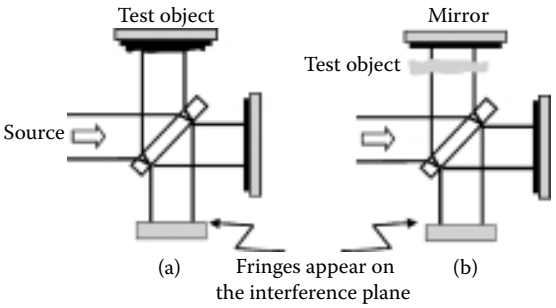

FIGURE 5.12
Twyman–Green interferometers: (a) method for measuring aberrations due to nonflat reflective surface and (b) Twyman–Green interferometer for measuring aberrations of a transmissive medium.

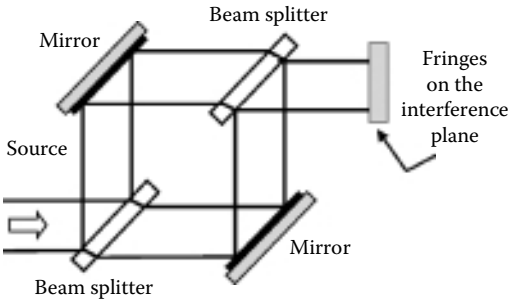

FIGURE 5.13
Mach–Zehnder interferometer.

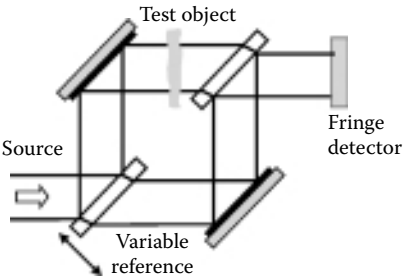

FIGURE 5.14
Real-time sensor using the Mach–Zehnder configuration.

transmissive test object. Note that the beam only passes through the test object once in the interferometer. As in other interferometers, a bright fringe will occur at the points of constructive interference, that is, when the OPD difference between the two beams at any point on the interference plane is an integral number of wavelengths (OPD = $m\lambda$, $m = 0, 1, 2, \ldots$).

The Mach–Zehnder interferometer has been used for many years for optical testing. Real-time uses of it include a system whereby a number of independent measurements of intensity are taken with the reference leg of the Mach–Zehnder having various known phase retardations. This "phase shifting" arrangement [230] is shown as the variable reference in Figure 5.14. The data beam field passing through the test object is

$$G(x,y) = |G(x,y)|\exp[i\theta(x,y)] \tag{5.67}$$

while the reference beam field passing through the retardation plate is

$$H(x,y) = K\exp[i(\phi_0 + \phi)] \tag{5.68}$$

where ϕ_0 is the different path OPD and ϕ is the retardation plate OPD. The intensity is the magnitude of the sum of these two fields, given by

$$I(\phi) = |G|^2 + K^2 + 2K|G|\cos(\theta - \phi_0 - \phi) \tag{5.69}$$

If three separate measurements (a "three-bin" approach) are made with retardation plates with phase shifts equal to 0, π, and $\pi/2$, the three intensities will be

$$\begin{aligned} I(0) &= |G|^2 + K^2 + 2K|G|\cos(\theta - \phi_0) \\ I(\pi) &= |G|^2 + K^2 - 2K|G|\cos(\theta - \phi\phi) \\ I(\pi/2) &= |G|^2 + K^2 + 2K|G|\sin(\theta - \phi_0) \end{aligned} \tag{5.70}$$

Combining the expressions in Equation 5.70, the phase of the data beam can be found from

$$\theta - \phi_0 = \arctan\left[2\frac{I\left(\frac{\pi}{2}\right) - \frac{1}{2}I(0) - \frac{1}{2}I(\pi)}{I(0) - I(\pi)} \right] \tag{5.71}$$

and the magnitude is

$$K|G| = \left\{ \frac{1}{16}[I(0) - I(\pi)]^2 + \frac{1}{4}\left[I\left(\frac{\pi}{2}\right) - \frac{1}{2}I(0) - \frac{1}{2}I(\pi) \right]^2 \right\}^{1/2} \tag{5.72}$$

The quadrant of the phase is determined by the signs of the real and imaginary parts of $K|G| \exp[-(\theta - \phi_0)]$.

If this process is performed as stated, three distinct measurements, with interim replacement of the phase retardation plates, are required. A variation of this method that allows real-time operation employs a shutter in both beam trains and a single $\lambda/2$ retardation plate in the reference beam.

As before, the intensities of the beams with the appropriate retardations are

$$I(0) = |G|^2 + K^2 + 2K|G|\cos(\theta - \phi_0) \tag{5.73}$$

$$I\left(\frac{\pi}{2}\right) = |G|^2 + K^2 + 2K|G|\sin(\theta - \phi_0) \tag{5.74}$$

By blocking the reference beam, that is, $K = 0$, the intensity on the detectors is

$$I_D = |G|^2 \tag{5.75}$$

and similarly, by blocking the data beam, that is, $G = 0$, the reference intensity is

$$I_R = K^2 \tag{5.76}$$

By combining the detector signals from these four conditions, the phase can be found from

$$\theta - \phi_0 = \arctan\left[\frac{I(\pi/2) - I_D - I_R}{I(0) - I_D - I_R} \right] \tag{5.77}$$

and the magnitude of the data beam is I_D^2. If the beam and the reference intensity are not coaxial, polarization techniques can be used to remove non-common path errors [554].

The interferometer system described by Frantz et al. [233] possesses the limitation that it cannot be used for an intermittent beam, since it is dependent upon temporally chopping the beam. A system that can be used with a pulsed beam is a modified Mach–Zehnder interferometer that is split twice rather than just once [56]. The interferometer, shown in Figure 5.15, will have intensity signals at each point in the beam according to

$$\begin{aligned} I_A &= I_1 - I_2 \cos\delta \\ I_B &= I_1 + I_2 \sin\delta \\ I_C &= I_1 + I_2 \cos\delta \end{aligned} \tag{5.78}$$

With the quarter-wave retardation plates, the phase can be reconstructed in real time from the intensity measurements as follows:

$$\delta = \frac{I_A - I_B}{I_C - I_B} \tag{5.79}$$

and the accuracy is only limited by the temporal and spatial response of the optical detectors. Compensation for nonsinusoidal waveforms has been demonstrated with an iterative algorithm [596].

In Twyman–Green or Mach–Zehnder interferometers, it is assumed that a plane wave reference beam is available and the test objects can be placed in a beam. In some cases of wavefront sensing, the beam itself, with no reference, is to be tested. Self-referencing interferometers, such as the Smartt point-diffraction interferometer [573,730], use a spatially filtered sample of the object beam itself for the reference. The spatial filtering, either by a transmissive pinhole (Figure 5.16a) or by a reflective pinhole (Figure 5.16b), creates an essentially unaberrated reference. This reference interferes with the object beam to create the interference pattern used in the analysis [49,803,55].

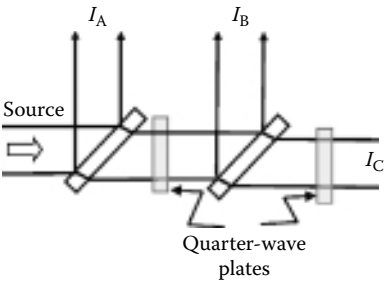

FIGURE 5.15
Double-split beam Mach–Zehnder interferometer.

5.3.1.2 Principle of a Shearing Interferometer

A fundamental modification to the Mach–Zehnder interferometer was introduced by Bates [66]. By tilting the mirrors of a Mach–Zehnder a small amount about their optic axis, the two beams that form the interference fringes do not totally overlap as shown in Figure 5.17. Their centers are separated by a distance s, called the shear distance. The pattern of fringes appears in the area of overlap; see Figure 5.18. The orders of the fringes are displaced by an amount proportional to the shear, Δm, which can be used to measure the differential OPD at any point in the beam and is given by

$$\Delta m \approx \frac{s}{\lambda}\frac{\mathrm{d}}{\mathrm{d}x}[\mathrm{OPD}(x)] \tag{5.80}$$

A simple one-dimensional analysis can show how the shearing interferometer produces an interference pattern that is proportional to the slope of the wavefront. Consider, first, the pattern produced by the interference of a wavefront $\Phi(x)$

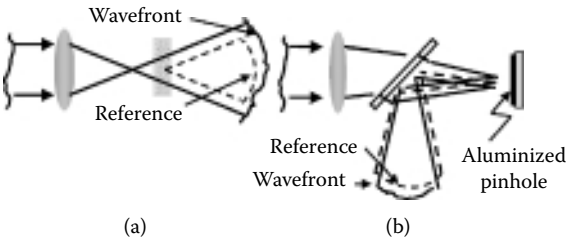

FIGURE 5.16
Smartt point-diffraction interferometer: (a) spatial filtering by transmissive pinhole and (b) spatial filtering by reflective pinhole.

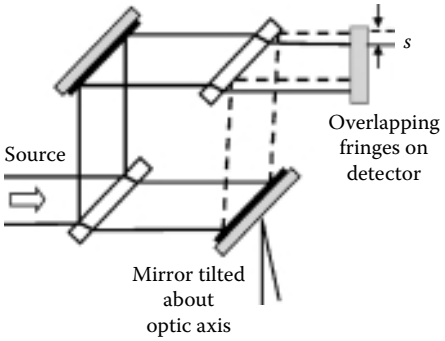

FIGURE 5.17
Example of a shearing interferometer.

in Figure 5.19a and a plane wave ($\Phi'(x) = 0$). The resultant interference pattern is proportional to the difference in phase and is given by

$$I = \Phi(x) - \Phi'(x) = \Phi(x) \tag{5.81}$$

If the wavefront is shifted in the x direction (sheared), the two wavefronts, $\Phi(x)$ and $\Phi(x - s)$, are interfered (Figure 5.19b) with the resultant pattern being the difference, given by

$$I = \Phi(x - s) - \Phi(x) \tag{5.82}$$

If the interference pattern is normalized by the shear distance s, the pattern can be represented by

$$I = \frac{[\Phi(x - s) - \Phi(x)]}{s} \tag{5.83}$$

If the shear distance is reduced, as shown in Figure 5.19c, the interference pattern then closely represents the slope of the wavefront, $d\Phi(x)/dx$. By taking the limit of Equation 5.83 as $s \to 0$ (Figure 5.19d), we have precisely the definition of "the derivative of a function," that is, $d\Phi/dx$. Thus, the interference

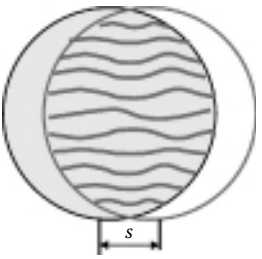

FIGURE 5.18
Overlap fringes in a shearing interferometer.

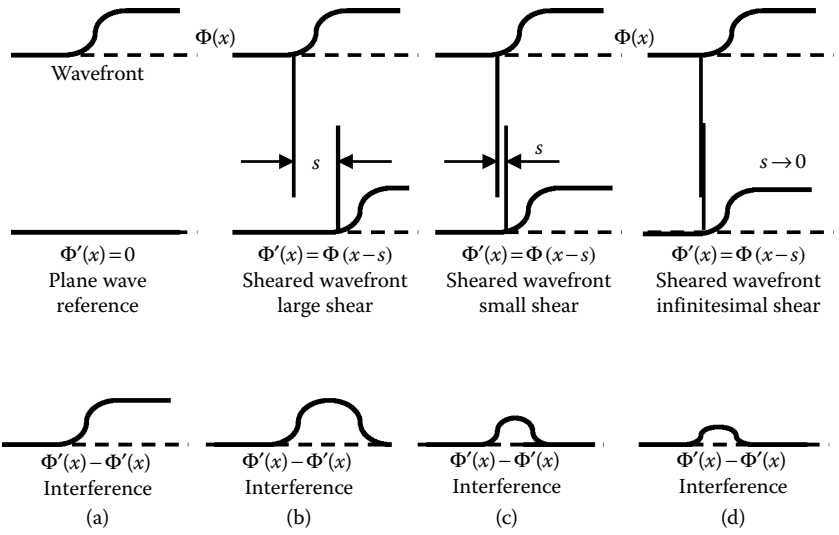

FIGURE 5.19
One-dimensional illustration of the principle of wavefront shearing: (a) interference with plane reference, (b) interference of two wavefronts with a large shear, (c) interference of two wavefronts with a small shear, and (d) interference of two wavefronts with a shear approaching zero.

pattern of a shearing interferometer is precisely the wavefront slope in the limit of small shear distances.

5.3.1.3 Practical Operation of a Shearing Interferometer

Shearing a wavefront makes use of the principle of self-referencing, that is, an interferogram can be produced without the need for a separate plane wave reference. The resultant interferogram of two sheared wavefronts becomes a map of regions of constant slope of the wavefront [355,396,689]. This is in contrast to the interferogram made between a wavefront and a plane wave, which results in a contour map of the wavefront, rather than the slope. The advantages of this form of measurement will be addressed in detail in the discussion of wavefront reconstruction in Chapter 7. Besides self-referencing, the advantage of shearing is the ability to distinguish "bumps" from "holes" in the wavefront. The sign of the slope is a direct realization of the "polarity" of the wavefront [439].

If a grating with spatial frequency ν is used to shear the wavefront, the wavefront slope can be extracted from the sinusoidal pattern of fringes in the interference plane. When there are four detectors (bins) across each sinusoidal fringe, and the intensities in the successive bins are I_1, I_2, I_3, and I_4, the phase angle ϕ is recovered by the four-bin algorithm,

$$\tan\phi = \frac{I_1 - I_3}{I_2 - I_4} \tag{5.84}$$

The wavefront slope is $d\phi/dx = \phi/s$ where the shear distance is $s = 2\lambda z\nu$. The displacement of the grating from the image plane is z.

5.3.1.4 Lateral Shearing Interferometers

The process of *producing* the shear is the topic of many engineering papers. Lateral shearing interferometers are categorized by the method of producing the shear and the type of modulation.* A dual-frequency grating shearing interferometer uses a Ronchi (square-wave) grating that diffracts the incoming light that is focused onto the grating. The multiple orders are interfered. By using a dual-frequency grating [885], the diffraction orders produced by the higher-order harmonics are outside the field of view and two low orders can be used. Referring to Figure 5.20, the beam containing the unknown wavefront is focused onto a grating that has two different line spacings,

* In all cases of lateral shearing interferometers, there is a duplicate shear in the orthogonal direction to gain wavefront information in that orientation. For clarity, the descriptions given here are limited to the x-shear direction and are simply duplicated for the y-shear direction by replacing x with y in the mathematics.

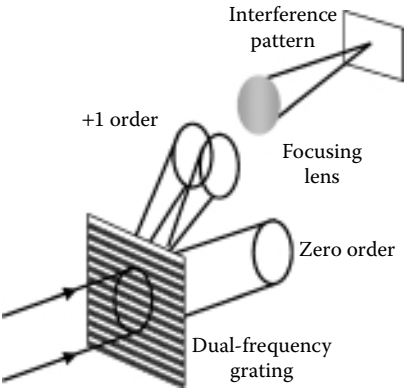

FIGURE 5.20
Dual-frequency grating shearing interferometer.

d_1 and d_2, at spatial frequencies ν_1 and ν_2. The only condition that must be met is that the lower spatial frequency, ν_1, must be

$$\nu_1 = \frac{1}{d_1} > \frac{1}{\lambda(\text{F number})} \tag{5.85}$$

The first-order diffracted beams follow the grating equation, which is

$$\sin\theta = \frac{\lambda}{d} \tag{5.86}$$

The shear between the two beams is then

$$\Delta\theta = \lambda(\nu_2 - \nu_1) \tag{5.87}$$

To detect the interference pattern, an array of detectors is placed in the interference plane. The method of ac heterodyning is used here. By translating the grating along its optical axis at a velocity υ, a Doppler shift occurs, which modulates the phase. The frequency of the Doppler shift is

$$\omega = 2\pi\upsilon(\nu_2 - \nu_1) \tag{5.88}$$

which causes the signal on each of the detectors to have a sinusoidal pattern proportional to

$$\sin[\omega t + \phi(x, y)] \tag{5.89}$$

The time t' when the signal passes through zero can be electronically detected. By substituting Equation 5.88 into Equation 5.89, we can find the phase of the fringe pattern as follows:

$$\phi(x, y) = \pi - \omega t' \tag{5.90}$$

which, as noted earlier, is proportional to the slope of the wavefront at (x, y).

Since interference only occurs between coherent beams, the shearing interferometer described earlier is limited to a single wavelength. Since many wavefronts are multiwavelength, the fringe pattern generated by these would become washed out. Errors associated with lateral shearing interferometers are described by Dente et al. [170]. Incoherent beams, or an extended source, affect the contrast of the interference pattern (Equation 5.102). Wyant [882] proposed a modification to the dual-frequency shearing interferometer that allowed its use in white light. By Equation 5.87, the shear between the two beams is proportional to the wavelength, and the phase is proportional to $2\pi/\lambda$; therefore, the fringe spacing is independent of wavelength. To make the absolute fringe position also independent of wavelength, a grating is placed between the first dual-frequency grating and the interference plane. If the angle of incidence to the first grating is θ, the angles of incidence leaving the dual-frequency grating are $\theta_1 - \theta = \lambda\nu_1$ and $\theta_2 - \theta = \lambda\nu_2$.

If the additional grating has a spatial frequency $(\nu_1 + \nu_2)/2$, the angles associated with the second grating are

$$\theta_1 - \theta_3 = \frac{\lambda(\nu_1 + \nu_2)}{2} \tag{5.91}$$

$$\theta_2 - \theta_4 = \frac{\lambda(\nu_1 + \nu_2)}{2} \tag{5.92}$$

and the angular deviation between the incident beam θ and the final beam is

$$\Delta_1 = \frac{\lambda(\nu_2 - \nu_1)}{2} \tag{5.93}$$

and

$$\Delta_2 = \frac{\lambda(\nu_1 - \nu_2)}{2} = -\Delta_1 \tag{5.94}$$

For a focal distance of f, the phase of the two beams on the interference plane will be $\phi_1(x - f\Delta, y)$ and $\phi_2(x + f\Delta, y)$. When these two beams interfere, a bright fringe will occur at $\phi_1 - \phi_2 = m\lambda$. By expanding the phase terms, the resultant expression for the pattern of bright fringes is

$$m\lambda = 2f\Delta\left[\frac{\partial\phi}{\partial x} + \frac{f^2\Delta^2}{3!}\frac{\partial^3\phi}{\partial x} + \frac{f^4\Delta^4}{5!}\frac{\partial^5\phi}{\partial x}\right] \tag{5.95}$$

which is the locus of points of equal wavefront slope even in the presence of white light.

Not all lateral shearing interferometers interfere two beams of the first diffracted order like the one just described [40]. One method [107] uses only one grating with a single frequency to diffract the beam. The two opposing first orders, ±1, are interfered. Although the result is the same, the description of the optical process can illustrate the general principle of shearing interferometers. Beams can be separated by polarization. A birefringent prism will produce separate orthogonally polarized beams. The interference is produced by using an analyzer oriented at 45° [326].

Figure 5.21 shows a lateral ac shearing interferometer with a rotating grating. The chopping frequency, at 6–10 times the control bandwidth, is used in the heterodyne modulation process to eliminate the need for detector calibration. With a focusing lens at the correct position, the wavefront $\Phi(x, y)$ that enters the system is Fourier transformed to $\tilde{W}(\nu, \eta)$ at the grating plane. The transmission of the grating, $G(x, y)$, is multiplied by the field at the grating plane and inverse Fourier transformed by the second lens. The resulting field on the detector plane is the convolution of the wavefront with the Fourier transform of the grating function, given by

$$U = \Phi(x, y) * \tilde{G}(\nu, \eta) \tag{5.96}$$

The periodic grating of period d is rotating at a velocity υ. In one dimension, the transform of this grating function is

$$\tilde{G}(x_0) = \int_{-\infty}^{\infty} (x_f - \upsilon t) \exp\left(-i \frac{k}{f} x_0 x_f\right) dx_f \tag{5.97}$$

where f is the focal length of the lenses, x_0 is in the input plane, and x_f is in the focal plane. For the periodic grating, this reduces to

$$\tilde{G}(x_0) = \exp\left[-i \frac{k}{f} x_0 \upsilon t\right] \sum_{n=-\infty}^{\infty} G_n \delta\left(\frac{x_0}{\lambda f} - \frac{n}{d}\right) \tag{5.98}$$

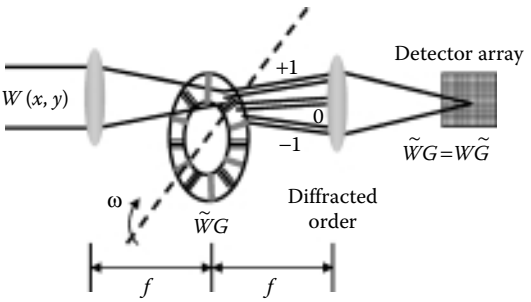

FIGURE 5.21
Rotating grating shearing interferometer.

where the Fourier coefficients are given by

$$G_n = \frac{1}{d}\int_{-d/2}^{d/2} \tilde{G}(\xi)\exp\left[-i\frac{2\pi}{d}n\xi\right]\mathrm{d}\xi \tag{5.99}$$

with the result for the sinusoidal grating given by

$$G = \begin{cases} 1 & n = 0, \\ \pm\dfrac{1}{2}i & n = 1, \\ 0 & \text{otherwise.} \end{cases} \tag{5.100}$$

The shear distance is $s = \lambda f/d$, and the wavefront entering the interferometer is

$$\Phi(x) = (\Upsilon I_t)^{1/2}\, e^{i\phi(x)} \tag{5.101}$$

where Υ is the degree of coherence ($\Upsilon = 1$ for a point source). From the van Cittert–Zernike theorem [86], for a target and aperture much smaller than the propagation distance z, the degree of coherence is

$$\Upsilon(s_x, s_y) = \frac{\left|\int\int I_t(\xi,\eta)\exp\left[-i\dfrac{k}{z}(\xi s_x + \eta s_y)\right]\mathrm{d}\xi\,\mathrm{d}\eta\right|}{\left|\int\int I_t(\xi,\eta)\,\mathrm{d}\xi\,\mathrm{d}\eta\right|} \tag{5.102}$$

where s_x and s_y are the x- and y-shears. By adjusting the grating period, so that half a cycle equals the object size, the lateral shearing interferometer can use an extended object as its source.

Equation 5.102 can be solved for specific cases: for a square target of side $2a$, angular size $L = (2a)/z$, we have

$$\Upsilon_{sq} = \left|\frac{\sin(2\pi Ls/\lambda)}{(2\pi Ls/\lambda)}\right| \tag{5.103}$$

or for a circular target of angular size L = diameter/z, the coherence is

$$\Upsilon_{circ} = \left|\frac{2J_1(2\pi Ls/\lambda)}{(2\pi Ls/\lambda)}\right| \tag{5.104}$$

The signal on the sensors is the convolution, given by

$$U = \Phi * \tilde{G} \tag{5.105}$$

$$(\Upsilon I_t)^{1/2}\, e^{i*}\left[G_{-1}\delta(x+s)\, e^{i\omega t} + G_0\delta(x) + G_{+1}\delta(x-s)\, e^{-i\omega t}\right] \tag{5.106}$$

or

$$U = (\Upsilon I_t)^{1/2}\left[G_{-1}\, e^{i[\phi(x+s)+\omega t]} + G_0\, e^{i\phi(x)} + G_{+1}\, e^{i[\phi(x-s)+\omega t]}\right] \tag{5.107}$$

The intensity on the detectors is the magnitude of the field squared and is given by

$$I(x,y) = |U|^2 \tag{5.108}$$

At this point, two options are available. Applying Equation 5.108 to the field of Equation 5.106 results in terms containing dc (zero temporal dependence), $1\omega t$, or $2\omega t$. If the signals are band-pass-filtered at frequency 1ω, the zero and first-order terms are processed and the result is

$$I(x,y) = 4G_0G_1\Upsilon I_t \cos\left[\frac{\phi(x+s)-\phi(x-s)}{2} + \omega t\right] \tag{5.109}$$

If the band-pass filter is set at $2\omega t$, the two opposing first-order terms are interfered and the resultant intensity is

$$I(x,y) = 2G_1^2\Upsilon I_t \cos[\phi(x+s)-\phi(x-s)+2\omega t] \tag{5.110}$$

In either case, the intensity is a sinusoidal function of wavefront slope, given by

$$\phi(x+s)-\phi(x-s) \tag{5.111}$$

and that slope can be determined. Each channel can have four detectors or, with time or frequency multiplexing, the interferometer will operate with one sensor per channel. A review of multiplexing and signal-processing techniques for shearing interferometers is given by Horwitz [355]. Since the shear is proportional to the wavelength, this interferometer can be used with broadband sources. Because of the temporal modulation, the ac shearing interferometer is best used with a continuous light source [326].

5.3.1.5 Rotation and Radial Shear Interferometers

Shearing interferometers are not limited to lateral shearing. *Rotational wavefront shearing* was introduced in 1965 by Armitage and Lohmann [31]. By rotating one beam 180°, the orthogonal component of radial shear (the tangential component) is measured. Rotational shearing interferometers have been developed [95,658] for turbulence-degraded wavefront measurement.

The most common shear variation is the *radial shear interferometer* [439]. In this type of wavefront sensor, the beams are separated and magnified by different values. When the beams are superimposed, with their axes coinciding, interference occurs at the area of overlap, within the diameter of the smaller beam. When the wavefront contains only radial aberrations, such as spherical aberration, radial shearing is very useful. One variation, which uses only the small central portion of the wavefront and magnifies it to the full aperture, generates a constant phase reference. The interference pattern then represents the phase rather than the slope. Because of the large attenuation by using only a small portion of the wavefront (similar to the point–diffraction interferometer), it is not very useful for low-light-level applications.

Figure 5.22 shows a system that uses radial shearing and another method of phase retrieval, *multiple interferometer multiplexing*, which Kwon [439] called "three-bucket phase-shifting interferometry." This method does not use modulation like that needed in heterodyning; rather, it compares multiple interference patterns that represent the same wavefront slopes similar to techniques described for direct wavefront retrieval.

In this interferometer, three orders, –1, 0, and +1, are separated. The ±1 orders are phase-shifted ±90°. The six beams are centered into three sheared pairs. The radial shear distance s is the ratio of beam diameters (magnifications)

$$0 < [s = f_r / f_R] < 1 \tag{5.112}$$

To satisfy the grating equation $\sin\theta = \nu\lambda$, the focal lengths of the afocal telescopes are related to the grating frequencies by

$$\nu_R f_R = \nu_r f_r \tag{5.113}$$

The phase slopes are retrieved from the three sets of signals through the use of Equation 5.70.

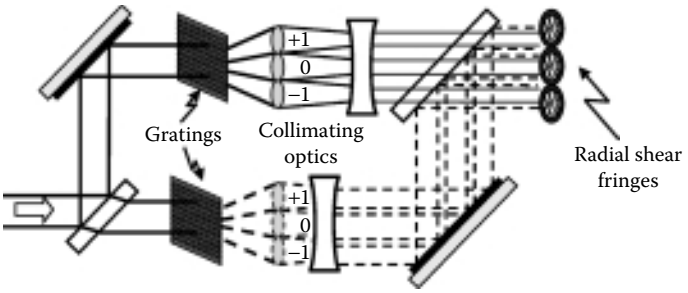

FIGURE 5.22
Radial shearing interferometer.

5.3.2 Shack–Hartmann Wavefront Sensors

One method for testing a lens or mirror employs an opaque mask with holes placed behind the optical element under test. Each of the holes acts as an aperture, and since the light passing through the lens is converging, the image produced is an array of spots. With proper calibration, the position of the spots is a direct indication of the local wavefront tilt at each hole, and thus is a description of the lens quality. This test is called the *Hartmann test* [332,333].

Variations of this technique, especially for real-time wavefront measurement, are used in adaptive optics wavefront sensors. Shack placed lenses in the holes, which increased the light-gathering efficiency of the mask and, with the spots focused, reduced the disturbing diffraction effects of the holes. A lens array for this purpose was first manufactured in 1971 [711]. Members of the astronomy community began to use this sensor in the late 1970s for testing of large telescope optics. Some astronomers use the term Hartmann–Shack (or Shack–Hartmann) wavefront sensor, but many shorten it to simply *Hartmann sensor*. The measurement of the tilt and how it relates to the position of the focused spots was addressed in Section 5.2.2. A description of some of the real-time techniques will show some of the diversity, advantages, and limitations of these noninterferometric methods.

The Hartmann wavefront sensor is shown in Figure 5.23. The wavefront is divided by a mask, as in the classical test, an array of gratings, or an array of transmissive lenses. Each of the beams in the subapertures is focused onto a detector. To detect the position of the spot, various forms of modulation, detector geometry, and electro-optical processing are used. For atmospheric turbulence compensation, the local wavefront tilt must be measured accurately in each subaperture of size r_0. To do this, the subaperture must be large enough to resolve the isoplanatic patch. During high turbulence, r_0 is small and anisoplanatism degrades the process. Hardy [318] discusses details of this large-versus-small subaperture trade for various optical and atmospheric parameters.

A Hartmann sensor is composed of an array of lenses for wavefront division and typically a CCD array with multiple pixels used for spot position (wavefront tilt) determination. The physical construction of lens arrays is a

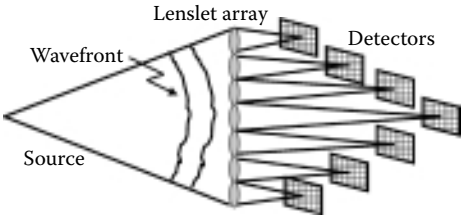

FIGURE 5.23
Hartmann wavefront sensing technique.

major area for advanced engineering development. One must achieve high alignment accuracy of the array along with the required high optical quality. Many of these processes are proprietary to manufacturers, but some techniques have been described in the open literature on the subject [34,42,310,626]. Techniques for designing and manufacturing lens arrays progress swiftly [160], and commercially available custom or catalog lens arrays are available from various sources [90,380,528,586,771].

A number of investigators have demonstrated Hartmann sensor modifications that can be used to overcome the drawbacks [678]. These can be done while maintaining the advantages of the Hartmann technique, that is, wide dynamic range [624], high optical efficiency, white light capability, no 2π ambiguity [906], the ability to use continuous or pulsed sources, and detection of phase singularities [129].

If there is no expected channel-to-channel error, but only global misalignment, from bench vibration, for instance, one channel can be chosen as a reference and all measurements can be made in relation to the position of the spot in that channel.

One method for removing alignment errors is the introduction of a reference beam. This beam should be a plane wave. It does not have to be the same wavelength as the unknown wavefront beam, since no interference is needed or desired. As shown in Figures 5.24 and 5.25, the reference must be distinctive so that the detector-processing electronics can discriminate between the signal beam and the reference beam.

A number of other methods have been used to enhance specific aspects of Hartmann sensors [91,483,585]. Optical binning [63] and optical amplification with an image intensifier [875] or rotating the square quadcells with

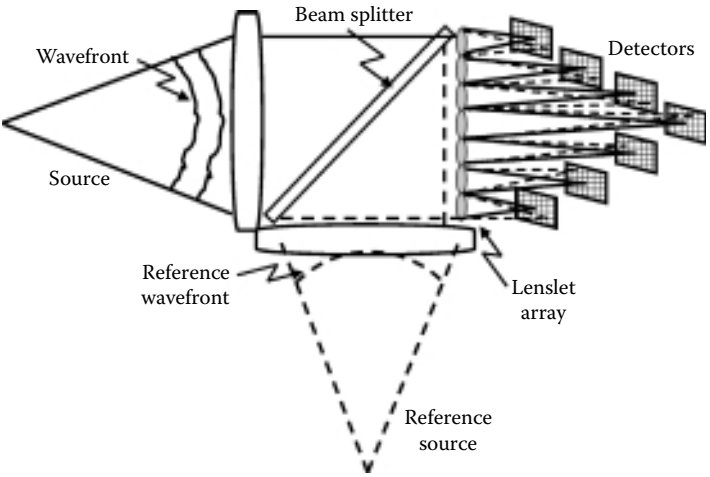

FIGURE 5.24
Hartmann sensor with reference.

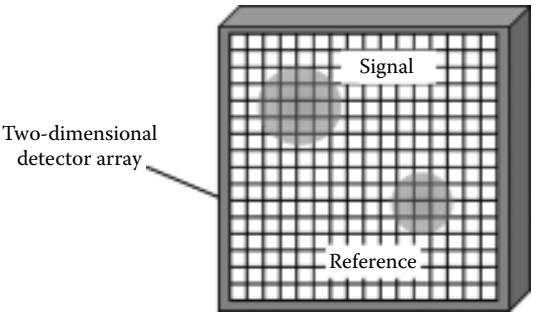

FIGURE 5.25
Hartmann spots on a 5×5 pixel region of a detector array.

respect to square subapertures eliminates the situation where zeros in the intensity pattern fall on the gaps between cells and introduce error. Each sensor must provide enough subapertures to resolve the high-frequency aberrations. For turbulence compensation, the subapertures cannot be too small, since each subaperture must resolve the isoplanatic patch. If the subapertures are too large, however, they can possibly resolve the source of the wavefront. Adjustable pupil sampling has been demonstrated [51]. If that source is an extended object, the shape of the object is convolved with the subaperture diffraction pattern on the quadcell. Intensity variation can seriously degrade the measurement accuracy of the centroid. To remove the effects of extended objects resolved by the subaperture, an optical correlation can be used. Von der Luhe [829] suggested the use of an addressable optical mask, whose transmission is derived from the image of the reference scene. The Hartmann detector array records a cross-correlation of the mask and the scene in each subaperture. Even if the object remains unresolved, the problems associated with subaperture higher-order aberrations will distort the pattern on the quadcell and decrease tilt-measurement accuracy. It has been shown [83] that the subaperture size should be less than $0.16\,\lambda/s$, where s is the angular subtense of the object producing the unknown wavefront.

For daytime astronomy with large background radiation, a field-of-view shifted Shack–Hartmann wavefront sensor can be used [458]. In solar imaging applications, each subaperture sees an image of the extended source, the sun. Cross-correlation algorithms (Section 5.3.6) are used to determine wavefront tilts, rather than centroids [652,653,721,880]. Increases in the speed of two- dimensional detector arrays and microprocessors have led to developments that utilize these advantages [702].

There are proposals to embed the lenslet array into the sensor array [807] or to use a liquid crystal display as both lenslet array and the corrector [30]. For visible-wavelength applications, silicon lateral effect photodiodes are used to detect spot position. The electric current output of these devices is proportional to the lateral position of the spot at the detector plane, but is very unstable.

5.3.3 Curvature Sensing

Roddier et al. [660,664] have shown how the methods of focus sensing described in Section 5.2.3 and the Hartmann subaperture division process can be combined. The method, called *curvature sensing*, measures local wavefront curvature (second derivative) in each subaperture [201]. By comparing two near-simultaneous irradiance distributions at equally spaced points on either side of the subaperture focal plane, the local curvature is found [213]. Referring to Figure 5.26, two irradiance distributions $I_1(\vec{r})$ and $I_2(\vec{r})$ are detected a distance s from focus on either side of the focal plane. The relationship between the irradiance and the phase is given by

$$\frac{I_1(\vec{r})-I_2(-\vec{r})}{I_1(\vec{r})+I_2(-\vec{r})}=\frac{f(f-s)}{s}\left[\nabla^2\Phi\left(\left(\frac{f}{s}\vec{r}\right)-\frac{\partial}{\partial\vec{n}}\Phi\left(\frac{f}{s}\vec{r}\right)\delta_c\right]=\frac{2f^2c_w}{s}\right. \tag{5.116}$$

where c_w is the local curvature at $\vec{r}$ expressed as $c_w = 1/r_w$ and r_w is the local radius of curvature. The Dirac delta δ_c represents the outward pointing normal derivatives on the edge of the signal. To reconstruct the wavefront from the known local curvatures and the edge derivatives, an iterative procedure can be followed [666] to solve Poisson's equation [663], or Zernike derivatives can be calculated [318]. Hickson [341] describes conditions, namely when $D/r_0 \le (r_0^2/\lambda z)^{6/5}$, in which the wavefront can be reconstructed with a single defocused image of a star. To use the approximations necessary to get the right side of Equation 5.116, the distance s should be

$$s \ge \frac{\lambda f^2}{\lambda f + r_0^2} \tag{5.117}$$

At optical wavelengths, this condition reduces to $s \ge \dfrac{\lambda f^2}{r_0^2}$. The standard deviation of a single curvature measurement is $\sigma_c = \dfrac{\lambda}{r_0^2 N_p^{1/2}}$ where N_p is the photon count [660].

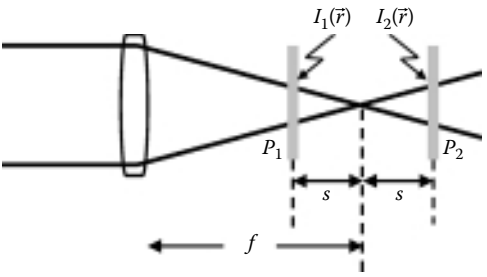

FIGURE 5.26
Wavefront curvature sensor geometry.

One appealing characteristic of this process is the possibility of applying a correction without the intermediate step of wavefront reconstruction. Since some correction devices, specifically membrane mirrors [312] and bimorphs [226], can deform locally into near-spherical shapes and can be driven directly by the output of a single subaperture that measures local wavefront curvature [890]. When the mirror gain is considered and the wavefront sensor subapertures and corrector actuators are aligned, a very efficient process for wavefront control results [305]. Curvature sensing can be applied to sense atmospheric layers [289,395] for curvature-based tomographic reconstruction of atmospheric distortions [578].

5.3.4 Pyramid Wavefront Sensor

Another pupil-plane wavefront sensor uses a pyramidal prism in the image plane to create four subbeams that are then optically relayed to a detector (see Figure 5.27) [637]. The intensity at position $\vec{r}(x,y)$ in each of the subbeams in the detector plane ($I_{0,0} > I_{0,1} > I_{1,0} > I_{1,1}$) is used to find the x and y wavefront slopes at $\vec{r}(x,y)$.

$$S_x(\vec{r}) = \frac{I_{0,0}(\vec{r}) - I_{1,0}(\vec{r}) + I_{0,1}(\vec{r}) - I_{1,1}(\vec{r})}{I_{\text{tt}}} \tag{5.118}$$

$$S_y(\vec{r}) = \frac{I_{0,0}(\vec{r}) + I_{1,0}(\vec{r}) - I_{0,1}(\vec{r}) - I_{1,1}(\vec{r})}{I_{\text{tt}}} \tag{5.119}$$

I_t is the average intensity over the detector plane. One advantage of the pyramid technique over the Shack–Hartmann sensor is that the spatial resolution of the sensor is the size of the detector pixel in contrast to the larger lenslet

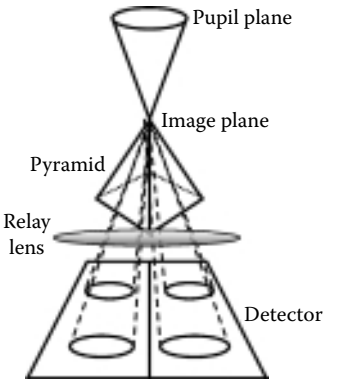

FIGURE 5.27
Pyramid wavefront sensor.

subaperture size of the Shack–Hartmann [820,821]. Various improvements to the basic pyramid sensor and reconstructor have been recorded in literature [203,427,428,619,820,884].

5.3.5 Selecting a Method

The diverse direct wavefront measurement techniques described in this section are used to detect information about the phase. It is important to consider specific requirements for the wavefront sensor in terms of the rest of the system [275]. The relationship between the subaperture geometry [654] and the placement of correcting actuators can steer the system design toward one method or another [197]. In some circumstances, wavefront sensors are used to directly detect coherent backscatter [369] or a satellite image [370]. If the wavefront sensor is used to determine the Zernike coefficients [850] or other aberration measurements in optical testing [703], the speed and spatial resolution requirements might differ from real-time adaptive optics compensation. In some circumstances, such as imaging of a solar disk, the source is extended. Cross-correlation techniques, rather than subaperture tilt measurement, must be used to properly detect the atmospheric distortions [650].

A direct comparison between Hartmann sensors and shearing interferometers has been reported [610] as has a comparison of different models used in wavefront sensor and system design [876]. Welsh et al. [857] report that both types of sensors are comparable for good seeing conditions and small beacons, however, for poor seeing and extended beacons, the Hartmann sensor has lower error levels. Similar theoretical comparisons between Hartmann sensors and curvature sensors [173,323] reveal the effects of seeing conditions and pixel readout noise. Under most seeing conditions, the Hartmann sensor performs better because of lower noise.

5.3.6 Correlation Tracker

When the wavefront source is an extended object, a centroid measurement, like that in a Shack–Hartmann sensor, is meaningless. Each subaperture contains a small image of the entire object with the image shifted according to subaperture tilt. To overcome this problem, one image $I_{\mathrm{R}}(\mathbf{x})$ is chosen as a reference. The cross-covariance between each image I is calculated by

$$CC(\delta) = \iint \mathrm{d}\,\mathbf{x}\, I(\mathbf{x}) I_{\mathrm{R}}(\mathbf{x}-\delta) = \Im^{+}\left\{\Im^{-}[I(\mathbf{x})] \times \Im^{-*}[I_{\mathrm{R}}(\mathbf{x}+\delta))\right\} \tag{5.120}$$

where $\mathbf{x}$ is the 2-D spatial coordinate, $\boldsymbol{\delta}$ is the 2-D image displacement, $\Im^{+}$ and $\Im^{-}$ is the forward and inverse Fourier transforms, and * indicates the complex conjugate. This method has been applied in solar telescopes where photons are plentiful, but the object is large.

5.4 Indirect Wavefront Sensing Methods

Many adaptive optics systems, including the human eye, do not carry out the process of making a measurement of the wavefront directly, calculating the amount of correction, and then applying that correction. Methods that avoid a direct calculation of the wavefront are called indirect methods. The indirect methods are mostly akin to trial and error. If an optical system has a way of altering the phase of the desired signal, whether it is an image or a propagated beam, and a way of determining the final result of that phase change, the system is closed-loop and, therefore, adaptive optics.

The coupling of the correction system and the indirect wavefront sensing system usually makes the two difficult to distinguish. To illustrate this, consider a simple system of Figure 5.28, where the propagation system has two channels with an unknown phase lag on one of them. By focusing the beams to a detector, the intensity pattern can be observed and processed. For a two-beam system, the intensity distribution will be the interference pattern described by Young's experiment, that is,

$$I = 4I_0 \cos^2\left(\frac{\delta_1}{2}\right) \tag{5.121}$$

where δ_1 is the unknown phase delay in the one beam.

As described in Section 5.3.1, the phase delay in the wavefront can be calculated from an intensity measurement of the peak. We could then apply an equivalent phase delay to the other beam to produce a maximum intensity in the detector plane. This would require a method of calculating the following equation in real time:

$$\delta_1 = 2\cos^{-1}\sqrt{\frac{I}{4I_0}} \tag{5.122}$$

Indirect methods do not make a calculation and apply specific correction. If the system of Figure 5.28 were modified so that the intensity detector was linked to the active phase delay device, a trial and error method of finding the phase that maximizes the intensity could be used (Figure 5.29).

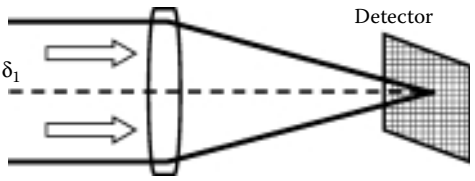

FIGURE 5.28
Two-beam simple adaptive optics system.

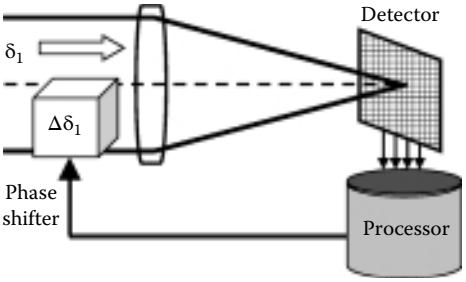

FIGURE 5.29
Indirect method of maximizing intensity.

If the active phase delay was continuously varied over one wavelength, the intensity would be modulated according to Equation 5.121. The intensity detected is coupled to the movement of the phase delay in a closed-loop fashion. When the phase delay moves in a direction that decreases the intensity, the delay is made to reverse direction. This simple feedback system is the basis for the indirect methods of wavefront sensing. It is indirect, since at no time does the system know exactly what the phase delay is; it just knows that it is not enough, analogous to climbing a hill until you reach the summit. Thus, the term *hill climbing* is used.

5.4.1 Multidither Adaptive Optics

If the unknown phase delay varies with time, the search process must be much faster to maintain stable control. We can maintain a stable system if we rapidly vary the corrective phase delay (dither) with a frequency much higher than the disturbance frequency. The intensity will be modulated at a high frequency with the time-varying unknown disturbance modulating the intensity at the lower frequencies. By synchronous detection, that is, filtering out the high-frequency dither modulation, the phase-correcting element can follow the time-varying unknown phase and keep the intensity maximized. A number of adaptive optics systems use modal or zonal dithering.

One such zonal system is the multidither adaptive optics system called *coherent optical adaptive techniques* (COAT). Developed for atmospheric turbulence correction in the 1970s [96,582], COAT systems maintained an advantage over direct systems because of the long time delays present in the wavefront sensing and reconstruction calculations. Unfortunately, COAT, and all multidither systems, cannot be scaled to large numbers of channels. They are limited by the number of channels that could be implemented within the finite bandwidth of the dither mirror. Other disadvantages of COAT, such as electronic noise, speckle noise, and bandwidth limitations for long propagation paths, have made COAT systems less popular. The process, however, is worthy of discussion, since the methods used still can be applied to a number of adaptive optics problems.

The multidither process is basically a replication of the two-beam process described earlier in as many channels as necessary for spatial resolution. For a system like the one shown in Figure 5.30, portions of the beam are tagged by phase-shifting elements that dither the phase. The field at the target is the sum of all the individual fields and is given by

$$U_{\text{tot}} = U_0 \sum_{n=1}^{N} A_n e^{i\Phi_n} p_0(x, y) \tag{5.123}$$

where $\Phi_n = \phi + \psi_0 \sin(\omega_n t)$, ϕ is the average phase of the channel, and p_0 is the aperture and intensity variance.

The intensity at the target is the square of the combined fields and is given by

$$I = U_0^2 p_0^2 \left[\sum_{n=1}^{N} A_n^2 + \sum_{\substack{k,m=1 \\ k \neq m}}^{N} A_k A_m \cos(\Phi_k - \Phi_m) \right] \tag{5.124}$$

where the phases of the individual beams, given by

$$\Phi_n = \phi + \psi_0 \sin(\omega_n t) \tag{5.125}$$

are dithered at amplitude ψ_0 and at unique frequencies ω_n. Equation 5.124 illustrates how the phase dithering translates into an intensity modulation on the target.

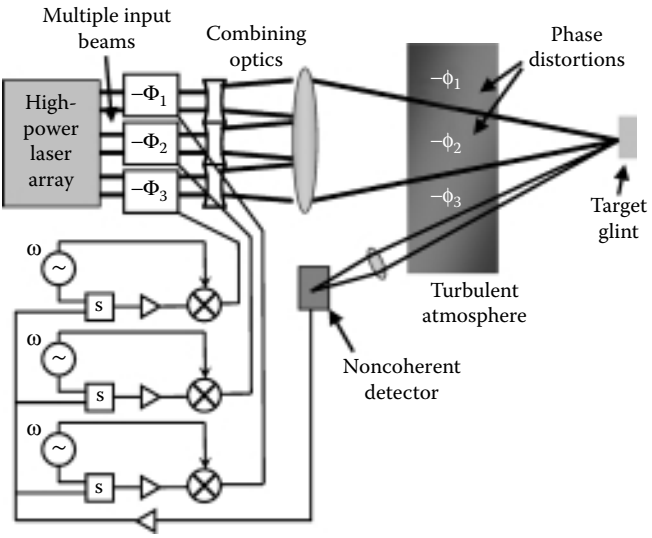

FIGURE 5.30
Multidither COAT system.

A noncoherent detector can be placed in the focal plane at a cooperative target and the modulated intensity can be sensed. For a noncooperative target, the detector can be placed near the transmitter as shown in Figure 5.30. Energy from a bright spot on the target (called a *glint*) is reflected into the detector. Light from the glint will have the same modulation in the intensity as on the target. When the propagation time delay is removed, the closed-loop control can band-pass the signal at each dither frequency, then beat the remainder with the dither. The resulting signal contains the information used for the servo to drive the average phase in the channel toward an intensity maximum [316].

Each element in the system attempts to drive itself and the weighted sum of all others to an intensity maximum. When the amplitudes and average phase errors within each channel are equal, the peak intensity is [582]

$$I_{\text{pk}} \propto A_n^2 \left[N + (N^2 - N) J_0^2(\psi_0) \right] \tag{5.126}$$

where N is the number of channels and ψ_0 is the dither amplitude. For a system that employs this concept, a tradeoff analysis must be performed. The SNR in the detector is proportional to the modulation strength, but a large modulation causes the peak intensity to be low because the modulation (the dither amplitude in Equation 5.126) will force the system to be somewhat out of phase at all times. The reduction in intensity caused by the Bessel function term in Equation 5.126 shows this. O'Meara [582] calculated a theoretical value for the optimum dither amplitude based on detector parameters such as quantum efficiency and bandwidth, as well as optical design parameters that regulate the power reflected into the detector.

Other COAT parameters are subject to restrictions placed by the methods used in decoding the dithered information. The maximum dither frequency [602] should be

$$f_{\text{max}} = [10 + 1.6(N - 1)] f_{\text{OL}} \tag{5.127}$$

where N is the number of channels, and f_{OL} is the open-loop unity-gain servo bandwidth. The range of dither frequencies [601] is

$$f_{\text{max}} - f_{\text{min}} = 3.2(N - 1) f_{\text{CL}} \tag{5.128}$$

where f_{CL} is the closed-loop control bandwidth that is desired. These are theoretical limits. When actual sensor noise and propagation time delays are considered, the minimum dither frequency should be at least 10 times the control bandwidth. The number of dither frequencies can be cut in half if each dither pair is exactly 90° out of phase, that is, a sine function dither and a cosine function dither. The signals at these frequencies can be band-pass-filtered, since the phase difference between the two is always an exact quadrant. Even with this method, known as *quadrature*, to avoid aliasing, the separation of dither frequencies should be no less than four times the control

bandwidth. The width of the band-pass filters must be slightly larger than the control bandwidth to retain the disturbance information [484].

A perfect COAT system will be stable for any number of channels [583]; however, most laboratory or field systems are far from perfect. Some of these imperfections have engineering solutions, but the overall utility of COAT systems is decreased. The first major problem with COAT occurs when there is no glint. The returned energy, the feedback, is absolutely required for the multidither principle to work. Variations of this problem occur if the glint is present and too dim, there are multiple glints, or the glint appears to move around because of changing target conditions (glint hopping). Any of these conditions reduce the system's ability to distinguish the intensity variations caused by the dithering.

It has been shown that cross-coupling between dithered phase elements, due possibly to continuous surface mirrors that have mechanical cross-coupling, will make possible an intensity maximization on a local rather than global maximum [584]. The need for many channels with a high control bandwidth [418] and a large overall phase excursion for atmospheric turbulence correction has made scalability to large apertures difficult using COAT. For atmospheric turbulence correction, with a propagation distance z, an aperture of diameter D, an atmospheric structure constant C_n^2, and a wavelength λ, the number of channels required for correction to a Strehl ratio of S is [605]

$$N = \left(\frac{2.01 C_n^2 z D^{5/3}}{\lambda^2 \ln(1/S)} \right)^{6/5} \tag{5.129}$$

The bandwidth of the atmospheric turbulence correction system must be

$$f_c \cong 0.65 v \left[\left(\frac{2\pi}{\lambda} \right)^2 C_n^2 z \right]^{3/5} \tag{5.130}$$

where v is the transverse wind velocity that moves the turbulence across the beam. The total phase excursion for any channel is

$$\Delta\phi = \frac{3.58}{\lambda} \left(C_n^2 z D^{5/3} \right)^{1/2} \tag{5.131}$$

when the diameter is about half the turbulence outer scale.

For very long propagation distances, the delay in the signal reaching the detector limits the control bandwidth. Even with lead–lag control compensation, the control signal phase delay must be kept below 30 or 40°. With the phase delay proportional to the propagation distance R, we have

$$\phi_{\text{delay}} = \left(\frac{2R}{c} \right) 2\pi f \tag{5.132}$$

one can see that the range–bandwidth (fR) product must remain below 2×10^7. This rules out atmospheric propagation from the ground to space (1000 km) using COAT, since the bandwidth achievable, 20 Hz, is well below the approximately 100 Hz correction bandwidth required.

Since COAT by definition uses coherent light, the phenomenon of speckle must be considered [240]. Any target that is rough, and they all are, will cause the signal at the receiver to appear speckled. The mutual interference of various portions of the beam reflected from the rough surface will appear as speckled dots to the receiver. A moving or spinning target will cause these dots to move across the receiver. The intensity of the light onto the detector will then be modulated at a frequency of $f = \upsilon_s/\lambda$, where υ_s is the speckle velocity across the receiver. The problem occurs when this modulation frequency is at or near a dither frequency [422]. The electrical interference of the signals causes a reduction in performance of the entire system. The intensity of the modulations at dither frequencies, I_D, degrades the COAT convergence level by

$$I_D = C\frac{P_D}{P_S}I_M \tag{5.133}$$

where C is the portion of ac modulation power that is near the dither frequency, P_D is the power in the detected dither signal, P_S is the power in the detected speckle signals, and I_M is the nonspeckle convergence level. The convergence level is roughly the Strehl ratio achieved by the system

$$I_M = \frac{1}{N} + J_0^2(\psi_0)\left(1-\frac{1}{N}\right)\frac{2}{\alpha^2}(1-\cos\alpha) \tag{5.134}$$

where α is the random distribution of phases of all the channels.

Kokorowski et al. introduced a method to automatically cancel speckle effects [420]. A system, shown in Figure 5.31, was devised where part of the

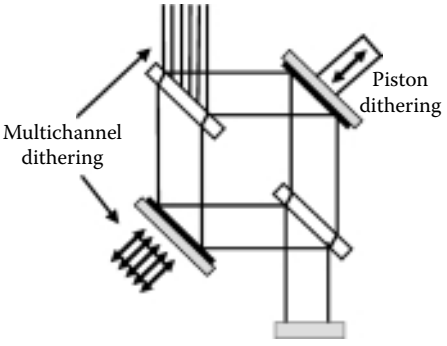

FIGURE 5.31
Automatic speckle cancellation technique.

outgoing beam was split off and separately phase (piston) dithered. The frequency of this dither was greater than other dither frequencies. This provided an envelope in which all the dither signals were confined. This reference was then used to subtract out the motion of the target. The Strehl ratio S for the automatic speckle-cancellation technique (ASPECT) is given as

$$S = \eta_1^2\left[\frac{1}{N} + J_0^2(\phi_0)\left(1 - \frac{1}{N}\right)\right] + 2\eta_1\eta_2 J_0(\phi_0)J_0(\phi_A) + \eta_2^2 \tag{5.135}$$

where ψ_A is the probe amplitude, η_1 is the fraction of energy in the principal beam, η_2 is the fraction of energy in the probe beam, and $\eta_1 + \eta_2 = 1$. For a nonspeckle system, where $\eta_2 = 0$, Equation 5.135 reduces to Equation 5.134.

The multidither technique is the most developed of the indirect adaptive optics methods. Experimental demonstrations and field demonstrations have been made and extensive analyses of the electronics [316] and the control algorithms [37] have been presented. It is, however, not the only indirect method used. The astronomy community has investigated a common method for many years. The principle of image sharpening shows promise in many instances.

5.4.2 Image Sharpening

The principle of image sharpening can be explained by examining Figure 5.32, a generic adaptive optics imaging system. The intensity in the focal plane must be such that the image degraded by some disturbance can be recovered. This requires manipulation of the phase-correcting elements while observing some function of the image. The historical use of this technique is to correct atmospherically degraded astronomical images where a sharp image is desired; hence the term *image sharpening*. A problem arises when one quantitatively tries to define the word "sharp." Numerous definitions have

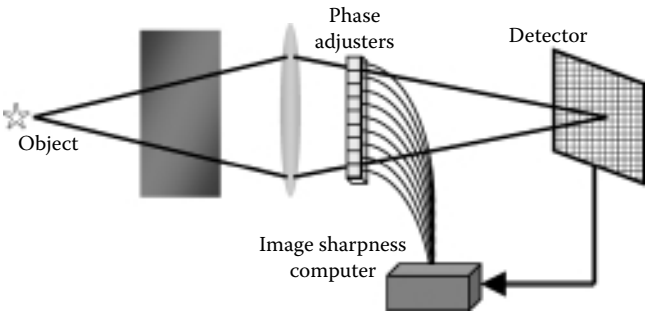

FIGURE 5.32
Image sharpness adaptive optics system.

been explored [547]. Many more descriptions of a "good image" have been developed in the rapidly advancing science of image processing. These latter developments are more structured to post–image processing than to real-time image formation, and they are not considered to be within the realm of adaptive optics.

The technique requires the maximization of a function defined as sharpness, *S*. The simplest thing to maximize, by changing the phase of various parts of the imaging system, is the intensity at one point, most likely the center of the image. This image-sharpening technique ($S = I(x_0, y_0)$) is simple—move each phase adjuster one at a time, watching the intensity at one point. Then move the phase adjusters through at least one wavelength and leave them on the point where the intensity is maximized. This, of course, has drawbacks; it does not use most of the information available and will only work well for bright point objects. They must be bright to generate enough photons at the point of observation, and they must be point objects to ensure that the center of the image is near the optical axis.

The most common image sharpness that is maximized is the integral of the square of the image intensity distribution [547], given by

$$S = \int I(x, y)^2 \, \mathrm{d}x \, \mathrm{d}y \tag{5.136}$$

This sharpness definition will be maximized when there is zero wavefront error even in the presence of irregular object radiance distributions. This amplitude insensitivity makes this method useful for large extended objects. Other sharpness functions, such as higher-order moments of the distribution, expressions related to the Fourier transform of the image [841], or entropy minimization functions given by Equation 5.137:

$$S = -\int I(x, y) \ln[I(x, y)] \, \mathrm{d}x \, \mathrm{d}y \tag{5.137}$$

have been tried and are proven to relate to low wavefront error. The electromechanical techniques required to implement an image-sharpening system are similar to the techniques used in multidither. In this case, however, the target is the image plane. Each element is individually adjusted by trial and error. The performance is limited by the number of degrees of freedom (channels) and the required bandwidth [547], because both cannot be increased simultaneously. For ground-based astronomy applications, as long as the aperture is within the same isoplanatic patch and enough light is present in each channel, the image-sharpening sensor methods can be, and have been, used successfully. For anisoplanatic situations, where the wavefront is derived from multiple planes, image sharpness methods can still be successful with nonlinear optimization techniques [774] or optimizing a laser spot on the target [620].

5.5 Wavefront Sampling

The wavefront sampling subsystem redirects a portion of the incoming beam to the wavefront sensor. It is often called by many less functional names, such as *beam splitter* or *grating*, usually because this subsystem often is a single component of a beam train. In any case, it is important that the wavefront sensor gets a sample of the wavefront that is a high-fidelity replication of the wavefront that needs correction. If a wavefront sensor is used in the purely diagnostic mode, there is no need for a sampler. The beam just enters the sensor and data can be recorded. Where conventional adaptive optics is used in a closed loop, the beam is propagated to a target or an image sensor with only a representative sample sent to the wavefront sensor. It is important that the sample represents the wavefront that is propagated along the rest of the system.

Many beam control systems, like the one shown in Figure 4.1, will show a beam splitter fulfilling the beam-sampling function. The beam splitters can be actual coated glass components commonly called beam splitters, or they can represent any device that separates the ongoing beam and the sampled beam. The details of the adaptive optics system and the operational requirements often dictate the type of component that is required.

5.5.1 Beam Splitters

Transmissive beam splitters come in a variety of configurations. They are generally specified as being flat-plate, cube, or pellicle beam splitters. When beams of different wavelengths must be separated, as required by some return wave adaptive optics, a dichroic beam splitter is used. Commercially available *flat-plate beam splitters* are usually thin glass plates with edges parallel on the order of a few milliradians. The surface incident to the beam, usually called the front surface, is coated with a film having partial reflection properties for the wavelength of interest (Figure 5.33a). The transmitted portion of the beam exits the back surface, which has a broadband antireflection (AR) coating. The reflection–transmission ratios are specified along with the incidence angle and, sometimes, the polarization state (for example, T/R 50:50 ±5%; 45°). Off-the-shelf components have a surface flatness that is typically a few waves across the device. For most applications in adaptive optics, this distortion can be corrected if it is passed to the wavefront sensor by the reflected beam and the distortion is imparted to the transmitted beam as well.

Another source of beam distortion occurs when the beam splitter is mounted. The stresses in the glass due to the clamping can distort the plane surface. As long as the distortion shows up on both the transmitted and the reflected beams and is within the range of the adaptive optics system,

the adaptive optics will be successful. Only when the sampled beam sees a different distortion than the transmitted beam will problems occur The sample, then, is not a high-fidelity sample. The adaptive optics system will try to correct for one distortion while the beam really has another distortion. This is analogous to the atmospheric anisoplanatism problem, but, fortunately, this fidelity problem is normally within the control of the optical engineer. The differences between the sampled beam and the transmitted beam are important considerations for adaptive optics system layout and component selection.

Cube beam splitters have some advantages over plate beam splitters. A *cube beam splitter* is a matched pair of right-angle prisms (Figure 5.33b). This type of beam splitter deforms much less than a flat plate when it is stressed by mounting. The partially reflecting coating is applied to the interface between the prisms before they are cemented together. This reduces long-term degradation because the coating is sealed. The specifications for cube splitters are similar to those for plate splitters.

Beam splitters can be used in an uncollimated portion of the beam if a compensating beam splitter is inserted in the beam train. This second splitter, tilted in the opposite direction, compensates for aberrations introduced by the first splitter. The finite thickness of the beam splitter imparts aberrations to the transmitted beam, thereby reducing the fidelity of the reflected sample. The amount of spherical aberration, chromatic aberration, and astigmatism can be significant. Since it is not imparted to the reflected beam, the adaptive optics system can have degraded performance.

One possible way of avoiding the low-fidelity problem is through the use of *pellicle beam splitters* (Figure 5.33c). These devices consist of a membrane stretched over a frame. Since the membrane is about 5 μm thick, the chromatic and spherical aberration of the transmitted beam are negligible. Wavefront sampling is then possible in a diverging beam where a collimated portion is not easily found. For example, in a photon-starved astronomical application, the addition of extra optics to provide a collimated beam may have too much absorption. A pellicle beam splitter is a possible solution. The nature of the pellicle beam splitter also can be a disadvantage. Its small thickness allows it to be easily distorted by mounting stress and acoustic

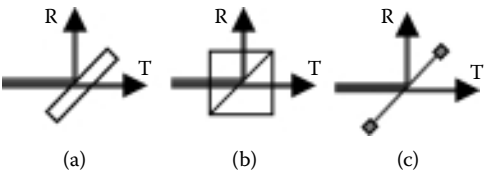

FIGURE 5.33
Beam splitters: (a) flat plate, (b) cube, and (c) pellicle. R is the reflected beam; T is the transmitted beam.

vibration. Because of its unprotected coating, it has a narrow wavelength range and is very fragile.

For an adaptive optics wavefront sampler that separates the sample from the transmitted beam by virtue of its wavelength, a dichroic beam splitter can be used. These dispersive devices have the same structure as neutral beam splitters, but they are coated in a manner that allows transmission at one wavelength and reflection of another. They are specified by the amount of light passed at each particular wavelength. For instance, T(94%)550 nm/R(98%)1.06 μm/flat plate/45° specifies a flat-plate 45°-incident beam splitter with visible transmission of at least 94% and IR reflection of at least 98%. Of course, other requirements such as shape, spatial dimensions, flatness, and parallelism should be specified and considered in the application.

5.5.2 Hole Gratings

In applications where transmissive optics cannot be used or the distortions from them are too large, a simple method of obtaining a high-fidelity sample of the beam is to use the *hole grating*. A hole grating is a flat mirror with a regular pattern of holes drilled in it. Depending on the size of the holes, most of the beam energy is reflected from the front surface. A small fraction, typically 1–10%, will pass through. The fidelity of the sample is independent of the reflecting surface of the mirror. Distortions of the reflective surface are not passed to the sample. The sample does not represent the entire wavefront, but, as seen in Chapter 6, if the holes are close enough in relation to the spatial frequency of the aberrations, the sample will be sufficient for reconstructing the entire wavefront.

Although this approach seems simple, it does have a few drawbacks. Finite-size holes reduce the fidelity of the sample. Because of diffraction, the fidelity is affected by the spatial frequency content of the sampled beam itself [704]. For the level of accuracy needed in many systems, this error can be removed in the sample reconstruction process [335]. The zero-order sample of the beam is insensitive to the spectral content of the beam. By allowing only the zero-order sample through an aperture plate (Figure 5.34), the greatly attenuated (10^{-5}) replica of the input beam far-field diffraction pattern can be observed [344,504]. By reimaging, the sample can be passed to a wavefront sensor.

5.5.3 Temporal Duplexing

When aberrations are slowly varying, continuous sampling is not required. Sampling a beam only part of the time can be a useful alternative. Figure 5.35 shows two concepts for sampling. In one method, an acousto-optic cell is used as a beam switch [371]. The cell is driven by a transducer, which sets up a diffraction grating in the cell. When the grating is present, the beam is deflected; when it is not present, the beam passes straight through. By alternately creating

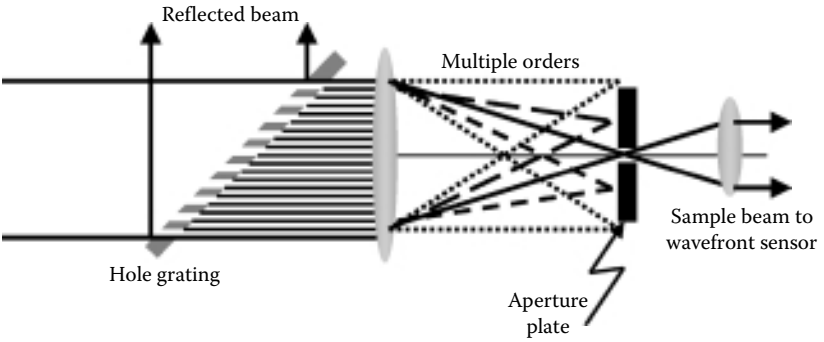

FIGURE 5.34
Use of a hole grating. The multiple orders from the grating are removed by the aperture plate.

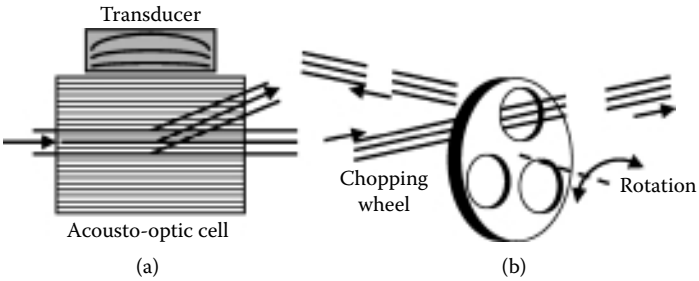

FIGURE 5.35
Temporal duplexing concepts: (a) acousto-optic cell and (b) mechanical chopper.

the grating and removing it, the switch can direct a beam toward a different beam path (Figure 5.35a). This is workable for low-power applications where distortion in the cell is not a problem. For a normally incident wave, the deflection angle θ_D for the first order Raman–Nath diffraction wave is

$$\sin \theta_D = \frac{\lambda}{\lambda_a} \tag{5.138}$$

where λ is the wavelength of the light and λ_a is the acoustic wavelength. Since the transducer can be switched on and off at very high rates (easily fO MHz), the beam samples can represent very high-frequency components of the disturbed wavefront. The major difficulties arise from the relatively small beams that can be used and the long paths required to separate the beams, since the ratio λ/λ_a is small.

When beams are larger or even high-power, mechanical choppers can be used. Figure 5.35b shows the conceptual makeup of such a device. The beam is alternatively reflected and transmitted by the chopper, which can have various duty cycles. For instance, a spinning flat plate with a hole equal to the beam diameter will transmit one sample per revolution. If the plate is

large enough to have four holes, the sample rate is RPM/15 Hz. For slowly varying aberrations such as thermal distortion, a chopper with a diameter of five beam diameters (accounting for 45° incidence angle) could sample a beam at 200 Hz. With consideration for control system delays, this could easily allow for a 20-Hz correction bandwidth.

An alternative design using precisely aligned blades would have the same performance parameters. In either case, the fidelity concerns are similar to those with beam splitters or hole gratings. The distortion imparted on the reflected beam must be as small as possible to have a sample that is representative of the zero-loss transmitted wavefront. Engineering concerns such as wobble, bearing and surface cooling, beam path environment control, and long-duration stability must be studied for each case.

5.5.4 Reflective Wedges

A simple *wedge* can be used when one needs to spectrally separate two beams. A wedge is a dispersive device that functions as a prism. If the sample beam is a different wavelength than the main beam, the characteristic index of refraction differences of materials can be used. Figure 5.36 shows two possible configurations of a sampling wedge. Figure 5.36a has an AR coating on the incident surface with a reflective coating on the back surface. Two superimposed beams of wavelengths λ_1 and λ_2 are incident at angle θ_i. For a wedge angle θ_W, the angle of the reflected beam from the front surface is

$$\sin\theta_R = n\sin 2\theta_W \cos\theta_i + \cos 2\omega_W \sin\theta_i \tag{5.139}$$

The different directions of the two beams arise because the index of refraction is slightly different for the two wavelengths. For example, with a wedge angle of 5° and an incident angle of 10°, using SF11 glass, a visible beam (λ = 500 nm) is separated from an IR beam (λ = 1500 nm) by over 1/2°. The indices of refraction [519] used are $n_{500\,\mathrm{nm}} = 1.80205$ and $n_{1500\,\mathrm{nm}} = 1.74525$.

If a larger angular spread is desired, the front surface of the wedge can be coated to reflect one of the wavelengths. From the preceding example, if the IR beam is reflected from the front surface, it leaves at an angle of 10°. The visible beam is refracted in the material and leaves at an angle of 28.63°.

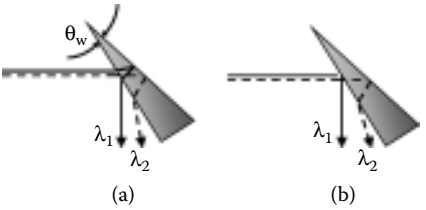

FIGURE 5.36
Reflective wedges: (a) dispersive method and (b) reflective method.

This separation has the advantage of requiring much shorter propagation distances for the sampled beam. It does suffer from fidelity problems, since the path for the refracted beam passes through the material and may pick up bulk material distortions, while the reflected beam picks up only surface distortions.

Although reflective wedges seem simple, they suffer from many of the same deficiencies as beam splitters. Deviation from flatness is a major concern. Maintaining a constant wedge angle is as difficult as maintaining the parallelism of a flat plate. Since their operation as adaptive optics wavefront samplers depends upon specialized reflective and antireflective coatings, the quality of the coating process must be at least as good as, if not better than, the coating process of other optics in the system.

5.5.5 Diffraction Gratings

Diffraction gratings are optical elements with a surface that is modulated with a regular groove or slit pattern. They are used in adaptive optics primarily as a method of separating two beams. One of the beams will be passed along (either by reflection or transmission) toward a wavefront sensor, which should retain the wavefront characteristics of the other beam. The details of the diffraction taking place have been discussed by a number of authors [368,714,747].

Modern photoresist techniques and lasers make the production of highly efficient gratings possible. The interference of two beams can produce a pattern of lines very close together. When an interference pattern exposes photoresist, a very fine pattern can be etched into an optical substrate. This *holographic grating* has an advantage over mechanically ruled gratings. When the interference pattern is made without collimating optics, the holographic grating can be used to focus a beam. Because the grooves are under optical rather than mechanical control, the unequal spacing can be used to manage the diffracted beams. Focusing gratings of this type are used throughout the imaging and adaptive optics communities.

Mathematical expressions from classical optics can be used for analyzing most types of gratings. The behavior of ruled gratings and holographic gratings is explained by diffraction theory. The different orders of diffraction for reflection or transmission gratings follow the basic grating equation

$$d(\sin\theta_m - \sin\theta_i) = m\lambda \tag{5.140}$$

where d is the separation of the grooves, θ_i is the incident angle measured from normal, and θ_m is the angle of the mth diffracted order. The plane of incidence is perpendicular to the grooves. When this strict condition is not met, the grating will operate with reduced fidelity (see Section 5.5.7). For focusing gratings, the d in Equation 5.136 depends on the angle of incidence, and the expression loses its linearity.

Most gratings in use in adaptive optics are either blazed or sinusoidal. *Blazed gratings* have triangular-shaped grooves with their depth specified by a *blaze angle*, θ_B. Low blaze angles (~2°) are insensitive to polarization and have a clearly defined efficiency peak at $\lambda/d = 2 \sin \theta_B$. Low blaze angle gratings exhibit almost 100% efficiency at this one order [478]. Higher blaze angle gratings show high efficiencies for the higher orders, but become more sensitive to polarization. The S-state polarization (light polarized perpendicular to the grooves) usually shows higher efficiency than the P-state (light polarized parallel to the grooves). Unusual behavior occurs for blaze angles larger than 20°, and each should be considered individually, depending upon the wavelength and the order of diffraction that is to be used [368].

Sinusoidal grooved gratings can be made easily with the photoresist process. The modulation ratio h/d (where h is the peak-to-peak height of the grooves) determines the efficiency. Low-modulation gratings ($h/d < 0.05$) exhibit a maximum efficiency at $\lambda = 3.4h$ with very low efficiency for high orders. When the modulation ratio is increased, the higher-order efficiency of the grating increases. Although the grating efficiency is a function of groove profile, wavelength, angle of incidence, and surface material optical constants, approximations can be made. For a perfectly conducting surface with sinusoidal grooves that have a depth that is short compared to the wavelength, scalar theory predicts that the efficiency E is

$$E = J_n^2\left(\frac{2\pi h}{\lambda}\right) \tag{5.141}$$

where J_n is the Bessel function for diffractive order n. In general, diffraction gratings are a proven method for wavefront sampling for monochromatic operation and have widespread use. Sensitivity to grating alignment and polarization effects are discussed in Section 5.5.7.

5.5.6 Hybrids

Many adaptive optics systems cannot use a simple grating or beam splitter for beam sampling. Transmissive beam splitters often cannot handle high-power flux without significant distortion or destruction. A number of hybrid concepts have been introduced to overcome shortcomings of single-component samplers. A variation on the wedge discussed in Section 5.5.4 is the *buried mirror*. Whereas the wedge works by reflecting a beam from the front surface in a different direction from a beam reflected from the back surface, a buried mirror is constructed so that the beam reflected from the back surface is focused differently than the beam reflected from the front surface. Figure 5.37 illustrates two methods of employing this concept. The system in Figure 5.37a has an annular outgoing beam coincident with an incoming beacon beam. The outgoing beam is reflected from the front surface of the optics. The buried mirror transmits the beacon wavelength through its coating toward the

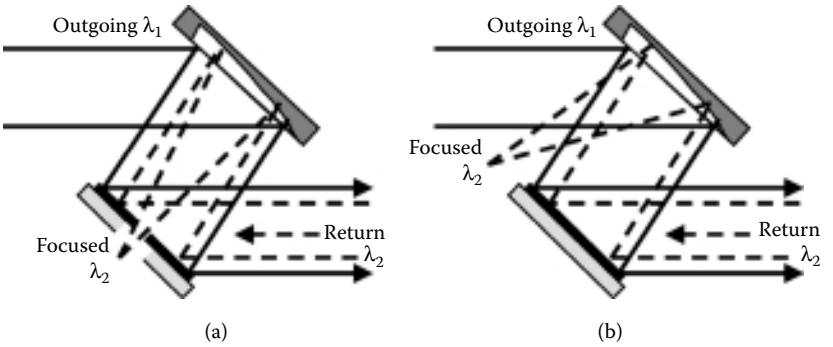

FIGURE 5.37
Buried mirror concepts: (a) annular outgoing beam coincident with an incoming beacon beam and (b) sample being focused to a point away from the outgoing or incoming beams.

concave substrate, and the converging beam sample is then sent through a hole in an adjacent mirror. If the outgoing beam is not annular, the concave surface can have an axis that is not parallel to the incident beam. The sample is then focused to a point away from the outgoing or incoming beams (Figure 5.37b). These concepts are not limited to plane front surfaces. The reflective front surface of a buried mirror can be any shape and perform other functions in the beam train.

If a grating is used to separate two beams of different wavelengths, the angular separation is governed by the grating equation, Equation 5.136. To bore-sight the samples, a *grating rhomb* is used. Figure 5.38 shows the orientation of the primary grating and its complement in a rhomb configuration. It is important that the complementary grating be an exact replica of the primary grating. If they differ, the samples could be uncollimated and contain distortions not present on the main beam. Since the primary grating will specularly reflect the main beam—possibly a high-power beam—control of absorption through coating selection is important. Techniques to overcome the difficulties with coating a high-power grating were discussed in some detail by Guha and Plascyk [314]. In some cases, two beams of different wavelengths must be sampled and made coincident. A hybrid concept to accomplish this is the *grating beam combiner* [707]. The concept, shown in Figure 5.39 is a grating that diffracts samples with two different wavelengths in a common direction.

Combining the effects of gratings and the elements of the buried wedge resulted in the concept of a *buried grating* [131]. When the grating is coated with a material that reflects one wavelength and transmits another, the buried grating is used as a beam sampler (Figure 5.40). If the line spacing of the grating is on the order of wavelengths, it is called a buried short-period grating (Figure 5.40a). It functions as a diffraction grating because the sample leaves as a higher order of the grating. When the line spacing of the grating

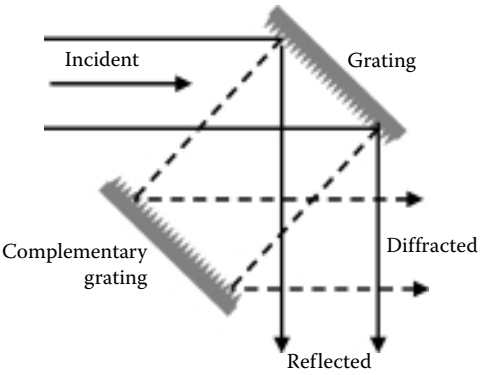

FIGURE 5.38
Grating rhomb.

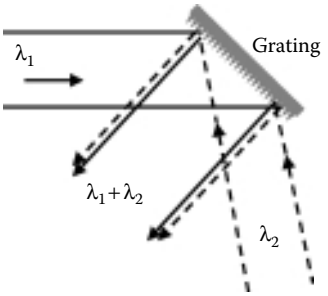

FIGURE 5.39
Grating beam combiner.

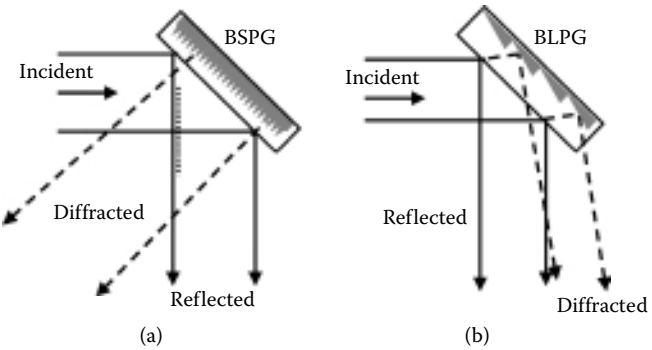

FIGURE 5.40
Buried gratings: (a) short period and (b) long period.

is on the order of millimeters, it is called a buried long-period grating (BLPG) and it functions more like a buried mirror (Figure 5.40b). The transmitted beam reaches the grating surface and specularly reflects from each facet like a buried wedge with a faceted back surface. Since the BLPG does not operate by diffraction, but rather by specular reflection, it is insensitive to polarization. It has low spectral dispersion (only what occurs from the transmissive layer) and it is aligned by normal mirror alignment techniques. Although a number of samples have been made, a large-scale buried mirror device is expensive and difficult to manufacture. Attempts to maintain surface contact between the faceted or grooved surface and the transmissive layer often result in disbonding.

A number of other interesting concepts have been proposed for separating a low-power beam sample from a high-power beam. A *compound interlaced grating* combines two gratings of different periods on one surface [131]. Each wavelength responds to both gratings. If the wavelengths are sufficiently separated (e.g., one visible and one LWIR), the grating spacings can be very different. For the case where the two spacings are an integer multiple of each other, the grating can be manufactured by standard methods. With those restrictions in mind, the buried and compound gratings could be used.

5.5.7 Sensitivities of Sampler Concepts

Many of the wavefront sampler concepts presented make use of transmissive materials, which are wavelength-sensitive, or diffraction gratings, which are sensitive to polarization or misalignment. Some of the concepts were developed solely to eliminate some of these sensitivities (e.g., the grating rhomb). Other concepts can be externally aligned to compensate for various anomalies in the sampler.

The efficiency of diffraction gratings for different orders is closely tied to the polarization of the beam being diffracted. When a beam is diffracted, the absolute value of the phase shift between its parallel and perpendicular components is given by [685]

$$\cos 2\phi = 1 - \frac{2[I(I_{\parallel} + I_{\perp} - I)]}{I_{\parallel} I_{\perp}} \tag{5.142}$$

where I is the minimum or maximum intensity, $I_{\parallel}$ is the intensity of the component parallel to the grating grooves, and $I_{\perp}$ is perpendicular to the grooves. The angle ϕ is assumed to be in either the first or second quadrant. This simple expression can be used to compute efficiencies for various orientations of a grating.

If the plane of incidence is not exactly perpendicular to the grooves of the grating, aberrations can appear in the diffracted sample that are not present

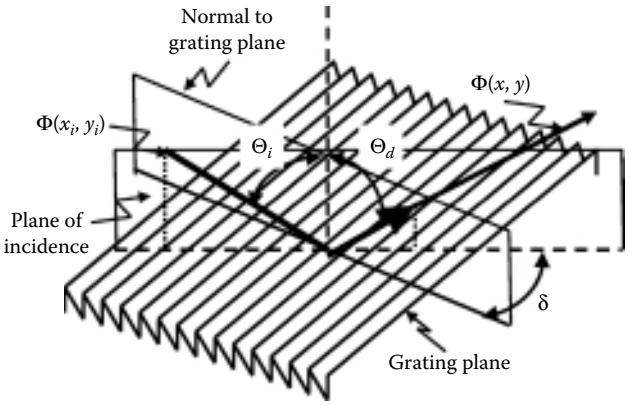

FIGURE 5.41
Geometry for a misaligned grating.

in the incident beam. The geometry is shown in Figure 5.41. If the wavefront of the incident beam is $\Phi_i(x', y')$ where the coordinate y' is nearly parallel to the grooves, differing by a small angle δ, the wavefront of the mth-order diffracted beam is $\Phi_m(x, y)$. Simon and Gil [283,725] present the relationship for the sampled wavefront as a function of the incident wavefront and the geometrical considerations. The incidence angle θ_i is related to the diffracted angle of order m, θ_m through the grating equation, Equation 5.140. The diffracted wavefront takes the form

$$\Phi_m(x,y) = \Phi_i\left(x\frac{\cos\theta_i}{\theta_m}, y\right) + \delta y - \frac{1}{2}\left(\frac{\partial\Phi_i}{\partial x'}\right)^2 \frac{\cos^2\theta_m \sin\theta_i + \cos^2\theta_i \sin\theta_m}{\cos^3\theta_m} x$$

$$-\left[\delta\left(\frac{\partial\Phi_i}{\partial y'}\right) + \frac{\delta^2}{2} + \frac{1}{2}\left(\frac{\partial\Phi_i}{\partial y'}\right)^2\right]\frac{\sin\theta_m + \sin\theta_i}{\cos\theta_m} x \tag{5.143}$$

Examination of this expression reveals that an angular deviation will introduce distortion into the diffracted wavefront. If the incident wave is plane ($\partial\Phi/\partial x' = \partial\Phi/\partial y' = 0$), the specularly reflected ($\theta_i = \theta_m$) wavefront is

$$\Phi_m = \Phi_i(x', y') + \delta y - \delta^2 x \tan\theta_i \tag{5.144}$$

which shows both x and y tilts in the diffracted beam. Clearly, if $\delta \to 0$, the equation reduces to $\Phi_m = \Phi_i$, which is the desired high-fidelity sample needed for adaptive optics.

5.6 Detectors and Noise

Sensing light intensity is fundamental to any wavefront sensor technique. Sensing methods, whether they use interferometric techniques, the Hartmann test, or indirect methods, require an electrical signal output that is proportional to the intensity of light. Electro-optical detectors provide this service.

Many volumes have been written on the manufacture and use of detectors for visible, ultraviolet, and infrared energy [417,529,640]. It is beyond the scope of this book to address all the issues relating to the physical processes involved or the electronic circuitry associated with each type of detector. A summary of the basic types of detectors, their important characteristics for wavefront sensors, and their uses are given

For visible light, the silicon (Si) photodiode is the most common detector used. It could be used in all types of wavefront sensors that are measuring the intensity of light in a small region. Silicon detectors, by application of the photoelectric effect, convert incident light into electric current. They are available for use from 350 nm (UV) to 1050 nm (IR) wavelengths.

Detectors are usually characterized by a few basic parameters. The responsivity (R) is a measure of the amount of electric current produced for each unit of incident light. Responsivity is wavelength-dependent and usually expressed in amps/watt. For silicon detectors, the peak responsivity is about 0.5–0.7 A/W. The rise time is the amount of time necessary for the detector to respond to the light. In silicon detectors, the rise time is a function of the charge collection process, the RC time constant of the equivalent electronic circuit, and the diffusion time for the electrons within the medium. Silicon detectors have rise times ranging from one nanosecond to a few microseconds. Both shot noise and thermal (Johnson) noise are present. The dominant noise source depends upon light intensity. The quantum efficiency of the detector is proportional to the responsivity and the inverse of the wavelength. Silicon detectors have quantum efficiencies ranging from 50 to 90%.

Wavefront sensing is very sensitive to noise [242], since many wavefront sensors have to perform in a photon-starved situation. With small apertures and long ranges to dim sources, the noise parameters of a detector are very important. The noise equivalent power (NEP) is a measure of detector "noisiness." It is expressed in units of power divided by the root of the bandwidth (watts/$\sqrt{\text{Hz}}$). Photodiodes made of silicon have NEPs from $10^{-15}\,\text{W}/\sqrt{\text{Hz}}$ to $10^{-12}\,\text{W}/\sqrt{\text{Hz}}$. Detectivity ($D^*$, pronounced "D-star") is related to this parameter. Detectivity normalizes the NEP by the size of the detector. It is given by the equation $D^* = \sqrt{\text{Area}}/\text{NEP}$. For silicon detectors, D^* ranges from 10^{11} to 10^{13} cm $\sqrt{\text{Hz}}/\text{W}$.

Many wavefront sensor applications are in the infrared region of the spectrum. The atmosphere has transmission bands in the 3–5 μm and 8–12 μm

regions, but other bands are often used, especially for nonatmospheric correction. An IR detector, by its nature, must detect small changes in the temperature, which are a result of the incident IR light. To keep scattered radiation from fogging the detectors, the device is often kept in an insulated container, called a Dewar. Although IR detectors that operate at room temperature exist, an understanding of the limitations in packaging and operation of cold detectors is needed before applying their capabilities to IR wavefront sensors. IR detectors are usually grouped into thermal detectors, such as thermopiles and pyroelectrics, and solid-state detectors, such as indium antimonide (InSb, or "inz-bee") and mercury cadmium telluride (HgCdTe, or "mercads").

Thermal detectors produce a voltage proportional to a light intensity. Pyroelectrics operate in the 8–14 μm range with responsivities from 10 to 50,000 V/W. They can have rise times from as fast as 2 ns to upward of 150 ms. Thermopiles can operate from 0.1 to 50 μm with responsivities up to 100 V/W. They are generally slower than pyros with rise times from a few milliseconds to a few seconds.

Solid-state detectors have responsivities in the 1–5 A/W range with D^* from 10^9 to 10^{12} cm $\sqrt{\text{Hz}}$/W. Indium antimonide detectors operate from 1 to 7 μm with about 500 ns rise times. Mercury cadmium telluride detectors have been operated in the 1–20 μm range, but the most common are used in the 5–12 μm range, with 1–500-second rise times. Germanium detectors operate in the low band (0.5–2 μm) with fast (0.1–50 ns) rise times. Lead sulfide IR detectors operate from 1 to 5.5 μm with rise times on the order of 200 ns. Gallium arsenide (GaAs, or "gas") detectors operate in the near infrared (0.7–0.9 μm) with very fast (0.03 ns) rise times. These and many other detector types are available. The latest trade journals or manufacturers' data sheets are the most helpful in evaluation for a specific use.

IR and visible detectors are fabricated in linear or two-dimensional arrays. Arrays are further classified as staring (observing the light continuously with the information output in parallel) or scanning (with the information or the deposition of the energy being dynamic). Both serial scanning and parallel scanning are used, sometimes in combination. Quadcells, such as high quantum efficiency avalanche photodiodes [80], are used in tilt sensing, target tracking, or in subapertures for multichannel wavefront sensors. Quadcells are often made by physically adjoining single detectors. Since 2×2 arrays can be made easily, or 2×2 portions of larger arrays can be used as pseudo-quadcells, arrays play a very important part in wavefront sensor development.

Silicon lateral effect photodiodes are single-element detectors that have output current proportional to the lateral position of the spot on the detector. These very sensitive devices are used for full-aperture tilt sensing or for subaperture tilt sensing in each channel of a Hartmann sensor. They have demonstrated position accuracies as low as 0.1% over the entire detector active area [804].

The most commonly used array for wavefront sensing applications is the *charge-coupled device* (CCD) *array* [501]. In silicon room-temperature arrays, a pocket of charge is created when light hits the material in an area called a picture element, or *pixel*. IR arrays are usually cooled, but operate on the same principle. The amount of charge is proportional to the integration time and the intensity. The pockets of charge are created in a small region called a *storage element*. Alternating pairs of electrodes surrounding these storage elements can be used to pass the charge out along a stream; that is, for each clock cycle, the charge pockets can be shifted over one pocket. When all pockets have been clocked out, the array is capable of starting the cycle over again. Like the operation of a computer's shift register, the CCD clocking process is a very low loss. This lack of noise and high efficiency is very useful for wavefront sensing [66,456]. Noise is often expressed in electrons/pixel with values as low as $4e^-$/pixel typical for low-noise CCDs. Circuits can process this information to determine the wavefront-sensitive issue, for example, the position or height of the peak, the centroid, or the difference between adjacent cells.

CCDs can be operated in the GHz range and are suitable for high-speed adaptive optics wavefront sensors [272,273]. The speed of the shifting of charge is generally limited by the speed of the electrons in the base material. With thousands of elements, the processing must be capable of handling the high-speed clocked information. The time it takes for all elements in the array frame to be clocked out is the frame time. Some frame times are quoted including forms of signal conditioning, such as automatic gain control or thresholding. The important question that must be asked for a wavefront sensing application is whether the total frame time, plus phase determination algorithm processing, is sufficiently fast to capture the dynamics of the wavefront [400]. One processing procedure that is well-suited to these types of signals is the N-bin phase detection algorithm [155]. This algorithm is a form of discrete quadrature detection in which N is the number of discrete samples used in the digital equivalent of a radio frequency mixer [517].

In very low light level conditions, very sensitive detectors are needed. A *photomultiplier tube* (PMT) is a sensitive detector where photons falling on a cathode generate surface photoelectrons. An electron multiplier (dynode) chain amplifies this photon flux to produce current at the anode. The output should be linearly proportional to the light intensity, but, because of saturation, the detector response can be nonlinear [214,491] and often lasts for a few milliseconds after a very bright pulse [146]. Cathode sensitivity (mA/W or A/lumen), amplification (10^3–10^8), spectral response, and dark noise (0.01–10 nA) are parameters to be considered during selection. Petroff et al. [618] describe a solid-state photomultiplier with a quantum efficiency of nearly 50%. The device has single-photon counting capability with operating wavelengths from 0.5 to 28 μm. A *microchannel plate* is a fast-response PMT with very closely spaced dynodes. A microchannel plate-based image intensifier for a Hartmann sensor used in astronomy was described by Clampin [141].

Avalanche photodiodes and other image intensifier applications to adaptive optics have been reported [142,494,676].

The noise characteristics of detectors are very important [615], and how they relate to the error in wavefront sensing has been explored [887]. For a single channel of a shearing interferometer, the signal current $i(t)$ is

$$i(t) = i_s[1 + \gamma \sin(\omega t + \phi)] \tag{5.145}$$

where ω is the modulation frequency, γ is the fringe visibility, and ϕ is the unknown phase. The phase is measured by determining the time of zero crossing of this signal and the time of a reference signal crossing [508]. It has been shown [729] that the error in this time determination is responsible for an error in the phase estimation. The phase error is inversely proportional to the SNR.

For a low light level photon-counting shearing interferometer, Wyant [887] showed that the variance in phase estimation is

$$\sigma^2 = \left[\frac{0.9 d_s}{s\gamma\sqrt{n}}\right]^2 \tag{5.146}$$

where d_s is the distance between wavefront measurement points, s is the shear distance, and n is the number of photon counts in a period, given by

$$n = \frac{N\Omega T A \tau R}{e^-} \tag{5.147}$$

In this expression, N is the radiance of the source, Ω is the solid angle of the optics, T is the transmission of the optics, A is the aperture area, τ is the integration time, R is the responsivity of the detector, and e^- is the electric charge. See also Equation 3.20 and the discussion in Chapter 3.

Other investigators [115,192] have analyzed the noise characteristics of wavefront sensors to explore the trades necessary between small apertures, which give high resolution, and large apertures, which maximize SNR. One measure of a bound-on-wavefront sensor error is the Cramer–Rao parameter [811], which is derived for shearing interferometers by Cederquist et al. [119].

In some cases of atmospheric propagation, it can be useful to sense the wavefront at one wavelength with a correction applied for propagation at another wavelength. For instance, one may want to propagate a carbon dioxide laser (10.6 μm) up through the atmosphere, but sense the aberrations from a visible beacon (0.5 μm) because of the availability of detectors. Chromatic anisoplanatism, mentioned in Chapter 3, would result. Phase conjugate theory for a uniform medium would predict that only a scale factor is needed to represent the difference in the index of refraction between the wavelengths. In such a system, however, diffraction of the beam causes interference effects

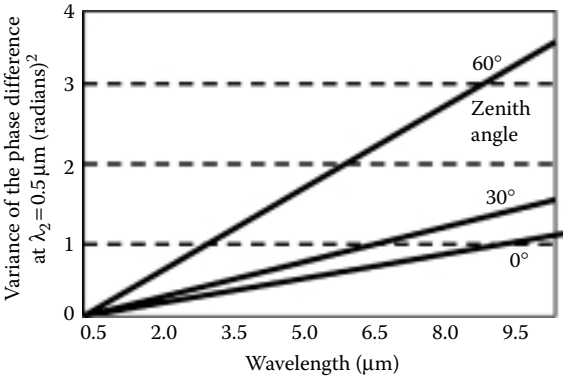

FIGURE 5.42
Phase difference for a laser transmitter at 0.5 μm with a sensor at another wavelength.

and amplitude modulation (scintillation). The difference in the measured wavefront and the wavefront needed to propagate a phase conjugate is a function of the zenith angle and the wavelength difference [348]. Figure 5.42 shows the variance of the phase differences for a propagated beam that is sensed at 0.5 μm. For transmission of short wavelengths, the adaptive optics sensing wavelengths must be close to the transmitted wavelength. For longer wavelength transmitters, the wavefront differences are less important.

6

Wavefront Correction

Wavefronts can be corrected using many of the same mechanisms that cause wavefront distortion. An image from a distorted mirror can be corrected by *distorting* another mirror into the proper shape to compensate for the wavefront variations. Local variations in the refraction index that were the cause of an aberration can be reversed, or conjugated, to provide the correction. Corrective lenses for eyes use this principle. The aberrations due to a malformed or strained lens in the eye are removed by placing an external lens in the path of the light entering the eye. The method of corrective eyeglasses is modal and static. Usually, only focus (curvature of field) and astigmatism are corrected and they do not have any active capability. This, then, is technically not *adaptive* optics; however, correction to the wavefront on most adaptive optics systems is based on the principle of adding a correcting device to the beam of light. When the correction is made active, that is, by moving the corrective element, it is said to be "inertial," with the correction linearly proportional to the stimulus.

As with sensing, there are both modal and zonal means of correction, in addition to nonlinear optical methods of correction based on the systems described in Chapter 4. The need to engineer better systems with higher spatial resolution, more stroke capability, and higher operational bandwidth has been a catalyst in developing actuators, faceplate materials, and analytical techniques that apply to many other areas of engineering.

Although compensation can be performed with active lenses [327], the most common devices are active mirrors. Devices used for real-time wavefront correction were reported in 1974 by several researchers [96,211,324,547]. These were primarily used for demonstrating the closed-loop technology needed for scaling to larger systems to compensate for atmospheric turbulence. Before the development of the deformable mirror (DM), however, scanning or tilt mirrors were widely used to correct for beam direction. Whether these devices are classified as modal adaptive-optics correction devices, or as image- or beam-tracking mirrors, is academic. The evolution of correction devices clearly emerged before the inception of adaptive optics as an engineering discipline.

Typical frequency ranges for correction devices are shown in Figure 6.1. A tilt mirror that can move very fast is restricted to only one mode, and therefore has limited spatial frequency capability. The opposite is the large active primary that can correct high spatial frequencies (many zones) but is limited in temporal frequency response. An active secondary mirror (SM)

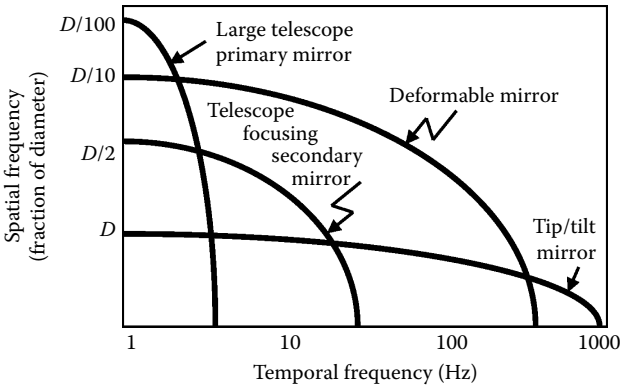

FIGURE 6.1
Spatial frequency versus temporal frequency of correcting elements: tilt/steering mirror; telescope secondary mirror focus correction; multiactuator deformable mirror; active telescope primary mirror.

on a telescope can be used to correct for focus, but because of strict requirements to maintain alignment, it has limited temporal bandwidth. A multiactuator DM can correct many zones at a high speed and is a candidate for an all-purpose device.

Figure 6.1 does not show the dynamic range or stroke of these devices, which is a major limiting factor in choosing a particular modality. One might conclude that the DM would be best for most temporal and spatial spectra, but unfortunately, this is not always possible. Low-order mode correction, such as tilt jitter, often requires large-amplitude motion. A DM will reach the end of its actuator stroke correcting for the beam tilt without leaving any margin for the actuators to correct for the high spatial frequency aberrations. For instance, a 20-cm DM, with a ±10 μm stroke limit, can only correct for a 1.0-mrad tilt. Many sources of tilt impart tens of milliradians into a system. A separate tip/tilt mirror in the system is normally required. However, a DM mounted on a two-axis tip/tilt platform can be used [861]. System design safety margins of at least 1.5 for temporal bandwidth and 2.0 for dynamic range are recommended.

For atmospheric compensation, the stroke requirements for the tilt mirror and the DM can be calculated. The standard deviation of the angular tilt imparted by the atmosphere is

$$\alpha_{SD} = 0.43\left(\frac{D}{r_0}\right)^{5/6}\frac{\lambda}{D} \tag{6.1}$$

where D is the telescope aperture. The total stroke of the tilt mirror must be about 2.5 times the standard deviation. The tilt mirror diameter, D_{TM}, is smaller than the telescope aperture diameter, and its angular motion is

demagnified. The angular motion of the tilt mirror must then be multiplied by the magnification of the optical system, namely D/D_{TM}. Combining the full-stroke requirement and the magnification requirement with Equation 6.1, the angular stroke of the tilt mirror will be

$$\alpha_{TMstroke} = \pm 1.1 \left(\frac{D}{r_0} \right)^{5/6} \frac{\lambda}{D_{TM}} \tag{6.2}$$

The requirements for a segmented mirror or a continuous faceplate DM can be determined similarly. The standard deviation of phase in a subaperture is

$$\phi_{SD} = 0.06 \left(\frac{D}{r_0} \right)^{5/6} \text{ waves} \tag{6.3}$$

The peak-to-peak motion is $5\phi_{SD}$. The mechanical stroke of a mirror is half the phase change placed on the beam; thus, the total stroke required for each actuator is

$$s = 0.15 \left(\frac{D}{r_0} \right)^{5/6} \lambda \tag{6.4}$$

There is no single *best* adaptive optics correcting device. Design choice depends on structural materials, actuator characteristics, and the working environment [187]. For example, evaluation of the expected aberrations and their dynamics is required before making the basic decision between a bimorph and a stacked actuator DM [304]. The correction requirements, bandwidth, stroke, and number of correction zones are driven by system considerations, such as sensing and control capability, and practical constraints, such as cost and complexity.

In some cases, an adaptive SM at the telescope is beneficial. The SM is common to all the telescope-imaging paths and it does not add another optical surface. A few problems are introduced with this approach. The most significant is that the DM is not near a conjugate image of atmospheric turbulence, which results in a smaller isoplanatic patch.

6.1 Modal-Tilt Correction

The simplest form of wavefront correction is variation of the beam direction, or the tilt of the wavefront. These methods preceded the concept of *adaptive optics* but serve as a basis for many more complicated forms of correction.

The amount of energy needed to control the tilt mode in an optical system is directly related to the stroke and bandwidth requirements for the steering mirror. For a constant diameter–thickness ratio, the inertia of the scanning flat-plate mirror is proportional to the fifth power of the mirror diameter. The subsequent force needed to move the mirror is proportional to the maximum required torque τ, divided by the mirror diameter D. The torque is given by the expression

$$\tau = I_m \omega^2 \theta \left[\left(1 - \left(\frac{\omega}{\omega_n} \right)^2 \right)^2 + \left(2d \frac{\omega}{\omega_n} \right)^2 \right]^{1/2} \tag{6.5}$$

where I_m is the mass moment of inertia, ω is the frequency of oscillation, ω_n is the mirror tilt-mode resonance, θ is the stroke of the mirror at frequency ω, and d is the system-damping factor. The amplitude (stroke) and bandwidth considerations (θ, ω) of the disturbance will drive the requirements for the tilt mirror. Equation 6.5 can be used for the initial approximations of the torque and the force required for tilt correction.

Tilt mirrors that incorporate specific requirements for their applications have been built. In addition to the stroke and bandwidth requirements for tilt and beam steering, some tilt mirrors have replaced the SMs of telescopes [147]. Others have met the requirement that they be reactionless [592], that is, the motion of the tilt mirror does not translate back into the optical bench or supporting structure. Tilt mirrors with both coarse and fine stroke separation [280] and magnetostrictive actuators [9] have been developed. Large-angle tilt mirrors are needed for wide-field-of-view systems. Shen et al. [719] describe a mirror with a 15-mrad stroke at 500 Hz and up to a 250-mrad stroke at 150 Hz. Each of these advancements provides for precision tracking of the object and, by itself, adaptive-optics correction for the lowest disturbance mode, the beam tilt.

6.2 Modal Higher-Order Correction

The next most common form of correction is an active focus system. When one peers through a telescope, an image is brought into focus by one's knowledge that a "fuzzy" image is out of focus while a "sharp" image is not. By cycling through the position of the sharpest focus, the system can be made to adapt to variations in the receiver's lens system, the observer's eye, or his or her camera. Specialized devices for remote focus-only correction were demonstrated as early as 1973 [84,530].

Astigmatism can be corrected by moving a single lens or mirror. If a cylindrical mirror or lens is aligned with the beam and moved along the optical

axis, astigmatism is changed. By having two mirrors or lenses with their cylinder axes oriented 45° to each other, astigmatism for all orientations can be corrected. When it is necessary to correct for modes higher than astigmatism, the wavefront can be divided spatially. Each part of the beam is corrected by applying the required strength of correction to that part. Devices that work in this manner are called *multichannel correctors*, such as segmented mirrors or continuous faceplate DMs.

6.3 Segmented Mirrors

The earliest implementation of a multichannel corrector was the segmented mirror. This is a mirror made up of a number of closely spaced small mirrors with piston- or tilt-correction capabilities (Figure 6.2). Thus, higher-order modes of correction can be applied by determining the individual contribution of each of the segments. Some segmented mirrors of this type have been operated in a *piston-only* mode, whereby each segment is confined to simple up-and-down motions. The *piston/tip/tilt* mode* has also been shown. Each segment operates with three degrees of freedom: the up/down piston mode and two orthogonal axes of tilt. A further consideration is the shape of the segments. Square, hexagonal, and circular segments have been used. A theoretical comparison of these shapes was reported by Malakhov et al. [498].

Segmented DMs can be used to correct static aberrations in an optical system [2] or to compensate for atmospheric turbulence [687]. Segmented mirrors are scalable to very large numbers of segments. Mirrors with as many as 512 segments (0.76 cm in size) have been built [321,363]. Modern technology, using modules as large as 14×14 segments, has made it possible to produce segmented mirrors with more than 10,000 segments. The relative ease of assembly and maintenance are important factors to consider. The cost and difficulty of replacing a single segment is much less than the equivalent maintenance of a continuous-surface mirror [178]. On the other end of the size spectrum, microelectromechanical systems (MEMS)–based segmented mirrors have been developed (Figure 6.3) and can be produced in large quantities at a relatively low cost [338].

When used with a broadband source, a segmented mirror must be absolutely phased, because modulo-2π steps would seriously degrade performance. Long stroke actuators are required to provide broadband correction. Segments with a 6- to 10-micron stroke have been incorporated into a segmented mirror [364]. However, the discontinuities (gaps) between segments have an impact on overall performance. Energy is lost through the gaps, and

* Tip/tilt is the same as two-axis tilt.

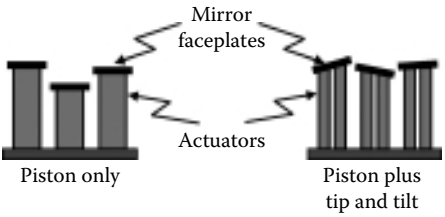

FIGURE 6.2
Segmented multichannel mirrors.

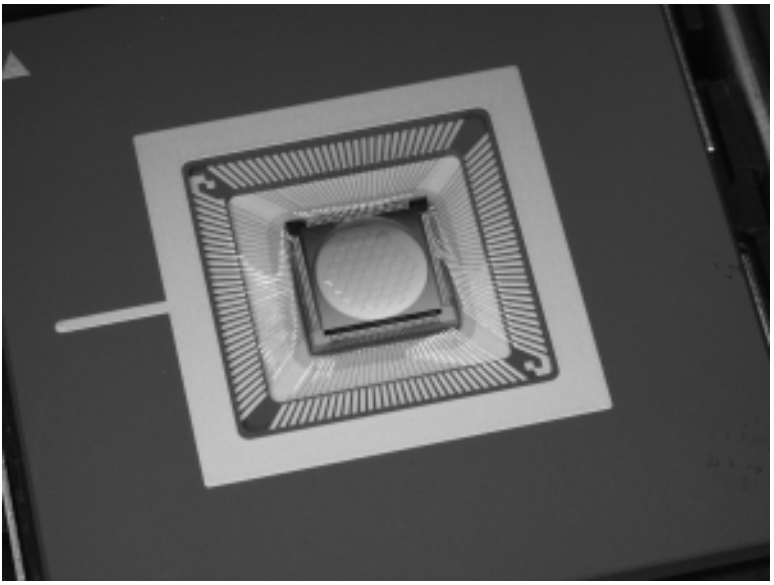

FIGURE 6.3
The Iris AO PTT111 segmented micromachined deformable mirror has 37 hexagonal segments with 111 degrees of freedom over a 3.5-mm aperture. (Photo courtesy of Iris AO, Inc. Berkeley, CA.)

because the gaps cause the mirror to act as a grating, energy is diffracted from the central lobe. It is important that the area of the gaps be below 2% [364]. Because each segment operates independently, there is no cross- coupling or need for actuator preloading. The step response for a segment can be as low as 100 μs. Segmented mirrors operating with closed-loop bandwidths as high as 5 kHz are currently in use [157,363]. In some cases, electronic cross-coupling between segments or groups of segments is needed to increase the control bandwidth. The 0.5-m phased-array mirror extensible large aperture [288] uses a control hierarchy that clusters segments and achieves a 2-kHz bandwidth [452].

6.4 Deformable Mirrors

Other multichannel correctors fall under the class *deformable mirrors* or DMs. These are generally continuous-surface mirrors with a mechanical means of deformation [606] to match the desired conjugate wavefront (Figure 6.4). The devices that perform the deformation—the actuators—can be continuous, such as in a membrane mirror [140,892] or a bimorph mirror [744]. They can also have discrete actuators perpendicular to the surface [325], or can have discrete actuators on the edges that impart bending moments [259], as shown in Figure 6.4. Because the surface of the mirror appears to bend similar to a rubber membrane stretched across a frame, continuous-surface DMs are often called "rubber mirrors."*

Concurrent with the need for propagating high-energy lasers, the requirement for correction devices that could provide high spatial frequency correction, along with being able to survive the high flux loads on the surfaces, also arose. Piezoelectric DMs with hundreds of actuators were developed by 1974.

Discrete actuator DMs with stacked piezoelectric actuators were developed in the late 1970s to address the large stroke requirements of infrared systems [184,186,235]. To generate enough force to deform the mirror surface by 0.8 μm, stacks of piezoelectric disks were made. The total voltage required for each stack was more than 1 kV, which usually is implemented by biasing to 500 V and then applying ±500 V. Development of high-power discrete actuator DMs was a difficult extension of passive high-power mirrors. Acomparison of molybdenum faceplate mirrors with up to 61 actuator stacks has been reported [409]. Various piezoelectric materials exhibit hysteresis, and actuator–faceplate configurations show different forms of influence functions [205].

Requirements for atmospheric turbulence compensation push the technology of DMs. Hundreds of actuators must be close together. Miniaturization of actuators, low operating voltages, position accuracy, and low hysteresis become important parameters [188,261,377]. The dynamics of an actuator in a DM force train are complicated by the linkage between the actuator and the optical surface [505]. Mechanical, chemical (glues), and electromagnetic connections are commonly used. The stricture, spring rates, and damping within the mechanical structure can contribute to hysteresis. Active control of hysteresis has been proposed [414], but low-hysteresis actuators reduce the complexity of the control system and increase the closed-loop bandwidth.

Mirrors with low-voltage lead–manganese–niobate, or $Pb(Mg_{1/3}Nb_{2/3})O_3$ (PMN), actuators [11] or magnetostrictive actuators [514] have been developed. For high-power laser applications, DMs with multiple-layer dielectric

* A rubber membrane will stretch laterally, whereas a thin-plate mirror is very rigid in-plane. Although not physically accurate, the jargon is still used.

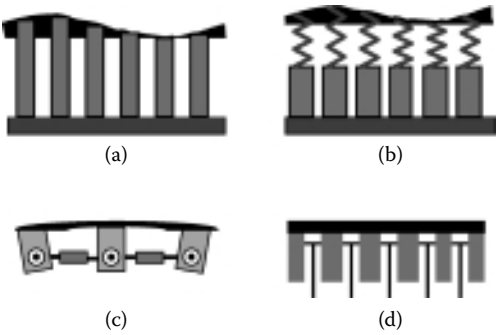

FIGURE 6.4
Continuous-surface deformable mirrors: (a) discrete position actuators, (b) discrete force actuators, (c) bending moment actuators, and (d) monolithic mirrors.

coatings with very high reflectivity must be used [121]. The coatings must withstand the thermal loads of the high-power beam and the stresses induced by the active deformation. Methods of quantifying and characterizing the performance of discrete actuator DMs have been evaluated [206,263]. In addition to hysteresis and influence functions, the linearity of the actuator response, the faceplate–actuator resonance, and the limits of actuator stroke (throw) are important characteristics for evaluating the utility and performance of a DM.

The need for adaptive optics in large telescope systems is clear. Because of the requirement to minimize the number of optical surfaces in the beam train to reduce losses due to absorption and scattering, DMs have been incorporated into other optical elements [684,840]. The SM of the converted Monolithic-Mirror Telescope (MMT) in Arizona, has 324 electromagnetic actuators [102,506]. The SM of the Gemini 8-m telescope will be the adaptive optics system DM, as well as the chopping secondary for infrared operation [134].

Because total actuator stroke and (nearest neighbor) interactuator stroke can be limited, some systems require a large-stroke, low-actuator-density DM working in combination with a small-stroke, high-actuator-density DM, a so-called "woofer-tweeter" approach [109,149,356,411,504].

6.4.1 Actuation Techniques

Actuators used for discrete actuator and edge actuator DMs are generally placed into one of two classes: force actuators and displacement actuators. The application and the mechanical structure define the conversion from force to displacement via Newton's second law. The most common materials used for DM actuators are piezoelectric ceramics [726], such as $Pb(Zr,Ti)O_3$ or PZT [5,744], whereas Kokorowski [421] and Sato et al. [696] report the use of polyvinylidene fluoride (PVDF). Developments in PMN ceramics have yielded large electrostrictions compared to PZTs [798].

By layering PVDF [697] or stacking PZT [605], large strokes can be obtained with submicron accuracy for corrections equivalent to many waves. The high voltages needed to drive the stacks of PZT (upward of 1000 V) often present serious design constraints that require large auxiliary support equipment. The development of Terfenol magnetostrictive actuators for DMs reduces the requirement for high voltages, because magnetostrictives operate at only a few volts [26,298]. However, the energy required to move the surface is the same [9]; thus, high currents (up to 1 A each) are required for these actuators. Cooling of the actuators is often required to avoid thermal creep and misalignments.

Other electromagnetic devices have been used for adaptive optics correcting devices. Voice coil (solenoid) actuators are common in scanning mirrors because of their large forces and displacements produced. A helical solenoid (helenoid) provides a very fast response time, which, when coupled with its low-voltage operation, results in a very attractive package for driving optics [16,709,724].

For low-frequency correction (up to 10 Hz), various types of mechanical drives have been used. Worm gears and direct-acting direct current (DC) motors [401], hydraulic actuators [601], and differential ball screws [290] have been used to drive mirror surfaces.

Ealey [185] presents the key design fundamentals and parametric trades necessary to choose a precise actuator for a specific application. The analysis includes a discussion of PZT, PMN, Terfenol, nickel–titanium-based NiTiNOL, bimetal alloys, and paraffin thermal actuators. Light-driven PVDF actuators have been demonstrated and show that the force is proportional to the power of the laser beam illuminator [691].

6.4.2 Actuator Influence Functions

Mirrors can be driven to many different shapes to compensate for a wide range of distorted wavefronts. The choice of a particular design is based on the amount and nature of the correction required and the cost and complexity of its operation Some mirrors with as few as four actuators have been shown to correct for both focus and astigmatism [218]. For instance, an astronomical imaging system with a 1.5-m aperture requires a DM with at least a ±0.6-μm stroke to correct for atmospheric turbulence. Many wavefront reconstructors provide direct-drive signals to the segments or DM actuators (see Section 7.4). The greater the number of degrees of freedom of the corrector, the greater is the number of wavefront variations it can correct. If many segments are placed close together, the constraint of flat surfaces fitting a curved wavefront can be overcome. The advantages of continuous-surface mirrors—the absence of surface gaps that affect diffraction, for instance—often are reduced by the structural constraints that limit the surface shape that can be formed. The stress and strain of the mirror materials result in structural coupling between elements of the mirror; this coupling conceivably could enhance, but usually limits, the utility of a particular DM.

The actual shape of a DM surface, when it is pushed by an actuator, is called its *influence function* [342]. It is a function of mirror faceplate parameters such as thickness, modulus of elasticity, and Poisson's ratio (Figure 6.5). The location and distribution of the applied force and the structural inhomogeneities contribute to the uniqueness of a particular mirror or a particular actuator within a mirror. Measurement of influence functions is a tedious, but necessary, process [263]. Modeling the shape of the mirror surface, its influence function, has been a topic of discussion for a number of years. To describe the shape of an actual DM would require detailed calculations, such as finite element analysis, that consider all the parameters mentioned in this section. Approximations to finite element methods are needed to describe multiactuator mirrors.

The spatial response of each channel (the influence function) is discussed by a number of authors. For correction of turbulence, Hudgin [360] derives the fitting error for (1) piston, Gaussian, and pyramidal influence functions; and (2) a prototype mirror. Taranenko et al. [754] derive analytical expressions in exponential form for the influence of soft and stiff metal surfaces. They also compute the resonant frequencies as functions of the material parameters as follows:

$$\nu_{\text{res}} = \frac{10.21h}{2\pi R^2}\sqrt{\frac{E}{12\rho(1-\sigma^2)}} \tag{6.6}$$

where h is plate thickness, ρ is material mass density, R is distance to the nearest clamped point, such as another actuator, E is Young's modulus, and σ is Poisson's ratio.

Claflin and Bareket [140] calculate the influence function for continuous-surface mirrors from Poisson's equation and then use least-squares principles to fit the surface of a multichannel mirror to Zernike polynomials for analysis. Harvey and Callahan [334] proposed using methods of linear

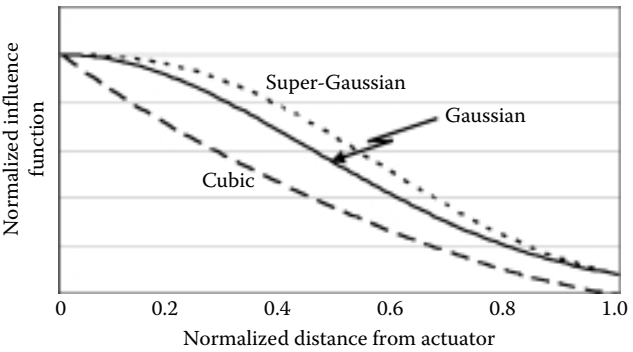

FIGURE 6.5
Analytical forms for DM influence functions: Gaussian $\exp(-\beta r^2)$; super-Gaussian $\exp(-\beta r^{2.5})$; cubic polynomial.

theory to relate the correcting capability of a continuous-faceplate mirror to the interactuator spacing and the wavefront autocovariance length. These system considerations have been discussed in detail in Sections 3.1 and 3.5.

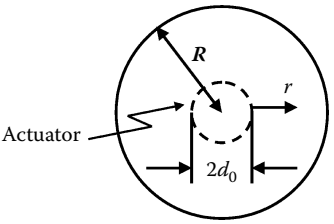

FIGURE 6.6
Influence function can be found by analyzing the stress and strain of a flat plate.

To simplify analysis and design of the complete adaptive optics system, one normally considers identical, symmetrical influence function models [522]. The effects of fixed edges or unusual patterns are treated as perturbations to the homogeneous set of mirror influence functions [10]. If one considers each actuator to be independent, the linear sum of the influence functions, $Z(x, y)$, would represent the mirror surface, $S(x, y)$, as follows:

$$S(x,y) = \sum_{i=1}^{N} A_i Z_i(x,y) \tag{6.7}$$

The actuator amplitudes are indicated by the variable A_i. One form of the influence function can be found by assuming that each actuator acts independently with a force W over an area πd_0^2 on a plate of thickness t that is unconstrained at the edge [655] (Figure 6.6). Converting to polar coordinates, the displacement of the circular plate of radius R at a distance r from the center of the force is

$$Z(r) = \Upsilon\left[\frac{(12m+4)(R^2-r^2)}{m+1} - \frac{2(m-1)d_0^2(R^2-r^2)}{(m+1)R^2} - (8r^2+4d_0^2)\ln\frac{R}{r}\right] \tag{6.8}$$

for $d_0 < r < R$, and

$$Z(r) = \Upsilon\left[4R^2 - 5d_0^2 + \frac{r^4}{d_0^2} - (8r^2+4d_0^2)\ln\frac{R}{d_0} - \frac{2(m-1)d_0^2(R^2-r^2)}{(m+1)R^2} + \frac{8m(R^2-r^2)}{m+1}\right] \tag{6.9}$$

for $r < d_0 < R$, where

$$\Upsilon = \frac{3W(m^2-1)}{16\pi E m^2 t^3} \tag{6.10}$$

with E the modulus of elasticity, and m equal to the reciprocal of Poisson's ratio [655]. When the edges are constrained, the influence function takes a slightly different form. For $d_0 < r < R$,

$$Z(r) = \Upsilon\left[4R^2 - (8r^2+4d_0^2)\ln\frac{R}{r} - \frac{2r^2d_0^2}{R^2} - 4r^2 + 2d_0^2\right] \tag{6.11}$$

and for $r < d_0 < R$,

$$Z(r) = \Upsilon\left[4R^2 - (8r^2 + 4d_0^2)\ln\frac{R}{d_0} - \frac{2r^2 d_0^2}{R^2} + \frac{r^4}{d_0^2} - 3d_0^2\right] \tag{6.12}$$

Although these expressions are quite accurate, a number of investigators have used different analytical forms to simplify their models. An influence function that maintains Cartesian symmetry of a square pattern of actuators follows the following cubic form [390]:

$$Z(x, y) \propto (1 - 3x^2 + 2x^3)(1 - 3y^2 + 2y^3) \tag{6.13}$$

Taranenko et al. [754] measured the influence functions for aluminum, copper, and steel plates and found them closely following either a Gaussian or a super-Gaussian form within 5%:

$$Z(r) = \exp(-\beta_1 r^2) \quad \text{for} \quad \text{Al, Cu} \tag{6.14}$$

$$Z(r) = \exp(-\beta_2 r^{2.5}) \quad \text{for} \quad \text{steel} \tag{6.15}$$

where $\beta_1 = 2.77$ and $\beta_2 = 3.92$. Similar Gaussian functional forms have been found experimentally [263,357]. A comparison of these functional forms (Figure 6.5) shows that although there are slight differences, the simple form—the Gaussian—represents a DM influence function quite well.

One difficulty occurs when the linear sum model is used. If all the actuators are pushed identically, the model shows a surface composed of bumps of equal height. This rippled surface does not correspond to the surface of an actual device with a stiff faceplate. Because the load is equally distributed, the mirror surface will rise in a piston mode, leaving the surface flat, rather than rippled. The model surface, appearing similar to a membrane backed by pins, exhibits an effect called *pinning error*.

Another difficulty arises because coupling occurs. If the stiffness of actuators is very high compared to the faceplate, there will be little coupling. The surface will deform in the direction of the force near the actuator and deform in the opposite direction past the adjacent actuator. This form is most often represented by the $\sin(r)/r$ function as follows:

$$Z(r) = \frac{\sin\left(\dfrac{\pi r}{r_s}\right)}{r} \tag{6.16}$$

where r_s is the interactuator spacing.

For simplicity, the Gaussian form (Equation 6.14) can be expressed in terms of its coupling, κ, as follows:

$$Z(r) = \exp\left[\frac{\ln(\kappa)}{r_s^2} r^2\right] \tag{6.17}$$

Actuators can be arranged in various geometric patterns. Many simple mirrors have square Cartesian layouts with 4, 9, or 16 actuators To avoid the expense of actuators being outside circular beams, the corner actuators are removed; thus, we see counts of 21 (5×5 minus 4 corner actuators), 69 (9×9 minus 12 corner actuators), 241 (17×17 minus 48 corner actuators), and 941 (35×35 minus 284 corner actuators). Maximizing the number of actuators in a circle results in hexagonal arrays of 1, 7, 19, 37, 61, 91, 127, and so forth. The number simply follows the following form:

$$1 + 6\sum_{n=1}^{N} n \tag{6.18}$$

where N is the number of encircled hexagons.

6.5 Bimorph Corrector Mirrors

A *bimorph* DM consists of a glass or metal mirror faceplate bonded to a sheet of piezoelectric ceramic [373]. The ceramic is polarized normal to its surface. The bonding is generally a glue that will not shrink after application. The glued interface between the mirror and the ceramic contains a conducting electrode. After the exposed piezoelectric ceramic is covered with a number of independent electrodes, the front is polished and coated to form the DM surface. Wires are attached to the single front electrode and the various back electrodes (Figure 6.7). Various patterns of back electrodes have been used. Steinhaus and Lipson [744] used conductive paint to form a pattern of 12 segments. Adelman [5] analyzed a pattern of concentric circles, and Halevi [317] used various patterns of large and small squares. A 36-element bimorph

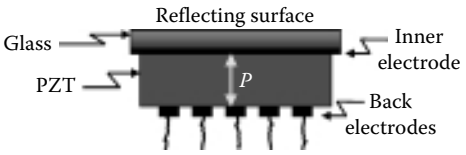

FIGURE 6.7
Cross section of a bimorph deformable mirror.

with three concentric rings of electrodes was optimized for the 8.2-m Subaru Telescope [593]. A modular silicon bimorph with thick-film piezoelectric actuation, containing up to 133 electrodes, has been described [667].

When a voltage is applied between the front and back electrodes, the dimensions of the piezoelectric material [533] change by an amount depending on the electric field and the coefficient of the piezoelectric tensor d_{13}. Neglecting the stiffness of the layers, the local radius of curvature of the mirror, R, changes in proportion to the applied voltage V, and is given by

$$R = \frac{V d_{13}}{t^2} \tag{6.19}$$

where t is the thickness of the ceramic plus the facesheet [467]. For a back electrode of diameter D, the voltage necessary for a center-to-edge deformation of one wavelength is given by

$$V_\lambda \approx \frac{2\,t^2\,\lambda}{D^2\,d_{13}} \tag{6.20}$$

Because the local *curvature* of the corrector is proportional to the voltage, bimorphs are particularly well suited for integration with a wavefront curvature sensor [467,646]. This greatly simplifies wavefront control and essentially eliminates an intermediate wavefront reconstructor.

Regardless of the hysteresis or depolarization properties, typical values for Equation 6.20, $d_{13} = 2 \times 10^{-12}$ m/V, $t = 1$ mm, $D = 10$ mm, $\lambda = 0.5$ μm, give a value of 50 V [744]. This voltage range is easily obtained in practical applications. Halevi's analysis [317] included a solution of the time-dependent equation of state for a bimorph mirror with accompanying expressions for mirror deformation and resonant frequencies.

Improvements on the basic design include the addition of a second piezoelectric sheet bonded to the first with reverse polarization. When a voltage is applied to this configuration, the thickness does not increase, because one plate contracts while the other expands. This opposing expansion–contraction results in the entire plate bending like a bimetal strip, with deformation occurring at the top and bottom surfaces. Kokorowski [421] provided a detailed analysis of this effect for infinite slabs and finite square slabs.

Vorontsov et al. improved the configuration by using a conductive faceplate, such as copper, rather than separate electrodes and glass faceplates [835]. Their flexible bimorph mirror was configured for both 9 and 13 back electrodes with auxiliary tilt mode control. They demonstrated nearly 0.1 waves of correction for astigmatism, coma, and spherical aberration by applying about 30 V. Vorontsov et al. [835] also reported the development of a cooled bimorph with an 80-mm aperture. Ning et al. [568] analytically compared bimorphs with various configurations of layers in terms of their response function and sensitivity.

6.6 Membranes and Micromachined Mirrors

Another form of continuous-surface mirror is the *membrane mirror* [312]. A reflective membrane is positioned between a transparent electrode and a series of individual electrodes at the back of the mirror, as shown in Figure 6.8. When no voltage differential is applied, the membrane remains flat. When a voltage is applied, however, the electrostatic attraction between the electrodes deforms the membrane into a desired shape. The local curvature of the surface can be represented as

$$\nabla^2 z(x,y) = \frac{\partial^2 z(x,y)}{\partial x^2} + \frac{\partial^2 z(x,y)}{\partial y^2} = -\frac{P(x,y)}{T} \tag{6.21}$$

where T is the membrane tension (force/length) and $P(x, y)$ is the pressure (force/area) at position x, y. The membrane is suspended in a partially evacuated environment to reduce damping. For large-stroke designs [438], damping has been found necessary, because the surface tends to be unstable and pins the membrane against the electrodes. In these circumstances, fluids are added to produce the required damping. Because no piezoelectric ceramic is used, this type of mirror exhibits virtually no hysteresis. The density of actuators is only limited by the need to place the back electrodes far enough apart so that they can withstand the voltages necessary for deflection of the membrane without snapping down the surface all the way to the substrate and destroying the mirror.

Takami and Iye describe a membrane mirror used in the Subaru Telescope [749]. The membrane is made of nitrocellulose of 50 mm diameter and 2 μm thickness, which allows a clear aperture of 25 mm. The aluminum coating acts as both the electrode and the reflective surface. A 3.3-kHz bandwidth was achieved. Another membrane mirror constructed at the University of Heidelberg [523] consists of an aluminized polypropylene membrane placed between a transparent electrode on a glass window and 109 hexagonal back

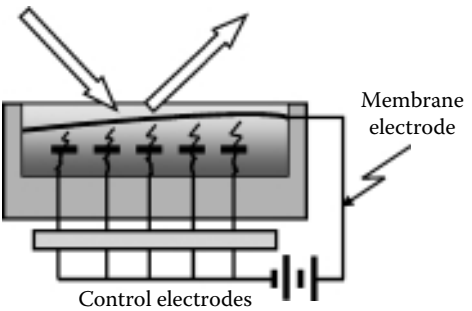

FIGURE 6.8
The principle of an electrostatic membrane mirror.

electrodes. This mirror was studied by Claflin and Bareket [140] for use as a laboratory aberration generator.

Stability between the electrostatic and mechanical energies of the membrane requires careful design and fabrication [437]. One new class of membrane mirrors, called MEMS–DMs, are made from components that are micromachined on silicon or metal substrates [81,82,815]. MEMS–DMs are the first low-cost mass-produced adaptive optics components [613]. These devices, built as microchips, can be segmented [338] or have continuous faceplates [816,828]. They use very little current to mechanically produce deformations [204] of the optical surface up to 20 μm [143]. Because of their small size, thousands of actuators can be applied to mirrors [437] and integrated into wavefront sensors and reconstructors on a single microchip (Figure 6.9).

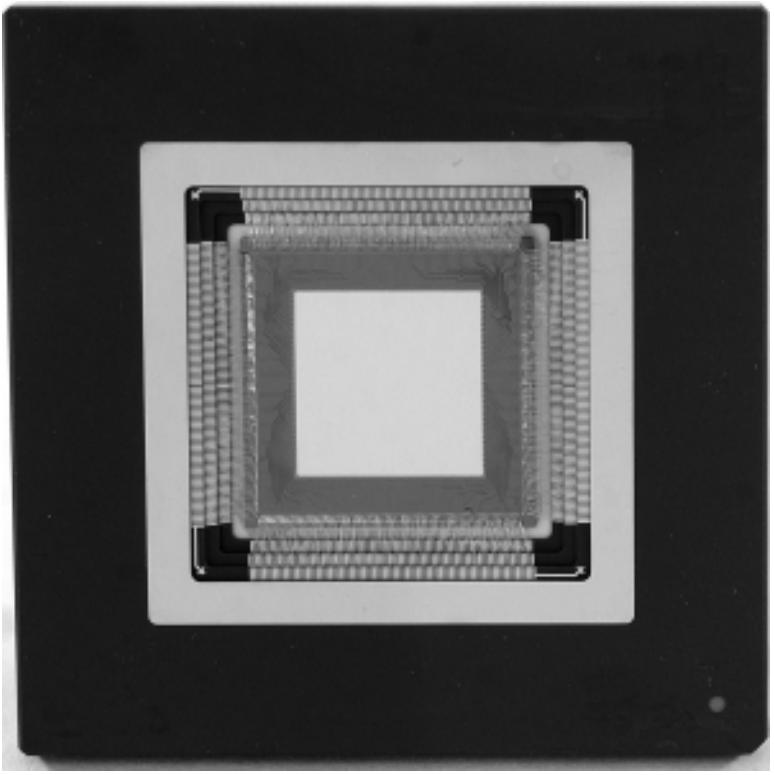

FIGURE 6.9
Boston Micromachines microelectricalmechanical system deformable mirror with a continuous surface and a 9.3-mm aperture. The electrostatically actuated mirror has 1020 actuators (32×32 array, with the corners cut off) and a stroke of 1.5 microns; it operates at speeds up to 60 kHz. (Photo courtesy of Boston Micromachines Corporation, Cambridge, MA.)

With large telescopes, very large numbers of actuators are required (up to 15,000 for the Thirty Meter Telescope [843]). MEMS–DMs can be driven modally or zonally [87,459].

6.7 Edge-Actuated Mirrors

DMs with actuators attached to the edge of the optical surface can be used to apply certain low-order optical modes. By moving the actuators in the same plane as the surface, bending moments that correspond to focus or astigmatism can be induced. A prototype mirror was demonstrated by Fuschetto [260]. Although the mirror was called a "three-actuator" mirror, it really consisted of six stacks of piezoceramic material placed 60° apart (Figure 6.10). The mirror substrate was molybdenum and it had a beryllium base for support and a reference surface for the actuators.

Analysis showed that about 10 μm of defocus error and 5 μm of astigmatism could be corrected with a bandwidth of about 100 Hz. Nichols et al. [561,562] report that the performance of this mirror exceeded predictions and had less than 10% coupling between the modes whenever corrections were applied.

An edge-actuated mirror made of Zerodur glass was demonstrated by Malin et al. [500]. The mirror surface was hexagonally shaped with a maximum dimension of 24 inches. It was deformed by two rings of 12 electrodynamic actuators. One ring was tangential to the mirror edge, while the other 12 were positioned to apply forces radially. This configuration supported both bending moments and shears. Experimental testing showed peak-to-valley focus compensation greater than 2 μm and astigmatic correction of about 1.5 μm.

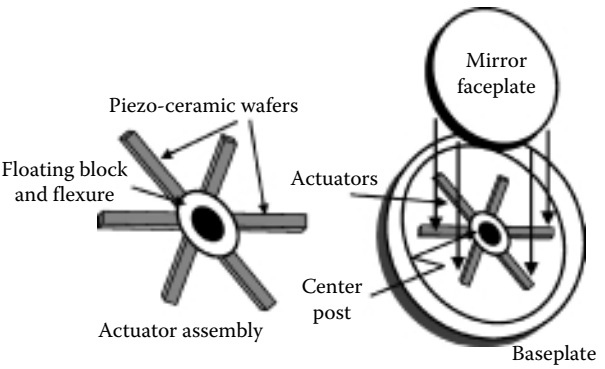

FIGURE 6.10
Edge-actuated deformable mirror.

6.8 Large Correcting Optics

Gravitational loads and surfacing difficulties of large optics result in distortions that cannot be removed before use. By placing actuators behind the faceplate of large primary mirrors, the latter become high spatial frequency DMs that can be self-correcting. They can remove wavefront errors that appear in large optical elements used in beam propagation and astronomy [38,59]. Performance trades arise because there is no "best" mirror facesheet thickness. More actuators are required to maintain control of a thin faceplate, because it is less stiff. However, if the faceplate is thickened, the actuators require more force. Segmentation of the mirror is required when the mirror sizes become very large. Although segmentation allows thinner individual facesheets, the segments require controlling mechanisms that maintain the alignment and phasing of the individual segments.

Each of the 10-m Keck telescopes [379,471,520,521,532] has 36 active 0.9-m segments with an independent piston and two-axis tilt control [557,558]. The Keck segmented primary mirror is not used for the compensation of the atmosphere. The segment control is primarily designed to remove local vibrations and deformations as the telescope is moved. An adaptive optics system for the two Keck telescopes operates in the near infrared region (1.0 to 2.2 μm) [511]. The adaptive optics system provides tip/tilt correction for the SM.

Large telescopes in space can avoid atmospheric effects and gravitational distortion. Optics larger than those of the Hubble Space Telescope are being developed by the National Aeronautics and Space Administration (NASA), industrial partners, and universities. The James Webb Space Telescope (JWST) will have a deployable 8-m primary mirror with a system designed for observing wavelengths from 0.5 to 12 μm. The JWST will include actuators on the primary mirror petals and a DM at a pupil of the optical system. A number of lightweight technologies have been investigated for DM applications [407,408].

6.9 Special Correction Devices

In addition to the conventional inertial correcting devices described in Sections 6.1 through 6.8 and nonlinear phase conjugation devices, a number of other devices are useful in correcting distorted wavefronts. They are used in specialized applications because of technical limitations. These special devices have not exhibited the necessary robustness for use in large systems or for application under high-power or adverse thermal or vibrational environments. They are employed mostly for low-power light valve applications in signal processing [675], compensated imaging [301], frequency filtering [253], and optical computing [512].

6.9.1 Liquid-Crystal Phase Modulators

Devices using liquid crystals [644] have been used in Fourier-plane filters for coherent optical processing and real-time correlators [223]. These are primarily intensity switches, rather than phase switches, needed for conventional adaptive optics. The response time of liquid crystals is about three magnitudes slower than that of the membranes [354]; however, the on–off modulation is usually greater than 90% [802]. Modeling results indicate that atmospheric distortions can be compensated with liquid-crystal devices [202,313]. There can be considerable fixed aberrations in some commercial systems [330]. Recent research into parallel-aligned liquid-crystal spatial light modulators (LC-SLMs) shows that the optical quality of the LC-SLMs after the correction of a 2.2-λ aberration can be as low as 0.124 λ with large numbers of pixels (1920×480) [117].

Nematic liquid crystals [486] can change their index of refraction by 0.2 under low applied voltages. Optically addressed liquid crystals [589] have been evaluated. An electrically addressable array can be used as a phase modulator with as much as 2.0 μm of phase change with 15 V applied [79]. A number of adaptive optics demonstrations or operational systems with liquid-crystal correctors have been reported [116,117,137,468,485,643].

6.9.2 Spatial Light Modulators

Spatial light modulators (SLMs) are transducers that modulate the incident light corresponding to the optical or electronic input. The light can be modulated in phase, intensity, polarization, or direction. Light modulation can be achieved by various electro-optical or magneto-optical effects [118]. A high-density electronic circuit can be integrated with SLM technologies to produce very high spatial resolution correcting devices. A 1000×1000 pixel array in a 1-inch square area is achievable. Full deflection of such devices can be achieved with 50 V or less at over 100-MHz rates. A thin metalized polymer membrane stretched over a supporting grid acts as the deformable surface. A 128×128 pixel device developed by Hornbeck [354], with 51-μm square pixels, had a peak deflection of 155 nm.

One all-optical approach for an adaptive optics system uses a SLM as the correcting element [219,220]. The monolithic SLM is placed behind a photocathode and a microchannel plate. Microchannel plates can have rise times of less than 1 ns with gains over 10^6 and more than a million channels [877]. When an interference pattern is imaged onto the photocathode, the electrons released are amplified by a microchannel plate and directed onto an electro-optical crystal that responds to the electric current. The resulting deformation is a map of the interference pattern and can be used as a phase conjugate. An interference phase loop [487] shows how an uncompensated signal beam can be corrected using such a device (Figure 6.11). Spatial resolution of a million pixels over a 5-cm aperture at frame rates greater than 1.0 kHz is

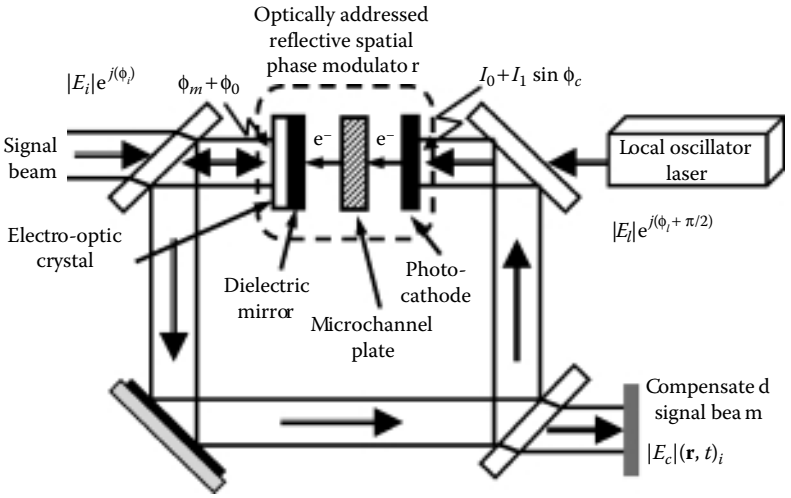

FIGURE 6.11
Spatial light modulator in interference loop.

feasible [701]. A variation on the interference loop configuration was demonstrated with an all-optical liquid-crystal phase modulator [86]. Another variation of this technology is the high-voltage electron beam driver of the charged large-array-flexible mirror [848].

6.9.3 Ferrofluid Deformable Mirrors

A magnetic liquid (ferrofluid) coated with a reflective metallic layer can be actuated by a magnetic field [442]. A 37-actuator version has been shown to have a stroke of up to 11 μm and a residual flatness of 0.05 μm [98].

7

Reconstruction and Controls

7.1 Introduction

Wavefront sensors, described in Chapter 5, measure the condition of the wavefront and produce signals that represent the wavefront. Both zonal and modal sensors may be used in a particular system. It is up to the reconstructor to sort out the meaning of those signals, and then it is the control system that must determine how to treat the signals and relay them to the appropriate correction device. In Chapter 4, many system concepts showed the control system as a "black box," that is, the controller received the signals from the wavefront sensor and magically translated them to signals for the correction devices. This chapter aims to remove the mystery of the controller and to describe the fundamental principles behind the adaptive optics control system.

Figure 7.1 is a rather complicated block diagram that shows the many paths that signals may take getting from the wavefront measurement to the correction system. In most cases, only a few of these paths are used. However, in many cases parallel paths are used whereby the system controls lower-order aberration modes, such as focus and tilt, via one path and simultaneously controls higher-order wavefront errors with a deformable mirror. This method has been used in many adaptive optics systems. The principles of those control methods are explained in detail in Section 7.3.

I will use a terminology convention that refers to control systems that generate a phase representation as *direct* and those that avoid an explicit determination of the phase as *indirect* [801]. Because the phase reconstruction is considered a fundamental intermediate step, any control system that avoids this step is hereafter called *indirect*. This may appear backwards, because the most direct route (less processing time, fewer electrical connections, less software, and so on) from wavefront sensor data to correction commands might bypass an intermediate phase representation step. The phase representation in the preceding context may take on many forms, such as a continuous phase map where the wavefront is evaluated at all points, a zonal phase map where the wavefront is known at only specific locations, or a modal phase map where the phase can be found at any point by adding the contributions from each mode. In addition, the phase representation may

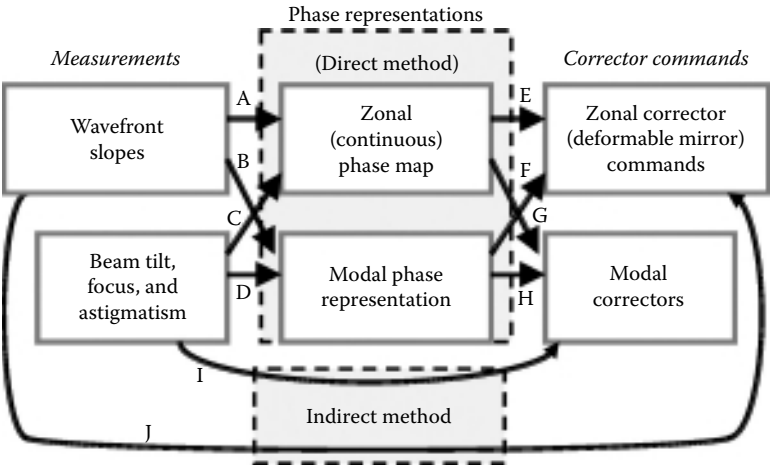

FIGURE 7.1
The various paths of wavefront control in a conventional adaptive optics system.

actually take the form of the derivatives of the wavefront at various points or even the derivatives of the aberration modes. In any case, whenever this step is explicit within the control system, it is deemed *direct*.

There are many books on linear control theory [43,113,126,513,579,810]. This chapter will take the important parts of control system theory and show how they apply to the specific field of compensating for an aberrated wavefront. Referring to Chapter 1, where adaptive optics was defined as being a *closed-loop* process, it is necessary to define the meaning of that term in a more formal manner.

Control systems are often classified as either *process control* or *servomechanisms*. The former control, also called *regulator control*, is designed so that the controlled variable or output is held to a constant or desired value. The human body-temperature regulation system is in the regulator control class. The body attempts to maintain a constant 98.6°F despite external disturbances. Servomechanisms do not maintain a constant output, but rather, they vary the output as the input varies. The output mechanism *serves* as a slave to the input master; thus, the term "servomechanism." Both classes of control are closed-loop. They respond to information from somewhere else in the system.

However, an *open-loop control* does not use feedback. A sequence control, where a series of switches turns on and off at predetermined times, is an example of open-loop control. This has application in optics, for example, when a telescope must point to a particular star following the rotation of the Earth. The preprogrammed movements are all that are necessary. We assume that the absolute position of the star will not vary significantly through one evening! Although adaptive optics control systems often analyze and direct many parallel channels of information, most of the systems in

practice are based on single-channel linear processing algorithms. Section 7.2 will address single-channel control from a temporal and frequency aspect. Section 7.3 addresses the spatial aspects of parallel control. The optical system under control may not be linear throughout its entire range; however, one can often assume that the optical and electronic signals are linear near the operating point of the control. We can use classical linear optimal control theory for designing and analyzing the system [343,434].

Adaptive optics control systems can be optical, analog electronic, digital electronic, and in some cases, fluidic. The actual implementation of the controls is left to the designer, who is often constrained by factors such as cost and size. Wavefront sensor signals can be gathered in the microvolt range, while corrector mirror drivers may need to operate in the kilovolt range. Hydraulic actuators may need to be controlled by relays and valves or other means. The details of electronic preprocessing, calibration, signal amplification, signal conditioning, power supply conditioning, isolation, and filtering will not be covered in this chapter. They will be addressed only when these specific processes become a part of the fundamental adaptive optics control problem. Subjects such as electronic or digitization noise will be treated according to standard methods.

7.2 Single-Channel Linear Control

The control of a single channel of an adaptive optics system is fundamental to the control of many channels of wavefront information. It also applies directly to the control of single-channel adaptive optics systems like beam-steering systems that only have tilt signals as input and single-mode steering mirrors as output. Although the two orthogonal axes of tilt may be operating simultaneously, it is usually possible to design a control to operate each axis as an individual linear control. The example of a beam tilt control (Figure 7.2)

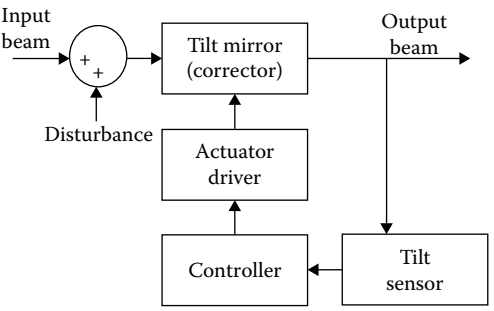

FIGURE 7.2
Single-channel closed-loop beam tilt control.

will be used as a basis for the discussion of single-channel linear control. An input beam enters the system from the left. A disturbance is added to the beam. The beam is deflected by a tilt mirror. The disturbance plus correction output is sensed. It is conditioned and amplified and fed to a controller that determines the degree of correction. The control signal is then conditioned and amplified and drives an actuator in the tilt mirror to remove the disturbance. The design of the controller will be an iterative process based on the results of analysis. The analysis will indicate the response of the system to changes in the input or disturbances. If that response is unsatisfactory, it often can be improved by changes in the controller algorithm, the amplifier, or the tilt mirror itself.

If the disturbance changes suddenly from one value to another constant value, a step-function input is assumed. There will be a certain period of time for the control system to respond so that the output levels off to its new value. This *transient* period should be sufficiently short, but not so sudden that the response of the system is oscillatory or results in unacceptable overshoot. After the transients have decayed, the system will demonstrate its *steady-state* response. Any errors between the input beam and the output beam should be small. The use of feedback, shown in Figure 7.2 as the tilt sensor–controller path, is the fundamental principle for the linear systems control operation. Feedback and adjustments to the parameters in the feedback loop are present to reduce the effects of parameter variations, reduce the effects of disturbances, improve the transient response, and reduce *steady-state* errors. The primary means of varying the control system, and its subsequent response, is by changing the gain of the control. One may think of the controller as a signal amplifier of the error signal. For large gains, the system response is more accurate (because small changes are noticed) and faster (because the tilt mirror responds more for a given input and, therefore, achieves its final position faster). The disadvantage of simply increasing the gain to achieve optimum control is the fact that the rapid response of the tilt mirror will result in an overshoot, because it cannot necessarily stop quickly when it reaches its desired position. Because the overshoot must then be compensated by continuing application of a counter-drive signal, the system oscillations can increase, and in the worst case, it never reaches the correct value because it is unstable. The relative stability of the system is maintained by keeping the overshoot of the response small. This compromise between large gain for rapid response and small gain for stability is the crux of the control problem in all aspects of adaptive optics.

7.2.1 Fundamental Control Tools

Linear control system theory is a well-developed field. Most controls analyses use *Laplace transforms*. They are used extensively as a manner of dealing with the complicated time-response of a system without having to constantly evaluate difficult integrals in the time domain. By transforming the equations of motion for the optical system into a Laplace space, the response can

be determined and analyzed by fairly straightforward algebraic operations. The variable in Laplace space is s. It is a complex number represented by a real part σ and an imaginary part $i\omega$, where ω is the frequency in radians per second. The Laplace transform of the function of time $f(t)$ is defined by

$$F(s) = L[f(t)] = \int_0^\infty f(t)e^{-st}dt \tag{7.1}$$

As mentioned in the preceding example, an important way of evaluating a control system is by observing its response to a step input. The step function of a constant amplitude A is given by $f(t) = 0$ for $t < 0$ and $f(t) = A$ for $t \geq 0$. The Laplace transform of the function is

$$L[f(t)] = \int_0^\infty Ae^{-st}dt = \frac{A}{s} \tag{7.2}$$

Another common test input is the ramp function $f(t) = At$, and its Laplace transform is

$$L[At] = \frac{A}{s^2} \tag{7.3}$$

The transient response of many optical systems is a decaying exponential $f(t) = Ae^{-\alpha t}$, which has the transform

$$L[Ae^{-\alpha t}] = \frac{A}{s+\alpha} \tag{7.4}$$

These and many other Laplace transforms can be found in handbooks and tables [1]. They are used extensively to relate the physical phenomena $f(t)$ to the controls phenomena $F(s)$. How these transform methods are used and how they relate to the language of the controls analysis will be explained next.

7.2.2 Transfer Functions

If the input of a system is given by the function $r(t)$ and the output is given by $c(t)$, assuming zero initial conditions ($c(0) = 0$, $r(0) = 0$), the dynamic behavior of a linear system is given by the differential equation

$$\frac{d^n c(t)}{dt^n} + a_{n-1}\frac{d^{n-1}c(t)}{dt^{n-1}} + \cdots + a_1\frac{dc(t)}{dt} + a_0 c(t) = \tag{7.5}$$

$$b_m\frac{d^m r(t)}{dt^m} + \cdots + b_1\frac{dr(t)}{dt} + b_0 r(t) \tag{7.6}$$

If the Laplace transforms of the functions are defined to be

$$C(s) = L[c(t)] \tag{7.7}$$

and

$$R(s) = L[r(t)] \tag{7.8}$$

then, the differential equation transforms to the following algebraic equation:

$$\left(s^n + a_{n-1}s^{n-1} + \cdots + a_1 s + a_0\right)C(s) = \left(b_m s^m + \cdots + b_1 s + b_0\right)R(s) \tag{7.9}$$

The *transfer function* of the system $G(s)$ is the ratio of the Laplace transforms of output and input and is given by

$$G(s) = \frac{C(s)}{R(s)} \tag{7.10}$$

The transform of the output $C(s)$, then, is the transfer function of the system times the transform of the input, and is given by

$$C(s) = G(s)R(s) \tag{7.11}$$

This is the temporal domain equivalent of the discussion of spatial optical transfer functions in Section 1.3.

The assumption of zero initial conditions can be overcome by using the principle of superposition: the response of a linear system is the sum of the response to the input plus the response to the initial conditions. If there are two elements of the control system (Figure 7.3) with individual transfer functions G_1 and G_2, linear theory shows that the open-loop transfer function of the system is the product of the transfer functions of the individual elements, as follows:

$$G(s) = G_1 G_2 \tag{7.12}$$

If the feedback loop transfer function (e.g., sensor element) is represented by $H(s)$, then the closed-loop transfer function is the product of the open-loop transfer function divided by unity plus the loop gain function (the product of all transfer functions around the loop), as follows:

$$\frac{C(s)}{R(s)} = \frac{G_1 G_2}{1 + G_1 G_2 H} \tag{7.13}$$

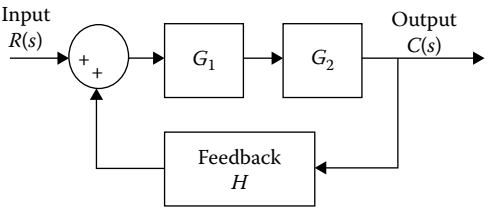

FIGURE 7.3
Transfer functions around a closed loop.

An example will be used to illustrate how one might use these methods to determine the performance of a control system. Consider a system such as that shown in Figure 7.3. Assume that the first element G_1 is composed of a simple amplifier of gain K. The second element is a voltage-driven tilt mirror whose position in relation to the applied voltage is represented by a transfer function,

$$G_2(s) = \frac{0.5}{s(0.25s + 1)} \tag{7.14}$$

Assuming unity feedback ($H(s) = 1$), we want to determine the output response of the system for a step-unit input. In other words, we need to derive an expression for the mirror output position $c(t)$ a time t after the mirror is commanded to go to the value +1. The Laplace transform of unit step input is $R(s) = 1/s$. The transform of the output $C(s)$ is the product of the input transform and the system transfer function and is given by

$$C(s) = R(s)G_{sys}(s) \tag{7.15}$$

From the preceding, we find

$$G_{sys}(s) = \frac{KG_2(s)}{1 + KG_2(s)} \tag{7.16}$$

and the output transform becomes

$$C(s) = \frac{2K}{s(s^2 + 4s + 2K)} \tag{7.17}$$

Our desired result is

$$c(t) = L^{-1}C(s) \tag{7.18}$$

A number of methods can be used to invert Equation 7.17. The most straightforward is a direct inverse Laplace transform, which can be found in tables [1]. The inverse transform of Equation 7.17 is given by

$$L^{-1}\left[\frac{\omega^2}{s(s^2 + 2\zeta s + \omega^2)}\right] = 1 + \frac{1}{\sqrt{1-\zeta^2}}\cos\left(\omega\sqrt{1-\zeta^2}t + \theta\right), \tag{7.19}$$

where

$$\theta = \tan^{-1}\left[\frac{\sqrt{1-\zeta^2}}{\zeta}\right] + \frac{\pi}{2} \tag{7.20}$$

By properly substituting the constants in Equation 7.19, $\omega = \sqrt{2K}$ and $\zeta = \sqrt{\frac{2}{K}}$, the output mirror position becomes

$$c(t) = 1 + \frac{1}{\sqrt{1 - \frac{2}{K}}} e^{-2t} \cos\left(\sqrt{2K - 4}t + \theta\right) \tag{7.21}$$

The phase angle θ is

$$\theta = \left(\tan^{-1}\sqrt{\frac{K}{2} - 1}\right) + \frac{\pi}{2} \tag{7.22}$$

Examination of Equation 7.21 reveals the properties of this solution. First, the solution is only valid for large gains, $K > 2$; it has a singularity at $K = 2$ and is imaginary for lower values. Second, the steady-state solution is easily found, $c(t) \to 1.0$ as $t \to \infty$. Third, for this high-gain solution, the mirror should respond rapidly. The disadvantage we see is overshoot during the transient. The maximum overshoot is found from the fraction preceding the exponential term, $1/\sqrt{1 - 2/K}$. For a gain near the instability, the overshoot is large ($K = 4$, overshoot = 41%). For higher gains, the overshoot is reduced ($K = 10$, overshoot = 11%), but the ringing remains large, increasing the settling time toward its steady state.

For the case in which the gain is less than 2, we must use another method of solution. *Partial fraction expansion* is used to determine the characteristic behavior of the system as well as to examine some of the more common terms used in control theory. Begin by expanding Equation 7.17 into partial fractions as follows:

$$C(s) = \frac{2K}{s(s^2 + 4s + 2K)} = \frac{A'}{s} + \frac{B'}{s + a} + \frac{C'}{s + b} \tag{7.23}$$

The primed constants are called *residues* of the output response. The term in the denominator, $s^2 + 4s + 2K$, can be factored into $(s + a)(s + b)$, where $a = 2 + 2\sqrt{1 - K/2}$ and $b = 2 - 2\sqrt{1 - K/2}$. We find the residues by multiplying $C(s)$ by the appropriate term and evaluating at the poles

$$A' = [sC(s)]_{s=0} = \left[\frac{2K}{(s + a)(s + b)}\right]_{s=0} = \frac{2K}{ab} = 1 \tag{7.24}$$

$$B' = [(s + a)C(s)]_{s=-a} = \left[\frac{2K}{(s)(s + b)}\right]_{s=-a} = \frac{2K}{-a(b - a)} = \frac{2K}{a(a - b)} \tag{7.25}$$

$$C' = [(s+b)C(s)]_{s=-b} = \left[\frac{2K}{(s)(s+a)}\right]_{s=-b} = \frac{2K}{-b(a-b)} = \frac{2K}{-b(a-b)} \tag{7.26}$$

The result is a reduced fraction representation of the output transform, as follows:

$$C(s) = \frac{1}{s} + \frac{\dfrac{2K}{8\sqrt{1-\dfrac{K}{2}+8-4K}}}{s+a} + \frac{\dfrac{2K}{-8\sqrt{1-\dfrac{K}{2}+8-4K}}}{s+b} \tag{7.27}$$

By the inverse Laplace transform of Equation 7.27, the time dependence for if $K < 2$ is found by

$$c(t) = 1 + \left[\frac{K}{4\sqrt{1-\dfrac{K}{2}+4-2K}}\right]e^{-at} + \left[\frac{K}{-4\sqrt{1-\dfrac{K}{2}+4-2K}}\right]e^{-bt} \tag{7.28}$$

This expression also converges to the steady-state solution properly, $c(t) \to 1$ as $t \to \infty$, and does not exhibit the drastic ringing that resulted from a high gain.

We can see from Equation 7.27 that the transfer functions and input and output transforms are, in general, ratios of polynomials in *s*. The *zeros* of the expression are the roots of the numerator polynomials. The *system zeros* are the roots of the numerator of the system transfer function *G*(*s*). Similarly, the *poles* are the roots of the denominators, and the *system poles* are the roots of the denominator of *G*(*s*). The system poles have significance when we want to examine the stability of the control system. Because the Laplace variable is complex, $s = \sigma + i\omega$, the poles can be plotted as points on a complex plane. For a control system to be used in adaptive optics, the transient solution should decay to zero. This will occur if all the real poles and the real parts of all complex poles are negative, that is, in the left half of the complex plane. In Equation 7.27 the poles $-a$ and $-b$ can be evaluated for different gains *K*, showing their regions of stability. If the transient is represented by an exponential, the *system time constant* is the time it takes for the decaying exponential to be reduced to a factor of $e^{-1} = 0.368$ of its original value.

The design of a stable control system that meets the system performance requirements reduces to establishing a transfer function with the proper characteristics. For instance, a tilt mirror or multiactuator deformable mirror will have mechanical constraints because of the inertia of the masses being

moved. This is a direct consequence of dealing with *inertial* adaptive optics systems. A motor position servo with gain K and a time constant $\tau = I/\gamma$, where I is the inertia and γ is the damping constant, would have a transfer function given by

$$G_{\text{motor}} = \frac{K}{s(\tau s + 1)} \tag{7.29}$$

Moving a large-mass (large inertia) servomotor to respond to optical signals can be difficult. A large gain is required to move it rapidly, but once it starts moving, it is equally difficult to stop. This results in severe overshoot. An increase in damping and various methods of feedback also can be used. For instance, damping that is proportional to the velocity of the system is very useful. If the damping is increased as the velocity is increased, the amount of overshoot can be curtailed. Detailed discussions of *velocity feedback* and other methods of tailoring feedback to specific transfer function characteristics can be found in a number of sources devoted to these specific design problems [127,435].

7.2.3 Proportional Control

If an input signal r controls an output c, and the output is a linear function of the input $c = Kr$, the system is said to have a *proportional* controller. If the proportionality constant, the gain K, is very large, the output will respond to very small changes in the input. A system with this characteristic may have the output moving from its minimum to its maximum range with only slight changes in the input. This "on–off" control is a basic form of control. When the gain is lower and the output responds smoothly and linearly to the input, one has a true proportional controller. If a resistance, or damping, is added near the output so that the system responds slowly, accumulating energy as time moves along (like winding up a watch), the controller is a proportional integral (PI) controller. The final steady-state output will be a combination of the linear portion (the proportional) and the time-accumulated portion (the integral). The transfer function of this system is a sum of the proportional and integral parts, $G(s) = K_p + K_i/s$. This type of system can show overshoot due to the accumulation of energy required for the control.

When the resistance is added near the input, the control is a combination of the proportional control and its derivative. The transfer function of a proportional derivative (PD) controller is $G(s) = K_p + K_d s$. Note that the Laplace transform of an integral is $1/s$ and the transform of a derivative is s. Controls of these types have been made by mechanical means (spring–mass–damper), electronic means (resistor–capacitor–inductor), thermal means (insulation–thermal capacitance), and fluidic means (fluid resistance–inertia–compressibility) [810].

7.2.4 First- and Second-Order Lag

The important aspects of the system time constant can be seen by observing the performance of a very common control, a *lag*. It has the transfer function

$$G(s) = \frac{1}{\tau s + 1} \tag{7.30}$$

For a step input, $R(s) = 1/s$, the output transform becomes

$$C(s) = \frac{\frac{1}{\tau}}{s\left(s + \frac{1}{\tau}\right)} = \frac{1}{s} + \frac{-1}{s + \frac{1}{\tau}} \tag{7.31}$$

The inverse transform of Equation 7.31 is the transient response

$$c(t) = 1 - e^{-t/\tau} \tag{7.32}$$

The first term is the forced solution, whereas the second one is the transient due to the system pole at $-1/\tau$. The output reduces to 0.368 of its original value when $e^{-t/\tau} = e^{-1}$ or when $t = \tau$. Thus, the time constant for a simple lag $G(s)$ is simply τ. The stability of the system is easily determined. If the pole $-1/\tau$ is positive, then the exponential grows instead of decays. This is an unstable situation. For the stable case, $\tau > 0$, the response speed can be made faster by reducing the time constant.

From the example in Section 7.2.2, Equation 7.17 takes on a very common form. The output transform has the form

$$C(s) = \frac{\omega^2}{s(s^2 + 2\zeta\omega s + \omega^2)} \tag{7.33}$$

In this form, ω is the value of the undamped natural frequency and ζ is the damping ratio. For $\zeta > 1$, the system is overdamped (see Equation 7.19). The transient is the sum of two decaying exponentials with the form

$$1 + ae^{-\omega(\zeta + \sqrt{\zeta^2 - 1})} + be^{-\omega(\zeta - \sqrt{\zeta^2 - 1})} \tag{7.34}$$

This is the same as saying that the system is a series connection of simple lags, called a *quadratic lag*. For $\zeta < 1$ (the $K > 2$ case in Section 7.2.2), the system is underdamped and overshoot occurs. The transient term is an oscillation with a damped natural frequency related to the *resonant frequency*, $\omega\sqrt{1 - \zeta^2}$, with a decaying amplitude $e^{-\zeta\omega t}$. The time constant for the system is $\tau = 1/(\zeta\omega)$.

The important characteristics of simple or quadratic lag controllers are summarized by the parameters important to the performance of the system. The time it takes for the system to come to 5% of its steady-state value is about 3τ. To reach 2% of its value, it takes 4τ. The percentage overshoot $W_{\%}$ is

$$W_{\%} = 100 \exp\left(\frac{-\pi\zeta}{\sqrt{1-\zeta^2}}\right) \tag{7.35}$$

and the time to reach its peak value is

$$\tau_{\text{peak}} = \frac{\pi}{\omega\sqrt{1-\zeta^2}} \tag{7.36}$$

7.2.5 Feedback

Feedback that is used to reduce the overshoot of a control system, as described in Section 7.2.2, is an example of the general application of feedback to adaptive optics controls. Feedback is used primarily to reduce the sensitivity of the control output to differences in the input or external disturbances. Equation 7.13 represents a standard control with a feedback loop as diagrammed in Figure 7.3. The closed-loop transfer function $T(s)$ is given by

$$T(s) = \frac{C(s)}{R(s)} = \frac{G_1 G_2}{1 + G_1 G_2 H} \tag{7.37}$$

where H is the feedback. If the loop gain, the product of the transfer functions around the loop, $G_1 G_2 H \gg 1$, then $T(s) = 1/H(s)$; that is, the closed-loop transfer function depends entirely on the feedback. The sensitivity of this relationship is the ratio of the change of the closed-loop transfer function to the change of the forward path transfer function and is given by

$$\text{Sensitivity} = \frac{\partial T(s)/T(s)}{\partial(G_1 G_2)/(G_1 G_2)} = \frac{1}{1 + G_1 G_2 H} \tag{7.38}$$

The static sensitivity is evaluated as $s \to 0$, and the dynamic sensitivity to frequency ω is evaluated for $s = i\omega$. High loop gains help reduce the sensitivity to parameter variations and disturbances. For a unity feedback system ($H = 1$; $G(s) = G_1(s)G_2(s)$), the steady-state error is

$$\varepsilon_{ss} = \lim_{t\to\infty}[c(t) - r(t)] = \lim_{s\to 0} \frac{sR(s)}{1 + G(s)} \tag{7.39}$$

Assuming a general form for $G(s)$, we have

$$G(s) = \frac{K\left(\alpha_k s^k + \cdots + \alpha_1 s + 1\right)}{s^n\left(\beta_l s^l + \cdots + \beta_1 s + 1\right)} \tag{7.40}$$

The gain K is the gain of the transfer function (when the constant terms are made unity) and is given by

$$K = \lim_{s \to 0} s^n G(s) \tag{7.41}$$

The exponent n of s in the denominator represents the *type number*. Because, from Laplace transforming, each s represents an integration, the type number represents the number of integrators in $G(s)$. The position error constant is K_p for $n = 0$; the velocity error constant is K_v for $n = 1$; and the acceleration error constant is K_a for $n = 2$. Higher-order constants are easily evaluated, but are not so easily named. The steady-state error for any type of control is found simply by

$$\varepsilon_{ss} = \lim_{s \to 0} \frac{sR(s)}{1 + \left(\frac{K}{s^n}\right)} \tag{7.42}$$

For example, for a step input ($R(s) = 1/s$) to a type-0 control, $\varepsilon_{ss} = 1/(1 + K)$. For a ramp input ($R(s) = 1/s^2$) to a type-2 control, $\varepsilon_{ss} = 0$. This shows that a type-0 control can respond to a step input with a constant steady-state error. Similar analysis shows that the type-0 control cannot respond (i.e., $\varepsilon_{ss} = \infty$) to a higher-order input. A type-2 control, with two integrators, can respond to both step and ramp inputs, leaving no steady-state error, and has a constant error for a second-order (acceleration) input. The fundamental principle described in this section is that sensitivity, response to disturbances, and steady-state errors are all improved by increased gain. Feedback can also be used to increase the dynamic response. The velocity feedback mentioned in Section 7.2.2 has various applications in controlling adaptive optics wavefront compensating devices. These will be described in the context in which they occur, but the reader is referred to a number of other texts for detailed explanations of the design principles and applications [113,579].

7.2.6 Frequency Response of Control Systems

An adaptive optics control system is often required to respond to a dynamic periodic input. The response to high-frequency noise or the response to a particular range of frequencies (bandwidth) is desired. A linear quadratic Gaussian control law is often used [616,617]. Based on the Laplace transform methods, frequency response analysis lets a control designer observe the system response in the frequency domain and stability of the system [480,481,482].

A control system with a transfer function $G(s)$ will respond to a sinusoidal input, $r(t) = A\sin(\omega t)$, in an interesting manner. Using Laplace transforms, the transform of the output will be

$$C(s) = \frac{A\omega G(s)}{s^2 + \omega^2} = \frac{A'}{s + i\omega} + \frac{B'}{s - i\omega} + \cdots \tag{7.43}$$

The coefficients of the expansion can be found by using the method of partial fractions as follows:

$$A' = \frac{AG(-i\omega)}{-2i} \tag{7.44}$$

and

$$B' = \frac{AG(i\omega)}{2i} \tag{7.45}$$

By inverse transforming, the forced response becomes

$$c(t) = \frac{A[-G(-i\omega)e^{-i\omega t} + G(i\omega)e^{i\omega t}]}{2i} = AW(\omega)\sin[\omega t + \phi(\omega)] \tag{7.46}$$

where W is the ratio of output to input amplitude as follows:

$$W(\omega) = \sqrt{g_r^2(\omega) + g_i^2(\omega)} \tag{7.47}$$

The parameters g_r and g_i are the real and imaginary parts of the transfer function $G(s)$ evaluated at $s = i\omega$, that is, $G(s)|_{s=i\omega} = g_r(\omega) + ig_i(\omega)$. The corresponding phase angle is the delay of the output relative to the input.

$$\phi(\omega) = \tan^{-1}\frac{g_i}{g_r} \tag{7.48}$$

From this result, we can see what happens to the general sinusoidal input. The output retains the shape (sine function) with an amplitude reduced by the function $W(\omega)$ and delayed by a phase factor $\phi(\omega)$. The simple lag control yields a common result. The transfer function for the lag is

$$G(s) = \frac{K}{s\tau + 1} \tag{7.49}$$

where the gain K and the time constant τ are given. For a sinusoidal input, the frequency response function becomes

$$G(i\omega) = \frac{K}{i\omega\tau + 1} \tag{7.50}$$

Its magnitude is

$$W(\omega) = \frac{K}{\sqrt{1 + (\omega\tau)^2}} \tag{7.51}$$

and the phase angle is

$$\phi(\omega) = -\tan^{-1} \omega\tau \tag{7.52}$$

Although this example considers only a simple lag, the results are fundamental to performance analysis. Most control systems in practice are a combination of various controls.

A control system is often composed of gain, integrators, differentiators, lead, or lag. The gain is represented by K, where

$$K = \lim_{s \to 0} s^n G(s) \tag{7.53}$$

n integrators are represented by $1/(i\omega)^n$ and n differentiators by $(i\omega)^n$. A simple lag is represented by $1/S = 1/(i\omega\tau + 1)$, and a simple lead is $S = (i\omega\tau + 1)$. Quadratic lag is $1/Q = 1/[(i\omega/\omega_n)^2 + 2\zeta(i\omega/\omega_n) + 1]$, and quadratic lead is $Q = (i\omega/\omega_n)^2 + 2\zeta(i\omega/\omega_n) + 1$. A general form for a frequency response function is then

$$G(i\omega) = \frac{K}{(i\omega)^n} \frac{S_1 S_2 \cdots}{S_{k+1} S_{k+2} \cdots} \frac{Q_1 Q_2 \cdots}{Q_{l+1} Q_{l+2} \cdots} \tag{7.54}$$

Substituting values for time constants τ, damping ratios ζ, and natural frequencies ω_n yields the necessary information to examine the system responses. If M controls are cascaded in series, the response $G(i\omega)$ is the product of the individual response. The magnitudes W are multiplied, and the phase angles are added as follows:

$$G(i\omega) = \prod_{j=1}^{M} G_j = W_1 e^{i\phi_1} W_2 e^{i\phi_2} \cdots = W_{\text{tot}} e^{i\phi_{\text{tot}}} \tag{7.55}$$

where

$$W_{\text{tot}} = \prod_{j=1}^{M} W_j \tag{7.56}$$

$$\phi_{\text{tot}} = \sum_{j=1}^{M} \phi_j \tag{7.57}$$

A plot of $W(\omega)$ or $\phi(\omega)$ versus ω is a simple graphical method for observing the performance of the control system. A convenient method of plotting the

performance, originated by Bode [810], uses a logarithmic frequency scale. The magnitude W is expressed in units of decibels (dB) and the phase angle is expressed in degrees. We can treat gain, integrators (or differentiators), and lag (or lead) as individual controllers that combine as shown in the preceding paragraph. A Bode plot of the gain is simply a straight horizontal line at $W(\text{dB}) = 20\log K$ and $\phi = 0°$.

Bode plots of other control parameters are relatively straightforward. n integrators have the form $W(\text{dB}) = 20\log|i\omega|^{-n} = -20n\log\omega$. On a log scale, the magnitude plot of an integrator is a straight line crossing the 0 dB axis at $\omega = 1$ with a slope of $-20n$ dB/decade. The phase angle is not a function of frequency, but is a constant $\phi = -n90°$. Differentiators are mirror images of integrators across the 0 dB and 0° axis.

A simple lag with time constant τ has a magnitude dependency

$$W(\text{dB}) = 20\log[1 + (\omega\tau)^2]^{-1/2} \tag{7.58}$$

and a phase dependency $\phi = -\tan^{-1}(\omega\tau)$. For very low frequencies ($\omega\tau \ll 1$), the magnitude W and the phase asymptotically approach 0 dB and 0°, respectively. For high frequencies ($\omega\tau \gg 1$), the magnitude W asymptotically approaches $-20\log\omega\tau$ and the phase approaches 90°. The asymptotes meet at the *break frequency* $\omega\tau = 1$. A simple lead will have the same characteristics as the lag, except that it is a mirror image across the 0 dB and 0° axis.

A more complicated, yet common, control is the quadratic lag or lead. Instead of having a simple dependence on the time constant, a quadratic lag or lead closely follows the characteristics of resonances and damping. The magnitude of a quadratic lag is given by

$$W(\text{dB}) = 20\log\left[\left(1 - \frac{\omega^2}{\omega_n^2}\right)^2 + \left(\frac{2\zeta\omega}{\omega_n}\right)^2\right]^{-1/2} \tag{7.59}$$

The parameter ω_n is the natural frequency of the system. The phase angle follows the form

$$\phi = -\tan^{-1}\frac{2\zeta\omega/\omega_n}{1 - \omega^2/\omega_n^2} \tag{7.60}$$

For frequencies much lower than the natural frequency ($\omega \ll \omega_n$), $W \to 0$ dB and $\phi \to 0°$. For frequencies much higher than the natural frequency ($\omega \gg \omega_n$), $W \to -40\log(\omega/\omega_n)$ and $\phi \to -180°$. For frequencies close to the natural frequency, Equation 7.59 should be used. The shape of the resonant peak is determined primarily by the damping ratio ζ. For small values, the magnitude peak is very sharp and the phase change from 0° to 180° is very

rapid. The Bode plot for a quadratic lead follows the form of the lag, except it is also a mirror image about the 0 dB and 0° axis.

Examples of Bode plots for various contributors are shown in Figures 7.4–7.9. The Bode plot of the gain of an integrator, Figure 7.4, shows the characteristic slope based on the number of integrators. The phase angle in Figure 7.5 is constant. The Bode plot of a simple lag controller, Figures 7.6 and 7.7, shows its break frequency at $1/\tau$. The designer can "tune" the control to a particular frequency characteristic. Similarly, the designer can tune the response by choosing the resonance of a quadratic lag or lead. The position of the peak in Figure 7.8 corresponds to the resonant frequency and the width of the peak, and the sharpness of the phase change in Figure 7.9 corresponds to the choice of the damping factor.

The combination of gain, lead, lag, integrators, and so on is a simple process for Bode plots. Because the vertical axis for the magnitude $W(\omega)$ is logarithmic and the W's are multiplicative, the Bode plots of each contributor

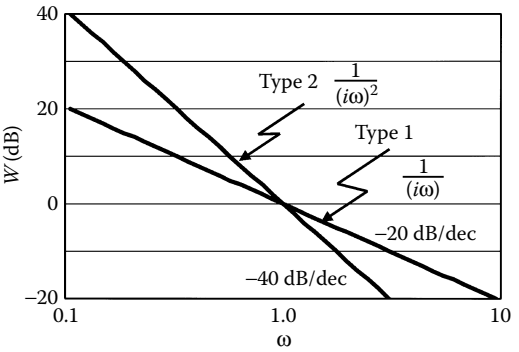

FIGURE 7.4
Bode plot of the gain of an integrator.

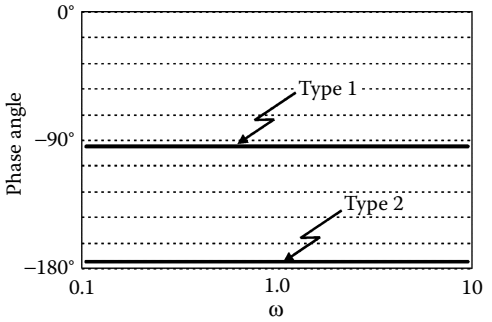

FIGURE 7.5
Bode plot of the phase of an integrator.

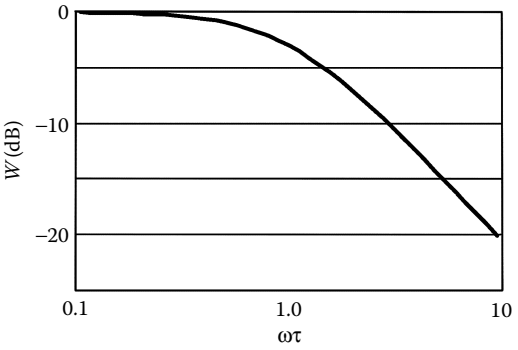

FIGURE 7.6
Bode plot of the gain of a simple lag.

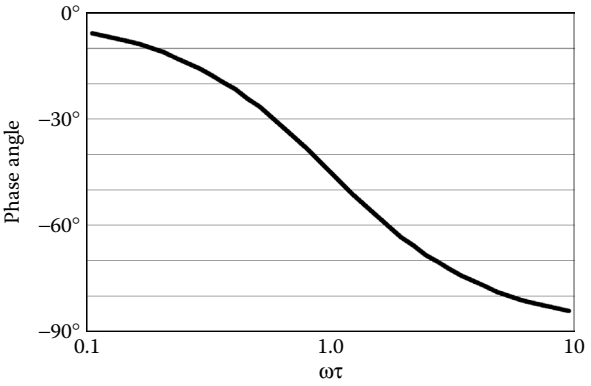

FIGURE 7.7
Bode plot of the phase of a simple lag.

can be added. Similarly, the Bode plots of phase are on a linear scale and are additive; therefore, the phase contributions are added as well.

Bode plots are useful for open-loop stable systems. Two important definitions arise from examination of Bode plots. The *phase margin* is defined as 180° plus the phase angle at the *crossover frequency* (where the magnitude curve crosses the 0 dB axis). The *gain margin* is defined as 1 divided by the magnitude at the frequency where the phase angle is –180°. For closed-loop systems, the frequency response is determined by a number of features. Many control systems have the form of the quadratic lag

$$\frac{C(i\omega)}{R(i\omega)} = \frac{1}{\left(\frac{i\omega}{\omega_n}\right)^2 + 2\zeta\left(\frac{i\omega}{\omega_n}\right) + 1} \tag{7.61}$$

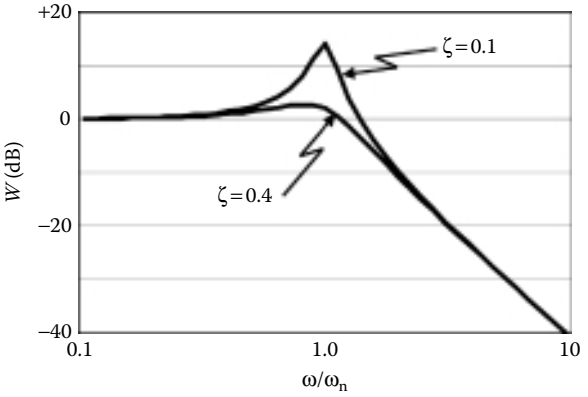

FIGURE 7.8
Bode plot of the gain of a quadratic lag.

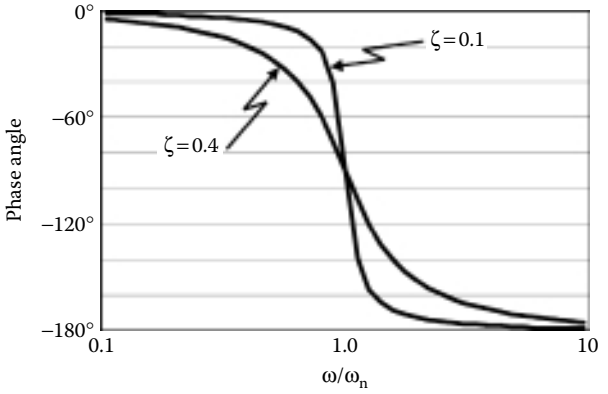

FIGURE 7.9
Bode plot of the phase of a quadratic lag.

The magnitude W is simply

$$W(\omega) = \frac{1}{\sqrt{\left(1 - \frac{\omega^2}{\omega_n^2}\right)^2 + \left(\frac{2\zeta\omega}{\omega_n}\right)^2}} \tag{7.62}$$

The resonant peak is a measure of relative stability. If the maximum of this function does not go *too* high, the system possesses relative stability. The peak magnitude W_{peak} is dependent upon the damping ratio

$$W_{\text{peak}} = \frac{1}{2\zeta\sqrt{1-\zeta^2}} \tag{7.63}$$

The system *bandwidth* represents the response speed of the control system. It is defined as the range of frequencies over which W is more than $\sqrt{2}/2$ (or 0.707) of its direct current (DC) value (the value at $\omega = 0$). From Equation 7.62, the bandwidth B is

$$B = \omega_n \left(1 - 2\zeta^2 + \sqrt{2 - 4\zeta^2(1-\zeta^2)}\right)^{1/2} \tag{7.64}$$

The resonant peak does not occur at the natural frequency ω_n. By taking the derivative of Equation 7.62, we see that the peak occurs at a frequency $\omega_p = \omega_n\sqrt{1-2\zeta^2}$. As seen in Equations 7.63 and 7.64, a low damping ratio ζ means severe resonant peaking and severe overshoot to a step input. However, raising the bandwidth B by reducing the damping ratio results in a reduced settling time and a quicker rise time response to the step input. This compromise is the ongoing concern of all control system designers, and it is a fundamental problem with adaptive optics as well as many other aspects of active control.

7.2.7 Digital Controls

Each of the control structures mentioned in Sections 7.2.3 through 7.2.5 is applicable to many types of adaptive optics problems. Analog computers and hard-wired circuits, such as resistor–capacitor–inductor networks [302], can implement various transfer functions. The flexibility of digital computers allows the control to be implemented in software rather than in hardware, greatly reducing the difficulty in modifying the control or even altering the control in real time (adaptive control) [36]. Adaptive optics systems are almost always dealing with multivariable controls. Many inputs and many outputs must be simultaneously adjusted, and cross talk or coupling between nearby feedback loops must be reduced. Digital construction of the control allows the flexibility to adjust parameters as the inputs change or the optical system hardware changes.

For a computer to monitor and control numerous signals at rapid rates, it must time-share, which results in a loss of information. As long as these lapses in information are understood and compensated for, the control can function as efficiently as a continuous analog system. This latency can be a combination of many sources, digitization, computation, storing, and so on. The time-sharing can be analyzed mathematically. Consider a signal that is varying with time $f(t)$. Sampling this function at equal intervals t' is equivalent to multiplying the function by a sum of impulse functions ($\delta(t) = 1$ for $t = 0$ and zero otherwise), as follows:

$$f_{\text{samp}}(t) = f(t)\sum_{n=0}^{\infty}\delta(t - nt') \tag{7.65}$$

Taking the function inside the summation and using the properties of the delta function, we have

$$f_{\text{samp}}(t) = \sum_{n=0}^{\infty} f(nt')\delta(t - nt') \tag{7.66}$$

This shows that the sampled function is only known at the various times given by

$$t = 0, t', 2t', 3t', \cdots \tag{7.67}$$

The Laplace transform of the sampled signal is

$$F_{\text{samp}}(s) = L[f_{\text{samp}}(t)] = \sum_{n=0}^{\infty} f(nt')\mathrm{e}^{-nt's} = \frac{1}{t'}\sum_{n=-\infty}^{\infty} F\left(s + \frac{in2\pi\pi}{t'}\right) \tag{7.68}$$

where $F(s) = Lf(t)$. The Laplace transform of the sampled signal is a sum of Laplace transforms of the original signal spaced exactly $2\pi/t'$ apart. The functions $F(s + in2\pi/t')$ for values of $n \neq 0$ are called *sidebands*. If the sidebands are close together, they overlap with the principal band and indeterminacy can occur. The value of the sampled transform is a summation. If *only one* term contributes to the value at each point in s frequency space, the problem can be avoided. If there is more than one nonzero component at each value of s, the signal is said to possess *aliases*. If the sampling frequency $2\pi/t'$ is at least twice the highest significant frequency in the signal $f(t)$, the aliases are suitably separated and no confusion occurs. This condition is known as the *Nyquist limit*. These conditions and problems must be overcome before implementing any sort of digital control. Control designers use filters to remove high-frequency aliases and other treatments extensively [39,53,465].

In addition to the disadvantages of discrete sampling, a digital control also is limited by the resolution of the digitization itself. The accuracy of the computations is limited by the accuracy of representing the continuous values by a digital bitstream. An 8-bit number, for example, can represent only 256 possible values. The subsequent accuracy of the numerical calculations is limited to one part in 256. This 0.4% limit is often sufficient; however, each control experiences the combined effect of many calculations. Often, digitization limitations require control systems to have 16- or even 32-bit data words. Although analog or digital electronic controls are most common, the use of optical processing for adaptive optics has not been overlooked [177].

7.3 Multivariate Adaptive Optics Controls

This book will not delve deeper into specifics of general control theory or design, but will focus now on specific problems related to adaptive optics. For any adaptive optics system, except for a single-mode control loop, for example, a one-axis tilt control, there is a need for controlling multiple coupled loops. Each loop can be represented by the temporal transfer functions described in Section 7.2. Spatial coupling between multiple loops is described in this section.

Referring to Figure 7.1, we can see how the adaptive optics control must often deal with sets of multiple coupled equations. The choice of a modal or zonal reconstruction is dependent upon the type of corrector, the bandwidth requirement, and the sensing geometry involved [278]. For low signal strength or a coarse spatial sample of phase measurements, a zonal system has been shown to be superior [735].

Calculations involving wavefront control can be digital, analog, or a hybrid of the two. In most cases, they involve either the real-time inversion of a matrix or matrices or the real-time multiplication of a vector times a matrix. Path A, for example, must calculate a continuous phase map from the measurement of wavefront slopes. Decoding a number of measurements into a number of phase points will be treated as a linear problem. Straightforward methods of linear algebra are usually sufficient, because most of the adaptive optics operation is in a linear regime. In general, any of the paths in Figure 7.1 represents the solution to a set of linear equations. Whether one is trying to determine the phase from measured modes or to determine the voltages for a deformable mirror from a Zernike representation of the phase, the methods of linear algebra can be used.

7.3.1 Solution of Linear Equations

In the wavefront reconstruction and control problem, one usually encounters a set of M equations with N unknowns. They can be written discretely as

$$\begin{aligned}
y_1 &= a_1B_{11} + a_2B_{12} + a_3B_{13} \cdots a_NB_{1N} \\
y_2 &= a_1B_{21} + a_2B_{22} + a_3B_{23} \cdots a_NB_{2N} \\
y_3 &= a_1B_{31} + a_2B_{32} + a_3B_{33} \cdots a_NB_{3N} \\
&\vdots \qquad\qquad \vdots \\
y_M &= a_1B_{M1} + a_2B_{M2} + a_3B_{M3} \cdots a_NB_{MN}
\end{aligned}$$

or as a matrix equation as follows:

$$(y) = [B](a) \tag{7.69}$$

The vectors and coupling matrix are defined simply as

$$y = \begin{pmatrix} y_1 \\ y_2 \\ \vdots \\ y_M \end{pmatrix} \quad a = \begin{pmatrix} a_1 \\ a_2 \\ \vdots \\ a_N \end{pmatrix} \tag{7.70}$$

$$B = \begin{bmatrix} B_{11} & B_{12} & \cdots & B_{1N} \\ B_{21} & B_{22} & \cdots & B_{2N} \\ B_{31} & B_{32} & \cdots & B_{3N} \\ \vdots & & & \vdots \\ B_{M1} & B_{M2} & \cdots & B_{MNN} \end{bmatrix} \tag{7.71}$$

The linearity requirement is satisfied when the parameters a_n are constants. The *basis functions* B_{mn} can have any functional form. They may be wave aberration polynomials needed for the calculation in path B in Figure 7.1, or they may be functions representing the coupling between actuator voltages for a deformable mirror and the wavefront at certain points, like that represented by path G in Figure 7.1.

In any case, the required solution is an inversion of Equation 7.69. We must find the parameters a_n that fit the series of basis functions B to the known or measured values y_m. When the number of equations M is less than the number of unknowns, it is an *underdetermined system* and cannot be solved uniquely. When $M = N$, the matrix $[B]$ is square and, as long as it is not singular, it can be directly inverted to solve Equation 7.69: $a = [B]^{-1}y$. In adaptive optics control system problems, one often encounters the case where the number of equations M is greater than the number of unknowns N. This *overdetermined system* is the basis for much research in numerical techniques, many of which apply to adaptive optics systems.

The problem reduces to calculating the values of the unknowns such that the error is small between the measured, or known, parameters y_m and the actual values of y. An inverse for a nonsquare matrix cannot be calculated directly. An approximation can be determined based on a specific merit function. The merit function that represents a good determination is often a consideration, because there should be only one solution if not for real-world errors such as noise.

One method, called a *Gauss reconstructor*, is the principal method used in calculating various multiparameter paths in a wavefront reconstruction or control. By defining the merit function as the sum of the squares of the differences between the actual value of y and the estimated value of y from $[B]a$, the elements of the vector a can be determined. The *method of least squares* finds the minimum of

$$\chi^2 = \sum_{i=1}^{M}\left[y_i - \sum_{k=1}^{N} a_k B_{ik} \right]^2 \tag{7.72}$$

By differentiating χ^2 with respect to each element a_k and setting $d\chi^2/da = 0$, a set of equations for the a's can be found. In matrix notation, this is equivalent to solving for the vector a by

$$a = [B^T B]^{-1}[B^T]y \tag{7.73}$$

where $[B^T]$ is the transpose of the matrix $[B]$. Note that the matrix $[B]$, for an overdetermined system, has M rows and N columns. The transpose has N rows and M columns, and the square invertible matrix $[B^T B]$ is M by M elements The matrix $[B^T B]^{-1}B^T$ is called the *pseudoinverse* of matrix $[B]$.

Although this method appears straightforward, a number of difficulties can arise. The inversion of matrix $[B^T B]$ is impossible if it is singular or if, numerically, it is close to singular. Unfortunately, this occurs in many cases of real-world adaptive optics. To get around this problem, *singular value decomposition*(SVD) is used. The method is easily explained. From the equation $y = [B]a$, we see that an inverse of $[B]$ is required. The following equation shows how the $M \times N$ matrix $[B]$ can be broken into product of three matrices:

$$[B] = [U][\bar{D}][V^T] \tag{7.74}$$

The matrix $[U]$ is also an $M \times N$ matrix; the matrix $[V^T]$ is an $N \times N$ square matrix; and the matrix $[\bar{D}]$ is an $N \times N$ matrix that has only nonzero elements on the diagonal and is given by

$$[\bar{D}] = \begin{pmatrix} d_1 & & & \bigcirc \\ & d_2 & & \\ & & \ddots & \\ \bigcirc & & & d_N \end{pmatrix} \tag{7.75}$$

The elements of each of these matrices can be found by SVD computational algorithms [629]. The inverse of the decomposed matrices is relatively straightforward.

$$[B]^{-1} = [V][\bar{D}]^{-1}[U^T] \tag{7.76}$$

$$= [V]\begin{pmatrix} 1/d_1 & & & \bigcirc \\ & 1/d_2 & & \\ & & \ddots & \\ \bigcirc & & & 1/d_N \end{pmatrix}[U^T] \tag{7.77}$$

If any of the diagonal elements d_i are zero, the matrix [B] is singular and no exact or unique solution can be found. However, this method allows the calculation of a solution that is the *closest* to the correct solution in a least-squares sense. By observing the elements of the diagonal matrix d_i, we can see explicitly where the singularities come from. The zero elements on the diagonal cannot be inverted. However, by simply zeroing the elements in the inverse diagonal matrix $[\bar{D}]^{-1}$ that came from zero elements of $[\bar{D}]$, we can solve the linear set and find the unknown vector a. Although it seems that we are arbitrarily discarding the sets of equations, it can be shown by formal proof [629] that we are discarding those sets of equations that corrupted the whole set by round-off error and were essentially useless anyway.

Linear least squares and SVD are not the only methods of solving the sets of linear equations that arise in adaptive optics reconstruction problems. Some optical parameters, such as the piston "aberration," can cause a wavefront sensor measurement vector and a reconstruction matrix to become singular. Problems of this type and problems with signals corrupted by noise can be overcome in other ways. Hunt [367] describes the methodology employed for reconstructing phase information from wavefront slope measurements. By premultiplying the linear least-squares solution, Equation 7.73, by the square matrix $[B^TB]$, the equation takes the form

$$[B^TB]a = [B^TB][B^TB]^{-1}[B^T]y = [B^T]y \tag{7.78}$$

The matrix $[\Upsilon] = [B^TB]$ can be decomposed into

$$[\Upsilon] = [L] + [D] + [R] \tag{7.79}$$

Although this appears similar to the SVD method, the decomposition here follows strict rules and is more general than the SVD. The matrix [L] is simply composed of the elements of [Υ] that are *left* and *below* the main diagonal. The matrix [R] is composed of the elements of [Υ] that are *right* and *above* the main diagonal. The matrix [D] is composed of the elements of [Υ] on the main diagonal. An iterative solution of the a vector unknowns, a_i, is found directly as follows:

$$a_{i+1} = [G]a_i + [H]y' \tag{7.80}$$

where the matrices [G] and [H] are determined as follows. When the matrices are defined as

$$[G] = -[D]^{-1}([R] + [L]) \tag{7.81}$$

$$[H] = [D]^{-1} \tag{7.82}$$

the method is called a *Jacobi iteration*. These methods have been used in adaptive optics reconstructions [241,360] When the matrices take on the slightly different form

$$[G] = -([D] + [L])^{-1}[R] \tag{7.83}$$

$$[H] = ([D] + [L])^{-1} \tag{7.84}$$

the method is a *Gauss–Seidel iteration*, which will converge faster than the Jacobi method. Using a variable relaxation parameter w in the definitions leads to the *successive-over-relation* recommended by Hunt [367], given by

$$[G] = ([D] + w[L])^{-1}\{(1-w)[D] - w[R]\} \tag{7.85}$$

$$[H] = w([D] + w[L])^{-1} \tag{7.86}$$

The parameter w can be found by a number of methods specifically mentioned in a text by Young [897]. The advantage of the successive-over-relation method is that it can converge as much as two orders of magnitude faster than the Jacobi method.

7.4 Direct Wavefront Reconstruction

7.4.1 Phase from Wavefront Slopes

The general methods described in Section 7.3.1 for solving sets of linear equations are used extensively in determining the control parameters of adaptive optics systems. One of the most common problems, illustrated by path A in Figure 7.1, is the determination of the phase at various points from knowledge of the wavefront slopes at other points on the wavefront plane [571]. This is a fundamental problem of adaptive optics [361]. The most common wavefront sensors (Shack–Hartmann sensors or pyramid sensors) produce output signals proportional to the wavefront slopes [8].

The number of unknown phase points is N and the number of wavefront slope measurements is M. When $M > N$, the system is overdetermined, and solutions can be found by direct least-squares methods, SVD, or other methods described in Section 7.3.1. The error between the calculated phase at the various points and the actual phase at those points (that produced the slope measurements) is important. It is not only the merit function for the least-squares solution, but it is a physical limitation on the performance of the adaptive optics system.

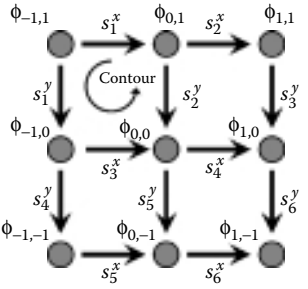

FIGURE 7.10
Example of the Hudgin configuration. Wavefront slope measurements superimposed on phase determination points.

The problem of phase determination from wavefront slopes depends upon the geometry of the problem and various numerical techniques [50,180]. The phase estimation at N locations is ϕ_n. The measured slopes at M locations are s_m. The matrix connecting the two is determined by the geometry of the problem. For instance, consider the geometry shown in Figure 7.10. The measured slopes from the wavefront sensor are represented by s_m^x or s_m^y. The superscripts represent the slope in the x or y direction. The phase is to be determined at the points $\phi_{-1,-1}, \phi_{-1,0} \ldots$, where the subscripts represent the coordinates of the unknown points. A set of equations can be constructed as follows:

$$\begin{aligned} s_1^x &= \phi_{-1,1} - \phi_{0,1} \\ s_2^y &= \phi_{0,1} - \phi_{0,0} \\ &\vdots \quad \vdots \end{aligned}$$

and can be written in matrix form

$$s = [B]\phi \tag{7.87}$$

where the matrix $[B]$ is the *geometry matrix*. Often, as in this example, $[B]$ is simply composed of sums and differences based on the geometrical configuration of wavefront sensor positions and phase determination positions. Many of the elements are +1 or –1. However, in some cases $[B]$ can be quite complicated. If the geometry matrix includes the effects of a corrector, such as deformable mirror influence functions, it is called the *influence matrix*. A derivation by Wallner [846] used weighting functions that were dependent upon the subaperture and the direction of the slope measurement in the subaperture. In actual wavefront sensors, the slope measurement is seldom a simple difference between two wavefront points, but usually it is a spatial average over the subaperture. Accounting for noise and spatial averaging, least-squares methods or SVD can be used to invert $[B]$ and reconstruct the phase from the measured slopes.

A number of researchers have investigated numerical and physical problems that occur when this method is used [190,281] For example, if the summation of wavefront slope measurements along a contour (Figure 7.10) is not zero, the least-squares method breaks down [748]. Although this is not a physical possibility, because the wavefront is continuous, the numerical calculation or interferometric method of wavefront slope measurement can yield 2π discontinuities.

The problem of singular matrices, which arise because of a nonunique solution to the set of equations, can be overcome by numerical methods. If the piston component of the wavefront is disregarded, the solution matrix $[B]^{-1}$ can be singular, because there are unlimited solutions that would give the same slope measurements. Adding another row to the matrix $[B]$ with each element equal to 1.0 forces the summation of all phase points to a particular value [694]. The addition of another value in the slope vector s specifies the piston value, which is usually set to 0. The fixed piston value allows inversion as follows:

$$\begin{pmatrix} s_1 \\ s_2 \\ \vdots \\ s_M \\ 0 \end{pmatrix} = \begin{bmatrix} & [B] & \\ & & \\ 1 & 1 & 1 \quad \cdots \quad 1 \end{bmatrix} \begin{pmatrix} \phi_1 \\ \phi_2 \\ \vdots \\ \vdots \\ \phi_N \end{pmatrix} \tag{7.88}$$

As an example of this process, consider the Hudgin geometry in Figure 7.10. Nine phase measurements should be computed from 12 slope measurements. For direct phase reconstruction with no cross-correlation between phase points, the $[B]$ matrix takes the form

$$[B] = \begin{bmatrix} 1 & -1 & 0 & 0 & 0 & 0 & 0 & 0 & 0 \\ 0 & 1 & -1 & 0 & 0 & 0 & 0 & 0 & 0 \\ 0 & 0 & 0 & 1 & -1 & 0 & 0 & 0 & 0 \\ 0 & 0 & 0 & 0 & 1 & -1 & 0 & 0 & 0 \\ 0 & 0 & 0 & 0 & 0 & 0 & 1 & -1 & 0 \\ 0 & 0 & 0 & 0 & 0 & 0 & 0 & 1 & -1 \\ 1 & 0 & 0 & -1 & 0 & 0 & 0 & 0 & 0 \\ 0 & 1 & 0 & 0 & -1 & 0 & 0 & 0 & 0 \\ 0 & 00 & 1 & 0 & 0 & -1 & 0 & 0 & 0 \\ 0 & 0 & 0 & 1 & 0 & 0 & -1 & 0 & 0 \\ 0 & 0 & 0 & 0 & 1 & 0 & 0 & -1 & 0 \\ 0 & 0 & 0 & 0 & 0 & 1 & 0 & 0 & -1 \\ 1 & 1 & 1 & 11 & 1 & 1 & 1 & 1 & 1 \end{bmatrix} \tag{7.89}$$

The pseudoinverse $[B^T B]^{-1}\,[B^T]$ can be calculated by Equation 7.73. With this result, a vector s of 12 wavefront slopes (and the dummy thirteenth element set to zero) can be converted to the 9 phase values.

$$\begin{pmatrix} \phi_{-1,1} \\ \phi_{0,1} \\ \phi_{1,1} \\ \phi_{-1,0} \\ \phi_{0,0} \\ \phi_{1,0} \\ \phi_{-1,-1} \\ \phi_{0,-1} \\ \phi_{1,-1} \end{pmatrix} = \left[[B]^{-1} \right] \begin{pmatrix} s_{11}^x \\ s_2^x \\ s_3^x \\ s_4^x \\ s_5^x \\ s_6^x \\ s_1^y \\ s_2^y \\ s_3^y \\ s_4^y \\ s_5^y \\ s_6^y \\ 0 \end{pmatrix} \tag{7.90}$$

If there is cross-correlation between actuators, as in the case of finite influence functions with coupling, the elements of matrix B are calculated by integrating the influence of each actuator to each slope measurement signals s_i^x and s_i^y using

$$s_i^x = \int_{\text{subap}} x\, I(x,y)_i \, \mathrm{d}x\, \mathrm{d}y \quad \text{and} \quad s_i^y = \int_{\text{subap}} y\, I(x,y)_i \, \mathrm{d}x\, \mathrm{d}y \tag{7.91}$$

for i = 1–9, the number of actuators, and inserting these results into the rows of $[B]$.

The most common problem that can corrupt the numerical computation is the inclusion of noise in the slope measurements. This is physically realistic, because the wavefront slope measurement has uncertainty associated with it. The equation that describes this process is a modification to Equation 7.87:

$$s = [B]\phi + n_{\text{o}} \tag{7.92}$$

where n_{o} represents noise. When the wavefront slope errors are not correlated and each measurement has an error represented by a variance σ_n^2, the mean square error of the Gauss reconstructor phase is [464]

$$\sigma^2_{\text{phase}} = \text{Tr}\left[\sigma_n^2 [B^T B]^{-1}\right] \tag{7.93}$$

where the trace Tr is the sum of diagonal elements of the matrix.

Not all noise is uncorrelated. If the noise at one time or one place is dependent upon the noise at another time or place, it is said to be correlated. One such example is the misregistration of the wavefront sensor subapertures with the centers of the actuators on the deformable mirror [274]. Errors of this sort may rotate with beam telescope pointing and may be spatially or temporally correlated. The *noise covariance matrix* C_n represents the relationship between the noise from one point in time or space and that from another. The covariance will be positive and high when the values are closely related. It will be negative and high when one value forces an opposite response from the other. The covariance will be zero when each value is independent (uncorrelated). The covariance matrix for uncorrelated noise will be diagonal with equal elements. If the noise is correlated with a covariance matrix $[C_n]$, the phase equation is derived from the Gauss-Markov estimate [694] as follows:

$$\phi = \left[B^T C_n^{-1} B\right]^{-1} [B^T][C_n]^{-1} s \tag{7.94}$$

and the mean square error is

$$\sigma^2_{\text{phase}} = \text{Tr}\ [B^T C_n^{-1} B]^{-1} \tag{7.95}$$

The matrix $\left[B^T C_n^{-1} B\right]^{-1} [B^T][C_n]^{-1}$ is the *reconstructor matrix*.

In some cases, the statistics of the phase noise are known. When this occurs, a Wiener estimate for the phase and the error can be used. For instance, atmospheric turbulence is represented by a covariance matrix $[C_W]$ with elements dependent upon the turbulence coherence length r_o [570]. The matrix representation of the phase is [694]

$$\phi = \left[C_W^{-1} + B^T C_n^{-1} B\right]\ B^T C_n^{-1} s \tag{7.96}$$

and the mean square error of the wavefront phase estimation is

$$\sigma^2_{\text{phase}} = \text{Tr}\left[C_W^{-1} + B^T C_n^{-1} B\right]^{-1} \tag{7.97}$$

If the wavefront statistics are not known, $C_W \to 0$, these expressions reduce to Equations 7.94 and 7.95.

The effect of different wavefront sensor choices and the method of adaptive estimation were described using the known statistics and temporal bandwidth requirements of atmospheric turbulence [37]. The shearing interferometer can be arranged in a configuration whereby the noise covariance

matrix is diagonal. Similarly, a Hartmann sensor covariance matrix is a block diagonal 2×2 matrix. This allows simple inversion of the covariance matrices and fast computation of the error matrices.

A number of researchers have determined how the error of the phase is affected by the geometry of wavefront slope measurements [845,864]. Figure 7.11 shows four possible configurations of wavefront slope measurements superimposed on a grid of points where the phase is to be determined: the Hudgin geometry [361]; the Southwell geometry [739]; the wavefront control experiment (WCE) geometry [864,866]; and the Fried geometry [241]

The number of slope measurements and the number of phase points N are constant. The geometry matrices $[B]$ would have different elements for each of the configurations. The wavefront measurement noise is proportional to the slope measurement noise and a function of the following general form [236,241,571]:

$$(\sigma_{\text{phase}})_{\text{config g}} = \sigma_n [a + b_{\text{g}} \ln K_{\text{g}}]^{1/2} \tag{7.98}$$

The parameter a is estimated to be $a \leq 0.13$; b and K depend on the configuration [236]

$$\begin{aligned} b_A &= 1/\pi; \quad K_A = N \\ b_B &= 1/\pi; \quad K_B = N \\ b_C &= 1.5/\pi; \quad K_C = N - 1 \\ b_D &= 3.0/\pi; \quad K_D = N - 1 \end{aligned} \tag{7.99}$$

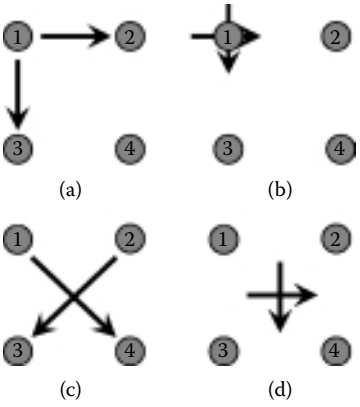

FIGURE 7.11
Four configurations for measuring wavefront slope superimposed on phase determination points: (a) Hudgin geometry, (b) Southwell geometry, (c) wavefront control experiment geometry, and (d) Fried geometry.

7.4.2 Modes from Wavefront Slopes

Path B in Figure 7.1 shows a phase representation in terms of its modal coefficients, another common method of direct phase reconstruction. The problem with reconstructing the phase modes from wavefront slopes is similar to that of reconstruction of the phase values at various points as discussed in Section 7.4.1. The wavefront phase ϕ is described by a polynomial expansion

$$\phi = \sum_{k=1}^{K} a_k Z_k(x, y) \tag{7.100}$$

where the coefficients are a_k and the polynomial basis functions (modes) are $Z_k(x, y)$. A Hartmann or shearing interferometer wavefront sensor measures the slopes of the wavefront at various positions m. There are M total measurements. For example, assume that half of the measurements are slopes in the x direction and half are in the y direction. The set of linear equations is

$$\left.\frac{\partial \phi}{\partial x}\right|_m = \sum_{k=1}^{K} a_k \left.\frac{\partial Z_k(x, y)}{\partial x}\right|_m \tag{7.101}$$

$$\left.\frac{\partial \phi}{\partial y}\right|_m = \sum_{k=1}^{K} a_k \left.\frac{\partial Z_k(x, y)}{\partial y}\right|_m \tag{7.102}$$

The subscript m implies evaluation at the coordinates (x_m, y_m). This set can be represented by the familiar matrix equation, $s = [B] \cdot a$, where the vector s is the slope vector and a is the mode coefficient vector, given by

$$s = \begin{pmatrix} \left.\frac{\partial \phi}{\mathrm{d}x}\right|_1 \\ \left.\frac{\partial \phi}{\mathrm{d}x}\right|_2 \\ \vdots \\ \left.\frac{\partial \phi}{\mathrm{d}x}\right|_{M/2} \\ \left.\frac{\partial \phi}{\mathrm{d}y}\right|_1 \\ \left.\frac{\partial \phi}{\mathrm{d}y}\right|_2 \\ \vdots \\ \left.\frac{\partial \phi}{\mathrm{d}y}\right|_{M/2} \end{pmatrix} \quad a = \begin{pmatrix} a_1 \\ a_2 \\ a_3 \\ \vdots \\ a_K \end{pmatrix} \tag{7.103}$$

while matrix [*B*] is

$$[B] = \begin{pmatrix} \left.\frac{\partial Z(x,y)_1}{\partial x}\right|_1 & \left.\frac{\partial Z(x,y)_2}{\partial x}\right|_1 & \cdots & \left.\frac{\partial Z(x,y)_K}{\partial x}\right|_1 \\ \left.\frac{\partial Z(x,y)_1}{\partial x}\right|_2 & \left.\frac{\partial Z(x,y)_2}{\partial x}\right|_2 & \cdots & \left.\frac{\partial Z(x,y)_K}{\partial x}\right|_2 \\ \vdots & & & \vdots \\ \left.\frac{\partial Z(x,y)_1}{\partial x}\right|_{\frac{M}{2}} & \left.\frac{\partial Z(x,y)_2}{\partial x}\right|_{\frac{M}{2}} & \cdots & \left.\frac{\partial Z(x,y)_K}{\partial x}\right|_{\frac{M}{2}} \\ \left.\frac{\partial Z(x,y)_1}{\partial y}\right|_1 & \left.\frac{\partial Z(x,y)_2}{\partial y}\right|_1 & \cdots & \left.\frac{\partial Z(x,y)_K}{\partial y}\right|_1 \\ \vdots & & & \vdots \\ \left.\frac{\partial Z(x,y)_1}{\partial y}\right|_{\frac{M}{2}} & \left.\frac{\partial Z(x,y)_2}{\partial y}\right|_{\frac{M}{2}} & \cdots & \left.\frac{\partial Z(x,y)_K}{\partial y}\right|_{\frac{M}{2}} \end{pmatrix} \tag{7.104}$$

In this case, matrix [*B*] is not simply sums and differences based on the geometrical configuration of wavefront sensor positions and phase determination positions. The elements are the derivatives of the polynomial basis functions evaluated at the wavefront sensor subaperture positions. A number of basis sets can be used; they should be linearly independent [156], but it is not necessary that they be orthogonal [738]. Naturally, there is also no requirement for a particular coordinate system. Polar coordinates and slopes measured in the polar directions are equally valid and useful. As before, the solution is found by finding the pseudoinverse of [*B*]

$$a = [(B^T B)^{-1} B^T]\, s \tag{7.105}$$

If the basis functions are Zernike polynomials (Section 1.3.3), the derivatives can be found explicitly [269]. A straightforward approach can be used because Zernike polynomials are orthogonal over a circle of radius R'. The elements of the pseudoinverse can be found directly. Recalling the notation of Section 1.3.3, the coefficients are found as a function of the derivatives of the phase with respect to Cartesian coordinates. With the known values $\partial\phi/\partial x$ and $\partial\phi/\partial y$, the modal coefficients are given as follows [499]:

$$A_{nm} = -\frac{n+1}{\pi m R'^2}\, i \int_0^{2\pi} \int_0^{R'} \frac{\partial \phi}{\partial \theta} R_n^m\left(\frac{r}{R'}\right) \mathrm{e}^{-im\theta} r \, \mathrm{d}r \, \mathrm{d}\theta \tag{7.106}$$

$$A_{n0} = \frac{n+1}{\pi n(n+2)} \int_0^{2\pi} \int_0^{R'} \frac{\partial \phi}{\partial r} \frac{\mathrm{d}R_n^0\left(\frac{r}{R'}\right)}{\mathrm{d}\left(\frac{r}{R'}\right)} \left[1 - \left(\frac{r}{R'}\right)^2\right] \left(\frac{r}{R'}\right) \mathrm{d}r\, \mathrm{d}\theta \tag{7.107}$$

where the derivatives have the form

$$\frac{\partial \phi}{\partial \theta} = r\left(\frac{\partial \phi}{\partial x} \sin\theta - \frac{\partial \phi}{\partial y} \cos\theta\right)$$

$$\frac{\partial \phi}{\partial r} = \frac{\partial \phi}{\partial x} \cos\theta - \frac{\partial \phi}{\partial y} \sin\theta$$

If the noise covariance matrix of the measurements is C_n, the pseudoinverse least-squares solution [801] is

$$a = \left[\left(B^T C_n^{-1} B\right)^{-1} B^T C_n^{-1}\right] \tag{7.108}$$

The accuracy of the modal estimation is determined by the noise and the amount of overdetermination of the system. Southwell [740] defines *undermodeling* as a system of reconstruction equations in which there are fewer modes required than can actually be projected out of the data. A more serious problem occurs when undersampling occurs. When the sampling density of the wavefront slopes is insufficient for the modes required, higher-order modes will appear as perturbations on the lower-order modes. Elimination of this form of wavefront aliasing requires careful examination of the number and form of the polynomials for the modes in terms of the number and placement of available wavefront slope measurements. In general, if more modes are desired, more samples should be acquired. They should be in a geometry sufficient for coding the wavefront information. For example, placing subapertures at the same radial distance from the optic axis, and only measuring tangential slopes, will be insufficient to determine the wavefront focus or spherical aberration.

7.4.3 Phase from Wavefront Modes

Finding the continuous phase representation is straightforward when lower-order wavefront modes have been measured. Path C in Figure 7.1 represents this operation. The wavefront is represented by the Seidel aberrations:

$$\Phi(r,\theta) = T_x r\cos\theta + T_y r\sin\theta + Fr^2 + A_{0^\circ} r^2 \cos 2\theta + A_{45^\circ} r^2 \cos\theta \sin\theta \tag{7.109}$$

where the constants are the measured values of each mode, T is the tilt, F is the focus, and A is the astigmatism. Each of these values must be

normalized according to the measurement method. For instance, T_x represents a center-to-edge tilt in the x direction. If the measurement is made by observing a centroid movement, the factor of 2 must be considered A measurement scheme that independently measures the primary modes *T, F,* and *A* can be used for this simple reconstructor.

7.4.4 Modes from Wavefront Modes

For completeness, path D in Figure 7.1 is shown. Although this method of reconstruction seems unnecessary at first, there may be situations where the desired phase representation is modal. If some of the low-order modes are measured directly and the higher-order modes are determined by wavefront slopes, this direct mode-to-mode calculation needs to be performed. The conversion of modal coefficients from their measurements to the specific representation needed is the only concern. The measured modes A_{m} can usually be converted to the modal representation A_{R} through a matrix multiplication as follows:

$$\begin{pmatrix} A_{\mathrm{R1}} \\ A_{\mathrm{R2}} \\ \vdots \\ A_{\mathrm{RM}} \end{pmatrix} = [C] \begin{pmatrix} A_{\mathrm{m1}} \\ A_{\mathrm{m2}} \\ \vdots \\ A_{\mathrm{mM}} \end{pmatrix} \tag{7.110}$$

where the conversion matrix is [*C*]. If the desired modal representation is Zernike polynomials and the measurements are taken in terms of a power series as in Section 7.4.3, the conversion matrix is known [151]. Similarly, if the wavefront sensor has a modal output proportional to the Zernike terms, the power-series representation can be determined from a known conversion matrix [787].

7.4.5 Zonal Corrector from Continuous Phase

Once a phase map or a modal representation is constructed, it is necessary to determine the application of that information for driving a wavefront corrector. The representation can be used in zonal correctors, such as deformable mirrors, or in modal correctors, such as tilt mirrors and focusing optics. The process is represented by path E in Figure 7.1.

A deformable mirror is assumed to be a linear system of electromechanical actuators that deform a mirror surface into a desired shape. The details of the shapes are not important in the general case; however, the precise influence of each actuator* is very important in the wavefront control scheme. The desired surface $S(x, y)$ is generated by applying the proper amplitude A_i to

* Discussed in Section 6.4.

N actuators. The effect of each actuator on the surface $Z_i(x, y)$ is its influence function. A set of linear equations can be constructed as follows:

$$S(x,y) = \sum_{i=1}^{N} A_i Z_i(x,y) \tag{7.111}$$

which can be written in matrix form as follows:

$$(S) = [Z](A) \tag{7.112}$$

For a surface represented by K points, the influence matrix $[Z]$ has K rows and N columns. A pseudoinversion of $[Z]$ is required using least-squares, SVD, or another method. The actuator commands are then derived from the actuator amplitude A_i by multiplying by the suitable gain factors and voltage conversions, and by accounting for the factor of $2\cos\beta$ multiplier between the wavefront and the mirror surface with an incidence angle of β.

Constructing the influence matrix $[Z]$ is not trivial. The effect of each actuator on a point (x, y) in the wavefront plane must be determined. Although the influences often couple, they are assumed to be linear. The influences are often unsymmetric, and are especially so when the edge of the mirror is caged. The geometric effect of clamping neighboring actuators has a complicated effect on the influence of each actuator. These considerations, and their temporal characteristics, must be taken into account before constructing the influence matrix and inverting it.

7.4.6 Modal Corrector from Continuous Phase

A system of modal correctors may be driven with knowledge of the correcting wavefront as a continuous phase map (see path F in Figure 7.1). The wavefront to be constructed by the modal devices, S', is a sum of modes with basis functions $\Psi_j(x, y)$ and coefficients c_j, and is given by

$$S'(x,y) = \sum_{j=1}^{J} c_j \Psi_j(x,y) \tag{7.113}$$

The modes of the wavefront for the corrector can be determined by inverting the linear set to solve for c_j as follows:

$$(c) = [\Psi]^{-1}(S') \tag{7.114}$$

If Ψ_j are orthogonal, the matrix is diagonal and the inversion is simple. If the modal correctors do not form an orthogonal set, such as the optics that create the primary Seidel aberrations, the inversion is more complicated, but achievable.

7.4.7 Zonal Corrector from Modal Phase

If the phase is constructed and the corrector devices respond to commands in a zonal sense, another set of linear equations must be formed (see path G in Figure 7.1). Two similar reconstruction problems are combined. The zonal corrector commands are derived by inverting the linear sum of influence functions as follows:

$$S(x,y) = \sum_{i=1}^{N} A_i Z_i(x,y) \tag{7.115}$$

If the wavefront Φ is represented by a sum of modes with basis functions $\Psi_j(x, y)$ and coefficients c_j and is given by

$$\Phi(x,y) = \sum_{j=1}^{J} c_j \Psi_j(x,y) \tag{7.116}$$

and the two summations can be equated as follows:

$$S = \Phi = \sum_{i=1}^{N} A_i Z_i(x,y) = \sum_{j=1}^{J} c_j \Psi_j(x,y) \tag{7.117}$$

then using matrix notation

$$[Z](A) = [\Psi](c) \tag{7.118}$$

and inverting, the vector of zonal actuator commands is obtained as follows:

$$(A) = [Z]^{-1}[\Psi](c) \tag{7.119}$$

Note that the matrices such as $[Z]$ and $[\Psi]$ are probably not square and they might be near singular, so least-squares pseudoinverse or SVD methods may have to be used.

7.4.8 Modal Corrector from Modal Phase

Another version of a direct reconstruction technique is modal correctors being driven by information from a modal phase representation. A bimorph mirror driven by a curvature sensor is uniquely suited to this approach because the bimorph can be driven in curvature-reproducing modes [708]. This is illustrated by path H in Figure 7.1. When the basis functions of the modal representation match the basis functions of the modal corrector, the commands are linearly proportional to the phase coefficients. However, the most common application of this method uses primary aberration modal correctors with a Zernike representation of the phase. Assume that the Zernike

coefficients A_{11} and A_{20} for tilt and focus are known, and we want to drive a tilt mirror that responds with the form $S_{11}x = S_{11}r\cos\theta$ and a focus mirror that responds with the form $S_{20}r^2$. The matrix for converting the Zernike coefficients A_{nm} to the drive commands S_{nm} is given by [787]

$$\begin{pmatrix} S_{11} \\ S_{20} \end{pmatrix} = \begin{bmatrix} 1 & 0 \\ 0 & \sqrt{2} \end{bmatrix} \begin{pmatrix} A_{11} \\ A_{20} \end{pmatrix} \tag{7.120}$$

Other basis function sets can be used as long as they conform to the criteria of linearity. They do not have to be orthogonal sets.

7.4.9 Indirect Reconstructions

Paths I and J in Figure 7.1 show an adaptive optics phase reconstruction process that bypasses the direct method by avoiding an explicit representation of the wavefront. The mathematics behind the indirect methods generally uses the intermediate step where the phase representation is shown, but then bury it in the matrix calculations that connect wavefront measurements to corrector commands.

Some systems that do not use an explicit representation of the wavefront, such as the multidither system, use the connection between the intensity of a beam on the target and the actuator commands that maximize that intensity. Most analyses show that reconstruction matrices can be determined rather simply except for the limitations imposed by system noise [464]. Asher and Ogrodnik [37] examined an optimal estimation technique that was used for a multidither system in the presence of photon noise, detector noise, and speckle. It was determined elsewhere that the stability of a multichannel multidither system depended on the stability of a single loop. Because each loop was actually acting independently against an average of the other loops, the cross-coupling between the loops was small [583].

7.4.10 Modal Corrector from Wavefront Modes

In some cases, an adaptive optics system may require correction of a few modes, such as tilt and focus, or just tilt, from measurements of the modes in a different coordinate system. Path I in Figure 7.1 shows this case and is similar to the path H determination. For example, consider the tilt correction device (the three-actuator steering mirror) shown in Figure 7.12. Three actuators must be driven to compensate for a center-to-edge tilt angle measured by the wavefront sensor or tilt sensor. If the tilt angles are given as α_x and α_y and the actuators are placed on a radius R', the following actuator commands are found from the set of linear equations:

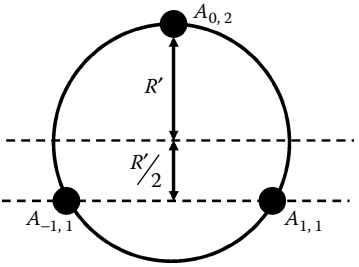

FIGURE 7.12
Actuator placement for a three-actuator tilt mirror.

$$A_{-1,1} = R'\left[\sqrt{3}\alpha_y - \alpha_x\right] \tag{7.121}$$

$$A_{0,2} = 2R'\alpha_x \tag{7.122}$$

$$A_{1,1} = -R'\left[\sqrt{3}\alpha_y - \alpha_x\right] \tag{7.123}$$

These three equations convert a modal measurement to a modal correction without directly computing the wavefront at any point or knowing the modal decomposition of the remainder of the wavefront.

7.4.11 Zonal Corrector from Wavefront Slopes

The most common and perhaps the most interesting problem in adaptive optics controls is the indirect method applied when the input is a number of wavefront slopes measured with a wavefront sensor, and the output of the control is a number of signals to various actuators that apply a correction to the wavefront. Unfortunately, there is hardly ever a one-to-one correspondence between the slope measurements and the actuator drive signals. Even if there were, the signals are corrupted by noise. Fortunately, the problem is linear and can be treated with the methods described in Section 7.3.

Combining the methods for paths A and E, the matrices of the indirect path J in Figure 7.1 can be determined. The measured slope vector s is given by

$$(s) = [B](\phi) \tag{7.124}$$

where $[B]$ is the geometry matrix. The phase is corrected by a surface S, which is a sum of actuator influence functions, as follows:

$$(\phi) = (S) = [Z](A) \tag{7.125}$$

Combining Equations 7.124 and 7.125 eliminates the central step of explicit phase representation,

$$(s) = [B][Z](A) \tag{7.126}$$

The matrix $[B]$ is $M \times P$, where M is the number of slope measurements and P is the number of phase points determined, and $[Z]$, the influence matrix, is $P \times J$, where J is the number of actuators; thus, the matrix $[B] \bullet [Z]$ is an $M \times J$ matrix. Pseudoinversion techniques can be used if it is overdetermined—that is, if the number of slopes, M, is greater than the number of actuator commands required, J.

Inverting the matrix $[B]$ $[Z]$ can be done by multiplying these two matrices and performing a pseudoinverse, or by inverting each one by the methods described in Sections 7.4.1 and 7.4.5.

$$([B][Z])^{-1} = [Z]^{-1}[B]^{-1} \tag{7.127}$$

The result is a linear conversion of measured wavefront slopes to actuator commands.

7.5 Beyond Linear Control

The first half of this chapter described general control theory as it applies to temporal lags between receiving a measurement signal and formulating a control signal to a corrector. The conversion in terms of transfer functions is the fundamental single-channel problem. The second half of this chapter dealt with the spatial reconstruction of phase information from measurements and derivation of the conversions to drive multichannel correction devices. The speed of the multichannel calculations and delays associated with converting digital signals to analog drive voltages and so on show up as the transfer functions on the control system.

In most cases, the difficult matrix inversions are system-configuration-dependent, and they need to be inserted into the system before operation, leaving only a single matrix multiplication, or possibly two, to be done in real time. This still is a difficult task, because we know that atmospheric turbulence may require a system to have thousands of actuators [365] and thousands of wavefront slope measurements [329]. Even with time-delayed measurements, the adaptive optics control system can be effective [600]. At very high bandwidths, control stability is a concern [24,527]. System bandwidth must be traded against spatial resolution and the statistics of the disturbances [823]. Remember, for atmospheric turbulence compensation, the wavefront error is a function of the system closed-loop bandwidth $f_{3\text{dB}}$.

$$\sigma^2_{\text{temp}} = \left(\frac{f_G}{f_{3\text{dB}}} \right)^{5/3} \tag{7.128}$$

Advances in digital computers allow these operations to be performed on general-purpose machines. Browne et al. [99] reported reconstructors capable of 500 reconstructions per second. Very high-speed response, which might be required for short-pulse lasers, may still dictate the need for special purpose digital or analog computers. With large telescopes demanding more complex control schemes, specialized algorithms such as those that separate spatial frequencies (woofer-tweeter controllers) are needed [449].

Adaptive wavefront estimators, that is, those that change their reconstruction matrices in real time in response to changing noise statistics, have been studied [35]. So-called *optimum reconstructors* [862,645] can iteratively solve difference equations in real time to make use of previous wavefront estimates within the time delay of each iteration [863]. The sparse matrix characteristics of Jacobi reconstructors and successive overrelaxation techniques make multiple matrix multiplies possible within a digital control system [865]. Variable gain reconstructors have been proposed [470]. With the increasing performance of digital signal processing, other reconstructors [343], such as those based upon reading the image rather than the wavefront and maximizing a particular parameter, such as sharpness or flux in the central core of the point spread function [790], may become commonplace in adaptive optics. Advanced methods and algorithms are needed for large telescopes and *extreme adaptive optics*. A multigrid algorithm [827] can deal with the waffle mode and actuator instabilities. A Fourier reconstructor can be used for finding the Shack–Hartmann wavefront slopes [287], and another method, predictive Fourier control, is used to decompose the turbulence spectrum [286, 628]. A method called *warm-starting*, in which the most recent wavefront estimate is used to initialize an iterative process, shows promise in open loop operation in a multiobject adaptive optics system [455]. In some cases, serial algorithms outperform parallel algorithms because the serial iteration is much faster [727].

Neural networks may be implemented within the wavefront sensor, where centroids can be estimated [535,536] or wavefront slopes are retrieved from detector signals and a trained net [41,262]. Neural nets also may be implemented in the reconstructor where the net converts measured slopes into correction signals [814] or where the net bases wavefront predictions on the spatiotemporal correlation of the disturbance [476]. Nonlinear control techniques [315,874] such as adaptive filters [477] or multiple control bandwidth techniques [196] have been explored and are being implemented in the most sophisticated adaptive optics systems. The current state-of-the-art is sufficient for the reconstruction and control of thousand-channel systems at kilohertz rates. The need to see further into the cosmos or to project a laser beam more efficiently will drive the technology of adaptive optics controls.

8

Summary of Important Equations

This chapter contains a summary of the most important equations and relationships in adaptive optics. The meaning and definition of each variable is described in the text near the original equation. See Figures 8.1 and 8.2 for some relationships between the parameters.

8.1 Atmospheric Turbulence Wavefront Expressions

Fried's coherence length for plane waves (Equation 2.21) and for spherical waves (Equation 2.23):

$$r_0 = \left[0.423k^2 \sec(\beta) \int_0^L C_n^2(z)\,\mathrm{d}z \right]^{-3/5} \tag{8.1}$$

$$r_{0\mathrm{sph}} = \left[0.423k^2 \sec(\beta) \int_0^L C_n^2(z) \left(\frac{z}{L} \right)^{5/3} \mathrm{d}z \right]^{-3/5} \tag{8.2}$$

The isoplanatic angle (Equation 3.27):

$$\theta_0 = \left[2.91k^2 \int_{\mathrm{path}}^L C_n^2(z) z^{5/3}\,\mathrm{d}z \right]^{-3/5} \tag{8.3}$$

Wavefront tilt variance (Equation 2.43):

$$\sigma_{\mathrm{tilt}}^2 = 0.2073k^2 \int_0^L \mathrm{d}z C_n^2(z) \times \int_{-\infty}^{\infty} \int_{-\infty}^{\infty} \mathrm{d}\vec{\kappa} [\vec{\kappa}^2 + k^2]^{-11/6} \left(\frac{16}{kD} \right)^2 \left[\frac{J_2\left(\frac{\kappa D}{2} \right)}{\frac{\kappa D}{2}} \right]^2 \tag{8.4}$$

Tilt angle due to atmospheric turbulence for two uncorrelated axes or each axis (Equation 2.45):

$$\alpha_{\mathrm{two-axis}}^2 = 0.364 \left(\frac{D}{r_0} \right)^{5/3} \left(\frac{\lambda}{D} \right)^2 \quad \text{or} \quad \alpha_{\mathrm{one-axis}}^2 = 0.182 \left(\frac{D}{r_0} \right)^{5/3} \left(\frac{\lambda}{D} \right)^2 \tag{8.5}$$

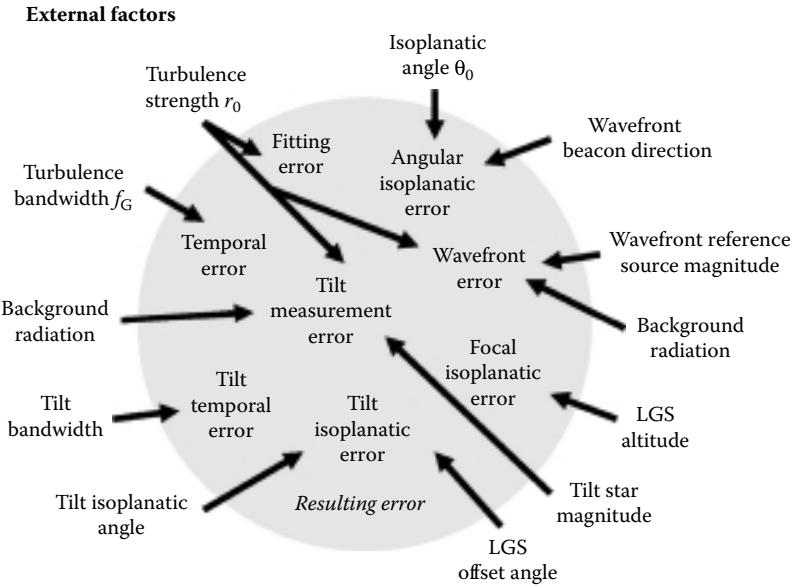

FIGURE 8.1
External factors and disturbances contribute to the resulting error that remains after compensation.

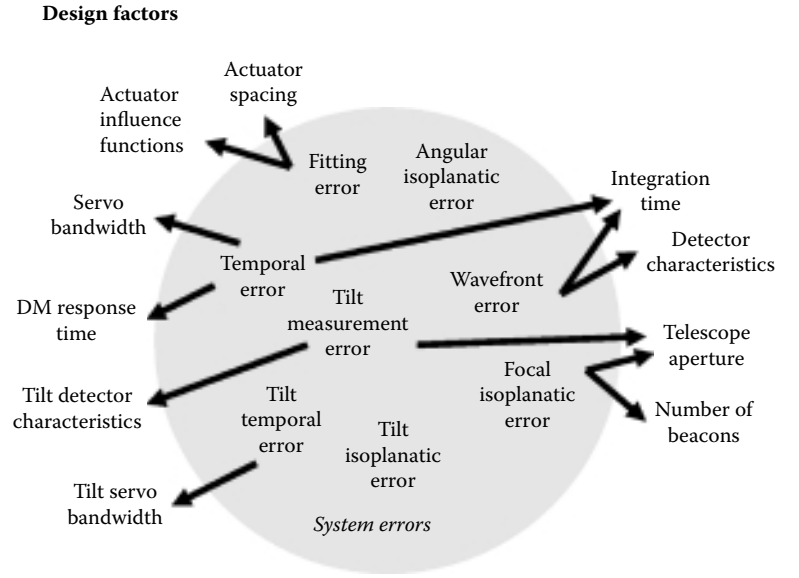

FIGURE 8.2
The allowable system errors drive the technology, design, and cost of the adaptive optics system.

Atmospheric turbulence tilt Greenwood frequency (Equation 2.54):

$$f_{\mathrm{T}} = 0.331 D^{-1/6} \lambda^{-1} \sec^{1/2} \beta \left[\int_0^L C_n^2(z) v_{\mathrm{w}}^2 \, \mathrm{d}z \right]^{1/2} \tag{8.6}$$

Full-aperture tilt through the atmosphere (from space) that will appear on a tilt sensor (Equation 5.16):

$$\alpha_{\mathrm{tilt}} = 2.2 \left(\frac{D}{r_0} \right)^{5/6} \frac{\lambda}{D} M_{\mathrm{tele}} \tag{8.7}$$

The standard deviation of angular tilt of the atmosphere (Equation 6.1):

$$\alpha_{\mathrm{SD}} = 0.43 \left(\frac{D}{r_0} \right)^{5/6} \frac{\lambda}{D} \tag{8.8}$$

The standard deviation of phase error of the atmosphere (Equation 6.3):

$$\phi_{\mathrm{SD}} = 0.06 \left(\frac{D}{r_0} \right)^{5/6} \text{ waves} \tag{8.9}$$

Higher-order atmospheric turbulence Greenwood frequency (Equation 2.70):

$$f_{\mathrm{G}} = 2.31 \lambda^{-6/5} \left[\sec \beta \int_0^L C_n^2(z) v_{\mathrm{w}}^{5/3}(z) \, \mathrm{d}z \right]^{3/5} \tag{8.10}$$

Focal anisoplanatism parameter d_0 (Equation 3.37):

$$d_0 = \lambda^{6/5} \cos^{3/5} \beta \left[19.77 \int \left(\frac{z}{z_{\mathrm{LGS}}} \right)^{5/3} C_n^2(z) \, \mathrm{d}z \right]^{-3/5} \tag{8.11}$$

Atmospheric turbulence modulation transfer function (Equations 2.74 and 2.75):

$$M_{\mathrm{turb}} = 1, \quad z << \left(0.4 k^2 C_n^2 L_0^{5/3} \right)^{-1} \tag{8.12}$$

$$M_{\mathrm{turb}} = \exp\left(- \left(\frac{2.01 \xi F \lambda}{r_0} \right)^{5/3} \right), \quad z >> \left(0.4 k^2 C_n^2 L_0^{5/3} \right)^{-1} \tag{8.13}$$

Hufnagel–Valley boundary model (Equation 2.18):

$$C_n^2 = 5.94\times10^{-23}\, z^{10}\, \mathrm{e}^{-z}\left(\frac{W}{27}\right)^2 + 2.7\times10^{-16}\, \mathrm{e}^{-2z/3} + A\,\mathrm{e}^{-10\ h} \tag{8.14}$$

Bufton wind model (Equation 2.17):

$$\upsilon(z) = 5 + 30\exp\left\{-\left[\frac{(z-309.4)}{4.8}\right]^2\right\} \tag{8.15}$$

8.2 Atmospheric Turbulence Amplitude Expressions

Log-amplitude variance for a plane wave (Equation 2.30) and a spherical wave (Equation 2.31):

$$\sigma_\chi^2 = 0.307k^{7/6}L^{11/6}C_n^2 \tag{8.16}$$

$$\sigma_\chi^2 = 0.124k^{7/6}L^{11/6}C_n^2 \tag{8.17}$$

Bradley–Herrmann thermal blooming distortion number (Equation 2.78):

$$N_\mathrm{B} = \frac{-4\sqrt{2}P(\mathrm{d}n/\mathrm{d}T)k\alpha L}{\rho C_\mathrm{p}\upsilon_\mathrm{w}2a} \tag{8.18}$$

8.3 Adaptive Optics Compensation Expressions

The uncompensated turbulence wavefront variance (Equation 2.61):

$$\sigma_\mathrm{uncomp}^2 = 1.02\left(\frac{D}{r_\mathrm{uncomp0}}\right)^{5/3} \tag{8.19}$$

The wavefront variance after two-axis tilt is removed (Equation 2.62):

$$\sigma_\mathrm{tiltcomp}^2 = 0.134\left(\frac{D}{r_0}\right)^{5/3} \tag{8.20}$$

The wavefront variance after tilt and focus are removed (derived from Equation 3.9):

$$\sigma_{\text{Foc}}^2 = 0.111\left(\frac{D}{r_0}\right)^{5/3} \tag{8.21}$$

The wavefront variance for higher-mode corrections (Equation 3.9):

$$\sigma^2 = 0.2944 N_{\text{m}}^{-\sqrt{3}/2}\left(\frac{D}{r_0}\right)^{5/3} \text{ (radians}^2\text{)} \tag{8.22}$$

The resultant Strehl ratio for higher-mode corrections (Equation 5.13):

$$S_{N>21} = \exp\left[-0.2944\, N^{-(\sqrt{3}/2)}\left(\frac{D}{r_0}\right)^{5/3}\right] \tag{8.23}$$

Adaptive optics correction fitting error (Equation 3.10):

$$\sigma_{\text{fit}}^2 = \kappa\left(\frac{r_{\text{s}}}{r_0}\right)^{5/3} \tag{8.24}$$

The angular tilt variance after compensation (Equation 3.17):

$$\alpha_{\text{comp}}^2 = \left(\frac{f_{\text{TG}}}{f_{\text{3dB}}}\right)^2\left(\frac{\lambda}{D}\right)^2 \tag{8.25}$$

The higher-order wavefront variance due to temporal constraints (Equation 3.18):

$$\sigma_{\text{temp}}^2 = \left(\frac{f_{\text{G}}}{f_{\text{3dB}}}\right)^{5/3} \tag{8.26}$$

The higher-order wavefront variance due to anisoplanatism (Equation 3.26):

$$\sigma_{\text{iso}}^2 = \left(\frac{\theta}{\theta_0}\right)^{5/3} \tag{8.27}$$

Shack–Hartmann wavefront sensor measurement variance (Equation 3.21):

$$\sigma^2_{\mathrm{WFS(H)}} = \frac{2\pi^2\left[\left(\frac{3}{16}\right)^2 + \left(\frac{s}{8}\right)^2\right]^{1/2}}{\mathrm{SNR}} \tag{8.28}$$

Shack–Hartmann wavefront sensor signal-to-noise ratio (Equation 3.22):

$$\mathrm{SNR} = \frac{N}{\left[N + n_{\mathrm{pix}}\left(\sigma_{\mathrm{r}}^2 + \sigma_{\mathrm{bg}}^2\right)\right]^{1/2}} \tag{8.29}$$

Quadcell angular tracking error (Equation 5.41):

$$\sigma = 0.6\frac{\lambda/D}{\mathrm{SNR_V}} \tag{8.30}$$

Quadcell signal-to-noise ratio (Equation 5.42):

$$\mathrm{SNR_V} = \frac{N_{\mathrm{S}}}{\sqrt{N_{\mathrm{S}} + 4(n_{\mathrm{B}} + n_{\mathrm{D}} + n_{\mathrm{e}}^2)}} \tag{8.31}$$

Quadcell tilt measurement error for resolved images (Equation 5.43):

$$\sigma_{\mathrm{qc}} = \frac{\pi\left[\left(\frac{3}{16}\right)^2 + \left(\frac{n}{8}\right)^2\right]^{1/2}\frac{\lambda}{2a}}{\mathrm{SNR_V}} \tag{8.32}$$

Wavefront curvature sensor relationship between irradiance and phase (Equation 5.116):

$$\frac{I_1(\vec{r}) - I_2(-\vec{r})}{I_1(\vec{r}) + I_2(-\vec{r})} = \frac{f(f-s)}{s}\left[\nabla^2\Phi\left(\frac{f}{s}\vec{r}\right) - \frac{\partial}{\partial\vec{n}}\Phi\left(\frac{f}{s}\vec{r}\right)\delta_{\mathrm{c}}\right] = \frac{2f^2c_{\mathrm{w}}}{s} \tag{8.33}$$

8.4 Laser Guide Star Expressions

The higher-order wavefront variance due to focal anisoplanatism (Equation 3.36):

$$\sigma^2_{\text{cone}} = \left(\frac{D}{d_0}\right)^{5/3} \tag{8.34}$$

Detected Rayleigh photon flux (Equation 3.42):

$$F_{\text{Rayleigh}} = \eta T_{\text{A}}^2 \frac{\sigma_{\text{R}} n_{\text{R}}}{4\pi z_0^2} \frac{\Delta z \lambda_{\text{LGS}} E}{hc} \tag{8.35}$$

Detected sodium photon flux (Equation 3.52):

$$F_{\text{Sodium}} = \eta T_{\text{A}}^2 \frac{\sigma_{\text{Na}} \rho_{\text{col}}}{4\pi z_0^2} \frac{\lambda_{\text{LGS}} E}{hc} \tag{8.36}$$

Laser brightness with wavefront error and jitter (Equation 4.28):

$$\text{Brightness} = \frac{\pi D^2 PTK \exp\left[-\left(\frac{2\pi\Delta\phi}{\lambda}\right)^2\right]}{4\lambda^2\left[1+\left(\frac{2.22\alpha_{\text{jit}} D}{\lambda}\right)^2\right]} \tag{8.37}$$

Bibliography

1. Abramowitz, M., and I. A. Stegun. *Handbook of Mathematical Functions*. New York: Dover, 1972.
2. Acton, D. S. "Correction of static optical errors in a segmented adaptive optical system." *Appl Opt* 34 (1995): 7965.
3. Acton, D. S., and R. B. Dunn. "Solar imaging at the National Solar Observatory using a segmented adaptive optics system." *Proc SPIE* 1920 (1993): 348.
4. Acton, D. S., and R.C. Smithson. "Solar imaging with a segmented adaptive mirror." *Appl Opt* 31 (1992): 3161.
5. Adelman, N. T. "Spherical mirror with piezoelectrically controlled curvature." *Appl Opt* 16 (1977): 3075.
6. Agrawal, G. P., and M. Lax. "Effects of interference on gain saturation in laser resonators." *J Opt Soc Am* 69 (1979): 1717.
7. Akkapeddi, P. R., E. T. Siebert, J. Baker, G. T. Volpe, and H. J. Robertson. "Target loop adaptive optics: thermal blooming correction." *Appl Opt* 20 (1981): 564.
8. Aksenov, V. P., and Y. N. Isaev. "Analytical representation of the phase and its mode components reconstructed according to the wavefront slopes." *Opt Lett* 17 (1992): 1180.
9. Aksinin, V. I., S. A. Chetkin, V. V. Kijko, and S. V. Muraviev. "Tilt corrector based on spring-type magnetostrictive actuators." *Opt Eng* 32 (1993): 447.
10. Alda, J., and G. D. Boreman. "Analysis of edge effects for deformable mirrors." *Opt Eng* 31 (1992): 2282.
11. Aldrich, R. E. "Requirements for piezoelectric materials for deformable mirrors." *Ferroelectrics* 27 (1980): 19.
12. Allen, J. B. Baran, L. Schmutz, and J. Yorsz. "Speckle and adaptive optics techniques." *Photonic Spectra* 22 (1988): 97.
13. Alzetta, G., S. Gozzini, A. Lucchesini, S. Cartaleva, T. Karaulanov, C. Marinelli, and L. Moi. "Complete electromagnetically induced transparency in sodium atoms excited by a multimode dye laser." *Phys Rev A* 69, (2004): 1.
14. Anafi, D., J. M. Spinhirne, R. H. Freeman, and K. E. Oughstun. "Intracavity adaptive optics. 2: Tilt correction performance." *Appl Opt* 20 (1981): 1926.
15. Anan'ev, Y. A., and V. E. Sherstobitov. "Influence of the edge effects on the properties of unstable resonators." *Sov J Quantum Electron* 1 (1971): 263.
16. Andersen, T., O.Garpinger, M.Owner-Petersen, F. Bjoorn, R. Svahn, and A. Ardeberg. "Novel concept for large deformable mirrors." *Opt Eng* 45 (2006): 073001.
17. Andrews, L. C. "Aperture-averaging factor for optical scintillations of plane and spherical waves in the atmosphere." *J Opt Soc Am A* 9 (1992): 597.
18. Andrews, L. C., and R. L. Phillips. *Laser Beam Propagation through Random Media*. Bellingham, WA: SPIE Opt. Eng. Press, 1998.
19. Andrews, L. C., R. L. Phillips, and C. Y. Hopen. *Laser Beam Scintillation with Applications*, Bellingham, WA: SPIE Press, 2001.
20. Angel, J. R. P. "Use of natural stars with laser beacons for large telescope adaptive optics," *Proc. Laser Guide Star Adaptive Optics Workshop* 2, 494. Albuquerque, NM: U. S. Air Force Phillips Laboratory, 1992.

21. Angelbeck, A. W., R. C. Pietro, E. D. Hasselmark, E. Gagnon, A. F. Greiner, W. C. McClurg, G. R. Wisner, and R. H. Freeman. "Development of a cooled metal mirror with active figure control." *Internal United Technologies Report*, United Technologies Corp., East Hartford, CT, 1975.
22. Wilson, J. K., et al. "Annual reports of astronomical observations and departments: University of Chicago" (abstract only), *Bull Am Astron Soc* 23, (1991): 173.
23. Antsiferov, V. N., A. G. Malinin, Y. V. Danchenko, and V. V. Timofeev. "Mathematical modeling of deformation of a large mirror made from a high-porosity honeycombed metal." *Sov J Opt Technol* 55 (1988): 8.
24. Anuskiewicz, J., M. J. Northcott, and J. E. Graves. "Adaptive optics at the University of Hawaii II: control system with real-time diagnostics." *Proc SPIE* 2201 (1994): 879.
25. AOptix Technologies, Inc., Campbell, CA. Available at www.aoptix.com.
26. Apollonov, V. V., V. I. Aksinin, S. A. Chetkin, V. V. Kijko, S. V. Muraviev, and G. V. Vdovin. "Magnetostrictive actuators in optical design." *Proc SPIE* 1543 (1991): 313.
27. Ardeberg, A., and T. Anderson. "Low turbulence–high performance." *Proc SPIE* 1236 (1990): 543.
28. Ardeberg, A., and T. Anderson. "Active optics at work." *Proc ICO-16 Satellite Conf on Active and Adap Opt, ESO Conf and Workshop Proc* 48 (1993) 433.
29. Ardila, A., R. Baptista, B. Blum, J. Rose, A. Tokovinin, and S. Zepf. "SOAR forward look instrument plan," 2008. Available at: www.lna.br/soar.
30. Arines, J., V. Duran, Z. Jaroszewicz, J. Area, E. Tajahuerce, P. Prado, J. Lancis, S. Bara, and V. Climent. "Measurement and compensation of optical aberrations using a single spatial light modulator." *Opt Expr* 15 (2007): 15287.
31. Armitage, J. D., and A. Lohmann. "Rotary shearing interferometry." *Optica Acta* 12, (1965): 185.
32. Arnoldus, H. F., and T. F. George. "Fresnel coefficients for a phase conjugator." *J Opt Soc Am B* 6 (1989) 30.
33. Arsenault, R., D. Salmon, F. Roddier, G. Monnet, J. Kerr, and J. Sovka. "The Canada–France–Hawaii Telescope adaptive optics instrument adaptor." *Proc SPIE* 1920 (1993): 364.
34. Artzner, G. "Microlens arrays for Shack-Hartmann wavefront sensors." *Opt Eng* 31 (1992): 1311.
35. Asher, R. B. "Wavefront estimation for adaptive optics, Interim Report I." U. S. Air Force Frank J. Seiler Research Laboratory, SRL-TR-76-0010, July 1976.
36. Asher, R. B., and R. D. Neal. "Adaptive estimation of aberration coefficients in adaptive optics." U. S. Air Force Frank J. Seiler Research Laboratory, SRL-TR-77-0009, May 1977.
37. Asher, R. B., and R. F. Ogrodnik. "Estimation and control in mutidither adaptive optics." *J Opt Soc Am* 67 (1977): 3.
38. Aspinwall, D. M., and R. D. Dotson. "Actuator configurations for segmented mirror figure control." *Proc SPIE* 365 (1982): 123.
39. Astrom, K. J., and B. Wittenmark. *Computer-Controlled Systems—Theory and Design*. 2nd ed. Englewood Cliffs, NJ: Prentice-Hall, 1990.
40. Atad, E., J. W. Harris, C. M. Humphries, and V. C. Salter. "Lateral shearing interferometry: evaluation and control of the optical performance of astronomical telescopes." *Proc SPIE* 1236 (1990): 575.

41. Atad, E., G. Catalan, J. W. Harris, C. M. Humphries, A. M. Smillie, A. F. Armitage, G. S. Hanspal, and R. J. McKeating. "Hartmann wavefront sensing with an artificial neural network processor." *Proc SPIE* 2201 (1994): 490.
42. Aubailly, M., M. C. Roggemann, and T. J. Schulz. "Approach for reconstructing anisoplanatic adaptive optics images." *Appl Opt* 46 (2007) 6055.
43. Auslander, D. M., Y. Takahashi, and M. J. Rabins. *Introducing Systems and Control*. New York: McGraw-Hill, 1974.
44. Avicola, K., J. M. Brase, J. R. Morris, H. D. Bissinger, J. M. Duff, H. W. Friedman, D. T. Gavel, C. E. Max, S. S. Olivier, R. W. Presta, D. A. Rapp, J. T. Salmon, and K. E. Waltjen. "Sodium-layer laser-guide-star experimental results." *J Opt Soc Am A* 11 (1994): 825.
45. Babcock, H. W. "The possibility of compensating astronomical seeing." *Publ Astron Soc Pac* 65 (1953): 229.
46. Babcock, H. W. "Adaptive optics revisited." *Science* 249 (1990): 253.
47. Babcock, H. W. "Astronomical background for adaptive optics," *Proc. Laser Guide Star Adaptive Optics Workshop* 1, 1. Albuquerque, NM: U. S. Air Force Phillips Laboratory, 1992.
48. Babcock, H. W., B. H. Rule, and J. S. Fassero. "An improved automatic guider." *Publ Astron Soc Pac* 68 (1956): 256.
49. Baker, K. L. "Interferometric wavefront sensors for high contrast imaging." *Opt Expr* 14 (2006): 10970.
50. Band, O., and N. Ben-Yosef. "Number of correcting mirrors versus the number of measured points in adaptive optics." *Opt Eng* 33 (1994): 466.
51. Baranec, C., and R. Dekany. "Study of a MEMS-based Shack-Hartmann wavefront sensor with adjustable pupil sampling for astronomical adaptive optics." *Appl Opt* 47 (2008): 5155.
52. Barat, J. "Some characteristics of clear-air turbulence in the middle stratosphere." *J Atmos Sci* 39 (1982): 2553.
53. Barbero, S., and L. N. Thibos. "Error analysis and correction in wavefront reconstruction from the transport-of-intensity equation." *Opt Eng* 45 (2006): 94001.
54. Barbieri, M., R. Alonso, S. Desidera, A. Sozzetti, A. F. M. Fiorenzano, J. M. Almenara, M. Cecconi, R. U. Claudi, D. Charbonneau, M. Endl, V. Granata, R. Gratton, G. Laughlin, and B. Loeillet. "Characterization of the HD 17156 planetary system." *Astro Astrophys* 503 (2009): 601.
55. Barchers, J. D., and T. A. Rhoadarmer. "Evaluation of phase-shifting approaches for a point-diffraction interferometer with the mutual coherence function." *Appl Opt* 41 (2002): 7499.
56. Bareket, N. "Three-channel phase detector for pulsed wavefront sensing." *Proc SPIE* 551 (1985): 12.
57. Barnard, J. J. "Fine scale thermal blooming instability: a linear stability analysis." *Appl Opt* 28 (1989): 438.
58. Barnes, W. P., Jr. Optical materials—reflective. In *Applied Optics and Optical Engineering*, Vol. VII, eds. R. R. Shannon and J. C. Wyant. New York: Academic Press, 1979.
59. Barr, L. D. "The 15-meter National New Technology Telescope - a progress report." *Proc SPIE* 365 (1982): 8.
60. Barrett, H. H., C. Dainty, and D. Lara. "Maximum-likelihood methods in wavefront sensing: stochastic models and likelihood functions." *J Opt Soc Am A* 24 (2007): 391.

61. Barrett, H. H., and S. F. Jacobs. "Retroreflective arrays as approximate phase conjugators." *Opt Lett* 4, (1979): 190.
62. Basden, A., T. Butterley, R. Myers, and R. Wilson. "Durham extremely large telescope adaptive optics simulation platform." *Appl Opt* 46 (2007): 1089.
63. Basden, A., D. Geng, D. Guzman, T. Morris, R. Myers, and C. Saunter. "Shack-Hartmann sensor improvement using optical binning." *Appl Opt* 46 (2007): 6136.
64. Basu, S., D. Voelz, and D. K. Borah. "Fade statistics of a ground-to-satellite optical link in the presence of lead-ahead and aperture mismatch." *Appl Opt* 48 (2009) 1274.
65. Batchelor, G. K. *The Theory of Homogeneous Turbulence*. London: Cambridge Univ. Press, 1953.
66. Bates, W. J. "A wavefront shearing interferometer." *Proc Phys Soc* 59 (1947): 940.
67. Beckers, J. M. "ESO symposium on large telescopes and their instrumentation," *ESO-Proc*. 693. Garching, 1988.
68. Beckers, J. M. "The VLT interferometer IV. The utility of partial adaptive optics." *Proc SPIE* 1236 (1990): 154.
69. Beckers, J. M. "The VLT interferometer II. Factors affecting on-axis operation." *Proc SPIE* 1236 (1990): 364.
70. Beckers, J. M. "Removing perspective elongation effects in laser guide stars and their use in the ESO Very Large Telescope," *Proc. Laser Guide Star Adaptive Optics Workshop* 2, 629. Albuquerque, NM: U. S. Air Force Phillips Laboratory, 1992.
71. Beckers, J. M. "Introduction to the conference." *Proc ICO-16 Satellite Conf on Active and Adap Opt, ESO Conf and Workshop Proc* 48 (1993).
72. Beland, R., and Krause-Polstorff, J. "Variation of Greenwood frequency measurements under different meteorological conditions," *Proc. Laser Guide Star Adaptive Optics Workshop* 1, 289. Albuquerque, NM: U. S. Air Force Phillips Laboratory, 1992.
73. Belen'kii, M. S. "Influence of stratospheric turbulence on infrared imaging." *J Opt Soc Am A* 12 (1995): 2517.
74. Belen'kii, M. S. "Effect of the inner scale of turbulence on the atmospheric modulation transfer function." *J Opt Soc Am A* 13 (1996): 1078.
75. Belmonte, A., and J. M. Kahn. "Capacity of coherent free-space optical links using atmospheric compensation techniques." *Opt Expr* 17 (2009): 2763.
76. Belsher, J. F., and D. L. Fried. *Adaptive Optics Mirror Fitting Error*. Placentia, CA: The Optical Sciences Co. Report TR-521, 1983.
77. Benedict, R., Jr., J. B. Breckinridge, and D. L. Fried. "Atmospheric compensation technology: Introduction." *J Opt Soc Am A* 11 (1994) 257.
78. Berkefeld, T., A. Glindemann, and S. Hippler. "Multi-conjugate adaptive optics with two deformable mirrors - requirements and performance." *Exp Astro* 11 (2001): 1.
79. Bickel, G., and G. Hausler. "Optical simulation of Huygens's principle." *J Opt Soc Am A* 5 (1988): 843.
80. Bienfang, J. C., C. A. Denman, B. W. Grime, P. D. Hillman, G. T. Moore, and J. M. Telle. "20 W of continuous-wave sodium D2 resonance radiation from sum-frequency generation with injection-locked lasers." *Opt Lett* 28 (2003): 2219.
81. Bifano, T., P. Bierden, and J. Perreault. "Micromachined deformable mirrors for dynamic wavefront control." *Proc SPIE* 5553 (2004): 1.

82. Bifano, T. G., R. K. Mali, J. K. Dorton, J. Perreault, N. Vandelli, M. N. Horenstein, and D. A. Castanon. "Continuous-membrane surface-micromachined silicon deformable mirror." *Opt Eng* 36 (1997): 1354.
83. Bikkannavar, S., C. Ohara, and M. Troy. "Autonomous phase retrieval control for calibration of the Palomar adaptive optics system." *Proc SPIE* 7015 (2008) 70155K.
84. Bin-Nun, E., and F. Dothan-Deutsch. "Mirror with adjustable radius of curvature." *Rev Sci Instrum* 44 (1973) 512.
85. Blanc, A., L. M. Mugnier, and J. Idier. "Marginal estimation of aberrations and image restoration by use of phase diversity." *J Opt Soc Am A* 20 (2003): 1035.
86. Bold, G. T., T. H. Barnes, and T. G. Haskell. "Aberration correction using optical feedback." *Proc Top Mtg on Adap Opt, ESO Conf and Workshop Proc* 54 (1996): 421.
87. Bonora, S., and L. Poletto. "Push-pull membrane mirrors for adaptive optics." *Opt Expr* 14 (2006): 11935.
88. Boreman, G. D., and C. Dainty. "Zernike expansions for non-Kolmogorov turbulence." *J Opt Soc Am A* 13 (1996): 517.
89. Born, M., and E. Wolf. *Principles of Optics*. 5th ed. Oxford: Pergamon, 1975.
90. Boston Micromachines Corp. Available at: www.bostonmicromachines.com.
91. Bowker, J. K. *Pulsed Laser Wavefront Sensor*. Cambridge, MA: Adaptive Optics Assoc. Tech. Report 78-1, 1978.
92. Bradley, L. C., and J. Herrmann. "Numerical calculation of light propagation in a nonlinear medium." *J Opt Soc Am* 61 (1971): 668 (abstract).
93. Brady, G. R., M. Guizar-Sicairos, and J. R. Fienup. "Optical wavefront measurement using phase retrieval with transverse translation diversity." *Opt Expr* 17 (2009): 624.
94. Breaux, H., W. Evers, R. Sepucha, and C. Whitney. "Algebraic model for cw thermal-blooming effects." *Appl Opt* 18 (1979): 15.
95. Breckinridge, J. B. "Coherence interferometer and astronomical applications." *Appl Opt* 11 (1972): 2996.
96. Bridges, W. D., P. T. Brunner, S. P. Lazzara, T. A. Nussmeier, T. R. O'Meara, J. A. Sanguinet, and W. P. Brown. "Coherent optical adaptive techniques." *J Appl Opt* 13 (1974): 2.
97. Briggs, R. J. *Models of High Spatial Frequency Thermal Blooming Instabilities*. Lawrence Livermore National Lab. UCID-21118, 1987.
98. Brousseay, D., E. F. Borra, and S. Thibault. "Wavefront correction with a 37-actuator ferrofluid deformable mirror" *Opt Expr* 15 (2007): 18190.
99. Browne, S. L., J. L. Vaughn, G. A. Tyler, and J. D. Gonglewski. "A computationally efficient method for wavefront reconstruction." *Proc Top Mtg on Adap Opt, ESO Conf. and Workshop Proc* 54 (1996): 125.
100. Bruno, T. L., and A. Wirth. "Adaptive optics finds down-to-Earth applications." *Photonics Spectra* (June 1996): 139.
101. Bruns, D. G. "Five-order adaptive optics for meter-class telescopes." *Top Mtg on Adap Opt, Opt Soc Am Tech Dig Series* 13 (1996): 63.
102. Bruns, D. G., T. K. Barrett, D. G. Sandler, H. M. Martin, G. Brusa, J. R. P. Angel, R. Biasi, D. Gallieni, and P. Salinari. "Force-actuated adaptive secondary mirror prototype." *Proc Top Mtg on Adap Opt, ESO Conf and Workshop Proc* 54 (1996): 251.
103. Bryant, J. J., J. W. O'Byrne, R. A. Minard, and P. W. Fekete. "Low order adaptive optics at the Anglo-Australian Telescope." *Proc Top Mtg on Adap Opt, ESO Conf and Workshop Proc* 54 (1996): 23.

104. Buchdahl, H. A. "Optical aberration coefficients." *J Opt Soc Am* 50 (1960): 539.
105. Buchheim, R. K., R. Pringle, and H. W. Schaefgen. "Lead-angle effects in turbulence-compensating reciprocity tracking systems." *Appl Opt* 17 (1978): 165.
106. Bufton, J. L. "Comparison of vertical profile turbulence structure with stellar observations." *Appl Opt* 12 (1973): 1785.
107. Bures, K. J. TASC Tech Inform. Memo 996-8, August 1977.
108. Burns, S. A., R. Tumbar, A. E. Elsner, D. Ferguson, and D. X. Hammer. "Large-field-of-view, modular, stabilized, adaptive-optics-based scanning laser ophthalmoscope." *J Opt Soc Am* 24 (2007): 1313.
109. Burrows, A., M. Marley, W. B. Hubbard, J. I. Lunine, T. Guillot, D. Saumon, R. Freedman, D. Sudarsky, and C. Sharp. "A nongray theory of extrasolar giant planets and brown dwarfs." *Astrophys J* 491 (1997): 856.
110. Buscher, D., P. Doel, R. Humphreys, R. Myers, M. Wells, A. Longmore, B. Gentles, G. Jones, and S. Worswick. "Natural guide star adaptive optics for the 4.2m William Herschel telescope." *Top Mtg on Adap Opt, Opt Soc Am Tech Dig Series* 13 (1996): 66.
111. Butts, R. R., and C. B. Hogge. "Phase conjugate adaptive optics using perimeter phase measurement." *J Opt Soc Am* 67 (1977): 278.
112. Calef, B., E. Therkildsen, and M. Roggemann. "Wavefront-sensor-based frame selection." *Opt Eng* 44 (2005): 116003.
113. Cannon, R. H. *Dynamics of Physical Systems*. New York: McGraw-Hill, 1967.
114. Carslaw, H. S., and J. C. Jaeger. *Conduction of Heat in Solids*. 2nd ed. London: Oxford University Press, 1980.
115. Cao, G., and X. Yu. "Accuracy analysis of a Hartmann-Shack wavefront sensor operated with a faint object." *Opt Eng* 33 (1994): 2331.
116. Cao, Z., Q. Mu, L. Hu, D. Li, Z. Peng, Y. Liu, and L. Xuan. "Preliminary use of nematic liquid crystal adaptive optics with a 2.16-meter reflecting telescope." *Opt Expr* 17 (2009): 2530.
117. Cao, Z., Q. Mu, L. Hu, Y. Liu, Z. Peng, X. Liu, and L. Xuan. "Achromatic system for a twisted alignment liquid crystal wavefront corrector." *Appl Opt* 47 (2008): 1020.
118. Casasent, D. "Spatial light modulators." *Proc IEEE* 65 (1977): 143.
119. Cederquist, J., S. R. Robinson, D. Kryskowski, J. R. Fienup, and C. C. Wackerman. "Cramer-Rao lower bound on wavefront sensor error." *Opt Eng* 25 (1986): 4.
120. Cense, B., E. Koperda, J. M. Brown, O. P. Kocaoglu, W. Gao, R. S. Jonnal, and D. T. Miller. "Volumetric retinal imaging with ultrahigh-resolution spectral-domain optical coherence tomography and adaptive optics using two broadband light sources." *Opt Expr* 17 (2009): 4095.
121. Chaffin, J. H. "Optical coatings for active components." *Proc SPIE* 1543 (1991): 165.
122. Chamot, S. R., C. Dainty, and S. Esposito. "Adaptive optics for ophthalmic applications using a pyramid wavefront sensor." *Opt Expr* 14 (2006): 518.
123. Chassat, F., G. Rousset, and J. Primot. "Theoretical and experimental evaluation of isoplanatic patch size for adaptive optics." *Proc SPIE* 1114 (1989): 14.
124. Checkland, P. *Systems Thinking, Systems Practice*. New York: Wiley, 1986.
125. Chen, C., H. Yang, X. Feng, and H. Wang. "Optimization criterion for initial coherence degree of lasers in free-space optical links through atmospheric turbulence." *Opt Lett* 34 (2009): 419.

126. Chen, C. F., and I. J. Haas. *Elements of Control Systems Analysis*, Englewood Cliffs, NJ: Prentice-Hall, 1968.
127. Chen, C. T. *Linear System Theory and Design*. New York: Holt, Rinehart, and Winston, 1984.
128. Chen, L., P. B. Kruger, H. Hofer, B. Singer, and D. R. Williams. "Accommodation with higher-order monochromatic aberrations corrected with adaptive optics." *J Opt Soc Am A* 23 (2006): 1.
129. Chen, M., F. S. Roux, and J. C. Olivier. "Detection of phase singularities with a Shack-Hartmann wavefront sensor." *J Opt Soc Am A* 24 (2007): 1994.
130. Chernov, L. A. *Wave Propagation in a Random Medium*. New York: McGraw-Hill, 1960.
131. Chi, C., N. B. James III, and P. L. Misuinas. "Spectral shared aperture component." *Proc SPIE* 171 (1979): 145.
132. Christopher, N. M., and I. Smail. "A catalogue of potential adaptive optics survey fields from the UKIRT archive." *Mon Not Roy Astron Soc* 365 (2006): 439.
133. Christou, J. C. "Blind deconvolution post-processing of images corrected by adaptive optics." *Proc SPIE* 2534 (1995): 226.
134. Christou, J. C. "Reference-less detection, astrometry, and photometry of faint companions with adaptive optics." *Astrophys J* 698 (2009): 28.
135. Christou, J. C. "Gemini Observatory adaptive optics instrumentation and capabilities." *Am Astro Soc* 215 (2009): 214.
136. Chui, T. Y. P., H. Song, and S. A. Burns. "Adaptive-optics imaging of human cone photoreceptor distribution." *J Opt Soc Am A* 25 (2008): 12.
137. Chung, C-Y., K-C. Cho, C-C. Chang, C-H. Lin, W-C. Yen, and S-J. Chen. "Adaptive-optics system with liquid-crystal phase-shift interferometer." *Appl Opt* 45 (2006): 3409.
138. Churchman, C. W. *The Systems Approach*. New York: Dell, 1983.
139. Churnside, J. H. "Aperture averaging of optical scintillations in the turbulent atmosphere." *Appl Opt* 30 (1991): 1982.
140. Claflin, E. S., and N. Bareket. "Configuring an electrostatic membrane mirror by least-squares fitting with analytically derived influence functions." *J Opt Soc Am A* 3 (1986): 1833.
141. Clampin, M. "Optimization of MCP intensifier tubes in astronomical adaptive optics sensors." *Proc SPIE* 1114 (1989): 152.
142. Clampin, M., J. Crocker, F. Paresce, and M. Rafal. "Optical Ranicon detectors for photon counting imaging: I." *Rev Sci Instrum* 59 (1988): 1.
143. Clark, R., J. Karpinsky, G. Borek, E. Johnson, and N. Clark. "High speed micro-machine device for adaptive correction of aero-optic effects." *Proc Top Mtg on Adap Opt, ESO Conf and Workshop Proc* 54 (1996): 433.
144. Claus, A. C. "On Archimedes' burning glass." *Appl Opt* 12 (1973): A14.
145. Clifford, S. F. "The classical theory of wave propagation in a turbulent medium." In *Laser Beam Propagation in the Atmosphere*, Chap. 2, J. W. Strohbehn, ed., New York: Springer-Verlag, 1978.
146. Coates, P. B. "A theory of afterpulse formation in photomultipliers and the pulse height distribution." *J Phys D: Appl Phys* 6 (1973): 1159.
147. Close, L. M., and D. W. McCarthy, Jr. "Infrared imaging using a tip-tilt secondary mirror." *Proc SPIE* 1920 (1993): 353.
148. Conan, R. "Mean-square residual error of a wavefront after propagation through atmospheric turbulence and after correction with Zernike polynomials." *J Opt Soc Am A* 25 (2008): 526.

149. Conan, R., C. Bradley, P. Hampton, O. Keskin, A. Hilton, and C. Blain. "Distributed modal command for a two-deformable-mirror adaptive optics system." *Appl Opt* 46 (2007): 4329.
150. Conan, R., O. Lardiere, G. Herriot, C. Bradley, and K. Jackson. "Experimental assessment of the matched filter for laser guide star wavefront sensing." *Appl Opt* 48 (2009): 1198.
151. Conforti, G. "Zernike aberration coefficients from Seidel and higher-order power-series coefficients." *Opt Lett* 8 (1983): 7.
152. Corrsin, S. "On the spectrum of isotropic temperature fluctuations in an isotropic turbulence." *J Appl Phys* 22 (1951): 469.
153. Costa, J. B., S. Hippler, M. Feldt, S. Esposito, R. Ragazzoni, P. Bizenberger, E. Puga, and T. F. E. Henning. "PYRAMIR: A near-infrared pyramid wavefront sensor for the Calar Alto adaptive optics system." *Proc SPIE* 4839 (2003): 280.
154. Crawford, D. P., R. K. Tyson, and R. J. Morgan. "Interaction of thermal blooming, turbulence, and slewing in ground-to-space propagation." *Proc SPIE* 1221 (1990): 146.
155. Creath, K. "Comparison of phase-measurement algorithms." *Proc SPIE* 680 (1986): 19.
156. Cubalchini, R. "Modal wavefront estimation from phase derivative measurements." *J Opt Soc Am* 69 (1979): 7.
157. Cuellar, L., P. Johnson, and D. G. Sandler. "Performance tests of a 1500 degree-of-freedom adaptive optics system for atmospheric compensation."*Proc SPIE* 1542 (1991): 468.
158. Dai, Y., Z. Liu, Z. Jin, J. Xu, and J. Lin. "Active control of a 30 m ring interferometric telescope primary mirror." *Appl Opt* 48 (2009): 664.
159. Dalimier, E., and C. Dainty. "Use of a customized vision model to analyze the effects of higher-order ocular aberrations and neural filtering on contrast threshold performance." *J Opt Soc Am A* 25 (2008): 2078.
160. Daly, D. *Microlens Arrays*. Boca Raton, FL: CRC Press, 2000.
161. Davies, R., S. Rabien, C. Lidman, M. LeLouarn, M. Kasper, N. M. Forster, Schreibner, V. Roccatagliata, N. Ageorges, P. Amico, C. Dumas, and F. Mannucci. "Laser guidestar adaptive optics without tip-tilt." *European Southern Observatory Messenger* 131 (2008): 7.
162. Davis, D. S., P. Hickson, G. Herriot, and C-Y. She. "Temporal variability of the telluric sodium layer." *Opt Lett* 31 (2006): 3369.
163. Dayton, D., B. Pierson, B. Spielbusch, and J. Gonglewski. "Atmospheric structure function measurements with a Shack-Hartmann wavefront sensor." *Opt Lett* 17 (1992): 1737.
164. de Chatellus, H. G., I. Moldovan, V. Fesquet, and J-P Pique. "Suppression of Rayleigh scattering noise in sodium laser guide stars by hyperfine depolarization of fluorescence." *Opt Expr* 14 (2006): 11494.
165. de Chatellus, H. G., J-P. Pique, and I. C. Moldovan. "Return flux budget of polychromatic laser guide stars." *J Opt Soc Am A* 25 (2008): 400.
166. Dekany, R. G. "The Palomar adaptive optics system." *Top Mtg on Adap Opt, Opt Soc Am Tech Dig Series* 13 (1996): 40.
167. DeMarco, T. *Structured Analysis and Systems Specification*. Englewood Cliffs, NJ: Prentice-Hall, 1979.
168. DeMaria, A. "High-power carbon dioxide lasers." *J Proc IEEE* 61 (1973): 6.

169. Denman, C. A., P. D. Hillman, G. T. Moore, J. M. Telle, J. E. Preston, J. D. Drummond, and R. Q. Fugate. "Realization of a 50 watt facility-class sodium guidestar pump laser." *Proc SPIE* 5707 (2005): 46.
170. Dente, G. C., D. C. Gardner, and P. D. Tannen. "Error propagation in lateral shearing interferometry." WJSA-R-86-A-018, Albuquerque, NM: W. J. Schafer Associates, Inc., 1986.
171. Devaney, N. "Adaptive optics specification for a 10m telescope on the ORM." *Top Mtg on Adap Opt, Opt Soc Am Tech Dig Series* 13 (1996): 24.
172. Dimov, N. A., A. A. Kornienko, G. N. Mal'tsev, and A. S. Pechenov. "Investigation of the quality of a spatial approximation of a wavefront for a zonal-modal correction." *Sov J Opt Technol* 52 (1985): 317.
173. Doel, P. "A comparison of Shack-Hartmann and curvature sensing for large telescopes." *Proc SPIE* 2534 (1995): 265.
174. Dolne, J. J., R. J. Tansey, K. A. Black, J. H. Deville, P. R. Cunningham, K. C. Widen, and P. S. Idell. "Practical issues in wavefront sensing by use of phase diversity." *Appl Opt* 42 (2003): 5284.
175. Dooling, D. "Peeking behind the veil of Venus." *Nat Sol Obs* Press release February 10, 2006.
176. Down, D. "Image-position error associated with a focal plane array." *J Opt Soc Am A* 9 (1992): 700.
177. Downie, J. D., and J. W. Goodman. "Accuracy requirements of optical linear algebra processors in adaptive optics imaging systems." *Appl Opt* 28 (1989): 4298.
178. Downie, J. D., and J. W. Goodman. "Optimal wavefront control for adaptive segmented mirrors." *Appl Opt* 28 (1989): 5326.
179. Drummond, J., J. Telle, C. Denman, P. Hillman, and A. Tuffli. "Photometry of a sodium laser guide star at the Starfire Optical Range." *Publ Astron Soc Pac* 116 (2004): 278.
180. Dubra, A. "Wavefront sensor and wavefront corrector matching in adaptive optics." *Opt Expr* 15 (2007): 2762.
181. Duffner, R. W. *The Adaptive Optics Revolution: A History*. Albuquerque, NM: University of New Mexico Press, 2009.
182. Dunkle, T. "The Big Glass," *Discover*, July 1989.
183. Dunphy, J. R., and D. C. Smith. "Multiple-pulse thermal blooming and phase compensation." *J Opt Soc Am A* 67 (1977): 295.
184. Ealey, M. A. "Deformable mirrors at Litton/Itek: A historical perspective." *Proc SPIE* 1167 (1989): Paper No. 4.
185. Ealey, M. A. "Actuators: Design fundamentals, key performance specifications, and parametric trades." *Proc SPIE* 1543 (1991): 346.
186. Ealey, M. A., and J. F. Washeba. "Continuous facesheet low voltage deformable mirrors." *Opt Eng* 29 (1990): 1191.
187. Ealey, M. A., and J. A. Wellman. "Deformable mirrors: Design fundamentals, key performance specifications, and parametric trades." *Proc SPIE* 1543 (1991): 36.
188. Ealey, M. A., and J. A. Wellman. "Xinetics low cost deformable mirrors with actuator replacement cartridges." *Proc SPIE* 2201 (1994): 680.
189. Edlen, B. "The refractive index of air." *Metrologia* 2 (1966): 71.
190. Eichel, P. H., and C. V. Jakowatz, Jr. "Phase-gradient algorithm as an optimal estimator of the phase derivative." *Opt Lett* 14 (1989): 1101.

191. Eichler, H. J., A. Haase, and R. Menzel. "Solid-state laser amplifier with SBS-phase conjugation." *Proc ICO-16 Satellite Conf on Active and Adap Opt, ESO Conf and Workshop Proc* 48, (1993): 401.
192. Elbaum, M., and P. Diament. "SNR in photocounting images of rough objects in partially coherent light." *Appl Opt* 15 (1976): 2268.
193. Elbaum, M., and P. Diament. "Estimation of image centroid, size, and orientation with laser radar." *Appl Opt* 16 (1977): 2433.
194. Elbaum, M., and M. Greenebaum. "Annular apertures for angular tracking." *Appl Opt* 16 (1977): 2438.
195. Ellerbroek, B. L. "First-order performance evaluation of adaptive-optics systems for atmospheric-turbulence compensation in extended-field-of-view astronomical telescopes." *J Opt Soc Am A* 11 (1994): 783.
196. Ellerbroek, B. L., C. Van Loan, N. P. Pitsianis, and R. J. Plemmons. "Optimizing closed loop adaptive optics performance using multiple control bandwidths." *Proc SPIE* 2201 (1994): 935.
197. Ellerbroek, B. L., and T. A. Rhoadarmer. "Optimization of closed-loop adaptive-optics control algorithms using measured performance data: Experimental results." *Top Mtg on Adap Opt, Opt Soc Am Tech Dig Series* 13 (1996): 233.
198. Ellerbroek, B. L., D. W. Tyler, and R. Racine. "Sky coverage calculations for Shack-Hartmann NGS AO systems." *Proc Top Mtg on Adap Opt, ESO Conf and Workshop Proc* 54 (1996): 357.
199. Elson, J. M., H. E. Bennett, and J. M. Bennett. Scattering from optical surfaces. In *Applied Optics and Optical Engineering*, eds. R. R. Shannon, J. C. Wyant, Vol. VII, New York: Academic Press, 1979.
200. Enguehard, S., and B. Hatfield. "Perturbative approach to the small-scale physics of the interaction of thermal blooming and turbulence." *J Opt Soc Am A* 8 (1991): 637.
201. Erry, G., P. Harrison, J. Burnett, D. Benton, A. Scott, and S. Woods. "Results of atmospheric compensation using a wavefront curvature based adaptive optics system." *Proc SPIE* 4884 (2003): 245.
202. Esposito, S., G. Brusa, and D. Bonaccini. "Liquid crystal wavefront correctors: Computer simulation results." *Proc ICO-16 Satellite Conf on Active and Adap Opt, ESO Conf and Workshop Proc* 48 (1993): 289.
203. Esposito, S., and A. Riccardi. "Pyramid wavefront sensor behavior in partial correction adaptive optic systems." *Astron Astrophys* 369 (2001): L9.
204. Evans, J. W., B. Macintosh, L. Poyneer, K. Morzinski, S. Severson, D. Dillon, D. Gavel, and L. Reza. "Demonstrating sub-nm closed loop MEMS flattening." *Opt Expr* 14 (2006): 5558.
205. Everson, J. H., R. E. Aldrich, and N. P. Albertinetti. "Discrete actuator deformable mirror." *Opt Eng* 20 (1981): 316.
206. Everson, J. H., and J. A. Greenough. "Evaluation of a deformable monolithic mirror/heat exchanger unit." *Proc SPIE* 179 (1979): 91.
207. Fabellinskii, I. L. *Molecular Scattering of Light*, New York: Plenum, 1968.
208. Fante, R. L. "The effect of source temporal coherence on light scintillations in weak turbulence." *J Opt Soc Am* 69 (1979): 71.
209. Fante, R. L. "Electromagnetic beam propagation in turbulent media: An update." *Proc IEEE* 68 (1980): 1434.
210. Feinleib, J. *Proposal 82-P4*. Cambridge, MA: Adaptive Optics Associates, 1982.
211. Feinleib, J., S. G. Lipson, and P. F. Cone. "Monolithic piezoelectric mirror for wavefront correction." *Appl Phys Lett* 25 (1974): 311.

212. Fender, J. S. ed. "Synthetic aperture systems." *Proc SPIE* 440 (1984).
213. Fengjie, X., J. Zongfu, X. Xiaojun, and G. Yifeng. "High-diffractive-efficiency defocus grating for wavefont curvature sensing." *J Opt Soc Am A* 24 (2007): 3444.
214. Fenster, A., J. C. Leblanc, W. B. Taylor, and H. E. Johns. "Linearity and fatigue in photo-multipliers." *Rev Sci Instrum* 44 (1973): 689.
215. Fernandez, E. J., and P. Artal. "Ocular aberrations up to the infrared range: From 632.8 to 1070 nm." *Opt Expr* 16 (2008): 21199.
216. Fienup, J. R. "Phase retrieval algorithms: A comparison." *Appl Opt* 21 (1982): 2758.
217. Fienup, J. R. "Phase-retrieval algorithms for a complicated optical system." *Appl Opt* 32 (1993): 1737.
218. Figueira, G., J. Wemans, H, Pires, N. Lopes, and L. Cardoso. "Single adjuster deformable mirror with four contact points for simultaneous correction of astigmatism and defocus." *Opt Expr* 15 (2007): 5664.
219. Fisher, A. D. "Self-referenced high resolution adaptive wavefront estimation and compensation." *Proc SPIE* 551 (1985): 102.
220. Fisher, A. D., and C. Warde. "Technique for real-time high-resolution adaptive phase compensation." *Opt Lett* 8 (1983): 353.
221. Fisher, R. A. *Optical Phase Conjugation*. New York: Academic Press, 1983.
222. Flath, L., J. An, J. Brase, C. Carrano, C. B. Dane, S. Fochs, R. Hurd, M. Kartz, and R. Sawvel. "Development of adaptive techniques for high-power lasers." *Proc 2nd Int Workshop on Ad Opt for Industry and Medicine*, G. Love, ed. Singapore: World Scientific, 1999.
223. Florence, J. M. "Joint-transform correlator systems using deformable-mirror spatial light modulators." *Opt Lett* 14 (1989): 341.
224. Foley, J. T., and M. A. Abdul Jalil. "Role of diffraction in phase retrieval from intensity measurements." *Proc SPIE* 351 (1982): 80.
225. Foo, G., D. M. Palacios, and G. A. Swartzlander, Jr. "Optical vortex coronagraph." *Opt Lett* 30 (2005): 3308.
226. Forbes, F. F. "Bimorph PZT active mirror." *Proc SPIE* 1114 (1989): 146.
227. Forbes, F. F., D. A. Morse, and G. A. Poczulp. "Site survey instrumentation for the National New Technology Telescope (NNTT)." *Opt Eng* 27 (1988): 845.
228. Ford, S. D., M. C. Roggemann, and B. M. Welsh. "Frame selection performance limits for statistical image reconstruction of adaptive optics compensated images." *Opt Eng* 35 (1996): 1025.
229. Foy, R., and A. Labeyrie. "Feasibility of adaptive optics telescope with laser probe." *Astron Astrophys* 152 (1985): L29.
230. Foy, R., A. Migus, F. Biraben, G. Grynberg, P. R. McCullough, and M. Tallon. "The polychromatic artificial sodium star: A new concept for correcting atmospheric tilt." *Astron Astrophys Supp Ser* 111 (1995): 569.
231. Foy, R., J. P. Pique, V. Bellanger, P. Chevrou, A. Petit, C. Hogemann, L. Noethe, M. Schock, J. Girard, M. Tallon, E. Thiebaut, J. Vaillant, F. C. Foy, and M. Van Dam. "Feasibility study of the polychromatic laser guide star." *Proc SPIE* 4839 (2003): 484.
232. Foy, R., M. Tallon, M. Sechaud, and N. Hubin. "ATLAS experiment to test the laser probe technique for wavefront measurements." *Proc SPIE* 1114 (1989): 174.
233. Frantz, L. M., A. A. Sawchuk, and W. von der Ohe. "Optical phase measurement in real time." *Appl Opt* 18 (1979): 19.

234. Freeman, R. H., R. J. Freiberg, and H. R. Garcia. "Adaptive laser resonator." *Opt Lett* 2 (1978): 3.
235. Freeman, R. H., H. R. Garcia, J. DiTucci, and G. R. Wisner. "High-Speed Deformable Mirror System," U.S. Air Force Weapons Laboratory Report AFWL-TR-76-146, Kirtland Air Force Base, New Mexico (unpublished), 1977.
236. Freischlad, K. R., and C. L. Koliopoulos. "Modal estimation of a wavefront from difference measurements using the discrete Fourier transform." *J Opt Soc Am A* 3 (1986): 11.
237. Fried, D. L. "The effect of wavefront distortion on the performance of an ideal optical heterodyne receiver and an ideal camera." *Conf on Atmospheric Limitations to Optical Propagation* Gaithersburg, MD: U. S. Nat Bur Stds CRPL, 1965.
238. Fried, D. L. "Statistics of a geometric representation of wavefront distortion." *J Opt Soc Am* 55 (1965): 1427.
239 Fried, D. L. "Limiting resolution looking down through the atmosphere." *J Opt Soc Am* 56 (1966): 1380.
240. Fried, D. L. *Effect of Speckle on Wavefront Distortion Sensing*. Placentia, CA: The Optical Sciences Company Report TR-251, 1977.
241. Fried, D. L. "Least-square fitting a wavefront distortion estimate to an array of phase-difference measurements." *J Opt Soc Am* 67 (1977): 370.
242. Fried, D. L. "Resolution, signal-to-noise ratio, and measurement precision." *J Opt Soc Am* 69 (1979): 399.
243. Fried, D. L. "Anisoplanatism in adaptive optics." *J Opt Soc Am* 72 (1982): 52.
244. Fried, D. L. "Analysis of focus anisoplanatism: The fundamental limit in performance of artificial guide star adaptive optics systems (AGS/AOS)." *Proc Laser Guide Star Adaptive Optics Workshop* 1, 37. Albuquerque, NM: U. S. Air Force Phillips Laboratory, 1992.
245. Fried, D. L. "Focus anisoplanatism in the limit of infinitely many artificial-guide-star reference spots." *J Opt Soc Am A* 12 (1995): 939.
246. Fried, D. L., and G. E. Mevers. "Evaluation of ro for propagation down through the atmosphere." *Appl Opt* 13 (1974): 11.
247. Fried, D. L., and J. L. Vaughn. *Focus Anisoplanatism for a Multiple Spot Artificial Guide-Star Pattern*. Placentia, CA: The Optical Sciences Company Report BC-641, 1991.
248. Fried, D. L., and J. F. Belsher. "Analysis of fundamental limits to artificial-guide-star adaptive-optics-system performance for astronomical imaging." *J Opt Soc Am A* 11 (1994): 277.
249. Friedman, H., K. Avicola, H. Bissinger, J. Brase, J. Duff, D. Gavel, J. Horton, C. Max, S. Olivier, D. Rapp, T. Salmon, D. Smauley, and K. Waltjen. "Laser guide star measurements at Lawrence Livermore National Laboratory." *Proc SPIE* 1920 (1993): 52.
250. Friedman, H., G. Erbert, T. Kuklo, T. Salmon, D. Smauley, G. Thompson, J. Malik, N. Wong, K. Kanz, and K. Neeb. "Sodium beacon laser system for the Lick Observatory." *Proc SPIE* 2534 (1995): 150.
251. Friedman, H., J. Morris, and J. Horton. "System design for a high power sodium laser beacon." *Proc Laser Guide Star Adaptive Optics Workshop* 2, 639. Albuquerque, NM: U. S. Air Force Phillips Laboratory, 1992.
252. Friedman, H., R. Foy, M. Tallon, and A. Migus. "First results of a polychromatic artificial sodium star for correction of tilt." *Top Mtg on Adap Opt, Opt Soc Am Tech Dig Series* 13 (1996): 78.

253. Fu, T. Y., and M. Sargent III. "Effects of signal detuning on phase conjugation." *Opt Lett* 4 (1979): 366.
254. Fugate, R. Q. "Laser beacon adaptive optics for power beaming applications," *Proc SPIE* 2121 (1994): 68.
255. Fugate, R. Q. "Observations of faint objects with laser beacon adaptive optics," *Proc SPIE* 2201 (1994): 10.
256. Fugate, R. Q., D. L. Fried, G. A. Ameer, B. R. Boeke, S. L. Browne, P. H. Roberts, R. E. Ruane, and L. M. Wopat. "Measurement of atmospheric wavefront distortion using scattered light from a laser guide star," *Nature* 353 (1991): 144.
257. Fugate, R. Q., C. H. Higgins, B. L. Ellerbroek, J. M. Spinhirne, B. R. Boeke, R. A. Cleis, D. W. Swindle, and M. D. Oliker. "Laser beacon adaptive optics with an unintensified CCD wavefront sensor and fiber optic synthesized array of silicon avalanche photodiodes for fast guiding," *Proc ICO-16 Satellite Conf on Active and Adap Opt, ESO Conf and Workshop Proc* 48 (1993): 487.
258. Fugate, R. Q., J. F. Riker, J. T. Roark, S. Stogsdill, and B. D. O'Neil. "Laser beacon compensated images of Saturn using a high-speed, near-infrared correlation tracker," *Proc Top Mtg on Adap Opt, ESO Conf and Workshop Proc* 54 (1996): 287.
259. Fuschetto, A. "Three-actuator deformable water-cooled mirror," *Opt Eng* 20 (1981): 310.
260. Fuschetto, A. "Three-actuator deformable water-cooled mirror," *Proc SPIE* 179 (1979).
261. Gaffard, J.-P., P. Jagourel, and P. Gigan. "Adaptive optics: Description of available components at LASERDOT," *Proc SPIE* 2201 (1994): 688.
262. Gallant, P. J., and G. J. M. Aitken. "Simple neural networks as wavefront slope predictors: Training and performance issues," *Top Mtg on Adap Opt, Opt Soc Am Tech Dig Series* 13 (1996): 253.
263. Garcia, H. R., and L. D. Brooks. "Characterization techniques for deformable metal mirrors," *Proc SPIE* 141 (1978): 74.
264. Gardner, C. S., B. M. Welsh, and L. A. Thompson. "Design and performance analysis of adaptive optical telescopes using laser guide stars," *Proc IEEE* 78 (1990): 1721.
265. Gaskill, J. D. *Linear Systems, Fourier Transforms, and Optics*. New York: Wiley, 1978.
266. Gavel, D. T. "Tomography for multiconjugate adaptive optics systems using laser guide stars," *Proc SPIE* 5490 (2004): 1356.
267. Gavel, D. T., C. E. Max, K. Avicola, H. D. Bissinger, J. M. Brase, J. Duff, H. W. Friedman, J. R. Morris, S. S. Olivier, D. A. Rapp, J. T. Salmon, and K. E. Waltjen. "Design and early results of the sodium-layer laser guide star adaptive optics experiment at the Lawrence Livermore National Laboratory," *Proc ICO-16 Satellite Conf on Active and Adap Opt, ESO Conf and Workshop Proc* 48 (1993): 493.
268. Gavel, D. T., and S. S. Olivier. "Simulation and analysis of laser guide star adaptive optics systems for the eight to ten meter class telescopes," *Proc SPIE* 2201 (1994): 295.
269. Gavrielides, A. "Vector polynomials orthogonal to the gradient of Zernike polynomials," *Opt Lett* 7 (1982): 526.
270. Gbur, G., and R. K. Tyson. "Vortex beam propagation through atmospheric turbulence and topological charge conservation," *J Opt Soc Am A* 25 (2008): 225.

271. Ge, J., B. Jacobsen, J. R. P. Angle, N. Woolf, J. H. Black, M. Lloyd-Hart, P. Gray, and R. Q. Fugate. "An optical ultrahigh resolution spectrograph with the adaptive optics," *Top Mtg on Adap Opt, Opt Soc Am Tech Dig Series* 13 (1996): 122.
272. Geary, J. C. "Rapid-framing CCDs with 16 output ports for laser guide star sensors," *Proc SPIE* 2201 (1994): 607.
273. Geary, J. C., and G. A. Luppino. "New circular radial-scan frame-storage CCDs for low-order adaptive optics wavefront curvature sensing," *Proc SPIE* 2201 (1994): 588.
274. Geary, J. M. "Ray misidentification errors in Hartmann-like wavefront sensors," *Opt Eng* 30 (1991): 1388.
275. Geary, J. M. *Introduction to Wavefront Sensors*. Bellingham, WA: SPIE Optical Engineering Press, 1995.
276. Gebhardt, F. G. "High power laser propagation," *Appl Opt* 15 (1976): 1479.
277. Gebhardt, F. G. "Twenty-five years of thermal blooming: An overview," *Proc SPIE* 1221 (1990): 2.
278. Gendron, E. "Modal control optimization in an adaptive optics system," *Proc ICO-16 Satellite Conf on Active and Adap Opt, ESO Conf and Workshop Proc* 48 (1993): 187.
279. Gerchberg, R. W., and W. O. Saxton. "A practical algorithm for the determination of phase from image and diffraction plane pictures," *Optic (Stuttgart)* 35 (1972): 237.
280. Germann, L. M. "Specification of fine-steering mirrors for line-of-sight stabilization systems," *Proc SPIE* 1543 (1991): 202.
281. Ghiglia, D. C., and L. A. Romero. "Direct phase estimation from phase differences using fast elliptic partial differential equation solvers," *Opt Lett* 14 (1989): 1107.
282. Giacconi, R. *VLT Whitebook*. European Southern Observatory: Garching bei Munchen, 1998.
283. Gil, M. A., and J. M. Simon. "Diffraction grating and optical aberrations: A new and exact formulation," *Appl Opt* 24: (1985): 2956.
284. Gilles, L., and B. Ellerbroek. "Shack-Hartmann wavefront sensing with elongated sodium laser beacons: Centroiding versus matched filtering," *Appl Opt* 45 (2006): 6568.
285. Gilles, L., and B. L. Ellerbroek. "Constrained matched filtering for extended dynamic range and improved noise rejection for Shack-Hartmann wavefront sensing," *Opt Lett* 33 (2008): 1159–61.
286. Give'on, A., N. J. Kasdin, R. J. Vanderbei, and Y. Avitzour. "On representing and correcting wavefront errors in high-contrast imaging systems," *J Opt Soc Am A* 23 (2006): 1063.
287. Glazer, O., E. N. Ribak, and L. Mirkin. "Adaptive optics implementation with a Fourier reconstructor," *Appl Opt* 46 (2007): 574.
288. Gleckler, A. D., D. J. Markason, and G. H. Ames. "PAMELA: Control of a segmented mirror via wavefront tilt and segment piston sensing," *Proc SPIE* 1543 (1991): 176.
289. Glindemann, A., and T. Berkefeld. "A new method for separating atmospheric layers using a Shack-Hartmann curvature sensor," *Top Mtg on Adap Opt, Opt Soc Am Tech Dig Series* 13 (1996): 153.
290. Goede, P., T. Heinz, F. Johnson, and A. MacCollum. "Diamond turned deformable mirror," *Proc SPIE* 365 (1982): 138.

291. Golbraikh, E., and N. Kopeika. "Turbulence strength parameter in laboratory and natural optical experiments in non-Kolmogorov cases," *Opt Commun* 242 (2008): 333.
292. Goldberg, D. *Genetic Algorithms in Search, Optimization and Machine Learning*. Reading, MA: Addison Wesley Longman, 1989.
293. Goncharov, A. V., N. Devaney, and C. Dainty. "Atmospheric dispersion compensation for extremely large telescopes," *Opt Expr* 15 (2007): 1534.
294. Gonglewski, J. D., D. G. Voelz, J. S. Fender, D. C. Dayton, B. K. Spielbusch, and R. E. Pierson. "First astronomical application of postdetection turbulence compensation: Images of α Aurigae, ν Ursae Majoris, and α Germinorum using self-referenced speckle holography," *Appl Opt* 29 (1990): 4527.
295. Gonsalves, R. "Phase retrieval from modulus data," *J Opt Soc Am* 66 (1976): 961.
296. Gonsalves, R. A. "Fundamentals of wavefront sensing by phase retrieval," *Proc SPIE* 351 (1982): 56.
297. Gonsalves, R. A. "Phase retrieval by differential intensity measurements," *J Opt Soc Am A* 4 (1987): 166.
298. Goodfriend, M. J., K. M. Shoop, and C. G. Miller. "High force, high strain, wide band width linear actuator using the magnetostrictive material, Terfenol-D," *Proc SPIE* 1543 (1991): 301.
299. Goodman, J. W. *Introduction to Fourier Optics*. New York: McGraw-Hill, 1968.
300. Goodman, J. W. *Statistical Optics*, 413. New York: Wiley, 1985.
301. Goodman, J. W., W. H. Huntley, Jr., D. W. Jackson, and M. Lehman. "Wavefront-reconstruction imaging through random media," *Appl Phys Lett* 8 (1966): 311.
302. Goodman, J. W., and M. S. Song. "Performance limitations of an analog method for solving simultaneous linear equations," *Appl Opt* 21 (1982): 502.
303. Gordeyev, S., T. E. Hayden, and E. J. Jumper. "Aero-optical and flow measurements over a flat-windowed turret," *AIAA J* 45 (2007): 347.
304. Gosselin, P., P. Jagourel, and J. Peysson. "Objective comparisons between stacked array mirrors and bimorph mirrors," *Proc SPIE* 1920 (1993): 81.
305. Graves, J. E. "Future directions for the University of Hawaii adaptive optics program," *Top Mtg on Adap Opt, Opt Soc Am Tech Dig Series* 13 (1996): 49.
306. Gray, D. C., W. Merigan, J. I. Wolfing, B. P. Gee, J. Porter, A. Dubra, T. H. Twietmeyer, and K. Ahmad. "In vivo fluorescence imaging of primate retinal ganglion cells and retinal pigment epithelial cells," *Opt Expr* 14 (2006): 7144.
307. Greenwood, D. P. "Bandwidth specification for adaptive optics systems," *J Opt Soc Am* 67 (1977): 390.
308. Greenwood, D. P. "Tracking turbulence-induced tilt errors with shared and adjacent apertures," *J Opt Soc Am* 67 (1977): 282.
309. Greenwood D. P., and C. A. Primmerman. "Adaptive optics research at Lincoln Laboratory," *Lincoln Lab J* 5 (1992): 3; Greenwood, D. P., and C. A. Primmerman. "The history of adaptive-optics development at the MIT Lincoln Laboratory," *Proc SPIE* 1920 (1993): 220.
310. Greivenkamp, J. E., and D. G. Smith. "Graphical approach to Shack-Hartmann lenslet array design," *Opt Eng* 47 (2008): 063601.
311. Grossman, S. B., and R. B. Emmons. "Performance analysis and size optimization of focal planes for point-source tracking algorithm applications," *Opt Eng* 23 (1984): 167.
312. Grosso, R. P., and M. Yellin. "The membrane mirror as an adaptive optical element," *J Opt Soc Am* 67 (1977): 399.

313. Gruneisen, M. T., R. C. Dymale, J. R. Rotge, L. F. DeSandre, and D. L. Lubin. Wavelength-dependent characteristics of a telescope system with diffractive wavefront compensation," *Opt Eng* 44 (2005): 068002.
314. Guha, J. K., and J. A. Plascyk. "Low-absorption grating beam samplers," *Proc SPIE* 171 (1979): 117.
315. Gully, S. W., J. Huang, N. Denis, D. P. Looze, A. Wirth, A. J. Jankevics, and D. A. Castaflon. "Experiments with adaptive nonlinear control systems for atmospheric correction," *Proc SPIE* 2201 (1994): 920.
316. Gurski, G. F., N. T. Nomiyama, R. J. Radley, and J. Wilson. "An initial evaluation of performance of adaptive optical systems with extended dynamic targets," *J Opt Soc Am* 67 (1977): 345.
317. Halevi, P. "Bimorph piezoelectric flexible mirror: Graphical solution and comparison with experiment," *J Opt Soc Am* 73 (1983): 110.
318. Han, I. "New method for estimating wavefront from curvature signal by curve fitting," *Opt Eng* 34 (1995): 1232.
319. Happer, W., G. J. MacDonald, C. E. Max, and F. J. Dyson. "Atmospheric-turbulence compensation by resonant optical backscattering from the sodium layer in the upper atmosphere," *J Opt Soc Am A* 11 (1994): 263.
320. Hardy, J. W. "Active optics: A new technology for the control of light," *Proc IEEE* 66 (1978): 651.
321. Hardy, J. W. "Instrumental limitations in adaptive optics for astronomy," *Proc SPIE* 1114 (1989): 2.
322. Hardy, J. W. "Adaptive optics—a progress review," *Proc SPIE* 1542 (1991): 2.
323. Hardy, J. W. *Adaptive Optics for Astronomical Telescopes*. New York: Oxford Univ. Press, 1998.
324. Hardy, J. W., J. Feinleib, and J. C. Wyant. "Real-time correction of optical imaging systems," *OSA Meeting on Optical Propagation through Turbulence*, Boulder, CO, 1974.
325. Hardy, J. W., J. E. Lefebvre, and C. L. Koliopoulos. "Real-time atmospheric compensation," *J Opt Soc Am* 67 (1977): 360.
326. Hardy, J. W., and A. J. MacGovern. "Shearing interferometry: A flexible technique for wavefront measurement," *Proc SPIE* 816 (1987).
327. Hardy, J. W. and E. P. Wallner. "Wavefront compensation using active lenses," *Proc SPIE* 2201 (1994): 77.
328. Harney, R. C. "Active laser resonator control techniques," *Appl Opt* 17 (1978): 11.
329. Harrington, P. M., and B. M. Welsh. "Frequency-domain analysis of an adaptive optical systems' temporal response," *Opt Eng* 33 (1994): 2336.
330. Hart, N. W., M. C. Roggemann, A. Sergeyev, and T. J. Schulz. "Characterizing static aberrations in liquid crystal spatial light modulators using phase retrieval," *Opt Eng* 46 (2007): 086601.
331. Hart, M., N. M. Milton, C. Baranec, T. Stalcup, K. Powell, E. Bendek, D. McCarthy, and C. Kulesa. "Wide field astronomical image compensation with multiple laser-guided adaptive optics," *Proc SPIE* 7486 (2009): L1.
332. Hartmann, J. "Bemerkungen uber den Bau und die Justirung von Spektrographen," *Z. Instrumentenkd* 20 (1900): 47.
333. Hartmann, J. "Objektuvuntersuchungen," *Z. Instrumentenkd* 24 (1904): 1.
334. Harvey, J. E., and G. M. Callahan. "Transfer function characterization of deformable mirrors," *J Opt Soc Am* 67 (1978).

335. Harvey, J. E. and M. L. Scott. "The hole grating beam sampler," *Opt Eng* 20 (1981): 881.
336. Harvey, J. E., J. L. Forgham, and K. von Bieren. "The spot of Arago and its role in wavefront analysis," *Proc SPIE* 351 (1982): 2.
337. Hatfield, B. *Thermal Blooming in the Presence of Turbulence and Diffusion*. Woburn, MA: North East Research Assoc., Inc., presented to PCAP Committee, Lexington, MA, 1988.
338. Helmbrecht, M. A., and T. Juneau. "Piston-tip-tilt positioning of a segmented MEMS deformable mirror," *Proc SPIE* 6467 (2007).
339. Hemmati, H., and Y. Chen. "Active optical compensation of low-quality optical system aberrations," *Opt Lett* 31 (2006):1630.
340. Herrmann, J. "Properties of phase conjugate adaptive optical systems," *J Opt Soc Am* 67 (1997): 290.
341. Hickson, P. "Wavefront curvature sensing from a single defocused image," *J Opt Soc Am A* 11 (1994): 1667.
342. Hiddleston, H. R., D. D. Lyman, and E. L. Schafer. "Comparisons of deformable mirror models and influence functions," *Proc SPIE* 1542 (1991): 20.
343. Hinnen, K., M. Verhaegen, and N. Doelman. "Exploiting the spatiotemporal correlation in adaptive optics using data-driven H2-optimal control," *J Opt Soc Am A* 24 (2007): 1714.
344. Hinz, P.M., A. N. Heinze, S. Sivanandam, D. L. Miller, M. A. Kenworthy, G. Brusa, M. Freed, and J. R. P. Angel. "Thermal infrared constraint to a planetary companion of Vega with the MMT adaptive optics system," *Astrophys J* 653 (2006): 1486.
345. Hippler, S., F. Hormuth, D. J. Butler, W. Brandner, and T. Henning. "Atmosphere-like turbulence generation with surface-etched phase-screens," *Opt Expr* 14 (2006): 10139.
346. Hogan, W. J., L. J. Atherton, and J. A. Paisner. "National ignition facility design focuses on optics," *Laser Focus World* 32 (1996): 107.
347. Hogge, C. B., and R. R. Butts. U. S. Air Force Weapons Laboratory Report, AFWL-TR-78-15, Kirtland Air Force Base, New Mexico (unpublished), 1978.
348. Hogge, C. B., and R. R. Butts. "Effects of using different wavelengths in wavefront sensing and correction," *J Opt Soc Am* 72 (1982): 606.
349. Holmes, D. A., and P. V. Avizonis. "Approximate optical system model," *Appl Opt* 15 (1976): 1075.
350. Holmes, R. "Scintillation-induced jitter of projected light with centroid trackers," *J Opt Soc Am A* 26 (2009): 313.
351. Hopkins, M. M. "The frequency response of a defocused optical system," *Optica Acta* 2 (1955): 91.
352. Hopkins, M. M. "The frequency response of optical systems," *Proc Phys Soc London, Sect* B 69 (1956): 562.
353. Hormuth, F., W. Brandner, S. Hippler, and T. Henning. "Astralux - the Calar Alto 2.2-m telescope lucky imaging camera," *J Phys Conf Series* 131 (2008): 012051.
354. Hornbeck, L. J. "128 x 128 deformable mirror device," *IEEE Trans Electron Dev* ED-30 (1983): 539.
355. Horwitz, B. A. "Multiplex techniques for real-time shearing interferometry," *Opt Eng* 29 (1990): 1223.
356. Hu, S., B. Xu, X. Zhang, J. Hou, J. Wu, and W. Jiang. "Double-deformable-mirror adaptive optics system for phase compensation," *Appl Opt* 45 (2006): 2638.

357. Huang, L., C. Rao, and W. Jiang. "Modified Gaussian influence function of deformable mirror actuators," *Opt Expr* 16 (2008): 108.
358. Hubin, N. "The ESO VLT adaptive optics programme," *Astro Astrophys Trans* 13 (1997).
359. Hubin, N., B. L. Ellerbroek, R. Arsenault, R. M. Clare, R. Dekany, L. Gilles, M. Kasper, G. Herriot, M. Le Louarn, E. Marchetti, S. Oberti, J. Stoesz, J. P. Veran, and C. Verinaud. "Adaptive optics for extremely large telescopes," *Proc IAU Symp* 232 (2005): 60.
360. Hudgin, R. H. "Wavefront compensation error due to finite corrector-element size," *J Opt Soc Am* 67 (1977): 393.
361. Hudgin, R. H. "Wavefront reconstruction for compensated imaging," *J Opt Soc Am* 67 (1977): 375.
362. Hufnagel, R. E. *Proc. Topical Meeting on Optical Propagation through Turbulence*, Boulder, CO, 1974; Hufnagel, R. E. "Propagation through atmospheric turbulence," *The Infrared Handbook*, eds. W. L. Wolfe and G. J. Zissis, Chap. 6.Ann Arbor, MI: Env. Res. Inst. Mich., 1989.
363. Hulburd, B., and Sandler, D. "Segmented mirrors for atmospheric compensation," *Opt Eng* 29 (1990): 1186.
364. Hulburd, B., T. Barrett, L. Cuellar, and D. Sandler. "High bandwidth, long stroke segmented mirror for atmospheric compensation," *Proc SPIE* 1543 (1991): 64.
365. Hull, W. C., R. B. Dunn, and M. J. Small. "A 256-channel digital wavefront reconstructor," *Proc SPIE* 1920 (1993): 200.
366. Humphreys, R. A., C. A. Primmerman, L. C. Bradley, and J. Herrmann. "Atmospheric-turbulence measurements using a synthetic beacon in the mesospheric sodium layer," *Opt Lett* 16 (1991): 1367.
367. Hunt, B. R. "Matrix formulation of the reconstruction of phase values from phase differences," *J Opt Soc Am* 69 (1979): 393.
368. Hutley, M. C. *Diffraction Gratings*. New York: Academic Press, 1982.
369. Idell, P. S., and J. D. Gonglewski. "Image synthesis from wavefront sensor measurements of a coherent diffraction field," *Opt Lett* 15 (1990): 1309.
370. Idell, P. S., and D. G. Voelz. "Non conventional laser imaging using sampled-aperture receivers," *Opt Phot News* 8 (April 1992).
371. Iizuka, K. *Engineering Optics*. 2nd ed. Berlin: Springer-Verlag, 1986.
372. Ikeda, O., M. Takehara, and T. Sato. "High-performance image-transmission system through a turbulent medium using multiple reflectors and adaptive focusing combined with four-wave mixing," *J Opt Soc Am A* 1 (1984): 176.
373. Ikramov, A. V., I. M. Rotshupkin, and A. G. Safronov. "Investigations of the bimorph piezoelectric mirrors for use in astronomic telescope," *Proc ICO-16 Satellite Conf on Active and Adap Opt, ESO Conf and Workshop Proc* 48 (1993): 235.
374. Ishimaru, A. *Wave Propagation and Scattering in Random Media*. New York: Academic Press, 1977.
375. Ivanov, V. Yu., V. P. Sivokon, and M. A. Vorontsov. "Phase retrieval from a set of intensity measurements: Theory and experiment," *J Opt Soc Am A* 9 (1992): 1515.
376. Jacobsen, B., T. Martinez, R. Angel, M. Lloyd-Hart, S. Benda, D. Middleton, H. Friedman, and G. Erbert. "Field evaluation of two new continuous-wave dye laser systems optimized for sodium beacon excitation," *Proc SPIE* 2201 (1994): 342.

377. Jagourel, P., and J.-P. Gaffard. "Adaptive optics components in laser-dot," *Proc SPIE* 1543 (1991): 76.
378. Jankevics, A. J., and A. Wirth. "Wide field of view adaptive optics," *Proc SPIE* 1543 (1991): 438.
379. Jared, R. C., A. A. Arthur, S. Andreae, A. K. Biocca, R. W. Cohen, J. M. Fuertes, J. Franck, G. Gabor, J. Llacer, T. S. Mast, J. D. Meng, T. L. Merrick, R. H. Minor, J. Nelson, M. Orayani, P. Salz, B. A. Schaefer, and C. Witebsky. "The W. M. Keck telescope segmented primary mirror active control system," *Proc SPIE* 1236 (1990): 996.
380. MEMS Optical, Technical Information Datasheets. www.memsoptical.com/techinfo/datasheets.htm.
381. Jeong, T. M., D. Ko, and J. Lee. "Method of reconstructing wavefront aberrations from the intensity measurement," *Opt Lett* 32 (2007): 3507.
382. Jeys, T. H., A. A. Brailove, and A. Mooradian. "Sum frequency generation of sodium resonance radiation," *Appl Opt* 28 (1989): 2588.
383. Jeys, T. H., R. M. Heinrichs, K. F. Wall, J. Korn, T. C. Hotaling, and E. Kibblewhite. "Optical pumping of mesospheric sodium," *Proc Laser Guide Star Adaptive Optics Workshop* 1, 238. Albuquerque, NM: U. S. Air Force Phillips Laboratory, 1992.
384. Ji, X., and X. Li. "Directionality of Gaussian array beams propagating in atmospheric turbulence," *J Opt Soc Am A* 26 (2009): 236.
385. Jiang, W., H. Li, C. Liu, X. Wu, S. Huang, H. Xian, Z. Rong, C. Wang, M. Li, N. Ling, and C. Guan. "A 37 element adaptive optics system with H-S wavefront sensor," *Proc ICO-16 Satellite Conf on Active and Adap Opt, ESO Conf and Workshop Proc* 48 (1993): 127.
386. Jiang, W., M. Li, G. Tang, M. Li, and D. Zheng. "Adaptive optical image compensation experiments on stellar objects," *Opt Eng* 34 (1995): 15.
387. Johansson, E. M., M. A. van Dam, P. J. Stanski, J. M. Bell, J. C. Chin, R. C. Sumner, P. L. Wizinowich, R. Biasi, M. Andrgihettoni, and D. Pescoller. "Upgrading the Keck wavefront controllers," *Proc SPIE* 7015 (2008): 70153E.
388. Johns, M. "The Giant Magellan telescope," *Proc SPIE* 6267 (2006).
389. Johns, M. "Progress on the GMT," *Proc SPIE* 7012 (2008): 701246.
390. Johnson, B., and D. V. Murphy. "Thermal blooming laboratory experiment, Part I." In *Lincoln Laboratory MIT Project Report*, Cambridge, MA: MIT Press, 1988.
391. Johnson, B., and C. A. Primmerman. "Experimental observation of thermal-blooming phase-compensation instability," *Opt Lett* 14 (1989): 12.
392. Johnson, B., and J. F. Schonfeld. "Demonstration of spontaneous thermal-blooming phase-compensation instability," *Opt Lett* 16 (1991): 1258.
393. Johnston, D. C., and B. M. Welsh. "Atmospheric turbulence sensing for a multiconjugate adaptive optics system," *Proc SPIE* 1542 (1991): 76.
394. Johnston, D. C., and B. M. Welsh. "Analysis of multiconjugate adaptive optics," *J Opt Soc Am A* 11 (1994): 394.
395. Johnston, D. C., B. L. Ellerbroek, and S. M. Pompea. "Curvature sensing analysis," *Proc SPIE* 2201 (1994): 528.
396. Johnson P., R. Trissel, L. Cuellar, B. Arnold, and D. Sandler. "Real time wavefront reconstruction for a 512 subaperture adaptive optical system," *Proc SPIE* 1543 (1991): 460.
397. Johnsopn, R., D. Montera, T. Schneeberger, and J. Spinhirne. "A new sodium guidestar adaptive optics system for the Starfire Optical Range 3.5 m telescope," AFRL-RD-PS, TP-2009-1018, 2009.

398. Jolissaint, L., J.-P. Veran, and R. Conan. "Analytical modeling of adaptive optics: Foundations of the phase spatial power spectrum approach," *J Opt Soc Am A* 23 (1006): 382.
399. Jonnal, R. S., J. Rha, Y. Zhang, B. Cense, W. Gao, and D. T. Miller. "In vivo functional imaging of human cone photoreceptors," *Opt Expr* 15 (2007): 16141.
400. Kane, T. J., C. S. Gardner, and L. A. Thompson. "Effects of wavefront sampling speed on the performance of adaptive astronomical telescopes," *Appl Opt* 30 (1991): 214.
401. Karcher, H. J., and H. Nicklas. "Active structural control of very large telescopes," *Proc SPIE* 1114 (1989): 320.
402. Karr, T. J. *Ground Based Laser Propagation: Status and Prospects*. Presented to DEW Technology Base Review Panel, San Diego, CA, 1987.
403. Karr, T. J. *Ground Based Laser Propagation Review*. Presented to JASON meeting, San Diego, CA, 1987.
404. Karr, T. J. "Thermal blooming compensation instabilities." *J Opt Soc Am A* 6 (1989):1038.
405. Karr, T. J. "Temporal response of atmospheric turbulence compensation." *Appl Opt* 30 (1991): 363.
406. Kelsall, D., and R. D'Amato. "AFWL/OPTICS optical degradation by aerodynamic boundary layers." MIT Lincoln Laboratory Report, ESD-TR-78-243, 1977.
407. Kenrew, S., P. Doel, D. Brooks, C. Dorn, C. Yates, R. M. Dwan, I. Richardson, and G. Evans. "Developments of a carbon fiber composite active mirror: design and testing." *Opt Eng* 45 (2006): 033401.
408. Kenrew, S., P. Doel, D. Brooks, A. M. King, C. Dorn, C. Yates, R. M. Dwan, I. Richardson, and G. Evans. "Prototype carbon fiber composite deformable mirror." *Opt Eng* 46 (2007): 094003.
409. Kenemuth, J. R. "Multiactuator deformable mirror evaluations." *Proc SPIE* 171 (1979): 32.
410. Kern, P., P. Lena, P. Gigan, J. Fontanella, G. Rousset, F. Merkle, and J. Gaffard. "COME-ON: An adaptive optics prototype dedicated to infrared astronomy." *Proc SPIE* 1114 (1989): 54.
411. Keskin, O., R. Conan, P. Hampton, and C. Bradley. "Derivation and experimental evaluation of a point-spread-function reconstruction from a dual-deformable-mirror adaptive optics system." *Opt Eng* 47 (2008): 046601.
412. Kibblewhite, E. "Laser beacons for astronomy," *Proc. Laser Guide Star Adaptive Optics Workshop* 1, 24. Albuquerque, NM: U. S. Air Force Phillips Laboratory, 1992.
413. Kibblewhite, E., W. Wild, B. Carter, M. Chun, F. Shi, and M. Smutko. "A description of the Chicago Adaptive Optics System (ChAOS)," *Proc. Laser Guide Star Adaptive Optics Workshop* 2, 522. Albuquerque, NM: U. S. Air Force Phillips Laboratory, 1992.
414. Kibblewhite, E., M. F. Smutko, and F. Shi. "The effect of hysteresis on the performance of deformable mirrors and methods of its compensation." *Proc SPIE* 2201 (1994): 754.
415. Kibblewhite, E. J., R. Vuilleumier, B. Carter, W. J. Wild, and T. H. Jeys. "Implementation of CW and pulsed laser beacons for astronomical adaptive optics systems." *Proc SPIE* 2201 (1994): 272.

416. Kim, Y. "Refined simplex method for data fitting." *Astron. Data Anal. Software and Sys*. 125 (1997): 206.
417. Kingslake, R., ed. *Applied Optics and Optical Engineering, Volume II: The Detection of Light and Infrared Radiation*. New York: Academic Press, 1965; Kingslake, R., and B. J. Thompson, eds. *Applied Optics and Optical Engineering, Volume VI: Coherent Optical Devices and Systems*. New York: Academic Press, 1980.
418. Kline-Schoder, R. J., and M. J. Wright. "Design of a dither mirror control system." *Mechatronics* 2 (1992): 115.
419. Kocher, D. G. "Point image focus sensing using an automated Foucault test." *Proc SPIE* 351 (1982): 148.
420. Kocher, D. G. "Automated Foucault test for focus sensing." *Appl Opt* 22 (1983): 1887.
421. Kokorowski, S. A. "Analysis of adaptive optical elements made from piezolectric bimorphs." *J Opt Soc Am* 69 (1979): 181.
422. Kokorowski, S. A., M. E. Pedinoff, and J. E. Pearson. "Analytical, experimental, and computer-simulation results on the interactive effects of speckle with multidither adaptive optics systems." *J Opt Soc Am* 67 (1977): 333.
423. Kokorowski, S. A., T. R. O'Meara, R. C. Lind, and T. Calderone. "Automatic speckle cancellation techniques for multidither adaptive optics." *Appl Opt* 19 (1980): 371.
424. Koliopoulos, C. L. "Avoiding phase-measuring interferometry's pitfalls." *Photon Spectra* (1988): 169.
425. Kolmogorov, A. "Dissipation of energy in locally isotropic turbulence." In *Turbulence, Classic Papers on Statistical Theory*, eds. S. K. Friedlander, and L. Topper. New York: Wiley (Interscience), 1961.
426. Konyaev, P. A., and V. P. Lukin. "Thermal distortions of focused laser beams in the atmosphere." *Appl Opt* 24 (1985): 415.
427. Korkiakoski, V., C. Verinaud, M. Le Louarn, and R. Conan. "Comparison between a model-based and a conventional pyramid sensor reconstructor." *Appl Opt* 46 (2007): 6176.
428. Korkiakoski, V., C. Verinaud, and M. Le Louarn. "Improving the performance of a pyramid wavefront sensor with modal sensitivity compensation." *Appl Opt* 47 (2008): 79.
429. Kornienko, A. A., and G. N. Mal'tsev. "Use of spectral expansions of Zernike polynomials for investigating the aberrations of adaptive optical systems." *Sov J Opt Technol* 55 (1988): 341.
430. Korotkova, O., L. C. Andrews, and R. L. Phillips. "The effect of partially coherent quasi-monochromatic Gaussian-beam on the probability of fade." *Proc SPIE* 5160 (2004): 68.
431. Kotani, T., S. Lacour, G. Perrin, G. Robertson, and P. Tuthill. "Pupil remapping for high contrast astronomy: results from an optical test bed." *Opt Expr* 17 (2009): 1925.
432. Krist, J. E., and C. J. Burrows. "Phase-retrieval analysis of pre- and post-repair Hubble Space Telescope images. *Appl Opt* 34 (1995): 4951.
433. Krupke, W. F., and W. R. Sooy. "Properties of an unstable confocal resonator CO_2 laser system." *IEEE J Quantum Electron* QE-5 (1969).
434. Kulesar, C., H. -F. Raynaud, C. Petit, J. -M. Conan, and P. V. de Lesegno. "Optimal control, observers and integrators in adaptive optics." *Opt Expr* 14 (2006): 7464.
435. Kuo, B. C. *Automatic Control Systems*. 5th ed. Englewood Cliffs, NJ: Prentice-Hall, 1987.

436. Kuo, C. "Optical tests of an intelligently deformable mirror for space telescope technology." *Opt Eng* 33 (1994): 791.
437. Kurczynski, P., H. M. Dyson, and B. Sadoulet. "Stability of electrostatic actuated membrane mirror devices." *Appl Opt* 45 (2006): 8288.
438. Kurczynski, P., H. M. Dyson, and B. Sadoulet. "Large amplitude wavefront generation and correction with membrane mirrors." *Opt Expr* 14 (2006): 509.
439. Kwon, O. Y., Real-time radial-shear interferometer." *Proc SPIE* 551 (1985): 32.
440. Laag, E. A., S. M. Ammons, D. T. Gavel, and R. Kupke. "Multiconjugate adaptive optics results from the laboratory for adaptive optics MCAO/MOAO testbed." *J Opt Soc Am A* 25 (2008): 2114.
441. Labeyrie, A. "Attainment of diffraction-limited resolution on large telescope by Fourier analyses speckle pattern in stars images." *Astron Astrophys* 6 (1970): 85.
442. Laird, P., E. F. Borra, R. Bergamesco, J. Gingras, L. Truong, and A. Ritcey. "Deformable mirrors based on magnetic liquids." *Proc SPIE* 5490 (2004): 1493.
443. Lam, J. F., and W. P. Brown. "Optical resonators with phase-conjugate mirrors." *Opt Lett* 5 (1980): 61.
444. Landis, G. A. "Letter." *Physics Today* 13, July 1992.
445. Lardiere, O., R. Conan, C. Bradley, K. Jackson, and G. Herriot. "A laser guide star wavefront sensor bench demonstrator to TMT." *Opt Expr* 16 (2008): 5527.
446. Large Aperture Mirror Program. *Large Optics Demonstration Experiment*. Washington, DC: Strategic Defense Initiative Organization, unpublished, 1985.
447. "Laser guide star teams with adaptive optics to shed light on massive star," *University of California Newsroon*, 26 February 2004.
448. Lauterbach, M. A., M. Ruckel, and W. Denk. "Light-efficient, quantum-limited interferometric wavefront estimation by virtual mode sensing." *Opt Expr* 14 (2006): 3700.
449. Lavigne, J. -F., and J. -P. Veran. "Woofer-tweeter control in an adaptive optics system using a Fourier reconstructor." *J Opt Soc Am A* 25 (2008): 2271.
450. Law, N. M., R. G. Dekany, C. D. Mackay, A. M. Moore, M. C. Britton, and V. Velur. "Getting lucky with adaptive optics: Diffraction-limited resolution in the visible with current AO systems on large and small telescopes." *Proc SPIE* 7014 (2008): 1152.
451. Lawrence, R. S., G. R. Ochs, and S. F. Clifford. "Measurements of atmospheric turbulence relevant to optical propagation." *J Opt Soc Am A* 60 (1970): 826.
452. Lazzarini, A., G. H. Ames, and E. Conklin. "Methods of hierarchical control for a segmented active mirror. *Proc SPIE* 2121 (1994): 147.
453. Lei, F., and H. J. Tiziani. "Atmospheric influence on image quality of airborne photographs." *Opt Eng* 32 (1993): 2271.
454. Lena, P. "Adaptive optics: a breakthrough in astronomy." *Exp Astron* 26 (2009): 35.
455. Lessard, L., M. West, D. MacMynowski, and S. Lall. "Warm-started wavefront reconstruction for adaptive optics." *J Opt Soc Am A* 25 (2008): 1147.
456. Levine, B. M., J. J. Janesick, and J. C. Shelton. "Development of a low noise high frame rate CCD for adaptive optics." *Proc SPIE* 2201 (1994): 596.
457. Levine, B. M., and K. Kiasaleh. "Intensity fluctuations in the Compensated Earth Moon Earth Laser Link (CEMERLL) experiment." *Proc SPIE* 2123 (1994): 409.
458. Li, C., H. Xian, C. Rao, and W. Jiang. "Field-of-view shifted Shack-Hartmann wavefront sensor for daytime adaptive optics system." *Opt Lett* 31 (2006): 2821.

459. Li, E., Y. Dai, H. Wang, and Y. Zhang. "Application of eigenmode in the adaptive optics system based on a micromachined membrane deformable mirror." *Appl Opt* 45 (2006): 5651.
460. Li, K. Y., and A. Roorda. "Automated identification of cone photoreceptors in adaptive optics retinal images." *J Opt Soc Am A* 24 (2007): 1358.
461. Li, M., X. Li, and W. Jiang. "Small-phase retrieval with a single far-field image." *Opt Expr* 16 (2008): 8190.
462. Liang, J., and D. R. Williams. "Aberrations and retinal image quality of the normal human eye." *J Opt Soc Am A* 14 (1997): 2873.
463. Liang, J., D. R. Williams, and D. T. Miller. "Supernormal vision and high-resolution retinal imaging through adaptive optics." *J Opt Soc Am A* 14 (1997): 2884.
464. Liebelt, P. B. *An Introduction to Optimal Estimation*. Reading, MA: Addison-Wesley, 1967.
465. Lindorff, D. P. *Theory of Sampled-Data Control Systems*. New York: Wiley, 1965.
466. Linnik, V. P. "On the possibility of reducing the influence of atmospheric seeing on the image quality of stars." *Opt Spectrosc* 3 (1957): 401.
467. Lipson, S. G., E. N. Ribak, and C. Schwartz. "Bimorph deformable mirror design." *Proc SPIE* 2201 (1994): 703.
468. Liu, Y., Z. Cao, D. Li, Q. Mu, L. Hu, X. Lu, and L. Xuan. "Correction for large aberration with phase-only liquid-crystal wavefront corrector." *Opt Eng* 45 (2006): 128001.
469. Liu, Y., and J. G. Walker. "Post-compensation for extended object imaging." *Proc ICO-16 Satellite Conf on Active and Adap Opt, ESO Conf and Workshop Proc* 48 (1993): 137.
470. Liu, Y. -T., and J. Steve Gibson. "Adaptive control in adaptive optics for directed-energy systems." *Opt Eng* 46 (2007): 046601.
471. Llacer, J., R. C. Jared, and J. M. Fuertes. "Analysis of the W. M. Keck telescope primary mirror control loop." *Proc SPIE* 1236 (1990): 1024.
472. Lloyd-Hart, M., R. Dekany, D. Sandler, D. Wittman, R. Angel, and D. McCarthy. "Progress in diffraction-limited imaging at the Multiple Mirror Telescope with adaptive optics." *J Opt Soc Am A* 11 (1994): 846.
473. Lloyd-Hart, M., R. Angel, B. Jacobsen, D. Wittman, D. McCarthy, E. Kibblewhite, B. Carter, and W. Wild. "Preliminary closed-loop results from an adaptive optics system using a sodium resonance guide star." *Proc SPIE* 2201 (1994): 364.
474. Lloyd-Hart, M., J. R. P. Angel, D. G. Sandler, P. Salinari, D. Bruns, and T. K. Barrett. "Progress toward the 6.5-m MMT infrared adaptive optics system." *Top Mtg on Adap Opt, Opt Soc Am Tech Dig Series* 13 (1996): 28.
475. Lloyd-Hart, M., C. Baranec, N. M. Milton, M. Snyder, T. Stalcup, and J. R. P. Angel. "Experimental results of ground-layer and tomographic wavefront reconstruction from multiple laser guide stars." *Opt Expr* 14 (2006): 7541.
476. Lloyd-Hart, M., and P. McGuire. "Spatio-temporal prediction for adaptive optics wavefront reconstructors." *Proc Top Mtg on Adap Opt, ESO Conf and Workshop Proc* 54 (1996): 95.
477. Lloyd-Hart, M., and T. Rhoadarmer. "Wavefront control optimization using adaptive filters." *Top Mtg on Adap Opt, Opt Soc Am Tech Dig Series* 13 (1996): 268.
478. Loewen, E. G., and M. Neviere. "Simple selection rules for VUV and XUV diffraction gratings." *Appl Opt* 17 (1978): 1087.

479. Logean, E., E. Dalimier, and C. Dainty. "Measured double-pass intensity point-spread function after adaptive optics correction of ocular aberrations." *Opt Expr* 16 (2008): 17384.
480. Looze, D. P. "Minimum variance control structure for adaptive optics systems." *J Opt Soc Am A* 23 (2006): 603.
481. Looze, D. P. "Discrete-time model of an adaptive optics system." *J Opt Soc Am A* 24 (2007): 2850.
482. Looze, D. P. "Linear-quadratic-Gaussian control for adaptive optics systems using a hybrid model." *J Opt Soc Am A* 26 (2009): 1.
483. Lors, C. A. "I-cubed sensor wavefront correction system." Pratt and Whitney Aircraft, FL. Internal memorandum. August 28, 1978.
484. Lors, C. A. "CLAWS multidither COAT system." Pratt and Whitney Aircraft, FL. Internal memorandum. May 26, 1978.
485. Love, G. D. "Wavefront correction and production of Zernike modes with a liquid-crystal spatial light modulator." *Appl Opt* 36 (1997): 1517.
486. Love, G., R. Myers, A. Purvis, R. Sharples, and A. Glindemann. "A new approach to adaptive wavefront correction using a liquid crystal half-wave phase shifter." *Proc ICO-16 Satellite Conf on Active and Adap Opt, ESO Conf and Workshop Proc* 48 (1993): 295.
487. Ludman, J. E., H. J. Caulfield, V. Morozov, and J. L. Sampson. "Wavefront reconstruction using self-referenced direct-drive adaptive optics." *Opt Eng* 33 (1994): 4020.
488. Lukin, V. P. *Atmospheric Adaptive Optics*. Bellingham, WA: SPIE Optical Engineering Press, 1995.
489. Lukin, V. P., B. V. Fortes, F. Y. Kanev, and P. A. Konyaev. "Potential capabilities of adaptive-optical systems in the atmosphere." *J Opt Soc Am A* 11 (1994): 903.
490. Lundstrom, L., S. Manzanera, P. M. Prieto, D. B. Ayala, N. Gorceix, J. Gustafsson, P. Unsbo, and P. Artal. "Effect of optical correction and remaining aberrations on peripheral resolution acuity in the human eye." *Opt Expr* 15 (2007): 12654.
491. Lush, H. J. "Photomultiplier linearity." *J Sci Instrum* 42 (1965): 597.
492. Lutomirski, R. F. "Atmospheric degradation of electrooptical system performance." *Appl Opt* 17 (1978): 3915.
493. Lutomirski, R. F., and H. T. Yura. "Propagation of a finite optical beam in an inhomogeneous medium." *Appl Opt* 10 (1971): 1652.
494. Lyons, A. "Design of proximity-focused electron lenses." *J Phys E* 8 (1985): 127.
495. Mach, L. "Communication of the notices of the Viennese Academy." *Z Instrumentenkd* 12 (1892): 89.
496. Mahajan, V. N. "Zernike annular polynomials for imaging systems with annular pupils." *J Opt Soc Am* 71 (1981): erratum 1408.
497. Makidon, R. B., A. Sivaramakrishnan, R. Soummer, B. R. Oppenheimer, L. C. Roberts Jr., J. R. Graham, and M. D. Perrin. "The Lyot project: Understanding the AEOS adaptive optics PSF." *Proc IAU Coll* 200 (2005): 603.
498. Malakhov, M. N., V. F. Matyukhin, and B. V. Pilepskii. "Estimating the parameters of a multielement mirror of an adaptive optical system." *Sov J Opt Technol* 51 (1984): 141.
499. Malakhov, M. N., and B. V. Prilepskii. "Method of determining the wavefront profile from information using a detector of the Hartmann type." *Opt Spectrosc (USSR)* 58 (1985): 271.

500. Malin, M., W. Macy, and G. Ferguson. "Edge actuation for figure control." *Proc SPIE* 365 (1982): 114.
501. Mannion, P. "CCDs ride the tailcoat of digital convergence." *Electron Prod* 27, April 1996.
502. Marchesini, S. "A unified evaluation of iterative projection algorithms for phase retrieval." *Rev Sci Instrum* 78 (2007): 011301.
503. Marchetti, E., and R. Ragazzoni. "Wavefront generator for adaptive optics testing." *Proc Top Mtg on Adap Opt, ESO Conf and Workshop Proc* 54 (1996): 229.
504. Marcy, G. W. "California and Carnegie planet search," 2005. Available at: http://exoplanets.org.
505. Marlow, W. C. "Dynamics of a deformable mirror actuator." *Opt Eng* 33 (1994): 1016.
506. Martin, H. M., and D. S. Anderson. "Techniques for optical fabrication of a 2-mm-thick adaptive secondary mirror." *Proc SPIE* 2534 (1995):134.
507. Marquet L. C. "Transmission diffraction grating attenuator for analysis of high power laser beam quality." *Appl Opt* 10 (1971): 960.
508. Massie, N. A., R. D. Nelson, and S. Holly. "High-performance real-time heterodyne interferometry." *Appl Opt* 18 (1979): 1797.
509. Massie, N. A., Y. Oster, G. Poe, L. Seppala, and M. Shao. "Low-cost, high-resolution, single-structure array telescopes for imaging of low-Earth-orbit satellites." *Appl Opt* 31 (1992): 447.
510. Max, C. E., K. Avicola, J. M. Brase, H. W. Friedman, H. D. Bissinger, J. Duff, D. T. Gavel, J. A. Horton, R. Kiefer, J. R. Morris, S. S. Olivier, R. W. Presta, D. A. Rapp, J. T. Salmon, and K. E. Waltjen. "Design, layout, and early results of a feasibility experiment for sodium-layer laser-guide-star adaptive optics." *J Opt Soc Am A* 11 (1994): 813.
511. Max, C. E., D. T. Gavel, S. S. Olivier, J. M. Brase, H. W. Friedman, K. Avicola, J. T. Salmon, A. D. Gleckler, T. S. Mast, J. E. Nelson, P. L. Wizinowich, and G. A. Chanan. "Issues in the design and optimization of adaptive optics and laser guide stars for the Keck telescopes." *Proc SPIE* 2201 (1994): 189.
512. McAulay, A. D. "Deformable mirror nearest neighbor optical digital computer." *Opt Eng* 25 (1986): 76; Caulfield, H. J., W. T. Rhodes, M. J. Foster, and S. Horvitz. "Optical implementation of systolic array processing." *Opt Commun* 40 (1981): 86; Pape, D. R., and L. J. Hornbeck. "Characteristics of the deformable mirror device for optical information processing." *Opt Eng* 22 (1983): 675.
513. McCausland I. *Introduction to Optimal Control*. New York: Wiley, 1979.
514. McDonald, T. B., and M. A. Ealey, personal communication, 1985.
515. McKinley, W. G., H. T. Yura, and S. G. Hanson. "Optical system defect propagation in ABCD systems." *Opt Lett* 13 (1988): 333.
516. McLaughlin, J. L. "Focus-position sensing using laser speckle." *Appl Opt* 18 (1979): 1042.
517. McLaughlin, J. L. and B. A. Horwitz. "Real-time snapshot interferometer." *Proc SPIE* 680 (1986): 35.
518. McLeod, J. H. "The axicon: A new type of optical element." *J Opt Soc Am* 44 (1954): 592.
519. *Melles Griot Optics Guide*, CVI Melles Griot, Irvine, CA, 2009.
520. Meng, J. D., R. Minor, T. Merrick, and G. Gabor. "Position control of the mirror figure control actuator for the Keck Observatory ten meter primary mirror." *Proc SPIE* 1114 (1989): 266.

521. Meng, J. D., J. Franck, G. Gabor, R. C. Jared, R.H. Minor, and B.A. Schaefer. "Position actuators for the primary mirror of the W. M. Keck telescope." *Proc SPIE* 1236 (1990): 1018.
522. Menikoff, A. "Actuator influence functions of active mirrors." *Appl Opt* 30 (1991): 833.
523. Merkle, F., K. Freischlad, and J. Bille. "Development of an active optical mirror for astronomical applications," ESO Conference, Garching: FRG, 1981.
524. Merkle, F., and J. M. Beckers. "Application of adaptive optics to astronomy." *Proc SPIE* 1114 (1989): 36.
525. Merkle, F., G. Rousset, P. Kern, and J. P. Gaffard. "First diffraction-limited astronomical images with adaptive optics." *Proc SPIE* 1236 (1990): 193.
526. Merkle, F., and N. Hubin. "Adaptive optics for the European very large telescope." *Proc SPIE* 1542 (1991): 283.
527. Merritt, P. H., L. Sher, and R. E. Walter. "Stability measures of adaptive optics control systems," *Proc. Laser Guide Star Adaptive Optics Workshop* 1, 352. Albuquerque, NM: U. S. Air Force Phillips Laboratory, 1992.
528. Microfab Technologies, Inc., Available at: www.microfab.com.
529. Middelhoek, S., and S. Audet. *Silicon Sensors*. London: Academic Press, 1989.
530. Mikoshiba, S., and B. Ahlborn. "Laser mirror with variable focal length." *Rev Sci Instrum* 44 (1973): 508.
531. Milman, M., A. Fijany, and D. Redding. "Wavefront control algorithms and analysis for a dense adaptive optics system." *Proc SPIE* 2121 (1994): 114.
532. Minor, R. H., A. A. Arthur, G. Gabor, H. G. Jackson, R. C. Jared, T. S. Mast, and B. A. Schaefer. "Displacement sensors for the primary mirror of the W. M. Keck telescope." *Proc SPIE* 1236 (1990): 1009.
533. Moini, H. "Systematic design of a deformable mirror with low-order wavefront compensation capability." *Opt Eng* 35 (1996): 2012.
534. Montagnier, G., T. Fusco, J.-L. Beuzit, D. Mouillet, J. Charton, and L. Jacou. "Pupil stabilization for SPHERE's extreme AO and high performance coronagraph system." *Opt Expr* 15 (2007): 15293.
535. Montera, D. A., B. M. Welsh, M. C. Roggemann, and D. W. Ruck. "Processing wavefront-sensor slope measurements using artificial neural networks." *Appl Opt* 35 (1996): 4238.
536. Montera, D. A., B. M. Welsh, M. C. Roggemann, and D. W. Ruck. "Use of artificial neural networks for Hartman sensor lenslet centroid estimation." *Top Mtg on Adap Opt, Opt Soc Am Tech Dig Series* 13 (1996): 250.
537. Montera, D. A., B. M. Welsh, M. C. Roggemann, and D. W. Ruck. "Prediciton of wavefront sensor slope measurements using artificial neural networks." *Top Mtg on Adap Opt, Opt Soc Am Tech Dig Series* 13 (1996): 226.
538. Moore, K. E., and G. N. Lawrence. "Zonal model of an adaptive mirror." *Appl Opt* 29 (1990): 4622.
539. Morris, D. "Simulated annealing applied to the Misell algorithm for phase retrieval." *IEE Proc Micro Ant Prop* 143 (1996): 208.
540. Morris, J. R. "Atmospheric propagation modeling: Closed-loop instability growth." Lawrence Livermore National Lab., presented to JASON group, La Jolla, CA, 1988.
541. Morris, J. R. "Efficient excitation of a mesospheric sodium laser guide star by intermediate-duration pulses." *J Opt Soc Am A* 11 (1994): 832.
542. Morris, T. J., and R. W. Wilson. "Optimizing Rayleigh laser guide star range-gate depth during initial loop closing." *Opt Lett* 32 (2007): 2004.

543. Moses, E. *Science and Technology Review*, Lawrence Livermore National Laboratory, April/May 2009. Available at: str.llnl.gov.
544. Mu, Q., Z. Cao, D. Li, L. Hu, and L. Xuan. "Liquid crystal based adaptive optics system to compensate both low and high order aberrations in a model eye." *Opt Expr* 15 (2007): 1946.
545. Mu, Q., Z. Cao, D. Li, L. Hu, and L. Xuan. "Open-loop correction of horizontal turbulence: system design and result." *Appl Opt* 47 (2008): 4297.
546. Mugnier, L. M., J.-F. Sauvage, T. Fusco, A. Cornia, and S. Dandy. "On-line long-exposure phase diversity: a powerful tool for sensing quasi-static aberrations of extreme adaptive optics imaging systems." *Opt Expr* 16 (2008): 18406.
547. Muller, R. A., and A. Buffington. "Real-time correction of atmospherically degraded telescope images through image sharpening," *J Opt Soc Am* 64 (1974): 1200.
548. Mumola, P. B., H. J. Robertson, G. N. Steinberg, J. L. Kreuzer, and A. W. McCullough. "Unstable resonators for annular gain volume lasers." *Appl Opt* 17 (1978): 936.
549. Murphy, D. V., C. A. Primmerman, B. G. Zollars, and H. T. Barclay. "Experimental demonstration of atmospheric compensation using multiple synthetic beacons." *Opt Lett* 16 (1991): 1797.
550. Myers, C. J., and R. C. Allen. "Development of an analytical mirror model addressing the problem of thermoelastic deformation." *Appl Opt* 24 (1985): 1933.
551. Myers, R. B. *Unified Theory of Thermal Blooming and Turbulence in the Atmosphere*. Woburn, MA: North East Research Assoc., Inc., 1988.
552. Myers, R., A. Longmore, R. Humphreys, G. Gilmore, B. Gentiles, M. Wells, and R. Wilson. "The UK adaptive optics programme." *Proc SPIE* 2534 (1995): 48.
553. Nadler, G. "Systems methodology and design." *Mech Eng* 108 (1986): 86.
554. Nakata, T., and M. Watanabe. "Ultracompact and highly sensitive common-path phase-shifting interferometer using photonic crystal polarizers as a reference mirror and a phase shifter." *Appl Opt* 48 (2009): 1322.
555. Neal, R. D., T. S. McKechnie, and D. R. Neal. "System requirements for laser power beaming to geosynchronous satellites." *Proc SPIE* 2121 (1994): 211.
556. Neichel, B., T. Fusco, and J.-M. Conan. "Tomographic reconstruction for wide-field adaptive optics systems: Fourier domain analysis and fundamental limitations," *J Opt Soc Am A*, 26 (2009): 219.
557. Nelson, J., T. Mast, and G. Chanan. "Aberration correction in a telescope with a segmented primary." *Proc SPIE* 1114 (1989): 241.
558. Nelson, J., and T. S. Mast. "The construction of the Keck observatory." *Proc SPIE* 1236 (1990): 47.
559. Newton, I. *Opticks*. 4th ed. New York: Dover, 1979.
560. Neyman, C. R., and L. A. Thompson. "Experiments to assess the effectiveness of multiple laser guide stars for adaptively corrected telescopes." *Proc SPIE* 2534 (1995): 161.
561. Nichols, J. S., and D.C. Duneman. "Frequency response of a thermally driven atmosphere." *Appl Opt* 21 (1982): 421.
562. Nichols, J. S., D. Duneman, and J. Jasso. "Performance evaluation of an edge-actuated, modal, deformable mirror." *Opt Eng* 22 (1983): 366.
563. Nicholls, T., N. J. Wooder, and C. Dainty. "Measurement of a non-Kolmogorov structure function." *Top Mtg on Adap Opt, Opt Soc Am Tech Dig Series* 13 (1996): 203.

564. Nicolle, M., T. Fusco, V. Michau, G. Rousset, and J.-L. Beuzit. "Optimization of star-oriented and layer-oriented wavefront sensing concepts for ground layer adaptive optics." *J Opt Soc Am A*, 23 (2006): 2233.
565. Nieto-Vesperinas, M. "Fields generated by a Fabry-Perot interferometer with a phase-conjugate mirror." *J Opt Soc Am A* 2 (1985): 427.
566. Nijboer, B. R. A. "The diffraction theory of optical aberrations; Part II: Diffraction pattern in the presence of small aberrations." *Physica* 23 (1947): 606.
567. Nikulin, V. V. "Fusion of adaptive beam steering and optimization-based wavefront control for laser communications in atmosphere." *Opt Eng* 44 (2005): 106001-1.
568. Ning, Y., W. Jiang, N. Ling, and C. Rao. "Response function calculation and sensitivity comparison analysis of various bimorph deformable mirrors." *Opt Expr* 15 (2007): 12030.
569. Nisenson, P., and R. Barakat. "Partial atmospheric correction with adaptive optics." *J Opt Soc Am A* 4 (1987): 2249.
570. Noll, R. J. "Zernike polynomials and atmospheric turbulence." *J Opt Soc Am* 66 (1976): 207.
571. Noll, R. J. "Phase estimates from slope-type wavefront sensors." *J Opt Soc Am* 68 (1978): 139.
572. Norton, M. A., N. P. Smith, and C. Higgs. "Laboratory multidither outgoing wave adaptive optics compensation for thermal blooming and turbulence," MIT Lincoln Laboratory Project Report, NLP-21, Lexington, MA, 1985.
573. Notaras, J., and C. Paterson. "Demonstration of closed-loop adaptive optics with a point-diffraction interferometer in strong scintillation with optical vortices." *Opt Expr* 15 (2007): 13745.
574. Novoseller, D. E. "Correction of aberrations displaced from the corrector mirror." *Appl Opt* 26 (1987): 4151.
575. Novoseller, D. E. "Zernike-ordered adaptive-optics correction of thermal blooming." *J Opt Soc Am A* 5 (1988): 1937.
576. O'Byrne, J. W., J. J. Bryant, R. A. Minard, P. W. Fekete, and L. E. Cram. "Adaptive optics at the Anglo-Australian telescope." *Pub Astron Soc Aust* 12 (1995): 106.
577. Ochs, G. R., and R. J. Hill. "Optical-scintillation method of measuring turbulence inner scale." *Appl Opt* 24 (1985): 2430.
578. O'Connor, D. J., J. E. Graves, M. J. Northcott, D. W. Toomey, R. D. Joseph, and J. C. Shelton. "Curvature-based adaptive optics for the NASA IRTF." *Proc SPIE* 4007 (2000): 180.
579. Ogata, K. *Modern Control Engineering*. NJ: Englewood Cliffs, 1970.
580. Olivier, S. S., and D. T. Gavel. "Tip-tilt compensation for astronomical imaging." *J Opt Soc Am A* 11 (1994): 368.
581. Olivier, S. S., J. An, K. Avicola, H. D. Bissinger, J. M. Brase, H. W. Friedman, D. T. Gavel, C. E. Max, J. T. Salmon, and K. E. Waltjen, "Performance of laser guide star adaptive optics at Lick observatory." *Proc SPIE* 2534 (1995): 26.
582. O'Meara, T. R. "The multidither principle in adaptive optics." *J Opt Soc Am* 67 (1977): 306.
583. O'Meara, T. R. "Stability of an N-loop ensemble-reference phase control system." *J Opt Soc Am* 67 (1977): 315.
584. O'Meara, T. R. "Theory of multidither adaptive optical systems operating with zonal control of deformable mirrors." *J Opt Soc Am* 67 (1977): 318.
585. O'Meara, T. R. "A comparison of conical scan Hartmann systems." *Conf. on Lasers and Electro-optics Applications*, Washington, DC, 1979.

586. Omron. Available at: www.omron.com.
587. O'Neill, E. L., and A. Walther. "The question of phase in image formation." *Optica Acta* 10 (1963): 33.
588. O'Neill, R. W., H. Kleiman, and H. R. Zwicker. "Experimental determination of single and multiple pulse propagation." *NATO Advisory Group for Aerospace Research and Development Conf. on Optical Propagation in the Atmosphere*, Lyngby, Denmark, 1975.
589. Onokhov, A. P., V. V. Reznichenko, D. N. Yeskov, and V. I Sidorov. "Optical wavefront corrector based on liquid crystal concept." *Proc SPIE* 2201 (1994): 1020.
590. Origlia, L., S. Lena, E. Diolaiti, F. R. Ferraro, E. Valenti, S. Fabbri, and G. Beccari. "Probing the galactic bulge with deep adaptive optics imaging: The age of NGC 6440." *Astrophys J* 687 (2008): L79.
591. Orlov, V. K., Ya. Z. Virnik, S. P. Vorotilin, V. B. Gerasimov, Yu. A. Kalinin, and A. Ya. Sagalovich. "Retroreflecting mirror for dynamic compensation of optical inhomogeneities." *Sov J Quantum Electron* 8 (1978): 799.
592. Ostaszewski, M. A., and R. T. Summers. "High performance reactionless scan mechanism." *Proc SPIE* 1920 (1993): 174.
593. Otsubo, M., H. Takami, and M. Iye, "Optimization of bimorph mirror electrode pattern for SUBARU AO system." *Top Mtg on Adap Opt, Opt Soc Am Tech Dig Series* 13 (1996): 265.
594. Oughstun, K. E. "Intracavity compensation of quadratic phase aberrations." *J Opt Soc Am* 72 (1982): 1529.
595. Oughstun, K. E. "Unstable-cavity sensitivity to spatially localized intracavity phase aberrations." *J Opt Soc Am A* 3 (1986): 1585.
596. Pan, B., Q. Kemao, L. Huang, and A. Asundi. "Phase error analysis and compensation for nonsinusoidal waveforms in phase-shifting digital fringe projection profilometry." *Opt Lett* 34 (2009): 416.
597. Papen, G. C., C. S. Gardner, and J. Yu. "Characterization of the mesospheric sodium layer." *Top Mtg on Adap Opt, Opt Soc Am Tech Dig Series* 13 (1996): 96.
598. Parenti, R. R. "Adaptive optics for astronomy." *The Lincoln Laboratory Journal* 5 (1992): 93.
599. Parmentier, E. M., and R. A. Greenberg, "Supersonic flow aerodynamic windows for high-power lasers." *AIAA J* 11(1973): 943.
600. Paschall, R. N., and D. J. Anderson. "Linear quadratic Gaussian control of a deformable mirror adaptive optics system with time-delayed measurements." *Appl Opt* 32 (1993): 6347.
601. Pearson, J. E. "Atmospheric turbulence compensation using coherent optical adaptive techniques." *Appl Opt* 15 (1976): 622.
602. Pearson, J. E. "Thermal blooming compensation with adaptive optics." *Opt Lett* 2 (1978): 7.
603. Pearson, J. E. "Recent advances in adaptive optics." *Conf. on Lasers and Electro-optical Systems*, San Diego, CA, 1980.
604. Pearson, J. E. S. A. Kokorowski, and M. E. Pedinoff. "Effects of speckle in adaptive optical systems." *J Opt Soc Am* 66 (1976): 1261.
605. Pearson, J. E., and S. Hansen. "Experimental studies of a deformable-mirror adaptive optical system." *J Opt Soc Am* 67 (1977): 325.
606. Pearson, J. E., and R. H. Freeman. "Deformable mirrors for all seasons and reasons." *Appl Opt* 21 (1982): 580.

607. Peleg, A., and J. V. Moloney, "Scintillation index for two Gaussian laser beams with different wavelengths in weak atmospheric turbulence," *J Opt Soc Am A* 23 (2006): 3114.
608. Penndorf, R. "Tables of the refractive index for standard air and the Rayleigh scattering coefficient for the spectral region between 0.2 and 20.0 μ and their application to atmospheric optics." *J Opt Soc Am* 47 (1957): 176.
609. Pennington, D. M., R. Beach, J. Dawson, A. Drobshoff, Z. Liao, S. Payne, D. Bonaccini, W. Hackenberg, and L. Taylor. "Compact fiber laser approach to generating 589 nm laser guidestars. "*Proc. Conf. Lasers and Electro-optics Europe*, (2003): 730.
610. Pennington, T. L., B. M. Welsh, and M. C. Roggemann. "Performance comparison of the shearing interferometer and Hartmann wavefront sensors." *Proc SPIE* 2201 (1994): 508.
611. Pepper, D. M. "Special issue on non-linear optical phase conjugation" *Opt Eng* 21 (1982): 155.
612. Pepper, D. M. Nonlinear optical phase conjugation. *Laser Handbook*, Vol. 4, eds. M. L. Stitch and M. Bass. Amsterdam: North Holland, 1985.
613. Perreault, J. A., T. G. Bifano, B. M. Levine, and M. N. Horenstein. "Adaptive optic correction using micro-electrical-mechanical deformable mirrors." *Opt Eng* 41 (2002): 561.
614. Perrone, M. R., and Y. B. Yao. "Improved performance of SBS mirrors excited by broad-band radiation." *Proc. ICO-16 Satellite Conf. on Active and Adap Opt, ESO Conf. and Workshop Proc*. 48 (1993): 389.
615. Peters, W. N., R. A. Arnold, and S. Gowrinathan. "Stellar interferometer for figure sensing of orbiting astronomical telescopes." *Appl Opt* 13 (1974): 1785.
616. Petit, C., J.-M. Conan, C. Kulesar, H.-F. Raynaud, and T. Fusco. "First laboratory validation of vibration filtering with LQG control law for adaptive optics." *Opt Expr* 16 (2008): 87.
617. Petit, C., F. Quiros-Pacheco, J.-M. Conan, C. Kulesar, H.-F. Raynaud, T. Fusco, and G. Rousset. "Kalman filter based control loop for adaptive optics." *Proc SPIE* 5490 (2004): 1414.
618. Petroff, M. D., M. G. Stapelbroek, and W. A. Kleinhous. "Direction of individual 0.4-28 micron wavelength photons via impurity-impact ionization in a solid-state photomultiplier." *Appl Phys Lett* 51 (1987): 6.
619. Phillion, D. W., and K. Baker. "Two-sided pyramid wavefront sensor in the direct phase mode." *Proc SPIE* 6272 (2006): 627228.
620. Piatrou, P., and M. Roggemann. "Beaconless stochastic parallel gradient descent laser beam control: Numerical experiments." *Appl Opt* 46 (2007): 6831.
621. Planchon, T. A., W. Amir, J. J. Field, C. G. Durfee, and J. A. Squier. "Adaptive correction of a tightly focused, high-intensity laser beam by use of a third-harmonic signal generated at an interface." *Opt Lett* 31 (2006): 2214.
622. Plass, G. N., and G. W. Kattawar. "Radiative transfer of the Earth's atmosphere-ocean-system II. Radiance in the atmosphere and ocean." *J Phys Oceanogr* 2 (1972): 139.
623. Pliakis, D., and S. Minardi. "Phase front retrieval by means of an iterative shadowgraph method." *J Opt Soc Am A* 26 (2009): 99.
624. Podanchuk, D. V., V. P. Dan'ko, M. M. Kotov, J.-Y. Son, and Y.-J. Choi. "Extended-range Shack-Hartmann wavefront sensor with nonlinear holographic lenslet array." *Opt Eng* 45 (2006): 053605.

625. Polejaev, V. I., A. V. Koryabin, and V. I. Shmalhausen. "Combined intra-cavity and outer cavity adaptive correction of aberrations in a solid state laser." *Top Mtg on Adap Opt, Opt Soc Am Tech Dig Series* 13 (1996): 187.
626. Popovic, Z. D., R. A. Sprague, and G. A. Neville Connell. "Technique for monolithic fabrication of microlens arrays." *Appl Opt* 27 (1988): 7.
627. Poyneer, L. A., D. Dillon, S. Thomas, and B. A. Macintosh. "Laboratory demonstration of accurate and efficient nanometer-level wavefront control for extreme adaptive optics." *Appl Opt* 47 (2008): 1317.
628. Poyneer, L. A., B. A. Macintosh, and J.-P. Veran. "Fourier transform wavefront control with adaptive prediction of the atmosphere." *J Opt Soc Am A* 24 (2007): 2645.
629. Press, W. H., B. P. Flannery, S. A. Teukolsky, and W. T. Vetterling. *Numerical Recipes*. Cambridge: Cambridge University Press, 1989.
630. Prieto, P. M., F. Vargas-Martin, S. Goelz, and P. Artal. "Analysis of the performance of the Hartmann-Shack sensor in the human eye." *J Opt Soc Am A* 17 (2000): 1388.
631. Primmerman, C. A., and D. G. Fouche. "Thermal-blooming compensation: Experimental observations using a deformable-mirror system." *Appl Opt* 15 (1976): 990.
632. Primmerman, C. A., D. V. Murphy, D. A. Page, B. G. Zollars, and H. T. Barclay. "Compensation of atmospheric turbulence optical distortion using a synthetic beacon." *Nature* 353 (1991): 141.
633. Primmerman, C. A., T. R. Price, R. A. Humphreys, B. G. Zollars, H. T. Barclay, and J. Hermann, "Atmospheric-compensation experiments in strong-scintillation conditions." *Appl Opt* 34 (1995): 2081.
634. Quirrenbach, A. "Adaptive optics at MPE: Astronomical results and future plans." *Top Mtg on Adap Opt, Opt Soc Am Tech Dig Series* 13 (1996): 166.
635. Rabien, S., N. Ageorges, R. Angel, G. Brusa, J.Brynnel, L.Busoni, R.Davies, M. Deysenroth, S. Esposito, W.Gaessler, R. Genzel, R. Green, M. Haug, M.Lloyd-Hart, E. Holzl, E. Masciadri, R. Pogge, A. Quirrenbach, M. Rademaker, H. W. Rix, P. Salinari, T. Schwab, T. Stalcup, J. Storm, M. Thiel, G. Weigelt, and J. Ziegleder. "The laser guide star program for the LBT." *Proc SPIE* 7015 (2008): 701515.
636. Racine, R., G. Herriot, and R. D. McClure. "The Gemini adaptive optics system." *Proc. Top. Mtg. on Adap Opt, ESO Conf. and Workshop Proc*. 54 (1996): 35.
637. Ragazzoni, R., and D. Bonaccini. "The adaptive optics system for the Telescopio Nazionale Galileo." *Proc. Top. Mtg. on Adap Opt, ESO Conf. and Workshop Proc*. 54 (1996): 17.
638. Rasigni, G., F. Varnier, M. Rasagni, J. P. Palmeri, and A. Llebaria. "Autocovariance functions for polished optical surfaces." *J Opt Soc Am* 73 (1983): 222.
639. Rayleigh, L. "Investigation in optics, with a special reference to the spectroscope: On the accuracy required in optical surfaces." *Philos Mag* 5 (1879): 8.
640. RCA. *Electro-optics Handbook*, Technical Series EOH-11, Haddonfield, NJ: RCA Corp., 1974.
641. Rediker, R. H., B. G. Zollars, T. A. Lind, R. E. Hatch, and B. E. Burke. "Measurement of the wavefront of a pulsed dye laser using an integrated-optics sensor with 200-nsec temporal resolution." *Opt Lett* 14 (1989): 381.
642. Reintjes, J. F. "Nonlinear and adaptive techniques control laser wavefronts." *Laser Focus* 12 (1988): 63.

643. Restaino, S. R., D. Dayton, S. Browne, J. Gonglewski, J. Baker, S. Rogers, S. McDermott, J. Gallegos, and M. Shilko. "On the use of dual frequency nematic material for adaptive optics systems: First results of a closed-loop experiment." *Opt Expr* 6 (2000): 2.
644. Reznichenko, V. V., V. V. Nicitin, A. P. Onokhov, M. V. Isaev, N. L. Ivanova, and L. A. Beresnev. "Liquid crystal spatial modulators with segmented mirror for adaptive optics." *Top Mtg on Adap Opt, Opt Soc Am Tech Dig Series* 13 (1996): 282.
645. Rhoadarmer, T. A., and B. L. Ellerbroek. "A method for optimizing closed-loop adaptive optics wavefront reconstruction algorithms on the basis of experimentally measured performance data." *Proc SPIE* 2534 (1995); 213.
646. Ribak, E., C. Schwartz, and S. G. Lipson. "Bimorph adaptive mirrors: construction and theory." *Proc. ICO-16 Satellite Conf. on Active and Adap Opt, ESO Conf. and Workshop Proc*. 48 (1993): 313.
647. Rigaut, F., and E. Gendron. "Laser guide star in adaptive optics: The tilt determination problem." *Astron Astrophys* 261 (1992): 677.
648. Rigaut, F., D. Salmon, R. Arsenault, S. McArthur, J. Thomas, O. Lai, D. Rouan, P. Gigan, J.-P. Veran, D. Crampton, M. Fletcher, J. Stilburn, B. Leckie, S. Roberts, R. Woof, C. Boyer, P. Jagourel, and J.-P. Gaffard. "First results of the CFHT adaptive optics bonnette on the telescope." *Top Mtg on Adap Opt, Opt Soc Am Tech Dig Series* 13 (1996): 46.
649. Rigaut, F., D. Salmon, R. Arsenault, J. Thomas, O. Lai, D. Rouan, J.-P. Veran, D. Crampton, J. M. Fletcher, and J. Stilburn. "Performance of the Canada-France-Hawaii Telescope adaptive optics bonnette." *Pub Astro Soc Pac* 110 (1998): 152.
650. Rimmele, T. R., and R. R. Radick. "Experimental comparison of two approaches for solar wavefront sensing." *Top Mtg on Adap Opt, Opt Soc Am Tech Dig Series* 13 (1996): 247.
651. Rimmele, T., K. Richards, J. Roche, S. Hegwer, and A. Tritschler. "Progress with solar multi-conjugate adaptive optics at NSO." *Proc SPIE* 6272 (2006): 627206.
652. Rimmele, T., K. Richards, J. M. Roche, S. L. Hegwer, R. P. Hubbard, E. R. Hanson, B. Goodrich, and R. S. Upton. "The wavefront correction system for the advanced technology solar telescope." *Proc SPIE* 6272 (2006): 627212.
653. Rimmele, T., O. von der Luhe, P. H. Wiborg, A. L. Widener, R. B. Dunn, and G. Spence. "Solar feature correlation tracker." *Proc SPIE* 1542 (1991): 186.
654. Rimmer, M. P. "Methods for evaluating lateral shear interferograms." *Appl Opt* 13 (1974): 623.
655. Roark, R. J. *Formulas for Stress and Strain*. 4th ed. New York: McGraw-Hill, 1965.
656. Robinson, S. R. "On the problem of phase from intensity measurements." *J Opt Soc Am* 68 (1978): 87.
657. Robinson, S. R. "Fundamental performance limitations for the phase retrieval problem." *Proc SPIE* 351 (1982): 66.
658. Roddier, C., F. Roddier, and J. Demarcq. "Compact rotational shearing interferometer for astronomical applications." *Opt Eng* 28 (1989): 66.
659. Roddier, C., and F. Roddier. "Wavefront reconstruction from defocused images and the testing of ground-based optical telescopes." *J Opt Soc Am A* 10 (1993): 2277.
660. Roddier, F. "Curvature sensing and compensation: A new concept in adaptive optics." *Appl Opt* 27 (1988): 1223.

661. Roddier, F. "Astronomical adaptive optics with natural reference stars," *Proc. Laser Guide Star Adaptive Optics Workshop* 1, 19. Albuquerque, NM: U. S. Air Force Phillips Laboratory, 1992.
662. Roddier, F., and C. Roddier. "NOAO infrared adaptive optics program II: Modeling atmospheric effects in adaptive optics systems for astronomical telescopes." *Proc SPIE* 628 (1986): 299.
663. Roddier, F., C. Roddier, and N. Roddier. "Curvature sensing: A new wavefront sensing method." *Proc SPIE* 976 (1988): 203.
664. Roddier, F., J. E. Graves, and E. Limburg. "Seeing monitor based on wavefront curvature sensing." *Proc SPIE* 1236 (1990): 475.
665. Roddier, N. "Atmospheric wavefront simulation using Zernike polynomials." *Opt Eng* 29 (1990): 1174.
666. Roddier, N. "Algorithms for wavefront reconstruction out of curvature sensing data." *Proc SPIE* 1542 (1991): 120.
667. Rodrigues, G., R. Bastaits, S. Roose, Y. Stockman, S. Gebhardt, A. Schoenecker, P. Villon, and A. Preumont. "Modular bimorph mirrors for adaptive optics." *Opt Eng* 48 (2009): 034001.
668. Roggemann, M. C. "Limited degree-of-freedom adaptive optics and image reconstruction." *Appl Opt* 30 (1991): 4227.
669. Roggemann, M. C. "Optical performance of fully and partially compensated adaptive optics systems using least-squares and minimum variance phase reconstruction." *Comput Electron Eng* 18 (1992): 451.
670. Roggemann, M. C., B. L. Ellerbroek, and T. A. Rhoadarmer. "Widening the effective field-of-view of adaptive optics telescopes using deconvolution from wavefront sensing: Average and signal-to-noise ratio performance." *Appl Opt* 34 (1995): 1432.
671. Roggemann, M. C., B. M. Welsh, D. Montera, and T. A. Rhoadarmer. "Method for simulating atmospheric turbulence phase effects for multiple time slices and anisoplanatic conditions." *Appl Opt* 34 (1995): 4037.
672. Roggemann, M. C., and B. Welsh. *Imaging through Turbulence*. FL: CRC Press, 1996.
673. Rosenberg, B., and P. R. Barbier. "Simulation of adaptive optics improvement on laser communication link performance." *Top Mtg on Adap Opt, Opt Soc Am Tech Dig Series* 13 (1996): 184.
674. Rosenstock, H. B., and J. H. Hancock. "Light propagation through a moving gas." *Appl Opt* 10 (1971): 1299.
675. Ross, W. E. *Electronic Imaging*, February 1984: 48.
676. Rougeot, H., and C. Baud. "Negative electron affinity photoemitters." *Adv Elect Electron Phys* 48 (1986): 1.
677. Rousset, G., J.-C. Fontanella, P. Kern, P. Lena, P. Gigan, F. Rigaut, J.-P. Gaffard, C. Boyer, P. Jagourel, and F. Merkle. "Adaptive optics prototype system for infrared astronomy, I: System description." *Proc SPIE* 1237 (1990): 336.
678. Rousset, G., J. L. Bauzit, N. Hubin, E. Gendron, C. Boyer, P. Y. Madec, P. Gigan, J. C. Richard, M. Vittot, J. P. Gaffard, F. Rigaut, and P. Lena. "The COME-ON- PLUS adaptive optics system: Results and performance." *Proc. ICO-16 Satellite Conf. on Active and Adap Opt, ESO Conf. and Workshop Proc*. 48 (1993): 65.
679. Rueckel, M., and W. Denk. "Properties of coherence-gated wavefront sensing." *J Opt Soc Am A* 24 (2007): 3517.

680. Rutten, T. P., P. J. Veitch, C. d'Orgeville, and J. Much. "Injection mode-locked guide star laser concept and design verification experiments." *Opt Expr* 15 (2007): 2369.
681. Rytov, S. M. "Diffraction of light by ultrasonic waves." *Izv Akad Nauk SSSR Ser Fiz* 2 (1937): 223.
682. Saito, N., K. Akagawa, M. Ito, A. Takazawa, Y. Hayano, Y. Saito, M. Ito, H. Takami, M. Iye, and S. Wada. "Sodium D2 resonance radiation in single-pass sum-frequency generation with actively mode-locked Nd:YAG lasers." *Opt Lett* 32 (2007): 1965.
683. Sakamoto, J. A., H. H. Barrett, and A. V. Goncharov. "Inverse optical design of the human eye using likelihood methods and wavefront sensing." *Opt Expr* 16 (2008): 304.
684. Salinari, P., C. Del Vecchio, and V. Biliotti. "A study of an adaptive secondary mirror." *Proc. ICO-16 Satellite Conf. on Active and Adap Opt, ESO Conf and Workshop Proc*. 48 (1993): 247.
685. Sanchez, H. R., M. C. Simon, and J. M. Simon. "Polarization properties of diffraction gratings." *J Opt Soc Am* 66 (1976): 1055.
686. Sandler, D. "A multiple spot laser beacon for high-order wavefront control: Theory and experiment," *Proc. Laser Guide Star Adaptive Optics Workshop* 1, 164. Albuquerque, NM: U. S. Air Force Phillips Laboratory, 1992.
687. Sandler, D. G., M. LeFebvre, L. Cuellar, S. Stahl, T. Barrett, R. Arnold, and F. Tart, "Atmospheric tests of shearing interferometry for laser guide star adaptive optics." *Proc ICO-16 Satellite Conf on Active and Adap Opt, ESO Conf and Workshop Proc* 48 (1993): 503.
688. Sandler, D. G., S. Stahl, J. R. P. Angel, M. Lloyd-Hart, and D. McCarthy. "Adaptive optics for diffraction-limited infrared imaging with 8-m telescopes." *J Opt Soc Am A* 11 (1994): 925.
689. Sandler, D. G., L. Cuellar, M. Lefebvre, T. Barrett, R. Arnold, P. Johnson, A. Rego, G. Smith, G. Taylor, and B. Spivey. "Shearing interferometry for laser-guide-star atmospheric correction at large *D/ro*." *J Opt Soc Am A* 11 (1994): 858.
690. Sarazin, M., and F. Roddier. "The ESO differential image motion monitor." *Astron Astrophys* 227 (1990): 294.
691. Sarkisov, S. S., M. J. Curley, L. Huey, A. Fields, S. S. Sarkisov II, and G. Adamovsky. "Light-driven actuators based on polymer films." *Opt Eng* 45 (2006): 034302.
692. Sasiela, R. J. "Wavefront correction by one or more synthetic beacons." *J Opt Soc Am A* 11 (1994): 379.
693. Sasiela, R. J. *Electromagnetic wave propagation—Evaluation and application of Mellin transforms*, Springer Series on Wave Phenomena. Berlin: Springer-Verlag, 1994.
694. Sasiela, R. J., and J. G. Mooney. "An optical phase reconstructor based on using a multiplier-accumulator approach." *Proc SPIE* 551 (1985): 170.
695. Sasiela, R. J., and J. D. Shelton. "Mellin transform techniques applied to integral evaluation: Taylor series and asymptotic approximations." *J Math Phys* 34 (1993): 2572.
696. Sato, T., H. Ishida, and O. Ikeda. "Adaptive PVDF piezoelectric deformable mirror system." *Appl Opt* 19 (1980): 1430.
697. Sato, T., H. Ishikawa, O. Ikeda, S. Nomura, and K. Uchino. "Deformable 2-D mirror using multilayered electrostrictors." *Appl Opt* 21 (1982): 3669; Sato, T., H. Ishikawa, and O. Ikeda. "Multilayered deformable mirror using PVDF films." *Appl Opt* 21 (1982): 3664.

698. Sauvage, J.-F., T. Fusco, G. Rousset, and C. Petit, "Calibration and precompensation of noncommon path aberrations for extreme adaptive optics." *J Opt Soc Am A* 24 (2007): 2334.
699. Sawyer, D. G., C. Corson, and A. Saha. "Optimizing the delivered image quality at the WIYN 3,5-m telescope." *Proc SPIE* 4004 (2000): 422.
700. Scheglov, P. V. "Site testing on Soviet Middle Asia in 1970–1980." *Proc. Conf. Astron. Climate and Telescope Efficiency* (1981): 126.
701. Schiller, C. M., T. N. Horsky, D. M. O'Mara, W. S. Hamnett, G. J. Genetti, and C. Warde. "Charge-transfer-plate deformable membrane mirrors for adaptive optics applications." *Proc SPIE* 1543 (1991): 120.
702. Schmutz, L. E. "Hartmann sensing at adaptive optics associates." *Proc SPIE* 779 (1987): 13.
703. Schmutz, L. E., and B. M. Levine. "Hartmann sensors detect optical fabrication errors." *Laser Focus World* 32 (1996): 111.
704. Scholl, M. S. "Wavefront distortion introduced by sampling with a hole grating." *Proc SPIE* 293 (1981): 74.
705. Schonfeld, J. F. "Analysis and modeling of thermal blooming compensation." *Proc SPIE* 1221 (1990): 118.
706. Schonfeld, J. F. "Linearized analysis of phase-conjugate instability with realistic adaptive optics," Lincoln Laboratory, Project Report BCP-14, 1989; Schonfeld, J. F. "Linearized theory of thermal-blooming phase-compensation instability with realistic adaptive-optics geometry." *J Opt Soc Am B* 9 (1992): 1803.
707. Schroeder, M. E., K. D. Stumpf, and M. A. Mullahy, "Grating beam combiner," Rome Air Development Center Report, RADC-TR-82-311, Griffiss AFB, New York, 1982.
708. Schwartz, C., E. Ribak, and S. G. Lipson. "Bimorph adaptive mirrors and curvature sensing." *J Opt Soc Am A* 11 (1994): 895.
709. Seilly, A. H. "Helenoid actuators—A new concept in extremely fast acting solenoids," presented at SAE Congress and Exposition, Detroit, 1979.
710. Sergeyev, A. V., P. Piatrou, and M. C. Roggemann. "Bootstrap beacon creation for overcoming the effects of beacon anisoplanatism in a laser beam projection system." *Appl Opt* 47 (2008): 2399.
711. Shack, R. B., and B. C. Platt. "Production and use of a lenticular Hartmann screen." *J Opt Soc Am* 61 (1971): 656.
712. Shamir, J., and D. G. Crowe. "Increasing the compensated field of view using multiple adaptive mirror telescope systems," *Proc. Laser Guide Star Adaptive Optics Workshop* 2, 591. Albuquerque, NM: U. S. Air Force Phillips Laboratory, 1992.
713. Shamir, J., D. G. Crowe, and J. W. Beletic. "Improved compensation of atmospheric turbulence effects by multiple adaptive mirror systems." *Appl Opt* 32 (1993): 4618.
714. Shannon, R., and J. Wyant, eds. *Applied Optics and Optical Engineering*. Vol. IX, Chap. 2, New York: Academic Press, 1983.
715. Shellan, J. B. "Phased-array performance degradation due to mirror misfigures, piston errors, jitter, and polarization errors." *J Opt Soc Am A* 2 (1985): 555.
716. Shellan, J. B., D. A. Holmes, M. L. Bernabe, and A. M. Simonoff. "Adaptive mirror effects on the performance of annular resonators." *Appl Opt* 19 (1980): 610.
717. Shelton, C., and S. Baliunas. "Results of adaptive optics at Mount Wilson Observatory." *Proc SPIE* 1920 (1993): 371.

718. Shelton, J. C., T. G. Schneider, D. McKenna, and S. L. Baliunas. "Results from the Cassegrain adaptive optics system of the Mount Wilson 100-inch telescope." *Top Mtg on Adap Opt, Opt Soc Am Tech Dig Series* 13 (1996): 43.
719. Shen, G., A. Gayhart, D. Eaton, E. Kaelber, and W. Zukowski. "Large angle fast steering mirrors." *Proc SPIE* 1543 (1991): 286.
720. Shen, Y. R. *The Principles of Nonlinear Optics*. New York: Wiley, 1984.
721. Sidisk, E., J. J. Green, R. M. Morgan, C. M. Ohara, and D. C. Redding. "Adaptive cross-correlation algorithm for extended scene Shack-Hartmann wavefront sensing." *Opt Lett* 33 (2008): 213.
722. Siegman, A. E. "Absolute frequency stabilization of a laser oscillator against a laser amplifier." *IEEE J Quantum Electron* QE-3 (1967): 377.
723. Siegman, A. E. "A canonical formulation for multi-element unstable resonator calculations." *IEEE J Quantum Electron* QE-12 (1976): 35.
724. Simmons, A. C., P. T. Stroud, and S. G. Simmons. "Application of helenoid actuators to deformable mirrors." *Appl Opt* 19 (1980): 1388.
725. Simon, J. M., and M. A. Gil. "Diffraction gratings and optical aberrations." *Appl Opt* 23 (1984): 1075.
726. Simonov, A. N., S. Hong, and G. Vdovin. "Piezoelectric deformable mirror with adaptive multiplexing control." *Opt Eng* 45 (2006): 070501.
727. Simpkins, T., J. Hui, and C. Warde. "Optimizing stochastic gradient descent algorithms for serially addressed adaptive-optics wavefront modulators." *Appl Opt* 46 (2007): 7566.
728. Sintsov, V. N., and A. F. Zapryagaev. "Aperture synthesis in optics." *Sov Phys Usp* 17 (1975): 931.
729. Skolnik, M. I. *Introduction to Radar Systems*. New York: McGraw-Hill, 1962.
730. Smartt, R. N., and W. H. Steel. "Theory and application of point-diffraction interferometers." *Jpn J Appl Phys* 14 (1975): 351.
731. Smith, D. C. "High-power laser propagation: thermal blooming." *IEEE J Quantum Electron* QE-5 (1969): 1679.
732. Smith, D. C. "High-power laser propagation: thermal blooming." *Proc IEEE* 65 (1977): 1679.
733. Smith, D. C., and R. G. Meyerand. Laser Radiation Induced Gas Breakdown. In *Principles of Laser Plasmas*, New York: Wiley, 1976.
734. Smithson, R. C., and M. L. Peri. "Partial correction of astronomical images with active mirrors." *J Opt Soc Am A* 6 (1989): 92.
735. Solomon, C. J., and D. L. Ash, "A study of wavefront reconstruction methods," *Proc. Top. Mtg. on Adaptive Optics, ESO Conf. and Workshop Proc*. 54 (1996): 113.
736. Soltau, D., D. S. Acton, T. Kentischer, M. Roser, W. Schmidt, and M. Stix. "Adaptive optics for a 70 cm solar telescope," *Top Mtg on Adap Opt, Opt Soc Am Tech Dig Series* 13 (1996): 53.
737. Song, H., G. Vdovin, R. Fraanje, G. Schitter, and M. Verhaegen. "Extracting hysteresis from nonlinear measurement of wavefront-sensorless adaptive optics system." *Opt Lett* 34 (2009): 61.
738. Southwell, W. H. "Wavefront analyzer using a maximum likelihood algorithm." *J Opt Soc Am* 67 (1977): 396.
739. Southwell, W. H. "Wavefront estimation from wavefront slope measurements." *J Opt Soc Am* 70 (1980): 998.
740. Southwell, W. H. "What's wrong with cross coupling in modal wavefront estimation?" *Proc SPIE* 365 (1982): 97.

741. Spinhirne, J. M., D. Anafi, R. H. Freeman, and H. R. Garcia. "Intracavity adaptive optics. 1: Astigmatism correction performance." *Appl Opt* 20 (1981): 976.
742. Spyromilio, J., F. Comeron, S. D'Odorico, M. Kissler-Patig, and R. Gilmozzi. "Progress on the European Extremely Large Telescope," European Southern Observatory, Garching bei Munchen, *The Messenger* 133 (2008): 2.
743. Stavroudis, O. N. "Comments on: On Archimedes' burning glass." *Appl Opt* 12 (1973): A16.
744. Steinhaus, E., and S. G. Lipson. "Bimorph piezoelectric flexible mirror." *J Opt Soc Am* 69 (1979): 478.
745. Stone, J., P. H. Hu, S. P. Mills, and S. Ma. "Anisoplanatic effects in finite-aperture optical systems." *J Opt Soc Am A* 11 (1994): 347.
746. Strohbehn, J. W. ed. *Laser Beam Propagation in the Atmosphere*. New York: Springer-Verlag, 1978.
747. Stroke, G. W. Diffraction Gratings. In *Handbuch der Physik*, Vol. 29, S. Flugge, ed., Berlin: Springer-Verlag, 1967.
748. Takajo, H., and T. Takahashi. "Noniterative method for obtaining the exact solution for the normal equation in least-square phase estimation from the phase difference." *J Opt Soc Am A* 5 (1988): 1818.
749. Takami, H., and M. Iye. "Membrane deformable mirror for SUBARU adaptive optics." *Proc SPIE* 2201 (1994): 762.
750. Takami, H., M. Iye, N. Takato, M. Otsubo, and K. Nakashima. "SUBARU adaptive optics program," *Proc. Top. Mtg. on Adaptive Optics, ESO Conf. and Workshop Proc*. 54 (1996): 43.
751. Talon, M., and R. Foy. "Adaptive telescope with laser probe: Isoplanatism and cone effect." *Astro Astrophys* 235 (1990): 549.
752. Talon, M., R. Foy, and J. Vernin. "Wide field adaptive optics using an array of laser guide stars," *Proc. Laser Guide Star Adaptive Optics Workshop* 2, 555. Albuquerque, NM: U. S. Air Force Phillips Laboratory, 1992.
753. Tango, W. J., and R. Q. Twiss. Michelson stellar interferometry. In *Progress in Optics*, Vol XVII, 239. Amsterdam: Elsevier, 1980.
754. Taranenko, V. G., G. P. Koshelev, and N. S. Romanyuk. "Local deformations of solid mirrors and their frequency dependence." *Sov J Opt Technol* 48 (1981): 650.
755. Tatarskii, V. I. *Wave Propagation in a Turbulent Medium*. New York: McGraw-Hill, 1961.
756. Tatarskii, V. I. *The Effects of the Turbulent Atmosphere on Wave Propagation*. Springfield, Virginia: U. S. Dept. of Commerce, National Technical Information Service, 1971.
757. Taylor, J. R. "Phase retrieval using a genetic algorithm on the systematic image-based optical alignment testbed," NASA/ASEE Faculty Fellowship Program, Marshall Space Flight Center, The University of Alabama, Part XLIX, 2002.
758. Teague, M. R. "Irradiance moments: their propagation and use for unique retrieval of phase." *J Opt Soc Am* 72 (1982): 1199.
759. Telle, J. M. "Exploring high altitude beacon concepts other than sodium," *Top Mtg on Adap Opt, Opt Soc Am Tech Dig Series* 13 (1996): 100.
760. ten Brummelaar, T. A., W. G. Bagnuolo, and S. T. Ridgway. "Strehl ratio and visibility in long-baseline stelolar interferometry." *Opt Lett* 20 (1995): 521.
761. Thelen, B. J., R. G. Paxman, D. A. Carrara, and J. H. Seldin. "Overcoming turbulence-induced space-variant blur by using phase-diverse speckle." *J Opt Soc Am A* 26 (2009): 206.

762. Thomas, S. "SAM—The SOAR Adaptive Module." *EAS Pub Series* 12 (2004): 177.
763. Thomas, S. J., S. Adkins, D. Gavel, T. Fisco, and V. Michau. "Study of optimal wavefront sensing with elongated laser guide stars." *Mon Not R Astron Soc* 387 (2008): 173.
764. Thompson, L. A. "Experimental demonstration of a Rayleigh guide star at 351 nm," *Proc. Laser Guide Star Adaptive Optics Workshop* 2, 491. Albuquerque, NM: U. S. Air Force Phillips Laboratory, 1992.
765. Thompson, L. A. "UnISIS: University of Illinois Seeing Improvement System; An adaptive optics instrument for the Mt. Wilson 2.5-m telescope." *Proc SPIE* 2201 (1994): 1074.
766. Thompson, L. A., and C. S. Gardner. "Excimer laser guide star techniques for adaptive imaging in astronomy." *Proc SPIE* 1114 (1989): 184.
767. Thompson, L. A., and R. M. Castle. "Experimental demonstration of a Rayleigh-scattered laser guide star at 351 nm." *Opt Lett* 17 (1992): 1485.
768. Thompson, L. A., S. W. Teare, C. R. Neyman, and D. G. Sandler. "UnISIS adaptive optics system at the 2.5-m telescope." *Proc SPIE* 4839 (2003): 44.
769. Thompson, L. A., and X. Yao-Heng. "Laser beacon system for the UnISIS adaptive optics system at the Mt. Wilson 2.5 meter telescope." *Proc SPIE* 2534 (1995): 38.
770. Thompson, S. J., A. P. Doel, R. G. Bingham, A. Charalambous, R. M. Myers, N. Bissonauth, P. Clark, and G. Talbot. "Results from the adaptive optics coronagraph at the WHT." *Mon Not Roy Astron Soc* 364 (2005), 1203.
771. Thorlabs. Available at: www.thorlabs.com
772. Tian, Y., C. Rao, and K. Wei. "Adaptive optics image restoration based on frame selection and multi-frame blind deconvolution." *Chinese Astron Astrophys* 33 (2009): 223.
773. Ting, C., M. K. Giles, and D. G. Voelz. "Effectiveness of high-order adaptive optics in ground-based stellar interferometry." *Opt Eng* 45 (2006): 026001.
774. Tippie, A. E., and J. R. Fienup. "Phase-error correction for multiple planes using a sharpness metric." *Opt Lett* 34 (2009): 701.
775. Travouillon, T., J. S. Lawrence, and L. Jolissaint. "Ground layer adaptive optics performance in Antarctica." *Proc SPIE* 5490 (2005): 934.
776. Trujillo, C. A., F. Rigaut, D. Graadour, and M. Hartung. "Science using the Gemini North laser adaptive optics system." *Bull Am Astro Soc* 39 (2007): 748.
777. Twyman, F., and A. Green. British Patent 103832, 1916.
778. Tyler, D. W. "Optimal wavelength selection for adaptive optics telescopes." *Proc SPIE* 2201 (1994): 227.
779. Tyler, G. A. "Turbulence-induced adaptive-optics performance degradation: evaluation in the time domain." *J Opt Soc Am A* 1 (1984): 251.
780. Tyler, G. A. "Summary of theoretical performance and limitations of laser guide star adaptive optics for astronomical applications," *Proc Laser Guide Star Adaptive Optics Workshop* 1, 405. Albuquerque, NM: U. S. Air Force Phillips Laboratory, 1992.
781. Tyler, G. A. "Bandwidth considerations for tracking through turbulence." *J Opt Soc Am A* 11 (1994): 358.
782. Tyler, G. A. "Merging: a new method for tomography through random media." *J Opt Soc Am A* 11 (1994): 409.

783. Tyler, G. A. "Rapid evaluation of do: the effective diameter of a laser guide-star adaptive-optics system." *J Opt Soc Am A* 11 (1994): 325.
784. Tyler, G. A. "Wavefront compensation for imaging with off-axis guide stars." *J Opt Soc Am A* 11 (1994): 339.
785. Tyler, G. A. "Assessment of the statistics of the Strehl ratio: predictions of central limit theorem analysis." *J Opt Soc Am A* 23 (2006): 2834.
786. Tyler, G. A., and D. L. Fried. "Image-position error associated with a quadrant detector." *J Opt Soc Am* 72 (1982): 804.
787. Tyson, R. K. "Conversion of Zernike aberration coefficients to Seidel and higher-order power-series aberration coefficients." *Opt Lett* 7 (1982): 262.
788. Tyson, R. K. "Using the deformable mirror as a spatial filter: application to circular beams." *Appl Opt* 21 (1982): 787.
789. Tyson, R. K. "Adaptive optics system performance approximations for atmospheric turbulence correction." *Opt Eng* 29 (1990): 1165.
790. Tyson, R. K. "Aperture sizing strategies for astronomical adaptive optics system optimization," *Proc. ICO-16 Satellite Conf. on Active and Adaptive Optics, ESO Conf. and Workshop Proc*. 48 (1993).
791. Tyson, R. K. "Adaptive optics and ground-to-space laser communications." *Appl Opt* 35 (1996): 3640.
792. Tyson, R. K. "Bit error rate for free space adaptive optics laser communications." *J Opt Soc Am A* 19 (2002): 753.
793. Tyson, R. K., and D. M. Byrne. "The effect of wavefront sensor characteristics and spatiotemporal coupling on the correcting capability of a deformable mirror." *Proc SPIE* 228 (1980): 21.
794. Tyson, R. K., and J. Schulte in den Bäumen, eds., *Adaptive Optics and Optical Structures*, *Proc SPIE* 1271 (1990).
795. Tyson, R. K., and D. E. Canning. "Indirect measurement of a laser communications bit error rate reduction with low order adaptive optics." *Appl Opt* 42 (2003): 4239.
796. Tyson, R. K., D. P. Crawford, and R. J. Morgan. "Adaptive optics system considerations for ground-to-space propagation." *Proc SPIE* 1221 (1990): 146.
797. Tyson, R. K., J. S. Tharpe, and D. E. Canning. "Measurement of the bit error rate of an adaptive optics free space laser communications system. Part 2: multichannel configuration, aberration characterization, and closed loop results." *Opt Eng* 44 (2005): 096003.
798. Uchino, K., Y. Tsuchiya, S. Nomura, T. Sato, H. Ishikawa, and O. Ikeda. "Deformable mirror using the PMN electrostrictor." *Appl Opt* 20 (1981): 3077.
799. Ulrich, P. B. "Requirements for experimental verification of thermal-blooming computer results." *J Opt Soc Am* 63 (1973): 897.
800. Ulrich, P. B. *Hufnagel–Valley Profiles for Specified Values of the Coherence Length and Isoplanatic Patch Angle*. Arlington, Virginia: W. J. Schafer Associates, WJSA/MA/TN-88-013, 1988.
801. Um, G. S., B. F. Smithgall, and C. L. O'Bryan. "Minimum variance estimation of wavefront aberration." *Proc SPIE* 351 (1982): 96.
802. Underwood, I., D. G. Vass, and R. M. Sillitto. "Evaluation of an nMOS VLSI array for an adaptive liquid-crystal spatial light modulator." *IEE Proc* 133, Pt. J (1986): 77.
803. Underwood, K., J. C. Wyant, and C. L. Koliopoulos. "Self-referencing wavefront sensor." *Proc SPIE* 351 (1982): 108.

804. United Detector Technology. 1990 Catalog, Hawthorne, CA. Updates available from www.udtinstruments.com.
805. U. S. Air Force Systems, Command Manual, AFSCM 375-5, Andrews Air Force Base, Maryland, 1964.
806. U. S. Military, Standards 490 and 490a, superseded by Mil. Std. 961 Air Force Material Command Standardization Office, 1995.
807. Vaillant, J. "Wavefront sensor architectures fully embedded in an image sensor." *Appl Opt* 46 (2007): 7110.
808. Valley, G. C. "Isoplanatic degradation of tilt correction and short-term imaging systems." *Appl Opt* 19 (1980): 574.
809. van Dam, M. A., A. H. Bouchez, D. Le Mignant, E. M. Johansson, P. L. Wizinowich, R. D. Campbell, J. C. Y. Chin, S. K. Hartman, R. E. Lafon, P. J. Stomski, Jr., and D. M. Summers. "The W. M. Keck Observatory laser guide star adaptive optics system: performance characterization." *Publ Astron Soc Pac* 118 (2006): 310.
810. Van de Vegte, J. *Feedback Control Systems*. 2nd ed. Englewood Cliffs, New Jersey: Prentice-Hall, 1990.
811. Van Trees, H. L. *Detection, Estimation, and Modulation Theory, Part I*. New York: Wiley, 1968.
812. Van Workum, J., J. A. Plascyk, and M. L. Skolnick. "Laser wavefront analyzer for diagnosing high-energy lasers." *Proc SPIE* 141 (1978): 58.
813. Vaughn, J. L., and D. L. Fried. "M-method performance for M=3," the Optical Sciences Co. Report, TR-995, Placentia, California, 1991.
814. Vdovin, G. "Model of an adaptive optical system controlled by a neural network." *Opt Eng* 34 (1995): 3249.
815. Vdovin, G., S. Middelhoek, M. Bartek, P. M. Sarro, and D. Solomatine. "Technology, characterization and applications of adaptive mirrors fabricated with IC-compatible micromachining." *Proc SPIE* 2534 (1995): 116.
816. Vdovin, G., O. Soloviev, A. Samokhin, and M. Loktev. "Correction of low order aberrations using continuous deformable mirrors." *Opt Express* 16 (2008): 2859.
817. Vedrenne, N., V. Michau, C. Robert, and J-M. Conan. "Cn2 profile measurement from Shack-Hartmann data." *Opt Lett* 32 (2007): 2659.
818. Velur, V., R. C. Flicker, B. C. Piatt, M. C. Britton, R. G. Dekany, M. Troy, J. E. Roberts, J. C. Shelton, and J. Hickey. "Multiple guide star tomography demonstration at Palomar observatory." *Proc SPIE* 6272 (2006): 62725C.
819. Venema, T. M., and J. D. Schmidt. "Optical phase unwrapping in the presence of branch points." *Opt Express* 16 (2008): 6985.
820. Verinaud, C. "On the nature of the measurements provided by a pyramid wavefront sensor." *Opt Commun* 233 (2004): 27.
821. Verinaud, C., M. Le Louarn, V. Korkiakoski, and M. Carbillet. "Adaptive optics for high-contrast imaging: pyramid sensor versus spatially filtered Shack-Hartmann sensor." *Mon Not R Astron Soc* 357 (2005): L26.
822. Vernet, E., C. Arcidiancono, A. Baruffolo, E. Diolaiti, J. Farinato, M. Lombini, and R. Ragazzoni. "Layer-oriented wavefront sensor for a multiconjugate adaptive optics demonstrator." *Opt Eng* 44 (2005): 096601.
823. Vernon, R. G., and D. J. Link. "Specifying servo bandwidth requirements for astronomical higher order and tilt control subsystems," *Proc. Laser Guide Star Adaptive Optics Workshop* 1, 311. Albuquerque, NM: U. S. Air Force Phillips Laboratory, 1992.

824. Vilupuru, A. S., N. V. Rangaswamy, L. J. Frishman, E. L. Smith III, R. S. Harwerth, and A. Roorda. "Adaptive optics scanning laser ophthalmoscopy for in vivo imaging of lamina cribrosa." *J Opt Soc Am A* 24 (2007): 1417.
825. Viswanathan, V. K., J. V. Parker, T. A. Nussmeier, C. J. Swigert, W. King, A. S. Lau, and K. Price. "An adaptive wavefront error correction system for the LASL Gemini laser fusion system." *J Quantum Electron* 15 (1979): 983.
826. Vogel, C. R., and Q. Yang. "Fast optimal wavefront reconstruction for multi-conjugate adaptive optics using the Fourier domain preconditioned conjugate gradient algorithm." *Opt Express* 14 (2006): 7487.
827. Vogel, C. R., and Q. Yang. "Multigrid algorithm for least-squares wavefront reconstruction." *Appl Opt* 45 (2006): 705.
828. Vogel, C. R., and Q. Yang. "Modeling, simulation, and open-loop control of a continuous facesheet MEMS deformable mirror." *J Opt Soc Am A* 23 (2006): 1074.
829. Von der Luhe, O. "Wavefront measurement error technique using extended, incoherent light sources." *Opt Eng* 27 (1988): 1078.
830. von der Luhe, O., T. Berkefeld, and D. Soltau. "Multi-conjugate solar adaptive optics at the Vacuum Tower Telescope on Tenerife." *C R Physique* 6 (2005): 1139.
831. Vorontsov, M. A. "All-optical adaptive systems: nonlinear optics approach for phase distortion suppression." *Top Mtg on Adap Opt, Opt Soc Am Tech Dig Series* 13 (1996): 312.
832. Vorontsov, M. A., and G. W. Carhart. "Adaptive optics based on analog parallel stochastic optimization: analysis and experimental demonstration." *J Opt Soc Am A* 17 (2000): 1440.
833. Vorontzov, M. A., G. W. Carhart, D. V. Pruidze, J. C. Ricklin, and D. G. Voelz. "Adaptive imaging system for phase-distorted extended source and multiple-distance objects." *Appl Opt* 36 (1997): 3319.
834. Vorontsov, M. A., V. V. Kolosov, and E. Polnau. "Target-in-the-loop wavefront sensing and control with a Collett-Wolf beacon: speckle-average phase conjugation." *Appl Opt* 48 (2009): A13.
835. Vorontsov, M. A., A. V. Kudryashov, S. I. Nazarkin, and V. I. Shmal'gauzen. "Flexible mirror for adaptive light-beam formation systems." *Sov J Quantum Electron* 14 (1984): 839.
836. Vorontsov, M. A., and S. L. Lachinova. "Laser beam projection with adaptive array of fiber collimators. I. Basic considerations for analysis." *J Opt Soc Am A* 25 (2008): 1949.
837. Vorontsov, M. A., and S. L. Lachinova. "Laser beam projection with adaptive array of fiber collimators. II. Analysis of atmospheric compensation efficiency." *J Opt Soc Am A* 25 (2008): 1960.
838. Vorontsov, M. A., J. Riker, G. Carhart, V. S. Rao Gudimetla, L. Beresnev, T. Weyrauch, and L. C. Roberts, Jr. "Deep turbulence effects compensation experiments with a cascaded adaptive optics system using a 3.63 m telescope." *Appl Opt* 48 (2009): A47.
839. Vorontsov, M. A., and V. P. Sivokin. "Stochastic parallel-gradient-descent technique for high-resolution wavefront phase-distortion correction." *J Opt Soc Am A* 15 (1998): 2745.
840. Walker, D. D., R. G. Bingham, and B. C. Bigelow. "Adaptive correction at telescope secondary mirrors," *Proc. ICO-16 Satellite Conf. on Active and Adaptive Optics, ESO Conf. and Workshop Proc*. 48 (1993).

841. Walker, K. N., and R. K. Tyson. "Wavefront correction using a Fourier-based image sharpness metric." *Proc. SPIE* 7468 (2009): 746821.
842. Wallace, J. "Presentation on atmospheric propagation to JASON committee," Far Field, Inc., presented to JASON group, San Diego, CA, 1988.
843. Wallace, B. P., P. J. Hampton, C. H. Bradley, and R. Conan. "Evaluation of a MEMS deformable mirror for an adaptive optics test bed." *Opt Express* 14 (2006): 10132.
844. Wallace, J., I. Itzkam, and J. Camm. "Irradiance tailoring as a method of reducing thermal blooming in an absorbing medium." *J Opt Soc Am* 64 (1974): 1123.
845. Wallner, E. P. "Comparison of wavefront sensor configurations using optimal reconstruction and correction." *Proc SPIE* 351 (1982): 42.
846. Wallner, E. P. "Optimal wavefront correction using slope measurements." *J Opt Soc Am* 73 (1983): 1771.
847. Wanek, J. M., M. Mori, and M. Shahidi. "Effect of aberrations and scatter on image resolution assessed by adaptive optics retinal section imaging." *J Opt Soc Am A* 24 (2007): 1296.
848. Wang, C. P., and P. L. Smith. "Charged-large-array-flexible mirror." *Appl Opt* 24 (1985): 1838.
849. Wang, J. Y. "Optical resolution through a turbulent medium with adaptive phase compensations." *J Opt Soc Am* 67 (1977): 383.
850. Wang, J. Y., and D. E. Silva. "Wavefront interpretation with Zernike polynomials." *Appl Opt* 19 (1980): 1510.
851. Wang, W. C., H. Lotem, and R. Forber. "Optical electric-field sensors." *Opt Eng* 45 (2006), 124402.
852. Ward, J. E., W. T. Rhodes, and J. T. Sheridan. "Lucky imaging and aperture synthesis with low-redundancy apertures." *Appl Opt* 48 (2009): A63.
853. Weinberg, G. M. *An Introduction to General Systems Thinking*. New York: Wiley, 1975.
854. Welsh, B. M., C. S. Gardner, and L. A. Thompson. "Effects of nonlinear resonant absorption on sodium laser guide stars." *Proc SPIE* 1114 (1989): 203.
855. Welsh, B. M., and C. S. Gardner. "Performance analysis of adaptive-optics systems using laser guide stars and slope sensors." *J Opt Soc Am A* 6 (1989): 1913.
856. Welsh, B. M., and C. S. Gardner. "Effects of turbulence-induced anisoplanatism on the imaging performance of adaptive-astronomical telescopes using laser guide stars." *J Opt Soc Am A* 8 (1991): 69.
857. Welsh, B. M., B. L. Ellerbroek, M. C. Roggemann, and T. L. Pennington. "Shot noise performance of Hartmann and shearing interferometer wavefront sensors." *Proc SPIE* 2534 (1995): 277.
858. Whitman, A. M., and M. J. Beran. "Two-scale solution for atmospheric scintillation from a point source." *J Opt Soc Am A* 5 (1988): 735.
859. Duignan, M. T., B. J. Feldman, and W. T. Whitney, "Stimulated Brillouin scattering and phase conjugation of hydrogen fluoride laser radiation." *Opt Lett* 12 (1987): 111.
860. Whitney, W. T., M. T. Duignan, and B. J. Feldman. "Stimulated Brillouin scattering phase conjugation of an amplified hydrogen fluoride laser beam." *Appl Opt* 31 (1992): 699.
861. Wilcox, C. C., J. R. Andrews, S. R. Restaino, S. W. Teare, D. M. Payne, and S. Krishna. "Analysis of a combined tip-tilt and deformable mirror." *Opt Lett* 31 (2006): 679.

862. Wild, W. J. "Optimal estimators for astronomical adaptive optics." *Top Mtg on Adap Opt, Opt Soc Am Tech Dig Series* 13 (1996): 230.
863. Wild, W. J. "Predictive optimal estimators for adaptive-optics systems." *Opt Lett* 21 (1996): 1433.
864. Wild, W., E. Kibblewhite, and V. Scor. "Quasi-hexagonal deformable mirror geometries." *Proc SPIE* 2201 (1994): 726.
865. Wild, W. J., E. J. Kibblewhite, and R. Vuilleumier. "Sparse matrix wavefront estimators for adaptive-optics systems for large ground-based telescopes." *Opt Lett* 20 (1995): 955.
866. Wild, W. J., E. J. Kibblewhite, R. Vuillemier, V. Scor, F. Shi, and N. Farmiga. "Investigation of wavefront estimators using the Wavefront Control Experiment at Yerkes Observatory." *Proc SPIE* 2534 (1995): 194.
867. Williams, K., P. Glezeu, and R. Gupta. "Real-time measurement of the spatial profile of a pulsed laser by photothermal spectroscopy." *Opt Lett* 13 (1988): 740.
868. Wilson, K., M. Troy, M. Srinivasan, B. Platt, V. Vilnrotter, M. W. Wright, V. Garkanian, and H. Hemmati. "Daytime adaptive optics for deep space optical communications," *Proc. 10th ISCOPS Conf.*, 2003.
869. Wilson, R. N., F. Franza, and L. Noethe. "Active optics I: A system for optimizing the optical quality and reducing the costs of large telescopes." *J Mod Opt* 34 (1987): 485.
870. Winick, K. A., and D. vL. Marquis. "Stellar scintillation technique for the measurement of tilt anisoplanatism." *J Opt Soc Am A* 5 (1988): 1929.
871. Winker, D. M. "Effect of finite outer scale on the Zernike decomposition of atmospheric optical turbulence." *J Opt Soc Am A* 8 (1991): 1568.
872. Winkler, I. C., M. A. Norton, and C. Higgs. "Adaptive phase compensation in a Raman look-through configuration." *Opt Lett* 14 (1989): 69.
873. Winocur, J. "Modal compensation of atmospheric turbulence induced wavefront aberrations." *Appl Opt* 21 (1982): 433.
874. Wirth, A., and A. J. Jankevics. "Adaptive nonlinear control systems for atmospheric correction." *Proc SPIE* 1920 (1993): 245.
875. Witthoft, C. "Wavefront sensor noise reduction and dynamic range expansion by means of optical image intensification." *Opt Eng* 29 (1990): 1233.
876. Wiu, Z., A. Enmark, M. Owner-Petersen, and T. Anderson. "Comparison of wavefront sensor models for simulation of adaptive optics." *Opt Express* 17 (2009): 20575.
877. Wiza, J. L. "Microchannel plate detectors." *Nucl Instrum Methods* 162 (1979): 587.
878. Wizinowich, P., D. S. Acton, A. Gleckler, T. Gregory, P. Stomski, K. Avicola, J. Brase, H. Friedman, D. Gavel, and C. Max. "W. M. Keck Observatory adaptive optics facility." *Top Mtg on Adap Opt, Opt Soc Am Tech Dig Series* 13 (1996): 8.
879. Wizinowich, P., D. Le Mignant, A. H. Bouchez, R. D. Campbell, J. C. Y. Chin, A. R. Contos, M. A. van Dam, S. K. Hartman, E. M. Johansson, R. E. Lafon, H. Lewis, P. J. Stomski, and D. M. Summers. "The W. M. Keck Observatory laser guide star adaptive optics system: overview." *Publ Astron Soc Pac* 118 (2006): 297.
880. Woger, F., and T. Rimmele. "Effect of anisoplanatism on the measurement accuracy of an extended-source Hartmann-Shack wavefront sensor." *Appl Opt* 48 (2009): A35.
881. Wood, R. W., and F. L. Mohler. "Resonance radiation of sodium vapor excited by one of the D lines." *Phys Rev* 11 (1918): 70.

882. Woodruff, C. J. "A comparison, using orthogonal coefficients, of two forms of aberration balancing." *Optica Acta* 22 (1975): 933.
883. Wright, M. W., J. Roberts, W. Farr, and K. Wilson. "Improved optical communications performance combining adaptive optics and pulse position modulation." *Opt Eng* 47 (2008): 016003.
884. Wulff, O., and D. Looze. "Nonlinear control for pyramid sensors in adaptive optics." *Proc SPIE* 6272 (2006): 62721S.
885. Wyant, J. C. "Double frequency grating lateral shear interferometer." *Appl Opt* 12 (1973): 2057.
886. Wyant, J. C. "White light extended source shearing interferometer." *Appl Opt* 13 (1974): 200.
887. Wyant, J. C. "Use of an ac heterodyne lateral shear interferometer with real-time wavefront correction systems." *Appl Opt* 14 (1975): 2622.
888. Xiao, X., and D. Voelz. "On-axis probability density function and fade behavior of partially coherent beams propagating through turbulence." *Appl Opt* 48 (2009): 167.
889. Yahel, R. Z. "Turbulence effects on high energy laser beam propagation in the atmosphere." *Appl Opt* 29 (1990): 3088.
890. Yang, Q., C. Ftaclas, and M. Chun. "Wavefront correction with high-order curvature adaptive optics systems." *J Opt Soc Am A* 23 (2006): 1375.
891. Yariv, A., and T. L. Koch. "One-way coherent imaging through a distorting medium using four-wave mixing." *Opt Lett* 7 (1982): 113.
892. Yellin, M. "Using membrane mirrors in adaptive optics." *Proc SPIE* 75 (1976): 97.
893. Yang, H., X. Li, C. Gong, and W. Jiang. "Restoration of turbulence-degraded extended object using the stochastic parallel gradient descent algorithm: numerical simulation." *Opt Express* 17 (2009): 3052.
894. Yang, P., M. Ao, Y. Liu, B. Xu, and W. Jiang. "Intracavity transverse modes controlled by a genetic algorithm based on Zernike mode coefficients." *Opt Express* 15 (2007): 17051.
895. Yang, P., M. Ao, B. Xu, and X. Yuan. "Way of detecting entire beam path aberrations of laser systems based on a phase-retrieval method." *Appl Opt* 48 (2009): 1402.
896. Au Yaung, J., D. Fekete, D. M. Pepper, and A. Yariv. "A theoretical and experimental investigation of the modes of optical resonators with phase-conjugate mirrors." *IEEE J Quantum Electron* 15 (1979): 1180.
897. Young, D. *Iterative Solution of Large Linear Systems*. New York: Academic Press, 1971.
898. Yura, H. T., and S. G. Hanson. "Optical beam wave propagation through complex optical systems." *J Opt Soc Am A* 4 (1987): 1931.
899. Zawadzki, R. J., B. Cense, S. M. Jones, S. S. Olivier, D. T. Miller, and J. S. Werner. "Ultra-high-resolution optical coherence tomography gets adaptive-optic 'glasses'." *Laser Focus World* 44 (2008): 55.
900. Zehnder, L. "A new interferometer." *Z Instrumentenkd* 11 (1891): 275.
901. Zel'dovich, B. Ya., and V. V. Shkunov. "Optical phase conjugation by a depolarized pump." *Sov Phys JETP Lett* 27 (1978): 214.
902. Zel'dovich, B. Ya., N. F. Pilipetsky, and V. V. Shkunov. *Principles of Phase Conjugation*, Springer Ser. Opt. Sci. 42, T. Tamir, ed., Berlin: Springer-Verlag, 1985.

903. Zernike, F. "Diffraction theory of the knife-edge test and its improved form, the phase contrast method." *Physica* 1 (1934): 689.
904. Zilberman, A., E. Golbraikh, and N. S. Kopeika. "Propagation of electromagnetic waves in Kolmogorov and non-Kolmogorov atmospheric turbulence: three-layer altitude model." *Appl Opt* 47 (2008): 6385.
905. Zommer, S., E. N. Ribak, S. G. Lipson, and J. Adler. "Simulated annealing in ocular adaptive optics." *Opt Lett* 31 (2006): 939.
906. Zon, N., O. Srour, and E. N. Ribak. "Hartmann-Shack analysis errors." *Opt Express* 14 (2006): 635.
907. Zuev, V. E., and V. P. Lukin. "Dynamic characteristics of optical adaptive systems." *Appl Opt* 26 (1987): 139.

Index

Physics

SERIES IN OPTICS AND OPTOELECTRONICS

SERIES EDITORS: E. ROY PIKE AND ROBERT G. W. BROWN

Principles of Adaptive Optics

Third Edition

Since the publication of the second edition of **Principles of Adaptive Optics**, the developments and applications in this area have increased tremendously. Observatories are now producing outstanding science through adaptive optics technology; components, such as micromachined deformable mirrors and very low noise detectors, are revolutionizing the field; and the industrial and medical arenas are harnessing the capabilities of adaptive optics tools in free-space laser communications, laser-induced fusion, and retinal imaging.

Although the complexity of these applications has intensified, the principles essentially remain the same. **Principles of Adaptive Optics, Third Edition** offers a comprehensive guide to the systems, components, and processes of adaptive optics. It presents the principles used to extract information from beams of light and improve the performance of optical systems by correcting distortions and aberrations.

Features

- Covers the background and history of adaptive optics technology
- Describes many types of optical disturbances and the pros and cons of various adaptive optics system configurations
- Highlights applications in astronomy, communication systems, and medical imaging
- Discusses the emergence of novel components, such as micromachined mirrors
- Details important equations for atmospheric turbulence, optical compensation, and laser guide stars
- Includes over 900 references that encompass recent papers, major contributions, and seminal papers

Condensing the vast array of literature into one accessible source, this edition incorporates recent developments and adds many new references. It discusses how the principles are applied to astronomical imaging systems, retinal imaging, and beam propagation systems. The book logically progresses from determining the sources of aberrations to designing and analyzing systems to describing major subsystems, such as wavefront sensors, correction devices, wavefront reconstruction, and real-time controls.

K10425

CRC Press
Taylor & Francis Group
an Informa business
www.crcpress.com

6000 Broken Sound Parkway, NW
Suite 300, Boca Raton, FL 33487
270 Madison Avenue
New York, NY 10016
2 Park Square, Milton Park
Abingdon, Oxon OX14 4RN, UK

ISBN: 978-1-4398-0858-0
90000
9 781439 808580

www.crcpress.com